GRAVITY-DRIVEN CONTINUOUS THIN FILM FLOW OVER TOPOGRAPHY

by

Sergii Veremieiev

Submitted in accordance with the requirements for the degree of

Doctor of Philosophy

The University of Leeds

School of Mechanical Engineering

February 2011

Abstract

This thesis is directed primarily at a systematic theoretical investigation of gravity-driven thin film flow over various topographical features, the effect of inertia being of particular interest. The problem is solved using a hierarchy of models based, in order of decreasing complexity, on (i) the full Navier-Stokes system of equations; (ii) a depth averaged form of the latter; (iii) the lubrication equations. Every effort has been made to solve the underlying discrete equation set in each case efficiently using state-of-the-art solution strategies, thus guaranteeing accurate and mesh-independent predictions. The solution of models (ii) and (iii) centres on the use of a multigrid methodology together with automatic, error controlled, time-stepping and the proper treatment of any associated nonlinear advective terms. A discrete analogue of model (i), for both two- and three-dimensional flows, is obtained using a finite element formulation with the free surface parametrised via the method of spines and the system solved using a parallel multifrontal method together with a memory-efficient out-of-core storage approach.

A comprehensive set of results is presented for flow over both one- and two-dimensional topography, generated using models (ii) and (iii); the predictions obtained are contrasted with each other and compared with existing related experimental data. The free-surface disturbance arising for the problems investigated is revealed to be influenced significantly by the presence of inertia which leads to an increase in the magnitude and severity of the resulting capillary ridge, surge and trough formations present. A complementary exploration, using model (i) is undertaken which reveals the attendant internal flow structure. It shows that two-dimensional flow over spanwise topography and three-dimensional flow over localised trench topography can lead to different internal, inertia dependent, flow topologies; findings that are consistent with previously reported results for the well-known lid-driven cavity problem.

Finally, the effect of a normal electric field on the free-surface disturbance generated by inertial thin film flow over topography is investigated using model (ii) coupled with a Fourier series separable solution of Laplace's equation for the electric potential. Results for both two- and three-dimensional flow reveal that a significant electric field strength can be used to effectively planarise the free-surface capillary ridges and depressions that arise. The two-dimensional solutions obtained are consistent with those reported elsewhere for the case when inertia is neglected and highlight the importance attached to choosing an appropriate means of embodying the latter. Furthermore, the novel results generated for three-dimensional flow demonstrate that as Reynolds number increases, larger electric field strengths are required to planarise the associated free-surface disturbance.

Publications

1. Veremieiev, S., Gaskell, P.H., Lee, Y.C. & Thompson, H.M. 2009 Electric fields as a means of controlling thin film flow over topography. In *Proceedings on CDROM of 2nd Micro and Nano Flows Conference MNF-2009*, pp. 21:1–8. Brunel University, West London, UK

2. Veremieiev, S., Thompson, H.M., Lee, Y.C. & Gaskell, P.H. 2010*a* Inertial thin film flow on planar surfaces featuring topography. *Comput. Fluids* **39** (3), 431–450

3. Veremieiev, S., Thompson, H.M., Lee, Y.C. & Gaskell, P.H. 2010*b* Inertial two- and three-dimensional thin film flow over topography. *Chem. Eng. Process.: Process Intens.* In Press, Corrected Proof

4. Veremieiev, S., Thompson, H.M., Lee, Y.C. & Gaskell, P.H. 2010*c* Three-dimensional inertial thin film flow on planar substrates containing occlusions. In *Proceedings on CDROM of 5th European Conference on Computational Fluid Dynamics ECCOMAS CFD 2010* (ed. J.C.F. Pereira, A. Sequeira & J.M.C. Pereira), pp. 01399:1–11. Lisbon, Portugal

5. Veremieiev, S., Gaskell, P.H., Lee, Y.C. & Thompson, H.M. 2011*a* Predicting three-dimensional inertial thin film flow over microscale topography. In *Computational Fluid Dynamics 2010*. Springer, Engineering series. In Press, Accepted for Publication

6. Veremieiev, S., Thompson, H.M., Scholle, M., Lee, Y.C. & Gaskell, P.H. 2011*b* Electrified thin film flow at finite Reynolds number on planar surfaces featuring topography. In Press, Submitted for Review

To my wife, Lenochka, for her unconditional love, support and patience.

Acknowledgements

First and foremost I wish to express my sincere gratitude to my supervisors Prof. Philip H. Gaskell and Dr. Harvey M. Thompson, because they introduced me to the subject area of thin film flow and guided my research with vivid interest. Without their professional advice and expertise, the thesis would not be possible. Also my sincere thanks go to my scientific advisor Dr. Yeaw Chu Lee for his invaluable support throughout my research work.

My thanks go to those who provided their expert technical assistance, Dr. Graham J. Blyth, Mr. Ted Allwood, Mrs. Margaret I. Gibson, Dr. Jon L. Summers, Dr. Mark C.T. Wilson and Dr. John H. Hodrien.

I would like to take this opportunity to express appreciation to my school and university teachers, especially Zhikulina Zoya Timofeevna, Klimenko Oleg Nikolaevich, Isaenko Vladimir Vasilievich, Melnichuk Tatiana Vladimirovna, Rusakov Vladimir Fedorovich, Kolomenskaya Valentina Vladimirovna, Rusanova Oksana Alexandrovna, Markovskaya Elena Vasilievna, Shaldyrvan Valeriy Anatolievich, Bagatyrev Valeriy Andreevich, Borodin Mikhail Alexeevich and others. I also owe special thanks to Semko Alexander Nikolaevich, who helped me to make the first steps into the world of science and made a huge contribution into my development as a young scientist.

In addition thanks are also due to my roommates, Akram, Cecilia, Juan and Marco, who were very kind and helpful to me at all times.

Above all, I wish to express my deep gratitude to my mum Victoria, my dad Alexander, my brother Andrey, my grandmothers Galina and Nina for their presence, continued support and encouragement. My special thanks go to my wife Lena; without her support this thesis would never have turned into reality.

Finally I gratefully acknowledge the financial support of the European Union Marie Curie Action, contract MEST-CT-2005-020599.

Contents

List of figures

List of tables

Nomenclature

Below is a list of symbols which have their general meaning in all chapters. A convention used throughout the thesis is that, unless otherwise indicated, upper case quantities are dimensional while lower case ones are dimensionless; in addition operators are identified using a mathematical caligraph font, while vectors and tensors are denoted by bold font.

Latin letters

A_m, B_n, $C_{m,n}$	Eigenfunctions of the Sturm-Liouville electric field problem
A_c	Chézy coefficient
C	Transpose of matrix of cofactors
Ca	Capillary number
$\boldsymbol{c}$	Global corrections vector
D, d	Distance between electrodes
$\boldsymbol{d}$	Global defects vector
$\boldsymbol{d}_k$	Fixed direction vector of spine
dim	Dimensionality of the problem
$\boldsymbol{E}$, $\boldsymbol{e}$	Vector of electric field strength
$\mathcal{E}$	Electric field Fourier operator
E_B, e_b	Dielectric breakdown strength
E_0	Strength of electric field
F, f	Coordinate of free surface
$\mathcal{F}$	Advective operator
Fr	Froude number
$\boldsymbol{G}, \boldsymbol{g}$	Acceleration due to gravity
G_0	Standard gravity constant
H, h	Film thickness
$\mathcal{H}$	Electric field Hilbert operator
H_0	Asymptotic film thickness

$h_{i,j}$	Discretised film thickness
h_k	Spinal distances
I	Inertia parameter
$\boldsymbol{I}$	Unity tensor
$\boldsymbol{I}_{k-1\to k}$	Bilinear interpolation operator
$\boldsymbol{i}$, $\boldsymbol{j}$, $\boldsymbol{k}$	Basis vectors of Cartesian coordinates
J	Jacobian of transformation from global to local natural coordinates
L_P, W_P, l_p, w_p	Length and spanwise width of domain
L_T, W_T, l_t, w_t	Length and spanwise width of topography
L_0	Capillary length
L_β	Local natural coordinates
$\bar{\boldsymbol{L}}$, $\bar{\boldsymbol{U}}$	Lower and upper triangular matrices
$\boldsymbol{M}$, $\boldsymbol{m}$	Maxwell stress tensor
$\mathcal{M}^h$, $\mathcal{M}^p$, $\mathcal{M}^u$, $\mathcal{M}^v$	Operator of averaged mass conservation, pressure, averaged stremwise and spanwise momentum equations
N	Gravity parameter
$\boldsymbol{N}$	Vector normal to free surface
$\boldsymbol{\mathcal{N}}$	Global residual vector
$\mathcal{N}^h$, $\mathcal{N}^p$, $\mathcal{N}^u$, $\mathcal{N}^v$	Residual of averaged mass conservation, pressure, averaged streamwise and spanwise momentum equations
N^f	Number of terms in truncated Fourier series
$\boldsymbol{\mathcal{N}}^{mom}$, $\mathcal{N}^{cont}$, $\mathcal{N}^{kin}$	Residual of Navier-Stokes, continuity and kinematic equations
$\boldsymbol{n}$	Unit vector normal to free surface
n^e, n^s	Total number of elements and free-surface elements

n^i, n^j, n^k	Total number of nodes of velocity/coordinates, pressure and free-surface velocity/coordinates
n_p	Total number of subdomains
n_x, n_y	Number of cells/nodes in streamwise and spanwise directions
n^α, n^β, n^γ	Total number of local nodes of velocity/coordinates, pressure and free-surface velocity/coordinates
P, p	Pressure
P_A, p_a	Atmospheric pressure/pressure of the gas
P_0	Pressure scale
Pe	Mesh Péclet number
$p_{i,j}$	Discretised pressure
p_j	Nodal values of pressure
p_β	Local nodal values of pressure
R	Curve bounding the free-surface
$\boldsymbol{\mathcal{R}}$	Global right-hand-side vector
$\mathcal{R}^h$, $\mathcal{R}^u$, $\mathcal{R}^v$	Right-hand-side of averaged mass conservation, averaged streamwise and spanwise momentum equations
$\boldsymbol{R}_{k\to k-1}$	Full-weighting restriction operator
Re	Reynolds number
Re_{cr}	Critical Reynolds number
S, s	Coordinate of topography
S_0, s_0	Depth/height of topography
St	Stokes number
T, t	Time
T_0	Time scale
$\boldsymbol{t}$	Unit vector tangential to free surface

$\boldsymbol{t}\|_R$	Unit vector tangential to free surface, but normal to curve R bounding it
trunc (x)	Truncation function from real to integer
U, V, W, u, v, w	Components of velocity in Cartesian coordinates
$\boldsymbol{U}$, $\boldsymbol{u}$	Vector of velocity in Cartesian coordinates
U_0	Velocity scale
$u_{i+1/2,j}$, $v_{i,j+1/2}$	Discretised depth-averaged streamwise and spanwise components of velocity
u_i, v_i, w_i	Nodal values of components of velocity
$\boldsymbol{u}_i$	Nodal values of vector of velocity
u_α, v_α, w_α	Local nodal values of components of velocity
$\boldsymbol{u}_\alpha$	Local nodal values of vector of velocity
$\bar{u}$, $\bar{v}$	Depth-averaged streamwise and spanwise components of velocity
V_B, v_b	Dielectric breakdown potential difference
W	Electric field parameter
We	Weber number
X, Y, Z, x, y, z	Cartesian coordinates
$\boldsymbol{X}$, $\boldsymbol{x}$	Vector of Cartesian coordinates
X_T, Y_T, x_t, y_t	Streamwise and spanwise coordinates of centre of topography
X^*, Y^*, x^*, y^*	Streamwise and spanwise coordinates shifted to centre of topography
x_i, y_i, z_i	Nodal values of coordinates
$\boldsymbol{x}_i$	Nodal values of coordinate vector
x_k^b, y_k^b, z_k^b	Fixed base coordinates of spine
$\boldsymbol{x}_k^b$	Fixed base coordinate vector of spine
x_α, y_α, z_α	Local nodal values of coordinates
$\boldsymbol{x}_\alpha$	Local nodal values of coordinate vector
$\boldsymbol{z}$	Global solution vector

Greek letters

α_t, β_t	Variables defining direction of vector tangential to free surface
γ	Adjustable integration parameter
Γ	Free-surface boundary
Γ_s	Domain of free-surface element
Δ, δ	Steepness of topography
$\Delta_{i,k}$, $\widetilde{\Delta}_{i,k}$	Boolean matrix relating global node to the corresponding free-surface node or spine
$\Delta^{(e)}_{i,\alpha}$, $\Delta^{(e)}_{j,\beta}$, $\Delta^{(s)}_{k,\gamma}$	Boolean matrices relating global node to the corresponding local node
Δt	Time increment
Δx, Δy	Streamwise and spanwise mesh increments
ε	Long-wave ratio
ε_e	Electrical permittivity
θ	Substrate inclination angle
K, κ	Free-surface curvature
λ_m, μ_n	Eigenvalues of Sturm-Liouville electric field problem
μ	Newtonian dynamic viscosity
ρ	Density
σ	Surface tension
$\boldsymbol{T}$, $\boldsymbol{\tau}$	Viscous stress tensor
Φ, ϕ	Electric potential
ϕ_i, ψ_j, ϕ_k	Basis functions for velocity/coordinates, pressure and free-surface velocity/coordinates
Ω	Flow domain
Ω_e	Domain of element

Abbreviations

ALE	Arbitrary Lagrangian-Eulerian
BLAS	Basic linear algebra subprograms
BLACS	Basic linear algebra communication subprograms
CGNR	Conjugate gradient normal residual method
CPU	Central processing unit
DAF	Depth-averaged form
DOF	Number degrees of freedom
EXP	Experiment
FAS	Full approximation storage
FMG	Full multigrid
IBL	Integral-boundary-layer approximation
LAPACK	Linear algebra package
LBB	Stability condition named after Ladyzhenskaya, Babuška and Brezzi
LTE	Local truncation error
LUB	Lubrication equations
LUBI	Lubrication equations with inertia
MPI	Message passing interface
MUMPS	Multifrontal massively parallel sparse direct solver
N-S	System of Navier-Stokes and continuity equations
PV	Principal value
ScaLAPACK	Scalable linear algebra package
TVD	Total variation diminishing

Chapter 1

Introduction

Contents

1.1 Motivation

Numerous manufacturing processes require the deposition of thin liquid films, involving a balance between viscous and surface tension forces, on a variety of substrates. In the coating industries for example, several devices exist which have been optimised specifically for the continuous production and fast throughput of uniform, defect free, films on flat homogeneous substrate, made from plastic, metal, paper, etc. These encompass a wide range of applications and about which much of the underpinning basic science is now reasonably well documented, see Kistler & Schweizer (1997) and Weinstein & Ruschak (2004) for example. The many roles and relevance of thin liquid films, whether they occur naturally or feature/arise as part of a particular engineering, technological or scientific application, is exemplified in the recent comprehensive review of Craster & Matar (2009).

The problem of thin film flow on substrates containing man-made, micro-scale topographical features with a pre-determined functionality, such as displays, printed circuits and sensors, is less well understood. Indeed, the areas in which such flow is encountered are endless, encompassing latterly the rapidly evolving area of microfluidics, see for example Tabeling (2005), and the need to manipulate flow on an ever decreasing scale in the context of lab-on-chip devices. In addition, one should not forget the consequence(s) associated with the presence of unwanted surface topography, contaminates such as dust specks or irregularities resulting from a particular stage in a manufacturing process.

Further examples of the above flow types can be found in many engineering applications such as: the manufacture of micro-scale sensors and devices, Menetrier-Deremble & Tabeling (2006); heat exchanger design, Focke & Knibbe (1986), Webb (1994) and Helbig, Nasarek, Gambaryan-Roisman & Stephan (2009); the production of electrolysis cells, Alekseenko *et al.* (1994), distillation trays, de Santos, Melli & Scriven (1991), and liquid cooled turbine

blades, Wilson, Duffy & Davis (2001); the performance of vaporization turbine combustion chambers, Helbig, Alexeev, Gambaryan-Roisman & Stephan (2005); the production of electronic components for photographic equipment, displays and printed circuits, Decré & Baret (2003); control of film uniformity in the microlithography processes, Ho, Tay, Lee & Schaper (2004).

The realisation that naturally occurring surface patterns, regular and randomly distributed, are a key feature of numerous biological systems provides a different impetus: thin liquid films being important in areas as diverse as tissue engineering, Gaver & Grotberg (1990), the redistribution of liquids in lung airways and linings, Grotberg (1994, 2001), bioadhesion, Gallez & Coakley (1996), plant disease control, Walters (2006), biofilms, Eberl & Sudarsan (2008), flows in the flexible tubes of the body, Grotberg & Jensen (2004), tear-film flows, Shyy, Francois, Udaykumar, N'dri & Tran-Son-Tay (2001), and water snail locomotion, Lee, Bush, Hosoi & Lauga (2008*a*). In addition the strong driver towards ultimately mimicking the behaviour of nature's surfaces, Abbott & Gaskell (2007), has brought the subject of film flow over topography into even sharper focus.

In a broader context there are several other important areas and applications involving thin film flows. For example: geophysically in the case of lava flows and melting spreads, Griffiths (2000); coastal flows, Helfrich & Melville (2006); debris, granular and mud flows together with the destructive evolution of a snow avalanche, Ancey (2007); gravity currents, Huppert (2006); ice sheet models, Baral, Hutter & Greve (2001).

The focus of this thesis is continuous thin film flow over micro-scale topographical features. Accordingly, this chapter presents a thorough review of the related existing experimental and theoretical investigations that have appeared in the literature. Section 1.2 provides an overview of the modelling work that has been reported based on the long-wave approximation for cases of both negligible and significant inertia; in contrast Section 1.3 covers the ap-

proaches that have involved solving the more general Stokes and Navier-Stokes problem. The complementary experimental studies that have been undertaken and the results reported therein are described. Next, the methods that have been suggested and explored for controlling the free-surface disturbance experienced by such films are discussed in Section 1.4. Section 1.5 covers the relevant literature that has appeared in relation to the stability and dynamics of free-surface film flow. Finally, an outline of the thesis is provided in Section 1.6.

1.2 Long-wave analysis

1.2.1 Negligible inertia

Using the unsteady Navier-Stokes and continuity (N-S) equations to solve and predict the behaviour of thin liquid films numerically represents a formidable task due to the large computational cost required to achieve the accuracy necessary to generate meaningful mesh-independent solutions, especially in three dimensions. Accordingly, the bulk of the theoretical work that has appeared to date has relied on the assumption that creeping flow conditions prevail allied to the fact that for many thin film flows encountered in practice the long-wave parameter, the ratio of the undisturbed asymptotic film thickness to that of the characteristic in-plane length scale of the flow, is small. Accordingly, if the velocity and pressure fields are expanded in terms of this small parameter and substituted into the N-S equations then, on retaining leading order terms, the result is a more tractable yet highly nonlinear degenerate fourth-order partial differential equation for the film thickness, commonly referred to as the lubrication approximation, which is still capable of capturing the dominant physics, see Oron, Davis & Bankoff (1997).

It is no surprise that the above lubrication approximation has proved popular,

especially for thin film flows over non-planar topography, where a simple generalisation is applied leading to the governing equation for the film thickness. Examples of long-wave analyses considering film flows over discrete, steep topographical features include the early work of Stillwagon, Larson & Taylor (1987), Stillwagon & Larson (1988, 1990) and Pritchard, Scott & Tavener (1992) who considered radial outflow during spin coating and gravity-driven flow down an inclined plane, respectively; a complementary set of experiments is provided as well. A key finding by both sets of authors is that lubrication theory proved surprisingly accurate for their modelling purposes; in addition Stillwagon & Larson (1990) are credited as being the first to obtain a one-dimensional analytic expression for the standing capillary wave which forms at the leading edge of a trench topography and its associated downstream exponential decay. In a similar vein, Peurrung & Graves (1991, 1993), reported both experimental and numerical results for spin coating that are in qualitative agreement. Of note also is the work of Kalliadasis, Bielarz & Homsy (2000), where the flow over a one-dimensional trench and mound is analysed by means of the lubrication approach over the governing parameter space, i.e. the depth/height of the trench and applied external body force. Their work revealed that the characteristic capillary ridge, that develops before the entrance to a trench or exit from a mound, is suppressed in the presence of a significant vertical component of gravity. The lubrication approximation has also been applied successfully for the understanding of gravity-driven rivulet flows, Wilson & Duffy (1998), Wilson, Duffy & Ross (2002) and Wilson & Duffy (2005), and the fingering problem that arises for film flow onto an inclined plane, Kondic & Diez (2001) and Kondic & Diez (2005).

Analytical solutions of the lubrication approximation have been constructed by means of a Green's function formulation for the case of small arbitrary one-dimensional spanwise topography (Fernandez Parent, Lammers & Decré, 1998; Lucea, Decré & Lammers, 1999) and two-dimensional localised topogra-

phy, Hayes, O'Brien & Lammers (2000). In the case of spanwise topography the Green's function solutions for step-up/down and trench/hump topography were verified via complementary numerical solutions and comparison with their own experimental measurements and those of Messé & Decré (1997); the solution for localised topography was verified subsequently following the experiments for steep, localised trench/hump topography reported by Baret & Decré (2000) and Decré & Baret (2003). In all cases the associated experimental free-surface disturbance data was obtained in the form of interference images created by beams reflected from the air-liquid and liquid-substrate interfaces bounding the flow. The same are found to be in very good agreement with the analytics, despite the fact that the Green's function solutions obtained are not strictly valid for topography whose height is comparable to the film thickness; plus the two-dimensional Green's function solution in Hayes *et al.* (2000) is for the case when the substrate is aligned vertically, rather than at some lesser angle as in Decré & Baret (2003). Figure 1.1 shows the sort of false colour representation obtained of the free-surface disturbances generated for flow over a localised rectangular trench topography, Decré & Baret (2003), the colour maps shown correspond to the degree of free-surface disturbance: red representing the planar asymptotic film.

The fourth-order lubrication equation for the film thickness mentioned earlier has been solved using a variety of numerical methods, with the semi-implicit, alternating direction, time-splitting scheme, Christov, Pontes, Walgraef & Velarde (1997) and Schwartz & Eley (1998), enjoying wide usage. The argument used for employing such schemes is that they combine some of the stability properties of implicit schemes with the cost efficiency of explicit ones. However, when fine meshes are required to ensure mesh-independent solutions the choice of time-step becomes severely restrictive. With this in mind an investigation concerning droplet motion underpinned by lubrication theory, Daniels, Ehret, Gaskell, Thompson & Decré (2001), showed that the alternative approach of

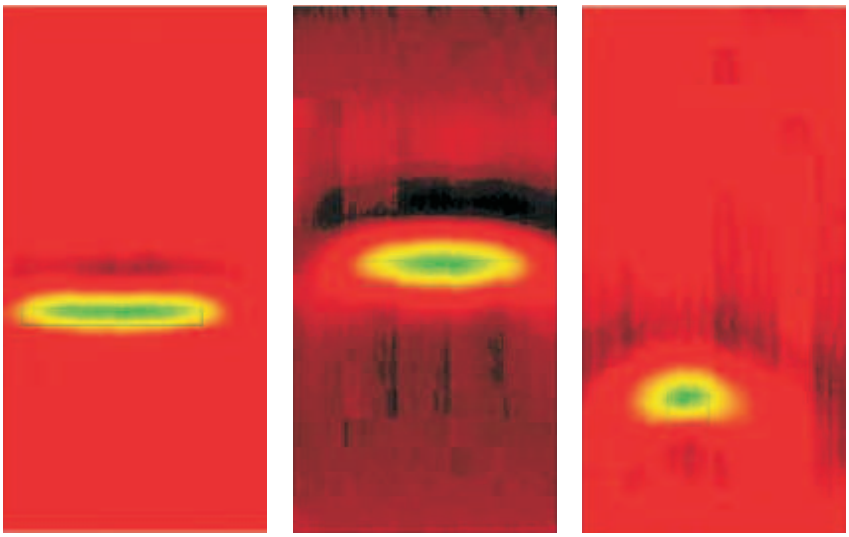

FIGURE 1.1: False colour map representation of the free-surface disturbances obtained from the experiments performed by Decré & Baret (2003) for the case of thin film flow over rectangular trench topography with spanwise width-length ratio: (from left to right) 8.33, 5 and 1. The colour corresponds to the degree of the free-surface disturbance: red representing the planar asymptotic film. Flow is from top to bottom.

solving a system of two coupled second-order lubrication equations for the film thickness and the pressure adopting a fully implicit multigrid formulation to: (i) be more robust; (ii) return an order of magnitude improvement in the rate of convergence for the levels of grid refinement required for accuracy; and (iii) utilise far less memory. The above points were reinforced further by Gaskell, Jimack, Sellier, Thompson & Wilson (2004*b*) who combined the same multigrid approach with error-controlled adaptive timestepping to solve the problem of the flow of gravity-driven thin liquid films on non-porous substrates with topography. Their work revealed that the long-wave approximation leads to very good solutions, even in regions of parameter space where it is not strictly valid. The methodology was subsequently refined to embody error-controlled automatic mesh adaption, especially suited for the case of film flow over localised or sparsely distributed topographical features that are either fully submerged, Lee, Thompson & Gaskell (2007), or extend through the film, Sellier, Lee, Thompson & Gaskell (2009). Significant further improvement in solution times have been achieved without loss of accuracy, even in the case of free-

surface film and droplet spreading flows over real, functional surfaces, Glass, Walters, Gaskell, Lee, Thompson, Emerson & Gu (2010), and for thin film flows with additional physics included, such as evaporation, see Gaskell, Jimack, Sellier & Thompson (2006) and over flexible substrate, Gaskell, Lee & Thompson (2010).

Parallelisation of the above underpinning multigrid algorithm and the use of multiple processor computing platforms has also been found to bring benefits and to be particularly well suited to predicting thin film flow on surfaces containing densely packed and complex topographical features, Gaskell, Jimack, Koh & Thompson (2008) and Lee, Thompson & Gaskell (2009*a*).

Furthermore, the recent study by Cowling, Gaskell, Lee & Thompson (2011) has conclusively shown that solving the lubrication system as two coupled second-order equations for the film thickness and the pressure, rather than just as a single fourth-order for the film thickness, within a multigrid framework, to be superior to and much more computationally efficient than using a time splitting approach.

1.2.2 Significant inertia

Several attempts to extend lubrication theory to cases with non-zero Reynolds number have been made; for example, accounting for inertia as in the early work by Benney (1966), a model that is now commonly referred to as the long-wave Benney-type model. The same type of approximation has appeared subsequently in the work of Lin (1974), Nakaya (1975) and Chang (1986). In a similar fashion to the lubrication equation, the Benney-type model is obtained via a perturbation analysis and expansion of the unknowns of the problem in terms of the long-wave parameter, which is assumed to be small. Inertia is taken into account in terms of the first-order dynamics of the perturbation analysis only, thus is applicable for flows with a Reynolds number of O(1).

The Benney-type model occurs as a natural generalisation of the lubrication approach for thin film flows with inertia and has been utilised by several researchers including Joo, Davis & Bankoff (1991), Bielarz & Kalliadasis (2003) and Tseluiko & Blyth (2009).

As an alternative to employing the above theory the influence of inertia on gravity-driven two-dimensional film flow over a plane surface has been explored in terms of the so-called integral-boundary-layer (IBL) approximation, that enables the above mentioned restriction on the Reynolds number to be relaxed; a key feature of IBL approximation is the assumption that the velocity profile across the film is parabolic. Its mathematical formulation, in which the resulting equations are expressed in terms of the film thickness and mean flow rate, can be traced back to Shkadov (1967, 1968), who used it to predict solitary waves in a thin viscous liquid layer on a uniform vertically aligned surface.

Refinements to the IBL approximation have been subsequently carried out by Ruyer-Quil & Manneville (1998, 2000, 2002) and Nguyen & Balakotaiah (2000): (i) by approximating the velocity profile using high-order polynomials (rather than just a parabolic function), whose coefficients are determined by gradient expansion of the solution and (ii) by retaining terms of second-order-accuracy in the long-wave expansion of the N-S equations and the free-surface stress boundary condition, leading to a system of equations for three unknowns - the film thickness, mean flow rate and shear stress at the surface. The latter model has been refined further still, Amaouche, Mehidi & Amatousse (2005), by retaining terms of third-order-accuracy and approximating the velocity profile by polynomials up to eighth-order whose coefficients are obtained by Galerkin projection. Another approach worth mentioning is the depth averaged kinetic energy balance or energy integral method based on a velocity weighted average of the N-S equations proposed by Usha & Uma (2004), which is shown to be a reasonable alternative to a standard IBL averaging of

the N-S equations.

Recently, Trifonov (2004) and Saprykin, Koopmans & Kalliadasis (2007*a*) have adopted the IBL approach for the case of flow over a surface containing topography; the former considered film flow on corrugated surfaces, while the latter investigated the problem of a thin film flowing down a vertical surface and encountering a steep step-down topography, with viscoelastic effects included, showing that increasing the Reynolds number leads to an amplification of the capillary ridge formed before the step. Analytical solutions of the IBL system of equations have been derived in Heining & Aksel (2010) via a perturbation analysis for the case of thin film flow of a Non-Newtonian power-law fluid down over undulating surface; their perturbation analysis is based on the assumption of a weak undulation, i.e. its amplitude being much smaller than the film thickness. It is revealed that the undulation has, in most cases, a stabilising influence on the free surface.

Last but not least, researchers have extended the use of the lubrication model by developing evolution equations using coordinate systems based on a curved substrate with a general form; this has been done by invoking the long-wave approximation in the case of both negligible inertia, Roy, Roberts & Simpson (2002) and Howell (2003), and significant inertia, see Roberts & Li (2006).

1.3 Solutions of full Stokes and Navier-Stokes equations

Solving the full Stokes or Navier-Stokes equations, subject to their attendant boundary conditions overcomes many of the restrictions associated with models based on the long-wave approximation - namely removing the constraint on choice of capillary number, film thickness or topography aspect ratio.

Perturbation analyses, underpinned by assumptions similar to those of the

long-wave approximation, have been applied effectively to construct analytical solutions of the Stokes and Navier-Stokes equations for both two-dimensional film flow over an undulating (wavy) substrate, Wang (1981, 1984) and Wierschem, Scholle & Aksel (2002), and three-dimensional film flow over wavy substrate with doubly-periodic corrugations, Wang (2005), Luo & Pozrikidis (2006, 2007) and Heining (2009). In Wierschem *et al.* (2002), for example, a perturbation analysis is utilised in two different limits by assuming the substrate's wavelength to be much larger than (i) the film thickness and (ii) its amplitude; complementary experimental measurements were obtained showing that the theory predicts the thickness of thin films over weakly undulating substrates very well. Increasing the film thickness as well as increasing the waviness of the substrate, however, results in quite large differences. In Luo & Pozrikidis (2007) a Stokes flow, while in Wang (2005), Luo & Pozrikidis (2006) and Heining (2009) a flow with a finite Reynolds number is assumed, and perturbation analyses performed in terms of undulations with a small amplitude.

The subsequent experiments by Wierschem *et al.* (2003) and Wierschem & Aksel (2004) revealed, however, a perturbation analysis to be incapable of predicting the eddy structure of the flow located within the valleys of the substrate, especially for the cases of a strongly undulating substrate or a strong inertial influence; Figure 1.2 shows an example of the visualisations of particle traces achieved by Wierschem *et al.* (2003) using fluorescence imaging. Their results were found to be consistent with earlier experimental studies for shear-driven flows over a cavity, see the corresponding particle paths visualisation in Figure 1.3 taken from Taneda (1979). In addition their experiments demonstrate that there is a strong coupling between inertia and topography effects, with the latter leading to remarkable stabilisation of the flow, particularly at high Reynolds numbers.

The earlier limitations associated with the use of perturbation analysis for the

case of thin film flow over wavy substrate, have been overcome by constructing semi-analytical solutions of the full Stokes equations, Scholle, Wierschem & Aksel (2004), Scholle, Rund & Aksel (2006) and Scholle & Aksel (2007); complex function theory is used to reduce the two-dimensional Stokes equations to a system of ordinary differential and integral equations for functions of one variable, which are solved by means of Fourier analysis and an iterative procedure. The solutions obtained are found to be in a perfect agreement with the experiments by Wierschem *et al.* (2003) and confirm the vortex structure present in the valleys of a wavy substrate. The inertial influence, which can be accounted for by solving the full Navier-Stokes equations, was predicted using finite elements by Scholle, Haas, Aksel, Wilson, Thompson & Gaskell (2008) as discussed later.

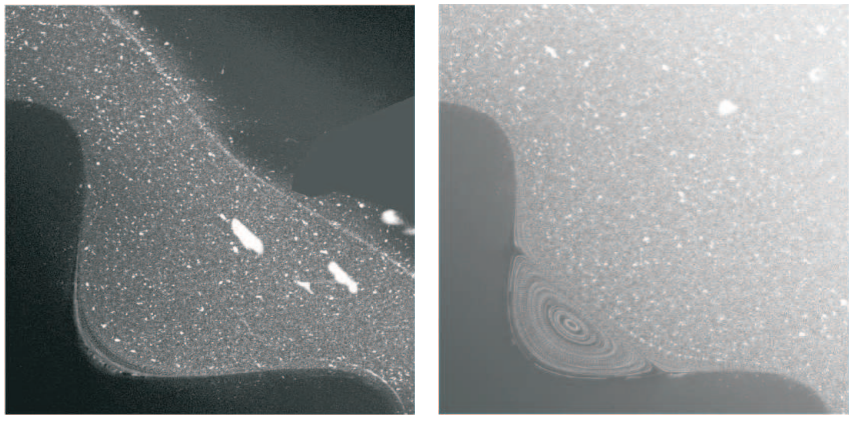

FIGURE 1.2: Experimental visualisation of particle paths for film flow over strongly undulating substrate with film thickness-wavelength ratio: 0.32 (left) and 2.4 (right), see Wierschem *et al.* (2003). Flow is from upper left to lower right. The undulating substrate is at the lower left, the film itself is seen as a flecked area, and its free surface as a thin bright line.

In contrast to flow over periodic wavy substrate, Stokes flow over substrate containing steep topographical features has been investigated, in the main numerically, by means of the boundary element method; this has been done in both two- and three dimensions. There are, however, only a few examples to be found in the literature since the computational resources required to obtain a full and accurate numerical solution of the Stokes equations using a

boundary element method, are much larger than when solving discrete forms of the long-wave models discussed earlier.

Examples of such two-dimensional Stokes flow include: flow over a periodic wall of arbitrary geometry, Pozrikidis (1988) and Tseluiko, Blyth, Papageorgiou & Vanden-Broeck (2008*a*); flow over a spanwise rectangular trench, Mazouchi & Homsy (2001); flow with a moving contact line over a surface either with or without topography by Mazouchi, Gramlich & Homsy (2004) and Gramlich, Mazouchi & Homsy (2004), respectively; the effect of an applied surface shear stress for thin film flow over a rectangular cavity, Shuaib, Power & Hibberd (2006); film flow on an inclined plane with an opening (a gap) at the bottom of the plane representing an outlet, Shuaib, Power & Hibberd (2009). In all these examples the results obtained were found to be in a good agreement with predictions from lubrication theory in the case of small capillary number and small topographic features.

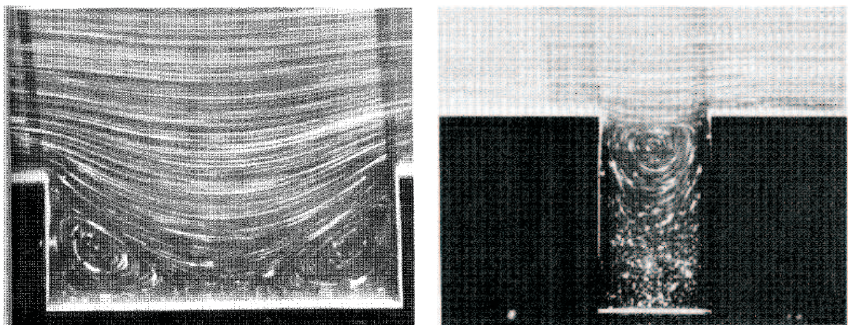

FIGURE 1.3: Experimental visualisation of particle paths for a shear-driven flow over a wall containing a rectangular cavity with depth-width ratio: 0.33 (left) and 3 (right), see Taneda (1979). Flow is from left to right.

Three-dimensional thin film Stokes flow problems, solved using the boundary element method are even scarcer. The flow over a particle adjacent to a flat surface has been considered by Pozrikidis & Thoroddsen (1991) and Blyth & Pozrikidis (2006), where it was shown that even a particle with a size much smaller than the film thickness can produce a significant deformation of the free surface, both upstream and downstream of it. Another problem investigated is that of gravity-driven film flow around hemispherical and cylindrical obstacles

that penetrate the free surface as explored by Baxter, Power, Cliffe & Hibberd (2009) and Baxter, Power, Cliffe & Hibberd (2010). This completes the list of full Stokes solutions for film flow in the presence of steep topography that can be found in the literature.

Finite element analysis of the full Navier-Stokes equations for non-zero Reynolds number film flow has, on the other hand, received even less attention, and to date has been more or less restricted to the case of steady-state two-dimensional flows only; this is due to the larger computational cost involved compared even to that required by the boundary element method. Bontozoglou & Serifi (2008), for example, explored the free-surface disturbance generated by film flow down a vertically aligned plane containing an isolated step topography, showing that for large capillary numbers increasing inertia first amplifies and then diminishes the capillary features; the latter effect would be impossible to capture with a long-wave analysis since it is valid for small capillary numbers only. The reader's attention is directed also to the investigations of Trifonov (1999), Malamataris & Bontozoglou (1999) and Gu, Liu, Yuan & Yu (2004), the latter finding good agreement with the experimental work of Zhao & Cerro (1992).

Recently, Scholle *et al.* (2008) considered the subtleties associated with the competing effects of geometry and inertia on the underpinning local flow structure in thick-gravity driven films on sinusoidally varying substrates; the Stokes flow was solved using a semi-analytical complex variable method, Scholle *et al.* (2004), while the Navier-Stokes flow was solved using a finite element approach. Good agreement was found, in the Stokes flow limit, with the corresponding experimental data and flow visualisations reported by Wierschem *et al.* (2003) and Wierschem & Aksel (2004); the finite element analysis revealed that the formation and presence of eddies can be manipulated not only by an increase in the corrugation steepness, that is kinematically, but also by increasing the Reynolds number of the flow, that is inertially. See also their related work on

eddy genesis and manipulation in a related shear-driven flows, Scholle, Haas, Aksel, Wilson, Thompson & Gaskell (2009*b*), and the study of Wierschem, Pollak, Heining & Aksel (2010) concerned with eddy suppression in film flow over topography.

Returning to the adoption of a long-wave approximation, the three-dimensional predictions obtained by Gaskell *et al.* (2004*b*) using an accurate numerical solution strategy, were the first of their kind to appear and found to agree extremely well with the benchmark experimental data of Decré & Baret (2003). Indeed, not only was lubrication theory shown to produce accurate results in regions of parameter space were it is not strictly valid, the authors were able to quantify the expected error in terms of Reynolds number and topography height/depth by a detailed comparison with complementary finite element solutions of the full Navier-Stokes equations for the case of spanwise topography. The above flow problem was revisited by Veremieiev, Thompson, Lee & Gaskell (2010*a*) and solved using a depth-averaged form of the Navier-Stokes and continuity equations, a method akin to integral boundary layer approximation, enabling inertia effects to be embodied within the long-wave approximation. It is this paper that forms the basis of the results presented in Chapter 3 of this thesis.

1.4 Controlling thin film free-surface profiles

Arguably the practical overarching goal apropos thin film flow over topography, is to minimise the free-surface disturbance that arises and thus guide its effective control, in order to yield optimum performance in terms of, for example, heat and mass transfer, Yoshimura, Nosoko & Nagata (1996) and Serifi, Malamataris & Bontozoglou (2004), and evaporation, Howison, Moriarty, Ockendon, Terrill & Wilson (1997) and Gaskell *et al.* (2006); or to maximise free-surface planarity in manufacturing applications to ensure predictable

functional or optical properties, Stillwagon & Larson (1988) and Stillwagon & Larson (1990). To this end, thermally-induced Marangoni stresses, Gramlich, Kalliadasis, Homsy & Messer (2002), or electrostatically induced Maxwell stresses, Tseluiko *et al.* (2008*b*), viscoelastic fluid behaviour, Saprykin *et al.* (2007*a*), careful topography design, Sellier (2008), Sellier & Panda (2010) and Heining & Aksel (2009), as suggested by Gaskell *et al.* (2004*b*), utilization of flexibility of the substrate, Matar, Craster & Kumar (2007) and Lee, Thompson & Gaskell (2009*b*), or surface chemical reactions, Gallez, Dewit & Kaufman (1996), the addition of insoluble surfactants Pozrikidis (2003), have each been suggested recently as a means of controlling the degree of free-surface disturbance generated.

The classical example of problems encountered in practice occurs in the manufacture of integrated circuits, in that the result is often an uneven topography profile above the circuit, see Stillwagon *et al.* (1987). In order to improve the quality of the surface finish, spin-coating is applied to deposit a thin film over the undesired topography to achieve the desired 'planarisation' or 'levelling' of the free-surface of the film; which, after the film has hardened, provides an artificial layer over the circuit with much better planarity than the circuit itself, see Figure 1.4, taken from Stillwagon *et al.* (1987), showing a schematic of the planarisation process.

The use of electric fields for manipulating the behaviour of thin liquid films stretches back several decades, having been investigated by various authors with particular applications in mind. In industrial coating processes, for example, electric fields are combined with charge distributions at the substrate to create electrostatic assist, thus widening the coating window by controlling the position of the associated dynamic wetting line in order to avoid/postpone the onset of air entrainment, Nakajima & Miyamoto (1993). In addition, electric fields have been used: to increase the micro-mixing of fluids, Oddy, Santiago & Mikkelsen (2001); in the context of electrostatic liquid film radia-

tors, Bankoff, Miksis, Kim & Gwinner (1994), Kim, Bankoff & Miksis (1994) and Bankoff, Griffing & Schluter (2002); to create patterns on films, Schaffer, Thurn-Albrecht, Russell & Steiner (2000), Craster & Matar (2009) and Wu, Pease & Russel (2005). They have similarly been utilised for the manipulation of droplets, Yeo, Craster & Matar (2007), and to align droplets in a particular direction, Mahlmann & Papageorgiou (2009).

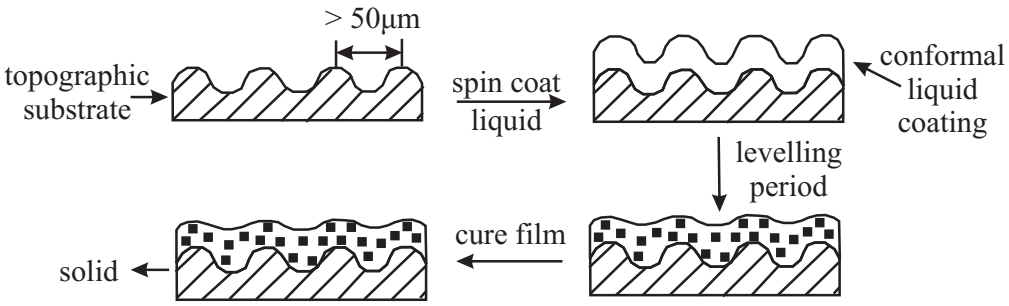

FIGURE 1.4: Schematic of the planarisation process using a low viscosity, liquid monomer from Stillwagon *et al.* (1987).

Of late Tseluiko, Blyth, Papageorgiou & Vanden-Broeck (2007) and Tseluiko *et al.* (2008*a*,*b*) have considered the effects of substrate topography on steady, two-dimensional film flow at zero Reynolds number subjected to a normal electrostatic field. They addressed gravity-driven Stokes flow over a trench topography and sinusoidally corrugated substrate, with comparisons drawn between predictions from lubrication theory, valid for topography small compared to the film thickness, against boundary element solutions, valid for corrugations and trench topography of an arbitrary size. The latter solutions were used to confirm the range of applicability of the lubrication analysis and to investigate the conditions under which eddies are generated adjacent to wavy topography. For the case of flow past trench topography it was shown that an electric field can either reduce or promote irregularities at the film surface, depending on the local geometry and the electrical properties of the liquid film: for one which is a perfect conductor/(dielectric) the height of the capillary ridge upstream of the trench was found to decrease/(increase) monotonically as the electric field strength increased. A related long-wave analysis was carried out

of flow over an inclined surface containing periodic steps, trenches and mound indentations with the liquid film assumed to be a perfect conductor and the air above it a perfect dielectric, Tseluiko *et al.* (2008*a*). This work revealed that an electric field, applied normal to the film, is able to eliminate the capillary ridge at a step-down topography at the expense of creating a free-surface ridge at an adjacent step-up one.

The above analyses were subsequently extended to consider, in a limited sense, the additional influence of inertia in determining the free-surface shape for the case of a perfect dielectric film flowing over a wavy wall, Tseluiko & Blyth (2009). Furthermore the analytical solutions of the lubrication equations for electrified films contained in Tseluiko, Blyth, Papageorgiou & Vanden-Broeck (2009), where obtained via an asymptotic expansion in powers of the topography amplitude. Solutions were derived for step-down, step-up and trench topography, valid for small-step asymptotics only, and found to compare favorably with corresponding numerical solutions of the lubrication equations; the latter being valid for larger scale topography.

The above theoretical electro-hydrodynamic analyses are directed at two-dimensional, spanwise flows only; investigations of three-dimensional ones have proved less common, a notable exception being a recent study of the dynamics of electric-field induced patterning of thin polymer films by Wu *et al.* (2005).

The prospect of using thermocapillary effects for controlling the dynamics of thin film flows has also attracted attention. Similar to the application of electrostatic fields, these flows are driven by an additional stress applied at the free surface; however, unlike the electrostatic Maxwell stress which is directed normally to the free surface, the thermocapillary Marangoni stress involved, and which appears due to the inhomogeneity of the surface tension, is directed tangentially to the free-surface boundary. The modelling of thermally-induced thin film flows has been undertaken: employing lubrication theory, Burelbach, Bankoff & Davis (1990); using the Benney-type model, Tan, Bankoff & Davis

(1990) and Joo *et al.* (1991); by utilizing the IBL type model, Kalliadasis, Demekhin, Ruyer-Quil & Velarde (2003*a*) and Saprykin, Trevelyan, Koopmans & Kalliadasis (2007*b*); by integration of the full Navier-Stokes and energy equations, Alexeev, Gambaryan-Roisman & Stephan (2005).

The influence of topography on thermocapillary thin film flows is discussed by Gramlich *et al.* (2002), Alexeev *et al.* (2005) and Saprykin *et al.* (2007*b*). Gramlich *et al.* (2002) use the lubrication equations to investigate optimal levelling of capillary free-surface disturbances by means of thermally-induced stresses produced by a localised heater; Marangoni stresses are found to be effective in reducing the height of the capillary ridge for two-dimensional flow over step-down topography. Alexeev *et al.* (2005) compare the results of experiments to full two-dimensional incompressible Navier-Stokes predictions, while Saprykin *et al.* (2007*b*) provide numerical predictions of the free-surface disturbance formed for flow over uniformly heated topography using the IBL approximation. In their work the liquid is shown to concentrate mainly in the troughs of the topography, where the surface tension is higher, while the accumulated fluid is shown to take the form of big drops surrounded by smaller ones that become 'attracted' to the former through the Marangoni effect.

Of note also is the recent work by Scholle, Haas, Aksel, Thompson, Hewson & Gaskell (2009*a*), where the heat transfer in an in-plane laminar shear flow in a sinusoidally varying channel has been investigated by means of a semi-analytical approach and finite element solutions of the full Navier-Stokes and energy equations.

1.5 Stability of thin film flows

Regarding the related issue of the stability of film flows, Benjamin (1957) and Yih (1963) have shown that in the case of two-dimensional, gravity-driven

flow down a flat inclined substrate, there exists a critical Reynolds number beyond which the flow becomes unstable to long waves, see also Chang (1994): a result that has been verified experimentally by Liu, Paul & Gollub (1993) and Liu & Gollub (1993, 1994), see Figure 1.5 for the results of experiments by Alekseenko *et al.* (1994) demonstrating the development of noise-driven large-amplitude three-dimensional waves for increased inertia in falling films over a plane wall. Complementary numerical investigations of waves at the surface of a flowing film have been reported by Ramaswamy, Chippada & Joo (1996) and Malamataris, Vlachogiannis & Bontozoglou (2002). The effect of an insoluble surfactant in increasing the critical Reynolds number at which instability is first encountered has been considered by Blyth & Pozrikidis (2004) utilizing a normal-mode analysis. Of note too, is the work of Usha & Uma (2004) which addresses the issue of high Reynolds number inertially induced instabilities.

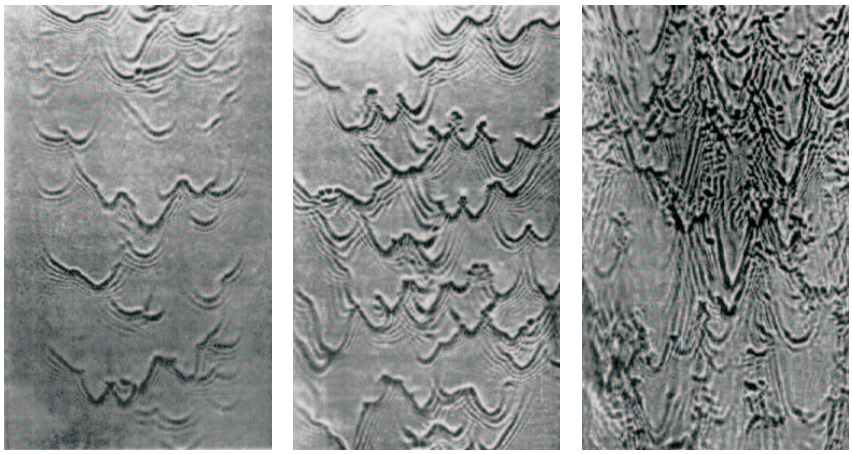

FIGURE 1.5: Experiments of a water-ethanol mixture film flowing down an inclined planar plate with increasing inertia: Reynolds numbers from left to the right are 15, 45 and 260 respectively, see Alekseenko *et al.* (1994).

The combined influence of inertia and topography on free-surface stability has been considered in several studies. For example, recent experiments by Vlachogiannis & Bontozoglou (2002), Wierschem, Lepski & Aksel (2005) and Argyriadi, Vlachogiannis & Bontozoglou (2006) have demonstrated that there is a strong coupling between these influences in the case of gravity-driven two-dimensional flow over substrates containing spanwise periodic features.

In particular, in the work of Argyriadi *et al.* (2006) steep corrugations are found to have a strong stabilising effect on the steady flow. Furthermore, Kalliadasis & Homsy (2001) and Davis & Troian (2005) discuss the influence of topography on the stability of thin film flow for the case of steep topography, such as a step-down; it is shown that the capillary ridge formed downstream of step topography is surprisingly stable for a wide range of the pertinent parameters owing to the net pressure gradient induced by the topography at small wavenumbers and by surface tension at high wavenumbers. The significant rise in critical Reynolds number that occurs due to the presence of surface topography, as observed experimentally, has also been predicted theoretically, see Wierschem & Aksel (2003).

Recently, Trifonov (2007) examined the stability of a viscous film flowing over a vertically aligned wavy surface, showing that there is a region of corrugation geometry (amplitude and period) where disturbances decay resulting in a stabilising effect; outside this region the flow is unstable. In addition, the reader is directed to the work of Khayat, Kim & Delosquer (2004), who provide a detailed account of the influence of inertia, topography and gravity on transient axisymmetric thin film flow, and to the investigations by Bontozoglou & Papapolymerou (1997), Bontozoglou (2000), Wierschem, Bontozoglou, Heining, Uecker & Aksel (2008) and Heining, Bontozoglou, Aksel & Wierschem (2009) in connection with resonance effects in viscous films on inclined wavy planes.

With particular reference to the influence of electric fields on flow stability, it has long been known that instabilities can be induced by applying a sufficiently strong electric field across a film, Melcher & Smith (1969). For gravity-driven, two-dimensional film flow down flat inclined substrates Kim, Bankoff & Miksis (1992) and González & Castellanos (1996) show that the presence of an electric field normal to it lowers the critical Reynolds number at which free-surface instability occurs. Several subsequent studies have carried out stability analyses for this problem using the long-wave approximation where the additional

Maxwell stress term in the free-surface stress boundary condition has been obtained by the solution of the associated two-dimensional Laplace equation for the electric potential. The work of Tseluiko & Papageorgiou (2006*a*,*b*), for example, showed that applying an electric field normal to a film can excite a long-wave instability even at zero Reynolds number. Such findings have been confirmed experimentally by Griffing, Bankoff, Miksis & Schluter (2006), whose complementary lubrication predictions of the dynamical effect of a strong normal electric field agree reasonably well with their data. More recently, Uma & Usha (2008) extended the range of their analytical approach to further investigate the destabilising mechanism caused by the application of an electric field across a liquid film.

The effect of an insoluble surfactant on the stability of an electrified thin film flow down an inclined plane has been considered by Blyth (2008); it is shown that similar to the non-electric field case considered by Blyth & Pozrikidis (2004), the surfactant is able to stabilise the electrified thin film flow for a set of modes which would otherwise be unstable for a clean electrified film.

Thermocapillary-driven fluid flows are liable to another kind of instability - Marangoni instability, that arises due to variation of the interfacial temperature and thus surface tension along the free-surface disturbance of the film; for general thermocapillary-driven fluid flows the Marangoni instability is discussed by Davis (1987). For thin film flows the Marangoni instability is also often called the long-wave thermocapillary instability with the rupture of the free surface being the main feature of this kind of manifestation; i.e. at some moment the thickness of the film becomes zero at some location, see the validation of the rupture effect for two-dimensional thin film flows over a planar uniformly heated topography predicted theoretically by Burelbach, Bankoff & Davis (1988), Oron & Rosenau (1992) and Joo, Davis & Bankoff (1993) and the experimental measurements by Burelbach *et al.* (1990) and VanHook, Schatz, McCormick, Swift & Swinney (1995).

Several studies have subsequently considered theoretically the stability and the dynamics of falling thermocapillary-driven two-dimensional liquid films over a substrate heated either uniformly, Joo *et al.* (1991), Kalliadasis *et al.* (2003*a*), Scheid, Ruyer-Quil, Kalliadasis, Velarde & Zeytounian (2005) and Ruyer-Quil, Scheid, Kalliadasis, Velarde & Zeytounian (2005), or by a local heat source, Scheid, Oron, Colinet, Thiele & Legros (2002); Skotheim, Thiele & Scheid (2003); Kalliadasis, Kiyashko & Demekhin (2003*b*). Joo *et al.* (1991) analyse the stability of the film by utilizing the Benney-type long-wave equation; in the subsequent analyses of Kalliadasis *et al.* (2003*a*) the limitations of the Benney-type model are revised using the IBL model. Both approaches are found to give similar solitary wave solutions for small Reynolds number, while for higher Reynolds number the solitary wave solution obtained by the Benney-type model is found to be unrealistic.

The numerical computations by Kalliadasis *et al.* (2003*b*) reveal that the flow over a plane wall with a local heat source develops a ridge upstream together with a depression downstream of the heater's centre, which is similar to the case of isothermal flow over a step-down topography discussed above, Kalliadasis *et al.* (2000). It is shown, however, in contrast to the step-down topography, to have a stabilising effect on the flow, Kalliadasis & Homsy (2001); the flow over a local heat source is unstable with respect to disturbances in the spanwise direction above a critical Marangoni number, which gives rise to rivulet formation and subsequent rupture. Subsequently, the joint influence of topography and a local heat source has been considered by Tiwari & Davis (2010); step-down topography is found to be very effective at stabilising the flowing film and increasing the critical Marangoni number. Of note also is the work of Oron (2000), Bestehorn, Pototsky & Thiele (2003), Scheid, Kalliadasis, Ruyer-Quil & Colinet (2008), where theoretical analysis of the stability of thin film thermocapillary flows is extended to three dimensions.

1.6 Thesis outline

Note that, for the problems of interest in this thesis analytic closed form solutions remain elusive. Accordingly models and associated numerical methods are used throughout to generate accurate solutions and hence predictions of the behaviour of such flows for the particular case of gravity-driven flow down an inclined substrate, as shown schematically in Figure 1.6.

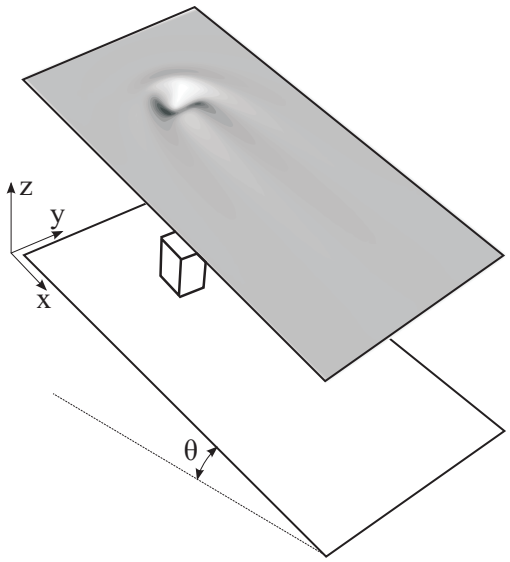

FIGURE 1.6: Schematic of a gravity-driven thin film flow over a substrate inclined at angle θ containing a fully submerged micro-scale topographical features, in this case a rectangular shaped peak. The coordinate system is as indicated.

The thesis has three main strands in relation to the investigation of gravity-driven thin film flow at finite Reynolds number:

(i) formulation of mathematical models based on the long-wave approximation, such as lubrication theory (LUB) and a depth-averaged form (DAF) of the Navier-Stokes and continuity equations, and comparison of these with full finite element solutions of the latter and with experimental data available in the literature;

(ii) the efficient and accurate numerical solution of the three models (LUB, DAF and N-S), especially for the case of three-dimensional flow when

there are significant computational challenges to overcome, utilizing state-of-the-art computational techniques including high performance computing when essential;

(iii) the prospects of using a normal electrostatic fields for controlling the free-surface disturbances associated with three-dimensional thin film flow over topography.

The thesis takes the following form:

The mathematical formulation and solution strategy implemented to achieve accurate mesh-independent solutions of the models implemented are provided in Chapter 2; the solution strategy includes an efficient full multigrid method together with error-controlled automatic adaptive time-stepping and proper treatment of the nonlinear advective terms present. A comprehensive set of results, showing the influence of inertia on thin film flow over planar surfaces featuring topography, is presented in Chapter 3. The free-surface profiles obtained by the DAF are verified by comparison with complementary experimental data where it exists and corresponding finite element solutions of the full free-surface N-S problem; the errors associated with both the LUB and the DAF predictions are estimated, taking the N-S solutions as the benchmark, for step-up and step-down topography in a vein similar to Gaskell *et al.* (2004*b*). Solutions for three-dimensional thin film flow over a steep, localised rectangular trench topography are presented also.

Complementary finite element solutions of the three-dimensional N-S equations for free-surface flow over a localised trench topography are presented in Chapter 4. An efficient direct multifrontal method, that combines a fast inversion of dense matrices arising for the free-surface problem with efficient memory utilization, including an out-of-core approach for storing matrix cofactors on the hard drive, is used to obtain mesh-independent predictions. The latter reveal both the underlying flow structure and the limitations associated

with the above approximate models based on the long-wave approximation.

Controlling the free-surface disturbance arising from thin film flow over topography by means of a normal electrostatic field is explored in Chapter 5; the hydrodynamics are modelled using the DAF equation set, while the solution of the coupled three-dimensional Laplace field equation for the electric potential is obtained in the form of a Fourier series in separable variables; the joint effect of inertia and electric field are considered.

Conclusions are drawn and recommendations for future work made in Chapter 6.

Chapter 2

Governing equations and methods of solution

Contents

This chapter provides a rigorous overview concerning the mathematical formulation of the equations governing free-surface thin film flows over topography. Three such formulations are considered: one involving the full Navier-Stokes and continuity equations (N-S); two based on the long-wave approximation of the latter equation set - a simple lubrication (LUB) model and a depth-averaged form (DAF). The N-S approach is the most general and therefore the most expensive of the three to compute, requiring a considerable amount of computational resource to achieve the accuracy necessary to generate mesh-independent solutions, especially for three-dimensional flows. The LUB model and DAF are much less resource intensive: the DAF, unlike the LUB approach, enables thin film flows with inertia to be predicted and its effect to be quantified. Efficient solution strategies for achieving mesh-independent solutions for all three approaches are presented. This involves the generation of accurate and fast solutions using a full multigrid (FMG) methodology for the LUB and DAF equation sets and parallel computing methodologies utilising a multifrontal solver to deal with the N-S equations.

2.1 Governing equations

2.1.1 Full Navier-Stokes equations

Consider, as illustrated in Figure 2.1, the case of time-dependent gravity-driven thin film flow down a planar surface containing a trench topography of depth S_0, length L_T and spanwise width W_T, that is inclined at an angle $\theta(\neq 0)$ to the horizontal. The liquid is assumed to be incompressible and to have constant density, ρ, dynamic viscosity, μ, and surface tension, σ. The chosen Cartesian streamwise, X, spanwise, Y, and normal, Z, components of the coordinate vector, $\boldsymbol{X} = X\boldsymbol{i} + Y\boldsymbol{j} + Z\boldsymbol{k}$, are as indicated; $\boldsymbol{i}$, $\boldsymbol{j}$, $\boldsymbol{k}$ are the corresponding basis vectors of the coordinate system. The solution domain

is bounded from below by the planar surface, $Z = S(X, Y)$, from above at time T by the free surface, $Z = F(X, Y, T)$, upstream and downstream by the inflow, $X = 0$, and outflow, $X = L_P$, planes, respectively, and to the left and right by the side planes at $Y = 0$ and $Y = W_P$. The film thickness, $H(X, Y, T)$, at any point in the (X, Y) plane at time T is given by $H = F - S$. The resulting laminar flow is described by the N-S and continuity equations, namely:

$$\rho\left(\frac{\partial \boldsymbol{U}}{\partial T} + \boldsymbol{U}\cdot\nabla\boldsymbol{U}\right) = -\nabla P + \nabla\cdot\boldsymbol{T} + \rho\boldsymbol{G}, \tag{2.1}$$

$$\nabla\cdot\boldsymbol{U} = 0, \tag{2.2}$$

where $\boldsymbol{U} = U\boldsymbol{i} + V\boldsymbol{j} + W\boldsymbol{k}$ and P are the fluid velocity and pressure, respectively; $\boldsymbol{T} = \mu\left(\nabla\boldsymbol{U} + (\nabla\boldsymbol{U})^T\right)$ is the viscous stress tensor, $\boldsymbol{G} = G_0\left(\boldsymbol{i}\sin\theta - \boldsymbol{k}\cos\theta\right)$ is the acceleration due to gravity where G_0 is the standard gravity constant.

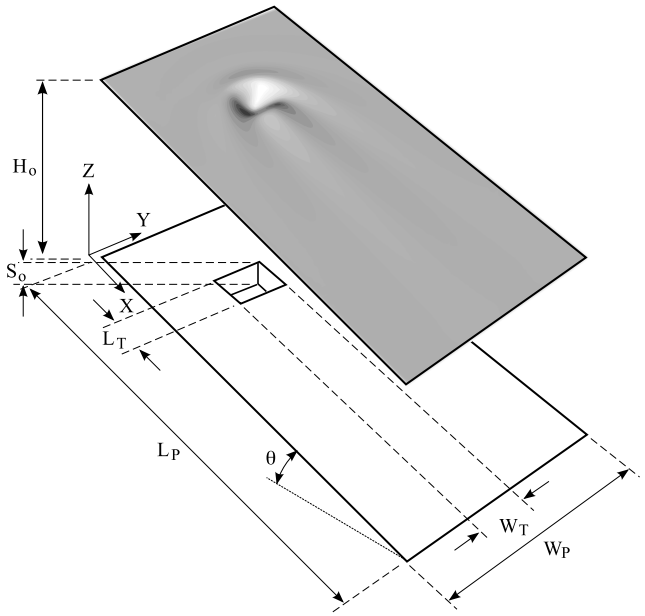

FIGURE 2.1: Schematic diagram of gravity-driven flow over a well-defined trench topography, showing the coordinate system adopted and surface geometry.

The general problem definition is complete following the specification of appropriate no-slip, inflow/outflow, kinematic and free-surface stress boundary

conditions, see Landau & Lifshitz (1987):

$$\boldsymbol{U}|_{Z=S} = \boldsymbol{0}, \tag{2.3}$$

$$H|_{X=0} = H_0, \quad \boldsymbol{U}|_{X=0,L_P;Y=0,W_P} = U_0 \frac{Z}{H_0}\left(2 - \frac{Z}{H_0}\right)\boldsymbol{i}, \tag{2.4}$$

$$\frac{\partial F}{\partial T} + U|_{Z=F}\frac{\partial F}{\partial X} + V|_{Z=F}\frac{\partial F}{\partial Y} - W|_{Z=F} = 0, \tag{2.5}$$

$$\left(-P\boldsymbol{I} + \boldsymbol{T}\right)|_{Z=F}\boldsymbol{n} = \left(\sigma K + P_A\right)\boldsymbol{n}, \tag{2.6}$$

where P_A is the atmospheric pressure, H_0 is the asymptotic, or fully developed, film thickness, $U_0 = \rho G_0 H_0^2 \sin\theta/2\mu$ is the free-surface (maximum) velocity apropos the classic Nusselt solution, Spurk & Aksel (2008), $\boldsymbol{I}$ is the unity tensor, $\boldsymbol{n} = \left(-\frac{\partial F}{\partial X}\boldsymbol{i} - \frac{\partial F}{\partial Y}\boldsymbol{j} + \boldsymbol{k}\right) \cdot \left[\left(\frac{\partial F}{\partial X}\right)^2 + \left(\frac{\partial F}{\partial Y}\right)^2 + 1\right]^{-1/2}$ is the unit normal vector pointing outward from the free surface and $K = -\nabla\cdot\boldsymbol{n}$ is twice the mean curvature of the free surface that, following Hayes *et al.* (2000) or Saprykin *et al.* (2007*a*), is taken to be positive when the surface is concave upwards. In what follows the pressure variable is shifted, $P \to P + P_A$, to denote a reference pressure instead.

Taking the reference length scale in all directions to be H_0 and scaling the velocities by U_0, the pressure (stress tensor) by $P_0 = \mu U_0/H_0$ and the time by $T_0 = H_0/U_0$, equations (2.1) - (2.6) can be rewritten in non-dimensional form as:

$$\mathrm{Re}\left(\frac{\partial \boldsymbol{u}}{\partial t} + \boldsymbol{u}\cdot\nabla\boldsymbol{u}\right) = -\nabla p + \nabla\cdot\boldsymbol{\tau} + \mathrm{St}\boldsymbol{g}, \tag{2.7}$$

$$\nabla\cdot\boldsymbol{u} = \boldsymbol{0}, \tag{2.8}$$

$$\boldsymbol{u}|_{z=s} = 0, \tag{2.9}$$

$$h|_{x=0} = 1, \quad \boldsymbol{u}|_{x=0,l_p;y=0,w_p} = z\left(2 - z\right)\boldsymbol{i}, \tag{2.10}$$

$$\frac{\partial f}{\partial t} + u|_{z=f}\frac{\partial f}{\partial x} + v|_{z=f}\frac{\partial f}{\partial y} - w|_{z=f} = 0, \tag{2.11}$$

$$\left(-p\boldsymbol{I} + \boldsymbol{\tau}\right)|_{z=f}\boldsymbol{n} = \frac{\kappa}{\mathrm{Ca}}\boldsymbol{n}, \tag{2.12}$$

where $\boldsymbol{x} = x\boldsymbol{i} + y\boldsymbol{j} + z\boldsymbol{k}$, $\boldsymbol{u} = u\boldsymbol{i} + v\boldsymbol{j} + w\boldsymbol{k}$, $\boldsymbol{\tau}$ and $\boldsymbol{g} = \boldsymbol{G}/G_0$ are the non-dimensional coordinate, velocity, viscous stress tensor and gravity component, respectively; h, s, f, t, p, κ together with s_0, l_t, w_t, l_p, w_p correspond to their dimensional counterparts. $\mathrm{Re} = \rho U_0 H_0/\mu$ is the Reynolds number, $\mathrm{Ca} = \mu U_0/\sigma$ is the capillary number and $\mathrm{St} = 2/\sin\theta$ the Stokes number; alternatively, the latter can be written as $\mathrm{St} = \mathrm{Re}/\mathrm{Fr}^2$, where $\mathrm{Fr} = U_0/\sqrt{H_0 G_0}$ is the Froude number.

The stress boundary condition (2.12) is expanded into normal and tangential parts by taking scalar products with respect to the unit vectors normal, $\boldsymbol{n}$, and tangential, $\boldsymbol{t} = \left[\alpha_t \boldsymbol{i} + \beta_t \boldsymbol{j} + \left(\alpha_t \frac{\partial f}{\partial x} + \beta_t \frac{\partial f}{\partial y}\right)\boldsymbol{k}\right] \cdot \left[\alpha_t^2 + \beta_t^2 + \left(\alpha_t \frac{\partial f}{\partial x} + \beta_t \frac{\partial f}{\partial y}\right)^2\right]^{-1/2}$, to the free surface, namely:

$$-p|_{z=f} + (\boldsymbol{\tau}|_{z=f} \cdot \boldsymbol{n}) \cdot \boldsymbol{n} = \frac{\kappa}{\mathrm{Ca}}, \tag{2.13}$$

$$(\boldsymbol{\tau}|_{z=f} \cdot \boldsymbol{n}) \cdot \boldsymbol{t} = 0, \tag{2.14}$$

where α_t and β_t are variables that define the direction of the tangent vector at any point in the tangent plane; thus formula (2.14) actually implies two boundary conditions.

2.1.2 Long-wave approximation

The above system of equations, (2.7)-(2.8), and boundary conditions, (2.9) - (2.11) and (2.13) - (2.14), can be simplified considerably by adopting a long-wave approximation, Oron *et al.* (1997), effectively reducing the dimensionality of the problem by one; the main assumption being that the long-wave ratio $\varepsilon = H_0/L_0 \ll 1$, where L_0 is the characteristic in-plane length scale.

Formulating the governing equations (2.7) and (2.8) in terms of L_0 is equivalent

to the following change of non-dimensional variables:

$$(x, y, l_t, w_t, l_p, w_p, t, p) \rightarrow (x, y, l_t, w_t, l_p, w_p, t, p)/\varepsilon, \quad w \rightarrow \varepsilon w, \tag{2.15}$$

leading to:

$$\varepsilon \mathrm{Re}\left(\frac{\partial u}{\partial t} + u\frac{\partial u}{\partial x} + v\frac{\partial u}{\partial y} + w\frac{\partial u}{\partial z}\right) = -\frac{\partial p}{\partial x} + \varepsilon^2\left(\frac{\partial^2 u}{\partial x^2} + \frac{\partial^2 u}{\partial y^2}\right) + \frac{\partial^2 u}{\partial z^2} + 2, \tag{2.16}$$

$$\varepsilon \mathrm{Re}\left(\frac{\partial v}{\partial t} + u\frac{\partial v}{\partial x} + v\frac{\partial v}{\partial y} + w\frac{\partial v}{\partial z}\right) = -\frac{\partial p}{\partial y} + \varepsilon^2\left(\frac{\partial^2 v}{\partial x^2} + \frac{\partial^2 v}{\partial y^2}\right) + \frac{\partial^2 v}{\partial z^2}, \tag{2.17}$$

$$\varepsilon^3 \mathrm{Re}\left(\frac{\partial w}{\partial t} + u\frac{\partial w}{\partial x} + v\frac{\partial w}{\partial y} + w\frac{\partial w}{\partial z}\right) = -\frac{\partial p}{\partial z} + \varepsilon^4\left(\frac{\partial^2 w}{\partial x^2} + \frac{\partial^2 w}{\partial y^2}\right) + \varepsilon^2\frac{\partial^2 w}{\partial z^2} - 2\varepsilon\cot\theta, \tag{2.18}$$

$$\frac{\partial u}{\partial x} + \frac{\partial v}{\partial y} + \frac{\partial w}{\partial z} = 0. \tag{2.19}$$

The normal vector, tangent vector, free-surface curvature and viscous stress tensor are given, respectively, by:

$$\boldsymbol{n} = \frac{-\varepsilon\frac{\partial f}{\partial x}\boldsymbol{i} - \varepsilon\frac{\partial f}{\partial y}\boldsymbol{j} + \boldsymbol{k}}{\sqrt{1 + \varepsilon^2\left[\left(\frac{\partial f}{\partial x}\right)^2 + \left(\frac{\partial f}{\partial y}\right)^2\right]}}, \tag{2.20}$$

$$\boldsymbol{t} = \frac{\alpha_t\boldsymbol{i} + \beta_t\boldsymbol{j} + \left(\alpha_t\varepsilon\frac{\partial f}{\partial x} + \beta_t\varepsilon\frac{\partial f}{\partial y}\right)\boldsymbol{k}}{\sqrt{\alpha_t^2 + \beta_t^2 + \varepsilon^2\left(\alpha_t\frac{\partial f}{\partial x} + \beta_t\frac{\partial f}{\partial y}\right)^2}}, \tag{2.21}$$

$$\kappa = \varepsilon^2\frac{\frac{\partial^2 f}{\partial x^2} + \frac{\partial^2 f}{\partial y^2} + \varepsilon^2\left[\frac{\partial^2 f}{\partial x^2}\left(\frac{\partial f}{\partial y}\right)^2 + \frac{\partial^2 f}{\partial y^2}\left(\frac{\partial f}{\partial x}\right)^2 - 2\frac{\partial^2 f}{\partial x\partial y}\frac{\partial f}{\partial x}\frac{\partial f}{\partial y}\right]}{\left\{1 + \varepsilon^2\left[\left(\frac{\partial f}{\partial x}\right)^2 + \left(\frac{\partial f}{\partial y}\right)^2\right]\right\}^{3/2}}, \tag{2.22}$$

$$\boldsymbol{\tau} = \begin{pmatrix} 2\varepsilon\frac{\partial u}{\partial x} & \varepsilon\left(\frac{\partial u}{\partial y} + \frac{\partial v}{\partial x}\right) & \frac{\partial u}{\partial z} + \varepsilon^2\frac{\partial w}{\partial x} \\ \varepsilon\left(\frac{\partial u}{\partial y} + \frac{\partial v}{\partial x}\right) & 2\varepsilon\frac{\partial v}{\partial y} & \frac{\partial v}{\partial z} + \varepsilon^2\frac{\partial w}{\partial y} \\ \frac{\partial u}{\partial z} + \varepsilon^2\frac{\partial w}{\partial x} & \frac{\partial v}{\partial z} + \varepsilon^2\frac{\partial w}{\partial y} & 2\varepsilon\frac{\partial w}{\partial z} \end{pmatrix}, \tag{2.23}$$

while the boundary conditions (2.13) and (2.14) become:

$$-p|_{z=f} + 2\varepsilon^2 \left\{ \frac{-\frac{\partial u}{\partial z}\frac{\partial f}{\partial x} - \frac{\partial v}{\partial z}\frac{\partial f}{\partial y} + \frac{\partial w}{\partial z}}{1+\varepsilon^2\left[\left(\frac{\partial f}{\partial x}\right)^2 + \left(\frac{\partial f}{\partial y}\right)^2\right]} \right.$$

$$\left. + \frac{\varepsilon^2\left[\frac{\partial u}{\partial x}\left(\frac{\partial f}{\partial x}\right)^2 + \frac{\partial u}{\partial y}\left(\frac{\partial f}{\partial y}\right)^2 + \left(\frac{\partial u}{\partial y} + \frac{\partial v}{\partial x}\right)\frac{\partial f}{\partial x}\frac{\partial f}{\partial y} - \frac{\partial w}{\partial x}\frac{\partial f}{\partial x} - \frac{\partial w}{\partial y}\frac{\partial f}{\partial y}\right]}{1+\varepsilon^2\left[\left(\frac{\partial f}{\partial x}\right)^2 + \left(\frac{\partial f}{\partial y}\right)^2\right]} \right\} |_{z=f} = \frac{\varepsilon\kappa}{\mathrm{Ca}}, \tag{2.24}$$

$$\left(\alpha_t\frac{\partial u}{\partial z} + \beta_t\frac{\partial v}{\partial z}\right)|_{z=f} + \varepsilon^2\left\{\left(\alpha_t\frac{\partial f}{\partial x} + \beta_t\frac{\partial f}{\partial y}\right)\left(-\frac{\partial u}{\partial z}\frac{\partial f}{\partial x} - \frac{\partial v}{\partial z}\frac{\partial f}{\partial y} + 2\frac{\partial w}{\partial z}\right)\right.$$

$$+ \alpha_t\left[-2\frac{\partial u}{\partial x}\frac{\partial f}{\partial x} - \left(\frac{\partial u}{\partial y} + \frac{\partial v}{\partial x}\right)\frac{\partial f}{\partial y} + \frac{\partial w}{\partial x}\right] + \beta_t\left[-2\frac{\partial v}{\partial y}\frac{\partial f}{\partial y}\right.$$

$$\left.\left. - \left(\frac{\partial u}{\partial y} + \frac{\partial v}{\partial x}\right)\frac{\partial f}{\partial x} + \frac{\partial w}{\partial y}\right] - \varepsilon^2\left(\frac{\partial w}{\partial x}\frac{\partial f}{\partial x} + \frac{\partial w}{\partial y}\frac{\partial f}{\partial y}\right)\right\}|_{z=f} = 0. \tag{2.25}$$

2.1.3 Lubrication equations

The lubrication approach is considered to be a first-order accurate long-wave approximation with the assumption that the Reynolds number is small, $\mathrm{Re} = O(\varepsilon)$, see Stillwagon & Larson (1988). For thin film flows the capillary pressure is of the same order as the fluid pressure; the capillary number is $O(\varepsilon^3)$ and following Hayes *et al.* (2000), Decré & Baret (2003) and Gaskell *et al.* (2004*b*) is taken as:

$$\mathrm{Ca} = \frac{\varepsilon^3}{6} = \frac{H_0^3}{6L_0^3}, \tag{2.26}$$

where $L_0 = (\sigma H_0/3\rho G_0 \sin\theta)^{1/3}$ represents the associated capillary length scale; the resulting lubrication approach is therefore valid for the case of small capillary numbers:

$$\varepsilon \ll 1 \quad \Rightarrow \quad \mathrm{Ca} = \frac{\varepsilon^3}{6} \ll 1. \tag{2.27}$$

The lubrication equations derive from the long-wave equations (2.16) - (2.19)

and boundary conditions (2.24) - (2.25) by neglecting terms of $O(\varepsilon^2)$:

$$0 = -\frac{\partial p}{\partial x} + \frac{\partial^2 u}{\partial z^2} + 2, \tag{2.28}$$

$$0 = -\frac{\partial p}{\partial y} + \frac{\partial^2 v}{\partial z^2}, \tag{2.29}$$

$$0 = -\frac{\partial p}{\partial z} - 2\varepsilon \cot\theta, \tag{2.30}$$

$$\frac{\partial u}{\partial x} + \frac{\partial v}{\partial y} + \frac{\partial w}{\partial z} = 0. \tag{2.31}$$

$$-p|_{z=f} = \frac{\varepsilon^3}{\mathrm{Ca}}\left(\frac{\partial^2 f}{\partial x^2} + \frac{\partial^2 f}{\partial y^2}\right), \tag{2.32}$$

$$\frac{\partial u}{\partial z}|_{z=f} = \frac{\partial v}{\partial z}|_{z=f} = 0. \tag{2.33}$$

Equation (2.30) results in a balance between the acceleration arising from the pressure gradient and that from gravity; integrating it with respect to z and applying boundary condition (2.32) gives:

$$\int_z^f \frac{\partial p}{\partial z} dz = p|_{z=f} - p = -\frac{\varepsilon^3}{\mathrm{Ca}}\left(\frac{\partial^2 f}{\partial x^2} + \frac{\partial^2 f}{\partial y^2}\right) - p = -2\varepsilon\,(f - z)\cot\theta,$$

and hence the following lubrication equation for the pressure (Gaskell *et al.*, 2004*b*):

$$p = -\frac{\varepsilon^3}{\mathrm{Ca}}\left(\frac{\partial^2 f}{\partial x^2} + \frac{\partial^2 f}{\partial y^2}\right) + 2\varepsilon\,(f - z)\cot\theta. \tag{2.34}$$

Since ∇p does not depend on z, equation (2.34) is used to integrate equations (2.28) and (2.29) twice with respect to z, making use of boundary conditions (2.9) and (2.33), to obtain the in-plane velocity components u and v:

$$\int_z^f \frac{\partial^2 u}{\partial z^2} dz = \frac{\partial u}{\partial z}|_{z=f} - \frac{\partial u}{\partial z} = -\frac{\partial u}{\partial z} = \left(\frac{\partial p}{\partial x} - 2\right)(f - z),$$

$$\int_s^z \frac{\partial u}{\partial z} dz = u - u|_{z=s} = u = \left(\frac{\partial p}{\partial x} - 2\right)(z - s)\left[\frac{1}{2}(z + s) - f\right], \tag{2.35}$$

$$\int_z^f \frac{\partial^2 v}{\partial z^2} dz = \frac{\partial v}{\partial z}|_{z=f} - \frac{\partial v}{\partial z} = -\frac{\partial v}{\partial z} = \frac{\partial p}{\partial y}(f-z),$$

$$\int_s^z \frac{\partial v}{\partial z} dz = v - v|_{z=s} = v = \frac{\partial p}{\partial y}(z-s)\left[\frac{1}{2}(z+s) - f\right]. \tag{2.36}$$

Integrating the continuity equation (2.31) using Leibniz's rule and applying boundary conditions (2.9) and (2.11) leads to the following depth-averaged equation for the conservation of mass:

$$\int_s^f \left(\frac{\partial u}{\partial x} + \frac{\partial v}{\partial y} + \frac{\partial w}{\partial z}\right) dz = \frac{\partial}{\partial x}\left(\int_s^f u dz\right) - u|_{z=f}\frac{\partial f}{\partial x} + u|_{z=s}\frac{\partial s}{\partial x} + \frac{\partial}{\partial y}\left(\int_s^f v dz\right)$$

$$- v|_{z=f}\frac{\partial f}{\partial y} + v|_{z=s}\frac{\partial s}{\partial y} - w|_{z=f} + w|_{z=s} = \frac{\partial h}{\partial t} + \frac{\partial (h\bar{u})}{\partial x} + \frac{\partial (h\bar{v})}{\partial y} = 0, \tag{2.37}$$

where the over-bar denotes the x and y depth-averaged components of velocity, namely:

$$\bar{u} = \frac{1}{h}\int_s^f u dz, \quad \bar{v} = \frac{1}{h}\int_s^f v dz. \tag{2.38}$$

For the lubrication approach they are derived by averaging the right-hand-sides of expressions (2.35) and (2.36) respectively:

$$\bar{u} = -\frac{h^2}{3}\left(\frac{\partial p}{\partial x} - 2\right), \quad \bar{v} = -\frac{h^2}{3}\frac{\partial p}{\partial y}. \tag{2.39}$$

After substitution of (2.39) into (2.37) the second lubrication equation of the conservation of mass (Gaskell *et al.*, 2004*b*) is obtained as follows:

$$\frac{\partial h}{\partial t} = \frac{\partial}{\partial x}\left[\frac{h^3}{3}\left(\frac{\partial p}{\partial x} - 2\right)\right] + \frac{\partial}{\partial y}\left[\frac{h^3}{3}\frac{\partial p}{\partial y}\right]. \tag{2.40}$$

The system of lubrication equations (2.34) and (2.40) contains three dimensionless parameters: ε, Ca and $\cot\theta$; however, since Ca and ε are related via (2.26) the lubrication equations depend on one dimensionless grouping only - the gravity parameter $\mathrm{N} = \mathrm{Ca}^{1/3} \cdot \cot\theta$.

The lubrication equations, (2.34) and (2.40), are closed by the assumption of

fully developed flow both upstream and downstream, namely:

$$\frac{\partial p}{\partial x}|_{x=0,l_p} = \frac{\partial p}{\partial y}|_{y=0,w_p} = 0, \tag{2.41}$$

$$h|_{x=0} = 1, \quad \frac{\partial h}{\partial x}|_{x=l_p} = \frac{\partial h}{\partial y}|_{y=0,w_p} = 0. \tag{2.42}$$

Alternatively, a single fourth-order partial-differential equation for the film thickness, h, can be derived by substituting equation (2.34) into the equation (2.40):

$$\frac{\partial h}{\partial t} = \frac{\partial}{\partial x}\left\{\frac{h^3}{3}\left[-\frac{\varepsilon^3}{\mathrm{Ca}}\left(\frac{\partial^3 f}{\partial x^3} + \frac{\partial^3 f}{\partial x \partial y^2}\right) + 2\varepsilon \cot\theta \frac{\partial f}{\partial x} - 2\right]\right\}$$

$$+ \frac{\partial}{\partial y}\left\{\frac{h^3}{3}\left[-\frac{\varepsilon^3}{\mathrm{Ca}}\left(\frac{\partial^3 f}{\partial x^2 \partial y} + \frac{\partial^3 f}{\partial y^3}\right) + 2\varepsilon \cot\theta \frac{\partial f}{\partial y}\right]\right\}, \tag{2.43}$$

the boundary conditions in this case being:

$$h|_{x=0} = 1, \quad \frac{\partial h}{\partial x}|_{x=0,l_p} = \frac{\partial^3 h}{\partial x^3}|_{x=l_p} = \frac{\partial h}{\partial y}|_{y=0,w_p} = \frac{\partial^3 h}{\partial y^3}|_{y=0,w_p} = 0. \tag{2.44}$$

Although having to solve just one equation, for h, rather than two, for h and p, may appear the more attractive it is the coupled system only that is considered in the course of this thesis. The reason for this is that recent work (Cowling *et al.*, 2011) has shown conclusively that from a computational stand point solving for h and p allows far greater time increments to be used and leads to much better computational performance when solved within a multigrid framework. Note that the latter issue of computational performance is consistent with the findings of other authors using a multigrid strategy to solve fourth-order biharmonic problems, Altas, Dym, Gupta & Manohar (1998) and Henn (2005).

2.1.4 Depth-averaged form

As in the case of the above LUB model, Oron *et al.* (1997), the DAF derived below can be thought of as a first-order accurate long-wave approximation but with no Reynolds number limitation. The DAF has the same disadvantage as the LUB model: the velocity across the film has a self-similar half-parabolic form, which is unable to capture the existence of eddies. The associated equation set derives from the long-wave equations (2.16) - (2.19) and boundary conditions (2.24) - (2.25) by neglecting terms of $O(\varepsilon^2)$:

$$\varepsilon \mathrm{Re}\left(\frac{\partial u}{\partial t}+u\frac{\partial u}{\partial x}+v\frac{\partial u}{\partial y}+w\frac{\partial u}{\partial z}\right)=-\frac{\partial p}{\partial x}+\frac{\partial^2 u}{\partial z^2}+2, \tag{2.45}$$

$$\varepsilon \mathrm{Re}\left(\frac{\partial v}{\partial t}+u\frac{\partial v}{\partial x}+v\frac{\partial v}{\partial y}+w\frac{\partial v}{\partial z}\right)=-\frac{\partial p}{\partial y}+\frac{\partial^2 v}{\partial z^2}, \tag{2.46}$$

$$0=-\frac{\partial p}{\partial z}-2\varepsilon\cot\theta, \tag{2.47}$$

$$\frac{\partial u}{\partial x}+\frac{\partial v}{\partial y}+\frac{\partial w}{\partial z}=0. \tag{2.48}$$

$$-p|_{z=f}=\frac{\varepsilon^3}{\mathrm{Ca}}\left(\frac{\partial^2 f}{\partial x^2}+\frac{\partial^2 f}{\partial y^2}\right), \tag{2.49}$$

$$\frac{\partial u}{\partial z}|_{z=f}=\frac{\partial v}{\partial z}|_{z=f}=0, \tag{2.50}$$

The DAF of the u-momentum equation (2.45) is obtained by making use of Leibniz's rule, boundary conditions (2.9), (2.11), (2.50) and equation (2.48), while noting that the integral of fluctuations about the average is zero, giving:

$$\int_s^f\left[\varepsilon \mathrm{Re}\left(\frac{\partial u}{\partial t}+u\frac{\partial u}{\partial x}+v\frac{\partial u}{\partial y}+w\frac{\partial u}{\partial z}\right)+\frac{\partial p}{\partial x}-\frac{\partial^2 u}{\partial z^2}-2\right]dz$$

$$=\int_s^f\left[\varepsilon \mathrm{Re}\left(\frac{\partial u}{\partial t}+\frac{\partial\left(uu\right)}{\partial x}+\frac{\partial\left(vu\right)}{\partial y}+\frac{\partial\left(wu\right)}{\partial z}\right)+\frac{\partial p}{\partial x}-\frac{\partial^2 u}{\partial z^2}-2\right]dz$$

$$=\varepsilon \mathrm{Re}\left[\frac{\partial}{\partial t}\int_s^f u dz-u|_{z=f}\frac{\partial f}{\partial t}+u|_{z=s}\frac{\partial s}{\partial t}+\frac{\partial}{\partial x}\int_s^f u^2 dz-u^2|_{z=f}\frac{\partial f}{\partial x}+u^2|_{z=s}\frac{\partial s}{\partial x}\right.$$

$$+\frac{\partial}{\partial y}\int_s^f uvdz-(uv)\left|_{z=f}\frac{\partial f}{\partial y}+(uv)\right|_{z=s}\frac{\partial s}{\partial y}+(uw)\left|_{z=f}-(uw)\right|_{z=s}\Bigg]$$

$$+h\frac{\partial p}{\partial x}-\frac{\partial u}{\partial z}|_{z=f}+\frac{\partial u}{\partial z}|_{z=s}-2h$$

$$=\varepsilon\mathrm{Re}\Bigg[\frac{\partial}{\partial t}\left(h\bar{u}\right)+\frac{\partial}{\partial x}\int_s^f\left[\bar{u}^2+2\bar{u}\left(u-\bar{u}\right)+\left(u-\bar{u}\right)^2\right]dz+\frac{\partial}{\partial y}\int_s^f\left[\bar{u}\bar{v}\right.$$

$$\left.+\bar{u}\left(v-\bar{v}\right)+\bar{v}\left(u-\bar{u}\right)+\left(u-\bar{u}\right)\left(v-\bar{v}\right)\right]dz\Bigg]+h\frac{\partial p}{\partial x}+\frac{\partial u}{\partial z}|_{z=s}-2h$$

$$=\varepsilon\mathrm{Re}\left[h\left(\frac{\partial\bar{u}}{\partial t}+\bar{u}\frac{\partial\bar{u}}{\partial x}+\bar{v}\frac{\partial\bar{u}}{\partial y}\right)+\frac{\partial}{\partial x}\int_s^f\left(\bar{u}-u\right)^2dz\right.$$

$$\left.+\frac{\partial}{\partial y}\int_s^f\left(\bar{u}-u\right)\left(\bar{v}-v\right)dz\right]+h\frac{\partial p}{\partial x}+\frac{\partial u}{\partial z}|_{z=s}-2h=0. \tag{2.51}$$

The DAF of the v-momentum equation is derived similarly:

$$\int_s^f\left[\varepsilon\mathrm{Re}\left(\frac{\partial v}{\partial t}+u\frac{\partial v}{\partial x}+v\frac{\partial v}{\partial y}+w\frac{\partial v}{\partial z}\right)+\frac{\partial p}{\partial y}-\frac{\partial^2 v}{\partial z^2}\right]dz$$

$$=\varepsilon\mathrm{Re}\left[h\left(\frac{\partial\bar{v}}{\partial t}+\bar{u}\frac{\partial\bar{v}}{\partial x}+\bar{v}\frac{\partial\bar{v}}{\partial y}\right)+\frac{\partial}{\partial x}\int_s^f\left(\bar{u}-u\right)\left(\bar{v}-v\right)dz\right.$$

$$\left.+\frac{\partial}{\partial y}\int_s^f\left(\bar{v}-v\right)^2dz\right]+h\frac{\partial p}{\partial y}+\frac{\partial v}{\partial z}|_{z=s}=0. \tag{2.52}$$

The DAF of the w-momentum (2.47) and continuity (2.48) equations are the pressure equation (2.34) and the depth-averaged mass conservation equation (2.37), which are as derived for the lubrication model in Subsection 2.1.3. After substitution of the pressure equation (2.34) into the DAF momentum equations, (2.51) and (2.52), and dividing through by the film thickness h, the resulting governing system of equations for the unknown averaged velocities $\bar{u}\left(x,y,t\right)$, $\bar{v}\left(x,y,t\right)$ and the film thickness $h\left(x,y,t\right)$ is:

$$\varepsilon\mathrm{Re}\left[\frac{\partial\bar{u}}{\partial t}+\bar{u}\frac{\partial\bar{u}}{\partial x}+\bar{v}\frac{\partial\bar{u}}{\partial y}+\frac{1}{h}\frac{\partial}{\partial x}\int_s^f\left(\bar{u}-u\right)^2dz+\frac{1}{h}\frac{\partial}{\partial y}\int_s^f\left(\bar{u}-u\right)\left(\bar{v}-v\right)dz\right]$$

$$=\frac{\partial}{\partial x}\left[\frac{\varepsilon^3}{\mathrm{Ca}}\left(\frac{\partial^2 f}{\partial x^2}+\frac{\partial^2 f}{\partial y^2}\right)-2\varepsilon f\cot\theta\right]-\frac{1}{h}\frac{\partial u}{\partial z}|_{z=s}+2, \tag{2.53}$$

$$\varepsilon \mathrm{Re}\left[\frac{\partial \bar{v}}{\partial t}+\bar{u}\frac{\partial \bar{v}}{\partial x}+\bar{v}\frac{\partial \bar{v}}{\partial y}+\frac{1}{h}\frac{\partial}{\partial x}\int_s^f (\bar{u}-u)(\bar{v}-v)\,dz+\frac{1}{h}\frac{\partial}{\partial y}\int_s^f (\bar{v}-v)^2\,dz\right]$$
$$=\frac{\partial}{\partial y}\left[\frac{\varepsilon^3}{\mathrm{Ca}}\left(\frac{\partial^2 f}{\partial x^2}+\frac{\partial^2 f}{\partial y^2}\right)-2\varepsilon f\cot\theta\right]-\frac{1}{h}\frac{\partial v}{\partial z}|_{z=s}, \tag{2.54}$$

$$\frac{\partial h}{\partial t}+\frac{\partial (h\bar{u})}{\partial x}+\frac{\partial (h\bar{v})}{\partial y}=0. \tag{2.55}$$

Since there is an additional dimensionless parameter that appears, namely Re, compared to the LUB model, the DAF depends on two dimensionless groupings: an inertia parameter $\mathrm{I}=\mathrm{Ca}^{1/3}\cdot\mathrm{Re}$ and, as defined previously, the gravity parameter $\mathrm{N}=\mathrm{Ca}^{1/3}\cdot\cot\theta$.

The problem is closed in terms of specified averaged inflow conditions and the assumption of fully developed flow both upstream and downstream, namely:

$$\bar{u}|_{x=0}=2/3,\quad \bar{v}|_{x=0}=\frac{\partial \bar{u}}{\partial x}|_{x=l_p}=\frac{\partial \bar{v}}{\partial x}|_{x=l_p}=\frac{\partial \bar{u}}{\partial y}|_{y=0,w_p}=\frac{\partial \bar{v}}{\partial y}|_{y=0,w_p}=0. \tag{2.56}$$

$$h|_{x=0}=1,\quad \frac{\partial h}{\partial x}|_{x=l_p}=\frac{\partial h}{\partial y}|_{y=0,w_p}=0. \tag{2.57}$$

2.1.5 Friction and dispersion terms

Equations (2.53)-(2.55) contain friction and dispersion terms of the form $\frac{\partial u}{\partial z}|_{z=s}$, $\frac{\partial v}{\partial z}|_{z=s}$ and $\int_s^f (\bar{u}-u)^2\,dz$, $\int_s^f (\bar{v}-v)^2\,dz$, $\int_s^f (\bar{u}-u)(\bar{v}-v)\,dz$, respectively. For the thin film flows of interest, these terms can be determined explicitly by assuming that the velocity profile within the film has the same and consistent self-similar form as the classical Nusselt solution, Spurk & Aksel (2008), namely:

$$u=3\bar{u}\left(\xi-1/2\xi^2\right),\quad v=3\bar{v}\left(\xi-1/2\xi^2\right), \tag{2.58}$$

where $\xi=(z-s)/h$. Note that, this assumption is consistent with the integral-boundary-layer approximation discussed in Subsection 1.2.2, namely that the velocity profile across the film is parabolic. The validity and robust-

ness of using the velocity profiles given by equation (2.58) in the present work is established in Sections 3.2 and 4.2, even for flow over deep topographic features, by comparison with complementary experimentally measured and numerically predicted free-surface profiles. Alternatives to the assumption of parabolic velocity profile, that have previously been suggested in the literature, are discussed above in Subsection 1.2.2.

Accordingly, using relations (2.58) and equation (2.37) leads to the following analytical expressions for the friction and dispersion terms:

$$\frac{\partial u}{\partial z}|_{z=s} = \frac{3\bar{u}}{h}, \tag{2.59}$$

$$\frac{\partial v}{\partial z}|_{z=s} = \frac{3\bar{v}}{h}, \tag{2.60}$$

$$\frac{\partial}{\partial x}\int_s^f (\bar{u}-u)^2\,dz + \frac{\partial}{\partial y}\int_s^f (\bar{u}-u)(\bar{v}-v)\,dz = \frac{1}{5}\left(h\bar{u}\frac{\partial \bar{u}}{\partial x} + h\bar{v}\frac{\partial \bar{u}}{\partial y} - \bar{u}\frac{\partial h}{\partial t}\right), \tag{2.61}$$

$$\frac{\partial}{\partial x}\int_s^f (\bar{u}-u)(\bar{v}-v)\,dz + \frac{\partial}{\partial y}\int_s^f (\bar{v}-v)^2\,dz = \frac{1}{5}\left(h\bar{u}\frac{\partial \bar{v}}{\partial x} + h\bar{v}\frac{\partial \bar{v}}{\partial y} - \bar{v}\frac{\partial h}{\partial t}\right). \tag{2.62}$$

Note too, that the above forms for the friction and dispersion terms ensure that the DAF equations (2.53) and (2.54) become equivalent to equations (2.39), when $\mathrm{Re} = 0$.

Note also that equations (2.53)-(2.55) are equivalent to well-known shallow water equations, Shinbrot (1970) and Hervouet (2007), for the case with no capillary pressure, or $\mathrm{Ca} \to \infty$, since these equations are generally used in oceanographic and environmental studies, hydraulic engineering and other fields of science where the influence of capillarity is negligible. The shallow water equations were firstly derived and published in 1871 by French mechanician and mathematician Adhémar Jean Claude Barré de Saint-Venant, and are therefore often referred to as the Saint-Venant equations, Saint-Venant (1871). In shallow water applications the dispersion terms are usually neglected, while

the friction terms are obtained using the empirical Chézy's law for the flow in open channels and noncircular closed conduits, for which the average wall shear stress is deemed to be closely proportional to the square of the velocity, Streeter & Wylie (1981) and Chanson (2004):

$$\frac{\partial u}{\partial z}|_{z=s} = A_c \bar{u}\sqrt{\bar{u}^2+\bar{v}^2}, \quad \frac{\partial v}{\partial z}|_{z=s} = A_c \bar{v}\sqrt{\bar{u}^2+\bar{v}^2}, \tag{2.63}$$

where A_c is the Chézy coefficient, that is dependent on the Reynolds number of the flow and consequently on its type (laminar or turbulent). The value of A_c for lubrication-type flows is estimated by substitution of the form (2.63) into the momentum equation (2.53) and evaluating it at the inflow boundary: giving $A_c = 2\left(h/\bar{u}\sqrt{\bar{u}^2+\bar{v}^2}\right)|_{x=0} = 9/2$. However using the Chézy's form to define the frictions terms leads to non-equivalence of the lubrication and DAF equations when $\mathrm{Re} = 0$ in a general three-dimensional case.

2.1.6 Topography definition

Attention is restricted to flows involving simple, well-defined topography, namely one-dimensional (spanwise) trench, step-up, and step-down features, and in two dimensions (localised) rectangular trenches. Note, however, that the DAF can be applied to flows over more complex topographies - see for example Lee, Thompson & Gaskell (2008*b*). Since the topography profile appears as a function in the governing equations, it is not possible to consider completely sharp features. Following previous authors (Stillwagon & Larson, 1990; Peurrung & Graves, 1993; Gaskell *et al.*, 2004*b*) the topography is therefore specified via arctangent functions. For example, one-dimensional step-up/down and two-dimensional rectangular trench/peak topographies, as illustrated in the Figure 2.2, are defined as follows:

$$s^{\tan^{-1}}_{step-up/down}(x^*) = s_0\left[\frac{1}{2} \pm \tan^{-1}\left(\frac{x^*}{\delta}\right)\right], \tag{2.64}$$

$$s^{\tan^{-1}}_{trench/peak}(x^*, y^*) = \frac{s_0}{4\tan^{-1}\frac{l_t}{2\delta}\tan^{-1}\frac{w_t}{2\delta}}\left[\tan^{-1}\left(\frac{x^* + l_t/2}{\delta}\right)\right.$$
$$\left. - \tan^{-1}\left(\frac{x^* - l_t/2}{\delta}\right)\right] \cdot \left[\tan^{-1}\left(\frac{y^* + w_t/2}{\delta}\right) - \tan^{-1}\left(\frac{y^* - w_t/2}{\delta}\right)\right], \quad (2.65)$$

where $s_0\,(= S_0/H_0)$ is the dimensionless depth ($s_0 < 0$) or height ($s_0 > 0$), with $l_t\,(= L_T/L_0)$, $w_t\,(= W_T/L_0)$ and δ the non-dimensional streamwise length, spanwise width and topography steepness factor, respectively. The coordinate system $(x^*, y^*) = (x - x_t, y - y_t)$ has its origin at the centre of the topography, (x_t, y_t).

For topography that is symmetrical about the streamwise centreline such that $s(x^*, y^*) = s(x^*, -y^*)$ the following spanwise symmetry conditions hold:

$$(u, w, p)(x^*, y^*, z) = (u, w, p)(x^*, -y^*, z), \quad (2.66)$$

$$v(x^*, y^*, z) = -v(x^*, -y^*, z), \quad h(x^*, y^*) = h(x^*, -y^*). \quad (2.67)$$

Exploiting the above the governing equations (N-S, LUB or DAF) need to be solved over only half of the solution domain by imposing the following boundary conditions at the symmetry plane:

$$\frac{\partial u}{\partial y}|_{y^*=0} = v|_{y^*=0} = \frac{\partial w}{\partial y}|_{y^*=0} = \frac{\partial p}{\partial y}|_{y^*=0} = \frac{\partial h}{\partial y}|_{y^*=0} = 0. \quad (2.68)$$

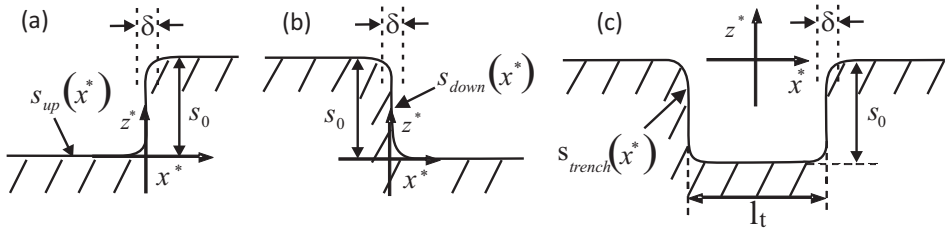

FIGURE 2.2: Examples of spanwise topography functions, $s(x^*)$: (a) step-up; (b) step-down; and (c) trench. The characteristic parameters associated with each topography type are shown.

Trench, step-up and step-down topography can be defined in other ways;

Tseluiko *et al.* (2008*b*), for example, used hyperbolic tangent functions:

$$s^{\tanh}_{step-up/down}\left(x^*\right) = \frac{s_0}{2}\left[1 \pm \tanh\left(\frac{x^*}{\delta}\right)\right]. \tag{2.69}$$

It is also possible to use linear functions:

$$s^{lin}_{step-up/down}\left(x^*\right) = \begin{cases} 0, & x^* < -\delta, \\ \frac{1}{2} + \frac{x^*}{2\delta}, & -\delta \leqslant x^* < \delta, \\ 1, & \delta \leqslant x^*. \end{cases} \tag{2.70}$$

In either case, the steepness of the topography, δ, is chosen to be small enough to ensure that results are steepness-independent.

2.2 Methods of solution

2.2.1 Full Navier-Stokes equations

2.2.1.1 Spatial discretisation

The full N-S system of equations, (2.7)-(2.8), and boundary conditions, (2.9)-(2.12), can be solved using an appropriate finite element formulation. For simplicity, the thin film flow problems of interest are considered to be steady-state:

$$\mathrm{Re}\boldsymbol{u}\cdot\nabla\boldsymbol{u} = -\nabla p + \nabla\cdot\boldsymbol{\tau} + \mathrm{St}\boldsymbol{g}, \tag{2.71}$$

$$\nabla\cdot\boldsymbol{u} = 0, \tag{2.72}$$

$$\boldsymbol{u}|_{z=s} = \boldsymbol{0}, \tag{2.73}$$

$$h|_{x=0} = 1, \quad \boldsymbol{u}|_{x=0,l_p;y=0,w_p} = z\left(2-z\right)\boldsymbol{i}, \tag{2.74}$$

$$\left(\boldsymbol{n}\cdot\boldsymbol{u}\right)|_{z=f} = 0, \tag{2.75}$$

$$(-p\boldsymbol{I} + \boldsymbol{\tau})\,|_{z=f}\boldsymbol{n} = \frac{\kappa}{\mathrm{Ca}}\boldsymbol{n}, \tag{2.76}$$

a complicating feature being the presence of a free surface, whose shape is not known a priori.

There are several techniques for tracking free and moving boundaries; these can, in general, be classified under three main headings: (a) surface tracking or predominantly Lagrangian methods; (b) volume tracking or Eulerian methods; (c) hybrid Arbitrary Lagrangian-Eulerian (ALE) methods that combine the advantages of the former two and allow accurate interface tracking with minimal mesh distortion at the same time, see Kistler & Schweizer (1997) and Shyy, Udaykumar, Rao & Smith (2007) for further details.

The ALE formulations together with finite element discretisations, reported in this section, have been applied effectively for tracking the free-surface location of two-dimensional coating flows for decades, see Christodoulou, Kistler & Schunk (1997) and the references contained therein. These include the spine method, Kistler & Scriven (1983), and its later modifications in generality and robustness based on the elliptic grid generation approach of Christodoulou *et al.* (1997) and the pseudo-solid mesh motion approach of Sackinger, Schunk & Rao (1996).

Despite there being a considerable amount of work devoted to free-surface tracking and the ALE approach coupled with finite element analyses, little of it considers fully three-dimensional free-surface problems, which represents one of the most important practical computational challenges for this class of problem, see Cairncross, Schunk, Baer, Rao & Sackinger (2000) and Baer, Cairncross, Schunk, Rao & Sackinger (2000). Example investigations include: three-dimensional bubble flow, Bunner & Tryggvason (1999); flow in a trapezoidal channel with bridge supports, Behr & Abraham (2002); surface-tension-dominated viscous flows, Walkley, Gaskell, Jimack, Kelmanson & Summers (2005); a study of the dynamics of three-dimensional liquid free surfaces with

surface tension and contact angle boundary conditions, Yue & Wang (2006); three-dimensional simulation of injection molding, Wang & Li (2010).

The numerical technique described below is a generalisation of both the spine method introduced in Kistler & Scriven (1983) and the three-dimensional ALE formulations of Cairncross *et al.* (2000). It shares the features of a strictly Lagrangian method, in which the grid is configured to conform to the shape of the free-surface interface and adapts continually to it, and those of a purely Eulerian formulation, in which the grid remains fixed where needed; thus in the general case the ALE formulation assumes the grid coordinates to be unknown.

In line with the underpinnings of the finite element method, the unknown velocity, pressure and grid coordinate fields are expanded in terms of basis functions (alternatively known as interpolation functions, trial functions or shape functions):

$$\boldsymbol{u} = \sum_{i=1}^{n^i} \boldsymbol{u}_i \phi_i, \quad p = \sum_{j=1}^{n^j} p_j \psi_j, \quad \boldsymbol{x} = \sum_{i=1}^{n^i} \boldsymbol{x}_i \phi_i, \tag{2.77}$$

where $i \in [1, n^i]$, $j \in [1, n^j]$, $\boldsymbol{u}_i = u_i \boldsymbol{i} + v_i \boldsymbol{j} + w_i \boldsymbol{k}$, p_j and $\boldsymbol{x}_i = x_i \boldsymbol{i} + y_i \boldsymbol{j} + z_i \boldsymbol{k}$ are the unknown nodal values of the velocity, pressure and coordinate fields, respectively; n^i is the total number of $\boldsymbol{u}/\boldsymbol{x}$-nodes and n^j is the total number of p-nodes; ϕ_i are basis functions for $\boldsymbol{u}/\boldsymbol{x}$ and ψ_j are basis functions for p. ϕ_i and ψ_j assume the value one at i and j nodes respectively, zero at any other nodes and intermediate values in between within the finite elements they touch, this is explained further and in more detail in Subsubsection 2.2.1.3. A 'mixed-interpolation' formulation with linear basis functions for pressure and quadratic basis functions for velocities and mesh coordinates is used, see Hood & Taylor (1974), that results in n^i and n^j being different. This type of interpolation, in contrast to 'equal-order-interpolation', satisfies the so called LBB stability condition named after Ladyzhenskaya (1963), Babuška (1971) and Brezzi (1974) and ensures that the pressure field is not polluted by so called

spurious nonphysical oscillations. The same second-order interpolation for velocities and coordinates is permitted, see Christodoulou *et al.* (1997), allowing second-order-accurate free-surface location to be obtained for almost the same computational cost. This enables V6/P3/X6 (6 $\boldsymbol{u}/\boldsymbol{x}$-nodes and 3 p-nodes) triangular or V10/P4/X10 (10 $\boldsymbol{u}/\boldsymbol{x}$-nodes and 4 p-nodes) tetrahedral element to be employed for two- and three-dimensional flow problems, respectively.

A popular Bubnov-Galerkin (B-G) weighted residual formulation, that assumes the weightings or test functions to be the same as the basis functions, is employed for the discretisation of equations (2.71), (2.72) and (2.75); this formulation has been applied successfully to various incompressible fluid flow problems, see Chung (2002). The momentum equation (2.71) is converted into a discretised system of algebraic equations by multiplying it with appropriate weighting functions, integrating over the computational domain, Ω, and transforming the result into a divergence form using equation (2.72) and the divergence theorem:

$$\boldsymbol{\mathcal{N}}_i^{mom} = \int_\Omega \left(\mathrm{Re}\boldsymbol{u}\cdot\nabla\boldsymbol{u} + \nabla p - \nabla\cdot\boldsymbol{\tau} - \mathrm{St}\boldsymbol{g}\right)\phi_i d\Omega$$

$$= \int_\Omega \Big[\nabla\left(\mathrm{Re}\boldsymbol{u}\otimes\boldsymbol{u} + p\boldsymbol{I} - \boldsymbol{\tau}\right) - \mathrm{St}\boldsymbol{g}\Big]\phi_i d\Omega = \boldsymbol{\mathcal{N}}_i^{mom,dom} + \Delta_{i,k}\boldsymbol{\mathcal{N}}_k^{mom,f.s.} = \boldsymbol{0}, \tag{2.78}$$

where $\otimes$ denotes dyadic product of two vectors.

$$\boldsymbol{\mathcal{N}}_i^{mom,dom} = \int_\Omega \Big[\left(-\mathrm{Re}\boldsymbol{u}\otimes\boldsymbol{u} - p\boldsymbol{I} + \boldsymbol{\tau}\right)\nabla\phi_i + \mathrm{St}\boldsymbol{g}\phi_i\Big] d\Omega, \tag{2.79}$$

is the integral over the interior of the flow domain Ω, and

$$\boldsymbol{\mathcal{N}}_k^{mom,f.s.} = -\int_\Gamma \left(-\mathrm{Re}\boldsymbol{u}\otimes\boldsymbol{u} - p\boldsymbol{I} + \boldsymbol{\tau}\right)\boldsymbol{n}\phi_k d\Gamma$$

$$= -\int_\Gamma \left(-p\boldsymbol{I} + \boldsymbol{\tau}\right)\boldsymbol{n}\phi_k d\Gamma = -\frac{1}{\mathrm{Ca}}\int_\Gamma \kappa\boldsymbol{n}\phi_k d\Gamma, \tag{2.80}$$

the integral over the boundary of the flow domain, Γ. Due to the presence of no-slip and specified inflow/outflow boundary conditions (2.73) and (2.74) $\boldsymbol{\mathcal{N}}_k^{mom,f.s.}$ is non-zero only at the free-surface boundary. The boundary conditions (2.75) and (2.76) are used to obtain the form (2.80). The Boolean matrix, $\Delta_{i,k}$, that relates the global $\boldsymbol{u}/\boldsymbol{x}$-node to the corresponding free-surface $\boldsymbol{u}/\boldsymbol{x}$-node for any $k \in \left[1, n^k\right]$, where $n^k\,(< n^i)$ is the total number of free-surface nodes, is defined as:

$$\Delta_{i,k} = \begin{cases} 1, \text{ if the global node } i \text{ corresponds to the free-surface node } k, \\ 0, \text{ otherwise.} \end{cases} \tag{2.81}$$

In two dimensions $d\Gamma$ is an arclength and the boundary-integral over Γ a line integral that can be simplified using the well-known expression for line curvature $\boldsymbol{n}\kappa = d\boldsymbol{t}/d\Gamma$ and integrating by parts:

$$\boldsymbol{\mathcal{N}}_k^{mom,f.s.,2D} = -\frac{1}{\mathrm{Ca}}\int_\Gamma \frac{d\boldsymbol{t}}{d\Gamma}\phi_k d\Gamma = \frac{1}{\mathrm{Ca}}\int_\Gamma \boldsymbol{t}\frac{d\phi_k}{d\Gamma}d\Gamma - \frac{1}{\mathrm{Ca}}\Big[(\boldsymbol{t}\phi_k)\,|_{x=l_p} - (\boldsymbol{t}\phi_k)\,|_{x=0}\Big], \tag{2.82}$$

where the terms in (2.82) with the inflow and outflow unit vectors tangent to Γ, $\boldsymbol{t}|_{x=0}$ and $\boldsymbol{t}|_{x=l_p}$ respectively, can be omitted due to the inflow/outflow boundary condition (2.74).

In three dimensions $d\Gamma$ is a surface area and the boundary-integral over Γ a surface integral that can be simplified using the surface divergence theorem, that lowers the order of spatial derivatives, and the well-known expression for surface gradient $\nabla_s\phi_k = \nabla\phi_k - \boldsymbol{n}\,(\boldsymbol{n}\cdot\nabla\phi_k)$, see Fosdick & Tang (2009):

$$\begin{aligned} \boldsymbol{\mathcal{N}}_k^{mom,f.s.,3D} &= -\frac{1}{\mathrm{Ca}}\int_\Gamma \kappa\boldsymbol{n}\phi_k d\Gamma = \frac{1}{\mathrm{Ca}}\int_\Gamma \nabla_s\phi_k d\Gamma - \frac{1}{\mathrm{Ca}}\oint_R \boldsymbol{t}|_R\phi_k dR \\ &= \frac{1}{\mathrm{Ca}}\int_\Gamma \Big[\nabla\phi_k - \boldsymbol{n}\,(\boldsymbol{n}\cdot\nabla\phi_k)\Big]d\Gamma - \frac{1}{\mathrm{Ca}}\oint_R \boldsymbol{t}|_R\phi_k dR, \end{aligned} \tag{2.83}$$

where dR is the arclength along R, the curve bounding Γ, and $\boldsymbol{t}|_R$ is a unit

vector along R, tangential to the free surface Γ but normal to R. The integration over R in (2.83) can be omitted due to the inflow/outflow boundary condition (2.74).

In a similar way the Bubnov-Galerkin formulation is applied to obtain the discrete forms of equation (2.72) and boundary condition (2.75):

$$\mathcal{N}_j^{cont} = \int_\Omega \nabla \cdot \boldsymbol{u} \psi_j d\Omega = 0, \tag{2.84}$$

$$\mathcal{N}_k^{kin} = \int_\Gamma (\boldsymbol{n} \cdot \boldsymbol{u})\, \phi_k d\Gamma = 0. \tag{2.85}$$

2.2.1.2 Spine method for representing free surfaces

The system of discrete equations (2.78), (2.84) and (2.85) is not yet complete, since the number of unknowns is larger than the number of equations $2dim \cdot n^i + n^j > dim \cdot n^i + n^j + n^k$, where dim is the dimensionality of the problem ($dim = 2$ and 3 for two- and three-dimensional problem, respectively). However it is necessary to remember that mesh node positions are not independent and the mesh moves synchronously to capture the free-surface location. Therefore it is necessary to specify the rule that relates the positions of the mesh nodes $\boldsymbol{x}_i$ to a set of free-surface parameters, whose values determine how the mesh changes in response to the moving free-surface boundary. The method of spines, Kistler & Scriven (1983), represents one technique for tying the deformation of the internal mesh to that of the interface. The basic idea of the spine method is to parametrise the free surface by its location along a series of conventionally placed, independent spines. Each spine is defined by the location of a fixed base node $\boldsymbol{x}_k^b$ and a fixed direction vector $\boldsymbol{d}_k$. The moving mesh nodes are chosen in such a way that each of them lies on some spine and therefore have the same fixed base node $\boldsymbol{x}_i^b = \widetilde{\Delta}_{i,k} \boldsymbol{x}_k^b$ and fixed direction vector $\boldsymbol{d}_i = \widetilde{\Delta}_{i,k} \boldsymbol{d}_k$; see Figure 2.3 for an example of spine locations for flow over a one-dimensional trench. The fixed mesh nodes, that do not move with the free surface, have

$\boldsymbol{d}_k = 0$. The Boolean matrix $\widetilde{\Delta}_{i,k}$ is defined as:

$$\widetilde{\Delta}_{i,k} = \begin{cases} 1, \text{ if the global node } i \text{ lies on the spine } k, \\ 0, \text{ otherwise.} \end{cases} \tag{2.86}$$

Since the ordering of the spines is the same as the ordering of the free-surface nodes, $\widetilde{\Delta}_{i,k}$ is equal to the previously defined $\Delta_{i,k}$ if i is a free-surface node. In this representation the 'free-surface parameters' are the spinal distances h_k along each spine between its base and free-surface node:

$$\boldsymbol{x}_i = \widetilde{\Delta}_{i,k} \left(\boldsymbol{x}_k^b + h_k \boldsymbol{d}_k \right) = \boldsymbol{x}_i^b + \widetilde{\Delta}_{i,k} h_k \boldsymbol{d}_i. \tag{2.87}$$

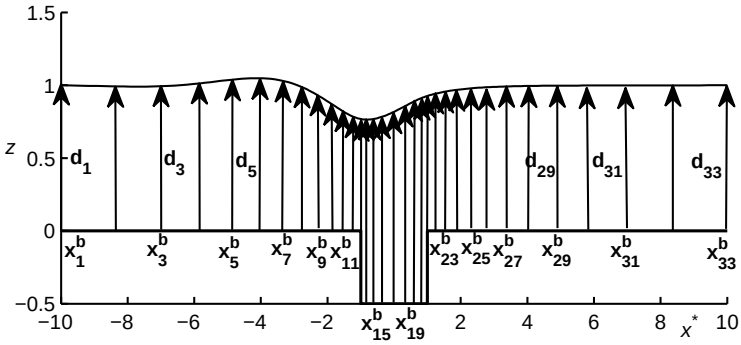

FIGURE 2.3: Spine fixed base nodes $\boldsymbol{x}_k^b$ and fixed direction vectors $\boldsymbol{d}_k$ for thin film flow over a one-dimensional trench with $l_t = 2.0$ and $s_0 = 0.5$. For illustration purposes the number of spines as well as free-surface $\boldsymbol{u}/\boldsymbol{x}$-nodes shown is for the case $n^k = 33$.

As a result the grid nodes have displacements that are intermediate between the free-surface node displacement and zero base nodes displacement depending on the direction vector length along the spine. Since the total number of spines is the same as the number of free-surface nodes, i.e. n^k, the full system of discretised equations is determined and can be written in the form:

$$\boldsymbol{\mathcal{N}}(\boldsymbol{z}) = \boldsymbol{0}, \tag{2.88}$$

where $\boldsymbol{\mathcal{N}}$ and $\boldsymbol{z}$ are the global residual and solution vectors, respectively:

$$\boldsymbol{\mathcal{N}} = \begin{pmatrix} \boldsymbol{\mathcal{N}}_i^{mom} \\ \mathcal{N}_j^{cont} \\ \mathcal{N}_k^{kin} \end{pmatrix}, \quad \boldsymbol{z} = \begin{pmatrix} \boldsymbol{u_i} \\ p_j \\ h_k \end{pmatrix}. \tag{2.89}$$

2.2.1.3 Calculation of domain integrals

Consider the case when the problem domain Ω is divided into n^e elements and the free-surface boundary Γ is divided into n^s free-surface elements:

$$\Omega = \bigcup_{e=1}^{n^e} \Omega_e, \quad \Gamma = \bigcup_{s=1}^{n^s} \Gamma_s, \tag{2.90}$$

where Ω_e is the local domain of element e and Γ_s is the local domain of free-surface element s. Due to the local non-zero nature of the basis and weighting functions it is possible to calculate the integrals (2.79) and (2.84) over the whole problem domain Ω or integrals (2.80) and (2.85) over the whole free-surface boundary Γ by assembling the corresponding integral contributions over each element domain, Ω_e, or free-surface, Γ_s, respectively:

$$\boldsymbol{\mathcal{N}}_i^{mom} = \bigcup_{e=1}^{n^e} \Delta_{i,\alpha}^{(e)} \boldsymbol{\mathcal{N}}_\alpha^{mom,dom,(e)} + \Delta_{i,k} \bigcup_{s=1}^{n^s} \Delta_{k,\gamma}^{(s)} \boldsymbol{\mathcal{N}}_\gamma^{mom,f.s.,(s)},$$

$$\mathcal{N}_j^{cont} = \bigcup_{e=1}^{n^e} \Delta_{j,\beta}^{(e)} \mathcal{N}_\beta^{cont,(e)}, \quad \mathcal{N}_k^{kin} = \bigcup_{s=1}^{n^s} \Delta_{k,\gamma}^{(s)} \mathcal{N}_\gamma^{kin,(s)}, \tag{2.91}$$

where $\alpha \in [1, n^\alpha]$, $\beta \in \left[1, n^\beta\right]$, $\gamma \in [1, n^\gamma]$ are the local numbers for $\boldsymbol{x}/\boldsymbol{u}$-node, p-node, and free-surface $\boldsymbol{x}/\boldsymbol{u}$-node, respectively; $\boldsymbol{\mathcal{N}}_\alpha^{mom,dom,(e)}$, $\mathcal{N}_\beta^{cont,(e)}$, $\boldsymbol{\mathcal{N}}_\alpha^{mom,f.s.,(e)}$, $\mathcal{N}_\gamma^{kin,(s)}$ are the local integrals that include integration over the local element domain, Ω_e, and free-surface, Γ_s, only; $\Delta_{i,\alpha}^{(e)}$, $\Delta_{j,\beta}^{(e)}$ and $\Delta_{k,\gamma}^{(s)}$ are Boolean matrices that relate the global node to a local one, see Chung (2002)

for further detail. For example, the matrix $\Delta_{i,\alpha}^{(e)}$ is defined as:

$$\Delta_{i,\alpha}^{(e)} = \begin{cases} 1, \text{ if the global node } i \text{ corresponds to the local node } \alpha \text{ of element } e \\ 0, \text{ otherwise} \end{cases} \tag{2.92}$$

while the matrices $\Delta_{j,\beta}^{(e)}$ and $\Delta_{k,\gamma}^{(s)}$ are similarly defined; $n^{\alpha} = (dim+1)(dim+2)/2$, $n^{\beta} = dim+1$ and $n^{\gamma} = dim(dim+1)/2$ are the total number of local $\boldsymbol{x}/\boldsymbol{u}$-nodes, p-nodes, and free-surface $\boldsymbol{x}/\boldsymbol{u}$-nodes in an element, respectively.

In order to calculate the local integrals for triangular element for a two-dimensional problem (tetrahedral element for a three-dimensional problem) it is convenient to introduce local natural coordinates L_β for $\beta \in \left[1, n^{\beta}\right]$, whose values are zero along its edges (faces) and unity at its vertices with a linear variation in between, see Chung (2002). These coordinates, L_β, are called 'area' coordinates for triangular element ('volume' coordinates for tetrahedral element), because the L_β are equal to areal (volumetric) fractions obtained by connecting the corner vertices of the element to any point within the element. Figure 2.4 shows the location of the local nodes for: (a) a triangular element in two dimensions; (b) a tetrahedral element in three dimensions, respectively.

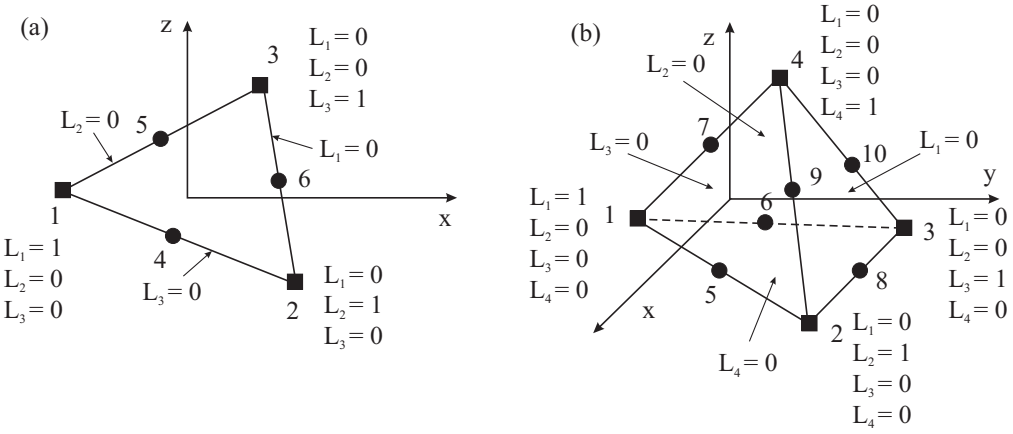

FIGURE 2.4: Natural coordinates for (a) triangular elements and (b) tetrahedral elements. Filled squares denote the positions of both $\boldsymbol{u}/\boldsymbol{x}$ and p variables, while filled circles denote the positions of $\boldsymbol{u}/\boldsymbol{x}$ variables only.

Using the local natural coordinates L_β it is possible to expand the unknown

solutions $\boldsymbol{u}$, p and $\boldsymbol{x}$ in a local series similar to (2.77):

$$\boldsymbol{u} = \sum_{\alpha=1}^{n^\alpha} \boldsymbol{u}_\alpha \phi_\alpha, \quad p = \sum_{\beta=1}^{n^\beta} p_\beta \psi_\beta, \quad \boldsymbol{x} = \sum_{\alpha=1}^{n^\alpha} \boldsymbol{x}_\alpha \phi_\alpha, \tag{2.93}$$

where $\boldsymbol{u}_\alpha$, p_β and $\boldsymbol{x}_\alpha$ are the values of local $\boldsymbol{u}$-nodes, p-nodes and $\boldsymbol{x}$-nodes, respectively; while ϕ_α and ψ_β are the basis/weighting functions expressed in terms of the local natural coordinates as:

$$\phi_\alpha = \begin{cases} L_\alpha \left(2L_\alpha - 1\right), \, \alpha \in \left[1, n^\beta\right], \\ 4L_{\alpha_1} L_{\alpha_2}, \, \alpha \in \left[n^\beta + 1, n^\alpha\right], \end{cases} \quad \psi_\beta = L_\beta, \, \beta \in \left[1, n^\beta\right], \tag{2.94}$$

where:

$$\alpha_1 \left(\alpha\right) = \text{trunc} \left[\frac{3 + \sqrt{8 \left(\alpha - n^\beta\right) - 7}}{2} \right], \alpha_2 \left(\alpha\right) = \alpha - n^\beta - \frac{\left(\alpha_1 - 1\right)\left(\alpha_1 - 2\right)}{2},$$

and $\text{trunc}\left(x\right)$ is the truncation function from real to integer. Note that in addition:

$$1 = \sum_{\beta=1}^{n^\beta} L_\beta, \tag{2.95}$$

expressing the fact that the sum of all fractions is equal to 1; makes the transformation $\boldsymbol{x}\left(L_1, L_2 ... L_{n^\beta}\right)$ unique with the number of equations equal to the number of independent variables, i.e. n^β;. Therefore, for example, in three dimensions the Jacobian of the transformation $\boldsymbol{x}\left(L_1, L_2 ... L_{n^\beta}\right)$ is:

$$J = \begin{pmatrix} 1 & 1 & 1 & 1 \\ \frac{\partial x}{\partial L_1} & \frac{\partial x}{\partial L_2} & \frac{\partial x}{\partial L_3} & \frac{\partial x}{\partial L_4} \\ \frac{\partial y}{\partial L_1} & \frac{\partial y}{\partial L_2} & \frac{\partial y}{\partial L_3} & \frac{\partial y}{\partial L_4} \\ \frac{\partial z}{\partial L_1} & \frac{\partial z}{\partial L_2} & \frac{\partial z}{\partial L_3} & \frac{\partial z}{\partial L_4} \end{pmatrix}. \tag{2.96}$$

Using the expressions (2.93), (2.94) and parametric mapping $\boldsymbol{x}\left(L_1, L_2 ... L_{n^\beta}\right)$ it is possible to present $\boldsymbol{\mathcal{N}}_\alpha^{mom,dom,(e)}$ as an integral of a fraction of polynomials

over a unit orthogonal triangle in two dimensions (unit orthogonal tetrahedral in three dimensions):

$$\boldsymbol{\mathcal{N}}_{\alpha}^{mom,dom,(e)} = \int_{\Omega_e} \Big[\left(-\mathrm{Re}\boldsymbol{u} \otimes \boldsymbol{u} - p\boldsymbol{I} + \boldsymbol{\tau}\right) \nabla\phi_\alpha + \mathrm{St}\boldsymbol{g}\phi_\alpha \Big] d\Omega_e$$

$$= \int_0^1 \int_0^{1-L_1} \ldots \int_0^{1-\sum_{\beta=1}^{dim-1} L_\beta} \Big[\left(-\mathrm{Re}\boldsymbol{u} \otimes \boldsymbol{u} - p\boldsymbol{I} + \boldsymbol{\tau}\right) \nabla\phi_\alpha + \mathrm{St}\boldsymbol{g}\phi_\alpha \Big] |J| \, dL_1 dL_2 \ldots dL_{dim}, \tag{2.97}$$

where $|J|$ is the determinant of the Jacobian matrix (2.96) and $\nabla\phi_\alpha$ is given by:

$$\nabla\phi_\alpha = \sum_{\beta=1}^{n^\beta} \frac{\partial\phi_\alpha}{\partial L_\beta} \frac{\partial L_\beta}{\partial \boldsymbol{x}} = \frac{1}{|J|} \sum_{\beta=1}^{n^\beta} \frac{\partial\phi_\alpha}{\partial L_\beta} \Big[\boldsymbol{i} C_{\beta x}(J) + \boldsymbol{j} C_{\beta y}(J) + \boldsymbol{k} C_{\beta z}(J) \Big]. \tag{2.98}$$

The $\partial\phi_\alpha/\partial L_\beta$ derivatives are calculated according to (2.94) and $\partial L_\beta/\partial \boldsymbol{x}$ are the elements of the inverse of the Jacobian matrix:

$$J^{-1} = \frac{1}{|J|} \begin{pmatrix} C_{11}(J) & C_{1x}(J) & C_{1y}(J) & C_{1z}(J) \\ C_{21}(J) & C_{2x}(J) & C_{2y}(J) & C_{2z}(J) \\ C_{31}(J) & C_{3x}(J) & C_{3y}(J) & C_{3z}(J) \\ C_{41}(J) & C_{4x}(J) & C_{4y}(J) & C_{4z}(J) \end{pmatrix}, \tag{2.99}$$

obtained using the well-known expression in terms of the transpose of the matrix of cofactors, $C(J)$, and the determinant, $|J|$.

In a similar way the local continuity integral, $\mathcal{N}_\beta^{cont,(e)}$, can be obtained as an integral over a unit orthogonal triangle in two dimensions (unit orthogonal tetrahedron in three dimensions):

$$\mathcal{N}_\beta^{cont,(e)} = \int_{\Omega_e} \nabla\cdot\boldsymbol{u}\psi_\beta d\Omega_e = \int_0^1 \int_0^{1-L_1} \ldots \int_0^{1-\sum_{\beta=1}^{dim-1} L_\beta} \nabla\cdot\boldsymbol{u} \, |J| \, \psi_\beta dL_1 dL_2 \ldots dL_{dim}. \tag{2.100}$$

The integrals (2.97) and (2.100) are calculated numerically using Gaussian

quadrature, a method that is one of the most accurate and widely used methods for the calculation of integrals arising from finite element discretisations, see Appendix A for further details.

2.2.1.4 Calculation of free-surface integrals

In order to calculate the local free-surface integrals, $\boldsymbol{\mathcal{N}}_{\gamma}^{mom,f.s.,2D,(s)}$, $\boldsymbol{\mathcal{N}}_{\gamma}^{mom,f.s.,3D,(s)}$ and $\mathcal{N}_{\gamma}^{kin,(s)}$, consider an element, whose edge in two dimensions (face in three dimensions) belongs to the free surface and assume without loss of generality, that the natural coordinate that is equal to zero at this edge (face) is L_1, i.e. the free surface is determined as:

$$\Gamma \equiv (L_1 = 0)\,. \tag{2.101}$$

Then the location of any point on the free surface is determined by the rest of the coordinates L_2,L_3...L_{n^β}. Using assumption (2.101) a vector normal to the free-surface edge in two dimensions (face in three dimensions) is obtained as:

$$\boldsymbol{N} = \left[\left(\frac{\partial \boldsymbol{x}}{\partial L_2} - \frac{\partial \boldsymbol{x}}{\partial L_4}\right) \times \left(\frac{\partial \boldsymbol{x}}{\partial L_3} - \frac{\partial \boldsymbol{x}}{\partial L_4}\right)\right] |_{L_1=0} = \left| \begin{array}{cccc} 0 & \boldsymbol{i} & \boldsymbol{j} & \boldsymbol{k} \\ 1 & \frac{\partial x}{\partial L_2} & \frac{\partial y}{\partial L_2} & \frac{\partial z}{\partial L_2} \\ 1 & \frac{\partial x}{\partial L_3} & \frac{\partial y}{\partial L_3} & \frac{\partial z}{\partial L_3} \\ 1 & \frac{\partial x}{\partial L_4} & \frac{\partial y}{\partial L_4} & \frac{\partial z}{\partial L_4} \end{array} \right| |_{L_1=0}$$

$$= \Big[\boldsymbol{i} C_{1x}(J) + \boldsymbol{j} C_{1y}(J) + \boldsymbol{k} C_{1z}(J)\Big] |_{L_1=0}, \tag{2.102}$$

where $\times$ denotes the vector product of two vectors. In other words, expression (2.102) means that components of the normal vector $\boldsymbol{N}$ are the elements of the matrix $C(J)$. The unit normal vector is calculated as $\boldsymbol{n} = \boldsymbol{N} / |\boldsymbol{N}|$.

In two dimensions the line integral (2.82) is obtained using the expressions for the unit tangential vector, $\boldsymbol{t} = \boldsymbol{i}\,(\boldsymbol{n} \cdot \boldsymbol{k}) - \boldsymbol{k}\,(\boldsymbol{n} \cdot \boldsymbol{i})$, and the full differential,

$d\phi_\gamma$, as follows:

$$\boldsymbol{\mathcal{N}}_\gamma^{mom,f.s.,2D,(s)} = \frac{1}{\mathrm{Ca}} \int_{\Gamma_s} \boldsymbol{t} \frac{d\phi_\gamma}{d\Gamma_s} d\Gamma_s$$

$$= \frac{1}{\mathrm{Ca}} \int_0^1 \Big[\boldsymbol{i} \left(\boldsymbol{n} \cdot \boldsymbol{k} \right) - \boldsymbol{k} \left(\boldsymbol{n} \cdot \boldsymbol{i} \right) \Big] \Big(\frac{\partial \phi_\gamma}{\partial L_2} - \frac{\partial \phi_\gamma}{\partial L_3} \Big) |_{L_1=0} dL_2, \tag{2.103}$$

and therefore simplifies to an integral of a fraction of polynomials over a unit segment in two dimensions (triangle in three dimensions) similar to (2.97).

In three dimensions expression (2.98) is used to obtain $\nabla \phi_\gamma |_{L_1=0}$ and together with the parametric form of the surface integral is gives the free-surface integral (2.83) in a form similar to (2.97):

$$\boldsymbol{\mathcal{N}}_\gamma^{mom,f.s.,3D,(s)} = \frac{1}{\mathrm{Ca}} \int_{\Gamma_s} \Big[\nabla \phi_\gamma - \boldsymbol{n} \left(\boldsymbol{n} \cdot \nabla \phi_\gamma \right) \Big] |_{L_1=0} d\Gamma_s$$

$$= \frac{1}{\mathrm{Ca}} \int_0^1 \int_0^{1-L_2} \Big[\nabla \phi_\gamma - \boldsymbol{n} \left(\boldsymbol{n} \cdot \nabla \phi_\gamma \right) \Big] |_{L_1=0} \left| \boldsymbol{N} \right| dL_2 dL_3, \tag{2.104}$$

where $|\boldsymbol{N}|$ is determined according to expression (2.102). Finally, in a similar way the local kinematic condition integral, $\mathcal{N}_\gamma^{kin,(s)}$, is obtained in the form of an integral over a unit segment in two dimensions (unit orthogonal triangle in three dimensions):

$$\mathcal{N}_\gamma^{kin,(s)} = \int_{\Gamma_s} \left(\boldsymbol{n} \cdot \boldsymbol{u} \right) |_{L_1=0} \phi_\gamma d\Gamma_s$$

$$= \int_0^1 \int_0^{1-L_2} ... \int_0^{1-\sum_{\beta=2}^{dim-1} L_\beta} \left(\boldsymbol{N} \cdot \boldsymbol{u} \right) |_{L_1=0} \phi_\gamma dL_2 dL_3 ... dL_{dim}. \tag{2.105}$$

The integrals (2.103), (2.104) and (2.105) are evaluated numerically using Gaussian quadrature, see Appendix A.

2.2.2 Multifrontal solver

Accurate and fast solutions to large three-dimensional free-surface problems can only be obtained via a parallel computing strategy. Thus the system of lin-

ear algebraic equations (2.106) is solved using a parallel multifrontal method, that is a variant of Gaussian elimination initially developed for indefinite sparse symmetric linear systems by Duff & Reid (1983) and then extended to unsymmetric matrices, Duff & Reid (1984). A widely used and efficient parallel implementation of the method from the MUltifrontal Massively Parallel sparse direct Solver (MUMPS) is employed, which is written in Fortran 90 with a C interface and invokes the well-known memory distributed parallel message passing interface (MPI) protocol, Snir, Otto, Huss-Lederman, Walker & Dongarra (1996), together with the BLAS, Dongarra, Du Cruz, Hammerling & Duff (1990), BLACS, and ScaLAPACK, Blackford *et al.* (1997) libraries. Only a brief description of the multifrontal method and the MUMPS library is given; for a more detailed overview of the multifrontal method see Liu (1992), while for the MUMPS library see Amestoy, Duff & L'Excellent (2000), Amestoy, Duff, L'Excellent & Koster (2001) and Amestoy, Guermouche, L'Excellent & Pralet (2006).

The Newton-Raphson method, see Appendix B, is used to linearise the global system of discrete N-S equations, (2.88):

$$\frac{\partial \boldsymbol{\mathcal{N}}}{\partial \boldsymbol{z}} \Delta \boldsymbol{z} = -\boldsymbol{\mathcal{N}}, \tag{2.106}$$

that is subsequently solved by the multifrontal method in three steps:

(i) an analysis step (or symbolic factorisation step), that only considers the pattern of the global Jacobian matrix, $\frac{\partial \boldsymbol{\mathcal{N}}}{\partial \boldsymbol{z}}$, and builds the necessary data structures for numerical computations;

(ii) a numerical factorisation step, that performes assembly of the global Jacobian matrix, see Appendix B, together with building the sparse factors (e.g., the elements of the lower triangular matrix $\bar{\boldsymbol{L}}$ and upper triangular matrix $\bar{\boldsymbol{U}}$, such that $\bar{\boldsymbol{L}}\bar{\boldsymbol{U}} = \frac{\partial \boldsymbol{\mathcal{N}}}{\partial \boldsymbol{z}}$);

(iii) a solution step, consisting of forward elimination (solves $\bar{\boldsymbol{L}}\boldsymbol{y} = -\boldsymbol{\mathcal{N}}$ for a temporary vector $\boldsymbol{y}$) and backward substitution (solves $\bar{\boldsymbol{U}}\Delta\boldsymbol{z} = \boldsymbol{y}$ for $\Delta\boldsymbol{z}$).

The first step in the multifrontal method is the analysis step intended to compute an efficient elimination tree that is used later in the factorisation stage. The elimination tree can be referred to as the smallest data structure representing dependencies between the operations required for factorisation, see Liu (1990). The multifrontal method employes a generalised version of the elimination tree - assembly tree, as introduced by Duff & Reid (1983) to determine the assembly order in the multifrontal method. Here the analysis stage is performed using an efficient routine METIS_NODEND from the METIS package, that is based on multilevel nested dissection and multiple minimum degree algorithms, see Karypis & Kumar (1998). In addition, in a parallel context, the analysis step maps the obtained assembly tree onto the target multiprocessor computer.

The second factorisation step of the multifrontal method is undertaken by performing a succession of partial factorisations of small dense matrices called 'frontal matrices', that are associated with each node of the assembly tree created during the analysis step. Each frontal matrix is divided into two parts: the factor block, also called fully summed block, which corresponds to the variables which are factorised when the elimination algorithm processes the frontal matrix; the contribution block which corresponds to the variables which are updated when processing the frontal matrix. Once the partial factorisation is complete, the contribution block is passed to the 'parent' node. When contributions from all 'children' are available on the 'parent' node, they are assembled (i.e. summed with the values contained in the frontal matrix of the parent), see Duff & Reid (1983, 1984).

For three-dimensional free-surface N-S problems, the multifrontal method re-

quires a large amount of memory, that can be much larger than the physical (in-core) memory available on the system. Thus an out-of-core approach must be used, see Agullo, Guermouche & L'Excellent (2008). This approach assumes that only the frontal matrices are held in main memory while the factors, which are accessed only during the final solution step, can be held in direct-access files stored on the hard drive. This approach allows much larger problems to be considered and reduces significantly memory usage (by a factor 5–10 on 1–4 processors, and a factor around 2 on 16–128 processors). In addition in a parallel context, increasing the number of processors, and therefore available physical memory, can help keep large frontal matrices in-core.

2.2.3 Lubrication equations

2.2.3.1 Spatial discretisation

Equations (2.34) - (2.40) are solved, subject to boundary conditions (2.41) and (2.42), on a rectangular computational domain, $(x, y) \in [0, l_p] \times [0, w_p]$, subdivided using a regular mesh arrangement of nodes with increments of Δx and Δy in x- and y-directions, respectively. The unknown variables, film thickness, h, and pressure, p are located at grid nodes (i, j). Following Kondic & Diez (2001), Zhornitskaya & Bertozzi (2000), Gaskell *et al.* (2004*b*) and Lee *et al.* (2007) the corresponding coupled second-order accurate discretisation scheme for h and p can be written:

$$\frac{\partial h}{\partial t}|_{i,j} = \frac{1}{3}\left[\frac{h^3_{i+1/2,j}\left(p_{i+1,j} - p_{i,j}\right) - h^3_{i-1/2,j}\left(p_{i,j} - p_{i-1,j}\right)}{\Delta x^2} + \right.$$

$$\left. + \frac{h^3_{i,j+1/2}\left(p_{i,j+1} - p_{i,j}\right) - h^3_{i,j-1/2}\left(p_{i,j} - p_{i,j-1}\right)}{\Delta y^2}\right] - \frac{2}{3}\frac{h^3_{i+1/2,j} - h^3_{i-1/2,j}}{\Delta x}, \tag{2.107}$$

$$p_{i,j} + \frac{\varepsilon^3}{\mathrm{Ca}} \left(\frac{f_{i+1,j} + f_{i-1,j} - 2f_{i,j}}{\Delta x^2} + \frac{f_{i,j+1} + f_{i,j-1} - 2f_{i,j}}{\Delta y^2} \right) - 2\varepsilon \cot\theta f_{i,j} = 0, \tag{2.108}$$

where the terms $h^3_{i\pm1/2,j}$ and $h^3_{i,j\pm1/2}$, sometimes referred to as prefactors, are formed using linear interpolation between the neighbouring nodes,

$$h^3_{i\pm1/2,j} = \frac{1}{2}\left(h^3_{i\pm1,j} + h^3_{i,j}\right), \quad h^3_{i,j\pm1/2} = \frac{1}{2}\left(h^3_{i,j\pm1} + h^3_{i,j}\right). \tag{2.109}$$

Dirichlet boundary conditions are assigned as exact values at the boundary points, whereas Neumann boundary conditions are implemented by employing ghost nodes at the edge of the computational domain.

To simplify the description of the calculation procedure presented below, it is convenient to separate the leading temporal h term and p term from the discretised continuity and pressure operators and to express them as functions $\mathcal{M}^h_{i,j}$ and $\mathcal{M}^p_{i,j}$, respectively. This enables equations (2.107)-(2.108) to be rewritten as:

$$\frac{\partial h}{\partial t}|_{i,j} + \mathcal{M}^h_{i,j}(h,p) = 0, \tag{2.110}$$

$$p_{i,j} + \mathcal{M}^p_{i,j}(h) = 0. \tag{2.111}$$

The locations of the independent variables (h,p), when determining the functions $\mathcal{M}^h_{i,j}$ and $\mathcal{M}^p_{i,j}$ are shown in Figure 2.5.

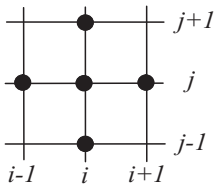

FIGURE 2.5: Stencils for defining the LUB functions: $\mathcal{M}^h_{i,j}$ and $\mathcal{M}^p_{i,j}$. The positions of the independent variables h and p are denoted by filled circles.

2.2.3.2 Temporal discretisation

The automatic adaptive time-stepping procedure adopted employs an estimate of the local truncation error (LTE) obtained from the difference between an explicit predictor stage and the current solution stage to optimise the size of time steps and minimise computational waste.

Fully explicit, second-order accurate in time discretisations of equations (2.110) - (2.111) can be used to predict (pr) values for h and p as follows:

$$h_{\mathrm{pr}}|_{i,j}^{n+1} = \gamma^2 h_{i,j}^{n-1} + \left(1-\gamma^2\right) h_{i,j}^{n} - \Delta t^{n+1}\left(1+\gamma\right)\mathcal{M}_{i,j}^{h}\left(h^n, p^n\right), \tag{2.112}$$

$$p_{\mathrm{pr}}|_{i,j}^{n+1} + \mathcal{M}_{i,j}^{p}\left(h_{\mathrm{pr}}|^{n+1}\right) = 0, \tag{2.113}$$

where n and $n+1$ denote values at the end of the nth and $(n+1)$st time steps, $t = t^n$ and $t = t^{n+1}$, respectively, and $\gamma = \Delta t^{n+1}/\Delta t^n = \left(t^{n+1} - t^n\right)/\left(t^n - t^{n-1}\right)$.

Adaptive time-stepping is performed by keeping the LTE for h_{pr} within a specified tolerance that provides a means of increasing the time step in a controlled manner. The LTE for h_{pr} at the predictor stage can be expressed via a Taylor series expansion of equation (2.112) in the form:

$$(\mathrm{LTE})_{\mathrm{pr}}|_{i,j} = \frac{(\Delta t^{n+1})\Delta t^n(1+\gamma)}{6}\frac{\partial^3 h}{\partial t^3}|_{i+1/2,j,t=t_p}, \tag{2.114}$$

with the third-order time derivative term evaluated at time $t_p \in (t^n, t^{n+1})$.

In the present work, an implicit and unconditionally stable Crank-Nicolson scheme, see Gaskell, Jimack, Sellier & Thompson (2004*a*), is used to advance the solution in time:

$$h_{i,j}^{n+1} + \frac{\Delta t^{n+1}}{2}\mathcal{M}_{i,j}^{h}\left(h^{n+1}, p^{n+1}\right) = h_{i,j}^{n} - \frac{\Delta t^{n+1}}{2}\mathcal{M}_{i,j}^{h}\left(h^n, p^n\right), \tag{2.115}$$

$$p_{i,j}^{n+1} + \mathcal{M}_{i,j}^{p}\left(h^{n+1}\right) = 0. \tag{2.116}$$

The LTE for h at the solution (sol) stage is similarly given by a Taylor series expansion of equation (2.115):

$$(\text{LTE})_{\text{sol}}|_{i,j} = -\frac{(\Delta t^{n+1})^3}{12}\frac{\partial^3 h}{\partial t^3}|_{i,j,t=t_s}, \quad t_s \in (t^n, t^{n+1}). \tag{2.117}$$

As described in Chapra & Canale (2002), the assumption that the third-order derivative term varies by only a small amount over the time step enables the LTE to be estimated as:

$$(\text{LTE})_{i,j} = \frac{h_{i,j}^{n+1} - h_{\text{pr}}|_{i,j}^{n+1}}{1 + 2[(1+\gamma)/\gamma]}, \tag{2.118}$$

which, following Dormand (1996), is used to obtain an estimate of the overall truncation error by finding its Euclidean norm that, in turn, is used to specify the next time step Δt^{n+2} via:

$$\Delta t^{n+2} = 0.9\Delta t^{n+1}\left(\frac{\text{TOL}}{||\text{LTE}||}\right)^{1/3}, \tag{2.119}$$

if $||\text{LTE}|| \leqslant \text{TOL}$, where $||\ ||$ denotes the Euclidean norm. The iteration is restarted with half the current time step if $||\text{LTE}|| > \text{TOL}$, where TOL is a user prescribed tolerance.

To simplify the explanation and the steps taken in the multigrid process, see Subsection 2.2.5, based on the system of discrete equations (2.115) to (2.116) it is convenient to introduce the following global time-dependent nonlinear operator, right-hand side function (defined by the solution on the previous time step) and solution vectors respectively:

$$\boldsymbol{\mathcal{N}} = \begin{pmatrix} \mathcal{N}_{i,j}^h \\ \mathcal{N}_{i,j}^p \end{pmatrix}, \quad \boldsymbol{\mathcal{R}} = \begin{pmatrix} \mathcal{R}_{i,j}^h \\ 0 \end{pmatrix}, \quad \boldsymbol{z}^n = \begin{pmatrix} h_{i,j}^n \\ p_{i,j}^n \end{pmatrix}. \tag{2.120}$$

2.2.4 Depth-averaged form

2.2.4.1 Spatial discretisation

Equations (2.53) to (2.55), incorporating expressions (2.60) to (2.62), are solved, subject to boundary conditions (2.56) and (2.57), on a rectangular computational domain, $(x, y) \in [0, l_p] \times [0, w_p]$, subdivided using a regular spatially staggered mesh arrangement of cells having sides of length Δx and width Δy. The unknown variables, film thickness, h, and the velocity components, $\bar{u}$, $\bar{v}$, are located at cell centres, (i, j), and cell faces, $(i + 1/2, j)$, $(i, j + 1/2)$, respectively. The use of a staggered mesh arrangement avoids the well-known checkerboard instability, Trottenberg, Oosterlee & Schüller (2001), that results if central differencing is applied to first-order pressure term derivatives and to the terms in the continuity equation when pressure and velocity components are collocated.

Solving the momentum equations (2.53) and (2.54) at cell faces, with the convection and time derivative terms grouped together to simplify their numerical treatment following the inclusion of the friction and dispersion terms, and the continuity equation (2.55) at cell centres, omitting for the sake of convenience the overbar denoting velocity averaging, results in the following second-order accurate discretisation scheme:

$$\begin{aligned}
&\varepsilon \mathrm{Re}\left(\frac{\partial u}{\partial t} - \frac{u}{5h}\frac{\partial h}{\partial t} + \frac{6}{5}\mathcal{F}\left[u\right]\right)|_{i+1/2,j} \\
&- \frac{\varepsilon^3}{\mathrm{Ca}}\left(\frac{f_{i+1,j+1} - 2f_{i+1,j} + f_{i+1,j-1} - f_{i,j+1} + 2f_{i,j} - f_{i,j-1}}{\Delta x \Delta y^2}\right. \\
&\left. + \frac{f_{i+2,j} - 3f_{i+1,j} + 3f_{i,j} - f_{i-1,j}}{\Delta x^3}\right) + 2\varepsilon \cot\theta \frac{f_{i+1,j} - f_{i,j}}{\Delta x} + \frac{3u_{i+1/2,j}}{h^2_{i+1/2,j}} - 2 = 0, \\
&\varepsilon \mathrm{Re}\left(\frac{\partial v}{\partial t} - \frac{v}{5h}\frac{\partial h}{\partial t} + \frac{6}{5}\mathcal{F}\left[v\right]\right)|_{i,j+1/2}
\end{aligned} \tag{2.121}$$

$$-\frac{\varepsilon^3}{\mathrm{Ca}}\left(\frac{f_{i+1,j+1}-2f_{i,j+1}+f_{i-1,j+1}-f_{i+1,j}+2f_{i,j}-f_{i-1,j}}{\Delta x^2\Delta y}\right.$$

$$\left.+\frac{f_{i,j+2}-3f_{i,j+1}+3f_{i,j}-f_{i,j-1}}{\Delta y^3}\right)+2\varepsilon\cot\theta\frac{f_{i,j+1}-f_{i,j}}{\Delta y}+\frac{3v_{i,j+1/2}}{h^2_{i,j+1/2}}=0, \tag{2.122}$$

$$\frac{\partial h}{\partial t}|_{i,j}+\frac{h_{i+1/2,j}u_{i+1/2,j}-h_{i-1/2,j}u_{i-1/2,j}}{\Delta x}+\frac{h_{i,j+1/2}v_{i,j+1/2}-h_{i,j-1/2}v_{i,j-1/2}}{\Delta y}=0, \tag{2.123}$$

where $\mathcal{F}[\omega]=u\frac{\partial\omega}{\partial x}+v\frac{\partial\omega}{\partial y}$ is the advective operator with the following terms interpolated from neighbouring nodes: $h_{i\pm1/2,j}=\left(h_{i\pm1,j}+h_{i,j}\right)/2$, $h_{i,j\pm1/2}=\left(h_{i,j\pm1}+h_{i,j}\right)/2$.

In the above discrete DAF analogue, as is the case for convection-diffusion problems, proper numerical treatment of the convection terms is very important, see Morton (1996) and Gaskell & Lau (1988). The mesh Péclet number, Pe, stability condition, see Trottenberg *et al.* (2001), defined as the ratio of the convection to friction term in the momentum equation, is given by:

$$\mathrm{Pe}=\frac{2\varepsilon\mathrm{Re}h^2\max\left(u,v\right)}{5\min\left(\Delta x,\Delta y\right)}\leqslant 2\Rightarrow\mathrm{Re}\leqslant\mathrm{Re}_{cr}=\frac{15\min\left(\Delta x,\Delta y\right)}{2\varepsilon}. \tag{2.124}$$

For typical mesh spacings of $\Delta x=\Delta y=0.05$ and with $\varepsilon=0.1$ the value of the critical Reynolds number, Re_{cr}, is small and equal to 3.75, illustrating the restrictiveness of this constraint apropos the accurate solution of the thin film flows of interest.

To alleviate this restriction the advective operator $\mathcal{F}[\omega]$ is discretised using a second-order accurate total variation diminishing (TVD) scheme, see Chung (2002), that at a general point (i,j) takes the form:

$$\mathcal{F}[\omega]|_{i,j}=\frac{u_{i,j}+|u_{i,j}|}{4\Delta x}\left\{\left(\omega_{i,j}-\omega_{i-1,j}\right)\left[2+\psi\left(\frac{\omega_{i+1,j}-\omega_{i,j}}{\omega_{i,j}-\omega_{i-1,j}}\right)\right]-\left(\omega_{i-1,j}-\omega_{i-2,j}\right)\right.$$

$$\left.\times\psi\left(\frac{\omega_{i,j}-\omega_{i-1,j}}{\omega_{i-1,j}-\omega_{i-2,j}}\right)\right\}+\frac{u_{i,j}-|u_{i,j}|}{4\Delta x}\left\{\left(\omega_{i+1,j}-\omega_{i,j}\right)\left[2+\psi\left(\frac{\omega_{i,j}-\omega_{i-1,j}}{\omega_{i+1,j}-\omega_{i,j}}\right)\right]\right.$$

$$- \left(\omega_{i+2,j} - \omega_{i+1,j}\right) \psi \left(\frac{\omega_{i+1,j} - \omega_{i,j}}{\omega_{i+2,j} - \omega_{i+1,j}} \right) \Bigg\}$$

$$+ \frac{v_{i,j} + |v_{i,j}|}{4\Delta y} \left\{ \left(\omega_{i,j} - \omega_{i,j-1}\right) \left[2 + \psi \left(\frac{\omega_{i,j+1} - \omega_{i,j}}{\omega_{i,j} - \omega_{i,j-1}} \right) \right] - \left(\omega_{i,j-1} - \omega_{i,j-2}\right) \right.$$

$$\left. \times \psi \left(\frac{\omega_{i,j} - \omega_{i,j-1}}{\omega_{i,j-1} - \omega_{i,j-2}} \right) \right\} + \frac{v_{i,j} - |v_{i,j}|}{4\Delta y} \left\{ \left(\omega_{i,j+1} - \omega_{i,j}\right) \left[2 + \psi \left(\frac{\omega_{i,j} - \omega_{i,j-1}}{\omega_{i,j+1} - \omega_{i,j}} \right) \right] \right.$$

$$\left. - \left(\omega_{i,j+2} - \omega_{i,j+1}\right) \psi \left(\frac{\omega_{i,j+1} - \omega_{i,j}}{\omega_{i,j+2} - \omega_{i,j+1}} \right) \right\}, \tag{2.125}$$

where $\psi(\eta) = (\eta^2 + \eta) / (\eta^2 + 1)$ is the well-known van Albada flux limiter, see Trottenberg *et al.* (2001). The formulation is easily shifted to the appropriate staggered grid location to obtain $\mathcal{F}[u]|_{i+1/2,j}$ or $\mathcal{F}[v]|_{i,j+1/2}$ and the following terms are interpolated from neighbouring nodes:

$$u_{i,j+1/2} = \left(u_{i-1/2,j} + u_{i+1/2,j} + u_{i-1/2,j+1} + u_{i+1/2,j+1}\right)/4, \tag{2.126}$$

$$v_{i+1/2,j} = \left(v_{i,j-1/2} + v_{i,j+1/2} + v_{i+1,j-1/2} + v_{i+1,j+1/2}\right)/4. \tag{2.127}$$

As with the LUB model described above, Dirichlet boundary conditions are assigned as exact values at the boundary points, whereas Neumann boundary conditions are implemented by employing ghost nodes at the edge of the computational domain.

To simplify the description of the calculation procedure presented below, it is convenient to separate the leading temporal u, v and h terms from the discretised u-momentum, v-momentum and continuity operators and to express them as functions $\mathcal{M}^u_{i+1/2,j}$, $\mathcal{M}^v_{i,j+1/2}$ and $\mathcal{M}^h_{i,j}$, respectively. This enables equations (2.121)-(2.123) to be rewritten as:

$$\varepsilon \mathrm{Re} \frac{\partial u}{\partial t}|_{i+1/2,j} + \mathcal{M}^u_{i+1/2,j}(u, v, h) = 0, \tag{2.128}$$

$$\varepsilon \mathrm{Re} \frac{\partial v}{\partial t}|_{i,j+1/2} + \mathcal{M}^v_{i,j+1/2}(u, v, h) = 0, \tag{2.129}$$

$$\frac{\partial h}{\partial t}|_{i,j} + \mathcal{M}^h_{i,j}(u, v, h) = 0. \tag{2.130}$$

The discrete form of the $\frac{\partial h}{\partial t}$ term, which appears in $\mathcal{M}^u$ and $\mathcal{M}^v$, of equations (2.121) and (2.122), is obtained at the appropriate staggered mesh location via equation (2.130). The locations of the independent variables (u, v, h), when determining the functions $\mathcal{M}^u_{i+1/2,j}$, $\mathcal{M}^v_{i,j+1/2}$ and $\mathcal{M}^h_{i,j}$ are shown in Figure 2.6.

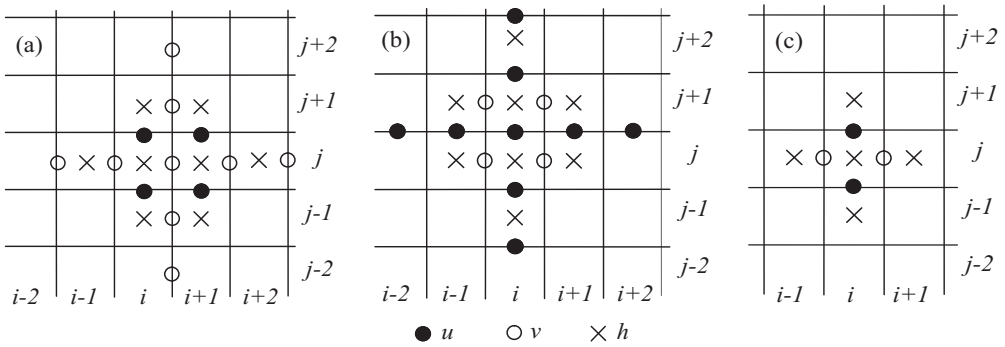

FIGURE 2.6: Stencils for defining the DAF functions: (a) $\mathcal{M}^u_{i+1/2,j}$; (b) $\mathcal{M}^v_{i,j+1/2}$; (c) $\mathcal{M}^h_{i,j}$. The positions of the independent variables u, v and h are denoted by open circles, filled circles and crosses, respectively.

Clearly, when Re $= 0$ the solution procedure simplifies considerably since the terms containing time derivatives on the left hand side of the momentum equations (2.128) and (2.129) disappear.

2.2.4.2 Temporal discretisation

The automatic adaptive time-stepping procedure adopted employs an estimate of the local truncation error (LTE) obtained from the difference between an explicit predictor stage and the current solution stage to optimise the size of time steps and minimise computational waste.

Fully explicit, second-order accurate in time discretisations of equations (2.128) - (2.130) can be used to predict (pr) values for u, v and h, as follows:

$$u_{\rm pr}|^{n+1}_{i+1/2,j} = \gamma^2 u^{n-1}_{i+1/2,j} + \left(1-\gamma^2\right) u^n_{i+1/2,j} - \frac{\Delta t^{n+1}}{\varepsilon \mathrm{Re}} \left(1+\gamma\right) \mathcal{M}^u_{i+1/2,j}\left(u^n, v^n, h^n\right), \tag{2.131}$$

$$v_{\rm pr}|_{i,j+1/2}^{n+1} = \gamma^2 v_{i,j+1/2}^{n-1} + \left(1-\gamma^2\right) v_{i,j+1/2}^{n} - \frac{\Delta t^{n+1}}{\varepsilon \mathrm{Re}} \left(1+\gamma\right) \mathcal{M}_{i,j+1/2}^{v} \left(u^n, v^n, h^n\right), \tag{2.132}$$

$$h_{\rm pr}|_{i,j}^{n+1} = \gamma^2 h_{i,j}^{n-1} + \left(1-\gamma^2\right) h_{i,j}^{n} - \Delta t^{n+1} \left(1+\gamma\right) \mathcal{M}_{i,j}^{h} \left(u^n, v^n, h^n\right), \tag{2.133}$$

where n and $n+1$ denote values at the end of the nth and $(n+1)$st time steps, $t = t^n$ and $t = t^{n+1}$ respectively, and $\gamma = \Delta t^{n+1}/\Delta t^n = \left(t^{n+1} - t^n\right) / \left(t^n - t^{n-1}\right)$.

Adaptive time-stepping is performed by keeping the LTE for $u_{\rm pr}$ within a specified tolerance that in practice automatically restricts the LTE for $v_{\rm pr}$ and $h_{\rm pr}$ and provides a means of increasing the time step in a controlled manner. The LTE for $u_{\rm pr}$ at the predictor stage can be expressed via a Taylor series expansion of equation (2.131) in the form:

$$(\mathrm{LTE})_{\rm pr}|_{i+1/2,j} = \frac{(\Delta t^{n+1})\Delta t^n (1+\gamma)}{6} \frac{\partial^3 u}{\partial t^3}|_{i+1/2,j,t=t_p}, \tag{2.134}$$

with the third-order time derivative term evaluated at time $t_p \in (t^n, t^{n+1})$.

In the present work, an implicit β-method, see Chung (2002), is used to advance the solution in time:

$$\begin{aligned}
u_{i+1/2,j}^{n+1} &+ \frac{\beta \Delta t^{n+1}}{\varepsilon \mathrm{Re}} \mathcal{M}_{i+1/2,j}^{u} \left(u^{n+1}, v^{n+1}, h^{n+1}\right) \\
&= u_{i+1/2,j}^{n} + \frac{\left(\beta - 1\right) \Delta t^{n+1}}{\varepsilon \mathrm{Re}} \mathcal{M}_{i+1/2,j}^{u} \left(u^n, v^n, h^n\right), \qquad (2.135) \\
v_{i,j+1/2}^{n+1} &+ \frac{\beta \Delta t^{n+1}}{\varepsilon \mathrm{Re}} \mathcal{M}_{i,j+1/2}^{v} \left(u^{n+1}, v^{n+1}, h^{n+1}\right) \\
&= v_{i,j+1/2}^{n} + \frac{\left(\beta - 1\right) \Delta t^{n+1}}{\varepsilon \mathrm{Re}} \mathcal{M}_{i,j+1/2}^{v} \left(u^n, v^n, h^n\right), \qquad (2.136) \\
h_{i,j}^{n+1} &+ \beta \Delta t^{n+1} \mathcal{M}_{i,j}^{h} \left(u^{n+1}, v^{n+1}, h^{n+1}\right) \\
&= h_{i,j}^{n} + \left(\beta - 1\right) \Delta t^{n+1} \mathcal{M}_{i,j}^{h} \left(u^n, v^n, h^n\right). \qquad (2.137)
\end{aligned}$$

Note that for $\beta = 1/2$ the method reduces to the second-order accurate in time, but conditionally stable Crank-Nicolson scheme, whereas $\beta = 1$ leads to the fully implicit first-order accurate in time unconditionally stable Laasonen

method.

The LTE for u at the solution (sol) stage is similarly given by a Taylor series expansion of equation (2.135):

$$(\text{LTE})_{\text{sol}}|_{i+1/2,j} = -\frac{(\Delta t^{n+1})^3}{12}\frac{\partial^3 u}{\partial t^3}|_{i+1/2,j,t=t_s}, \quad t_s \in (t^n, t^{n+1}). \tag{2.138}$$

As described in Chapra & Canale (2002), the assumption that the third-order derivative term varies by only a small amount over the time step enables the LTE to be estimated as:

$$(\text{LTE})_{i+1/2,j} = \frac{u^{n+1}_{i+1/2,j} - u_{\text{pr}}|^{n+1}_{i+1/2,j}}{1 + 2[(1+\gamma)/\gamma]}, \tag{2.139}$$

which, following Dormand (1996), is used to obtain an estimate of the overall truncation error by finding its Euclidean norm that, in turn, is used to specify the next time step Δt^{n+2} via:

$$\Delta t^{n+2} = 0.9\Delta t^{n+1}\left(\frac{\text{TOL}}{||\text{LTE}||}\right)^{1/3}, \tag{2.140}$$

if $||\text{LTE}|| \leqslant \text{TOL}$. The iteration is restarted with half the current time step if $||\text{LTE}|| > \text{TOL}$, where TOL is a user prescribed tolerance.

To simplify the explanation and the steps taken in the multigrid process, see Subsection 2.2.5, based on the system of discrete equations (2.135) to (2.137) it is convenient to introduce the following global time-dependent nonlinear operator, right-hand side function (defined by the solution on the previous time step) and solution vectors respectively:

$$\boldsymbol{\mathcal{N}} = \begin{pmatrix} \mathcal{N}^u_{i+1/2,j} \\ \mathcal{N}^v_{i,j+1/2} \\ \mathcal{N}^h_{i,j} \end{pmatrix}, \quad \boldsymbol{\mathcal{R}} = \begin{pmatrix} \mathcal{R}^u_{i+1/2,j} \\ \mathcal{R}^v_{i,j+1/2} \\ \mathcal{R}^h_{i,j} \end{pmatrix}, \quad \boldsymbol{z}^n = \begin{pmatrix} u^n_{i+1/2,j} \\ v^n_{i,j+1/2} \\ h^n_{i,j} \end{pmatrix}. \tag{2.141}$$

2.2.5 Multigrid solver

At the solution stage of the temporal discretisation, the system of the equations:

$$\boldsymbol{\mathcal{N}}\left(\boldsymbol{z}^{n+1}\right) = \boldsymbol{\mathcal{R}}\left(\boldsymbol{z}^{n}\right), \tag{2.142}$$

is solved using a multigrid formulation that enables a system with N unknowns to be solved in only $O\left(\mathrm{N}\right)$ operations; the methodology has been successfully applied for the solution of the lubrication equations by Gaskell *et al.* (2004*a*,*b*), Lee *et al.* (2007) and Gaskell *et al.* (2010). The basis of the approach, as described in several comprehensive texts – see for example Briggs, Henson & McCormick (2000) and Trottenberg *et al.* (2001), exploits the convergence rates of iterative solvers, such as Gauss-Seidel or Jacobi smoothers, to effectively reduce local (high-frequency) errors present in the solution on a particular computational grid, while global (low-frequency) errors are reduced by employing a hierarchy of successively finer grids, $G^0, \ldots, G^k, \ldots, G^K$, where G^0 denotes the coarsest and G^K the finest grid level.

For a specified number of cells on the coarsest grid G^0 with n_x^0 and n_y^0 in the x and y directions respectively, the number of cells on an arbitrary grid G^k say, is $n_x^k = n_x^0 2^k$, $n_y^k = n_y^0 2^k$. This results in grid spacings on G^k of $\Delta x^k = l_p/n_x^k = \Delta x^0 2^{-k}$, $\Delta y^k = w_p/n_y^k = \Delta y^0 2^{-k}$, where $\Delta x^0 = l_p/n_x^0$ and $\Delta y^0 = w_p/n_y^0$ are the grid spacings on G^0.

In the present work a combined full approximation storage (FAS) and full multigrid (FMG) technique is employed to solve (2.142). It is based on the fact that an initial guess (Gs) for the multigrid solver on each grid $G^k \in \left[G^1, G^K\right]$ is provided by FMG interpolation of the solution (Sl) from the coarser grid G^{k-1} (see Figure 2.7) using bilinear interpolation operators $\boldsymbol{I}_{k-1\to k}$ (see Appendix C for examples of these operators):

$$\boldsymbol{z}_k^{\mathrm{Sl}} = \boldsymbol{I}_{k-1\to k}\left(\boldsymbol{z}_{k-1}^{\mathrm{Sl}}\right), \tag{2.143}$$

where, for the sake of simplicity, the time indices have been omitted.

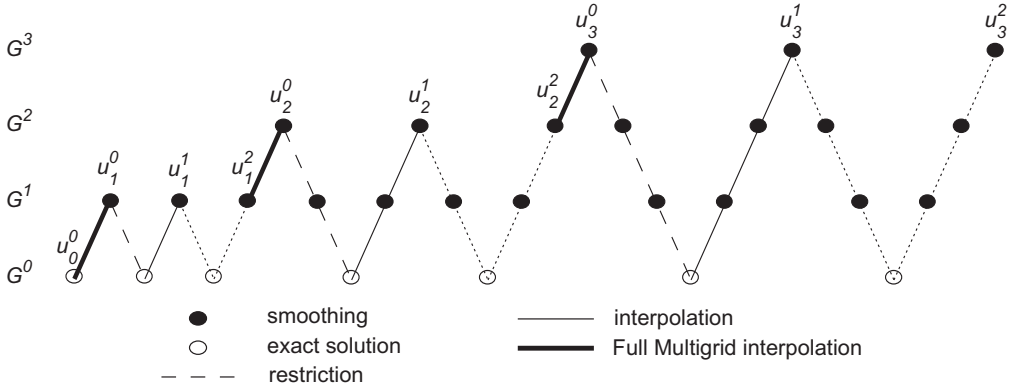

FIGURE 2.7: The Full Multigrid structure based, for illustration purposes, on four grid levels. u_0^0 is the initial solution on the coarsest grid provided by the predictor stage, u_k^0 is the solution on the $G^k \in \left[G^1, G^3\right]$ grid provided by FMG interpolation; while u_k^1 and u_k^2 is the solution on the $G^k \in \left[G^1, G^3\right]$ grid after the first and second FAS V-cycle, respectively.

The multigrid solution process consists of performing a fixed number of FAS V-cycles on intermediate grid levels $G^k \in [G^1, G^{K-1}]$, see Briggs *et al.* (2000) and Trottenberg *et al.* (2001), (usually 1 to 3 V-cycles) and up to 10 V-cycles on the finest grid level G^K (that is, sufficient V-cycles are executed until the residuals have been reduced to a specified tolerance). The structure of a single FAS multigrid V-cycle on an arbitrary grid level G^k may be described in the same pseudo-code formalism as in Trottenberg *et al.* (2001):

$$\boldsymbol{z}_k^{\mathrm{Sl}} = \mathrm{FASCYC}\left(k, \boldsymbol{z}_k^{\mathrm{Gs}}, \boldsymbol{\mathcal{R}}_k, \nu_{\mathrm{pre}}, \nu_{\mathrm{post}}\right), \tag{2.144}$$

where ν_{pre} and ν_{post} are number of pre- and post-relaxations of the multigrid cycle (usually $\nu_{\mathrm{pre}} = \nu_{\mathrm{post}} = 2$).

1. Pre-smoothing stage

   - Apply the relaxation scheme (see Appendix D) ν_{pre} times to obtain first corrected appproximation (Rl):

$$\boldsymbol{z}_k^{\mathrm{Rl}} = \mathrm{RELAX}^{\nu_{\mathrm{pre}}}\left(\boldsymbol{z}_k^{\mathrm{Gs}}, \boldsymbol{\mathcal{R}}_k\right). \tag{2.145}$$

2. Coarse-grid correction stage

- Compute the defects:

$$\boldsymbol{d}_k = \boldsymbol{\mathcal{R}}_k - \boldsymbol{\mathcal{N}}_k \left(\boldsymbol{z}_k^{\mathrm{Rl}} \right), \tag{2.146}$$

- Restrict the defects to the next coarser grid level using full-weighting restriction operators $\boldsymbol{R}_{k \to k-1}$ (see Appendix C):

$$\boldsymbol{d}_{k-1} = \boldsymbol{R}_{k \to k-1} \left(\boldsymbol{d}_k \right), \tag{2.147}$$

- Restrict the solution to get the initial guess for the next coarser grid level:

$$\boldsymbol{z}_{k-1}^{\mathrm{Gs}} = \boldsymbol{R}_{k \to k-1} \left(\boldsymbol{z}_k^{\mathrm{Rl}} \right), \tag{2.148}$$

- Compute the right-hand side on the next coarser grid level:

$$\boldsymbol{\mathcal{R}}_{k-1} = \boldsymbol{d}_{k-1} + \boldsymbol{\mathcal{N}}_{k-1} \left(\boldsymbol{z}_{k-1}^{\mathrm{Gs}} \right), \tag{2.149}$$

  If $k = 0$, a coarsest grid solver is employed (equations (2.142) can be solved directly or, as is the case here, using relaxation, see Appendix D). If $k > 0$ the FAS cycle is used to update the next $k-1$ coarser grid solution:

$$\boldsymbol{z}_{k-1}^{\mathrm{Sl}} = \mathrm{FASCYC} \left(k-1, \boldsymbol{z}_{k-1}^{\mathrm{Gs}}, \boldsymbol{\mathcal{R}}_{k-1}, \nu_{\mathrm{pre}}, \nu_{\mathrm{post}} \right), \tag{2.150}$$

- Compute the corrections:

$$\boldsymbol{c}_{k-1} = \boldsymbol{z}_{k-1}^{\mathrm{Sl}} - \boldsymbol{z}_{k-1}^{\mathrm{Gs}}, \tag{2.151}$$

- Interpolate the corrections on the fine grid level using bilinear interpo-

lation operators $\boldsymbol{I}_{k-1\to k}$ (see Appendix C):

$$\boldsymbol{c}_k = \boldsymbol{I}_{k-1\to k}\left(\boldsymbol{c}_{k-1}\right), \tag{2.152}$$

- Compute the second corrected approximation (Cr):

$$\boldsymbol{z}_k^{\mathrm{Cr}} = \boldsymbol{z}_k^{\mathrm{Rl}} + \boldsymbol{c}_k, \tag{2.153}$$

3. Post-smoothing stage

- Apply the relaxation scheme (see Appendix D) ν_{post} times to get the final solution (Sl):

$$\boldsymbol{z}_k^{\mathrm{Sl}} = \mathrm{RELAX}^{\nu_{\mathrm{post}}}\left(\boldsymbol{z}_k^{\mathrm{Cr}}, \boldsymbol{\mathcal{R}}_k\right). \tag{2.154}$$

Chapter 3

Inertial thin film flow

Contents

In this chapter the influence of inertia on free-surface thin film flows over topography is explored by solving the depth-averaged equation set (DAF) derived in the previous chapter; a comprehensive set of numerical predictions is provided showing how inertia effects impact on the flow. For two-dimensional flow, comparisons are made with experimental results from the literature and corresponding solutions obtained with the lubrication (LUB) model and from solving the full Navier-Stokes (N-S) equations; error estimates, taking the latter as the benchmark, are provided. For three-dimensional flow, only DAF solutions are presented; a more detailed study and comparisons with corresponding finite element solutions of the full N-S problem for the case of flow over a localised trench topography is considered subsequently, see Chapter 4.

3.1 Calculation procedure

The DAF solutions are generated using the implicit time-stepping scheme described in Subsection 2.2.4, with $\beta = 3/4$, starting with the initial condition of a flat free-surface ($h = 1 - s$) and velocity profile $u = \frac{2}{3}h^2$, $v = 0$ (commensurate with Re $= 0$). A computational domain with $l_p = w_p = 100$ was chosen, large enough to ensure fully developed flow both upstream and downstream of the topography and of sufficient extent to negate edge effects; the results shown in subsequent figures do not cover the full extent of the solution domain, just the region of interest where there is a free-surface disturbance. The coarsest multigrid level G^0 had $n_x^0 = n_y^0 = 64$ ($n_x^0 = 64$ for two-dimensional flow) and a finest grid level G^4 with $n_x^4 = n_y^4 = 1024$ (G^5 with $n_x^5 = 2048$ for two-dimensional flow) uniformly spaced cells. At each time step a sufficient number of multigrid V-cycles are performed to reduce residuals on the finest mesh level to below 10^{-6}. A typical value of the time adaptive tolerance used in the computations is TOL $\approx 10^{-3}$. The choice of steepness parameter, δ, is also important in ensuring the mesh independence of solutions; for all the

topography types considered (one-dimensional trench, step-up, step-down and two-dimensional trench), the results obtained were found to be independent of δ provided $\delta \leqslant \delta_{cr} = 10^{-3}$. Figure 3.1 shows that for step-up/down topographies defined via arctangent functions, equation (2.64), this is indeed the case.

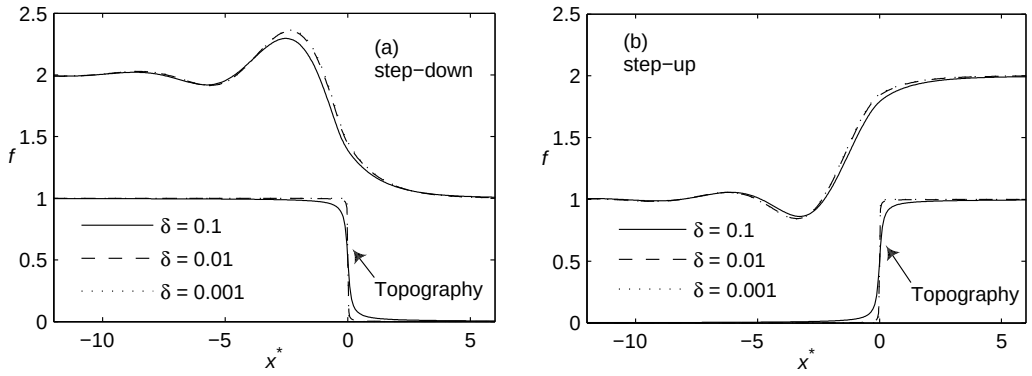

FIGURE 3.1: DAF predicted free-surface profiles for thin film flow, Re = 30, $|s_0| = 1.0$, $\theta = 90°$, over topography defined via arctangent functions showing the influence of the steepness factor, δ: (a) step-down; (b) step-up. The topography profiles, s, are as indicated.

In order to facilitate direct comparison with the experiment of Decré & Baret (2003), the focus of the ensuing investigation is that of gravity-driven flow of thin water films with fixed fluid properties $\rho = 1000\text{kg} \cdot \text{m}^{-3}$, $\mu = 0.001\text{Pa} \cdot \text{s}$ and $\sigma = 0.07\text{N} \cdot \text{m}^{-1}$. As such, θ is taken to be 30° unless stated otherwise, with spanwise topography located with its centre at $x_t = 50$ and localised topography shifted upstream slightly and centred on $(x_t, y_t) = (30.77,\ 50)$. Consequently, for specified values of θ and Re the other parameters appearing in the calculation can easily be derived in terms of them and the fixed fluid properties; for example, H_0 and Ca, can be written as:

$$H_0 = \left(\frac{2\mu^2}{\rho^2 G_0}\right)^{1/3} \left(\frac{\text{Re}}{\sin\theta}\right)^{1/3}, \quad \text{Ca} = \left(\frac{G_0\mu^4}{2\rho\sigma^3}\right)^{1/3} \left(\text{Re}^2 \sin\theta\right)^{1/3}. \qquad (3.1)$$

Two detailed sets of results are presented; Table 3.1 summarises the range of flow parameters investigated and how, for fixed fluid properties, the non-

dimensional groupings involved change in concert. Accordingly, other than for simple step-up and step-down spanwise features, it is convenient to utilise a coordinate system scaled by the fixed streamwise dimension of the topography, namely $(x^o, y^o) = (x^*, y^*)/l_t$; in all cases the planar incline containing the topography and the free-surface location are scaled with respect to the fixed height/depth of the topography, namely $s^* = s/s_0$ and $f^* = (f-1)/s_0$, respectively.

TABLE 3.1: Range of flow parameters investigated showing how, for fixed fluid properties, they and the non-dimensional groupings change in concert.

$\theta,^\circ$	Re	$H_0, \mu m$	L_0, mm	U_0, mm $\cdot$ s^{-1}	Ca, 10^{-3}	N	I
30	0.15	39.4	0.572	3.8	0.05	0.07	0.01
30	2.45	100.0	0.781	24.5	0.35	0.12	0.17
30	2.84	105.0	0.794	27.0	0.39	0.13	0.21
30	5	126.8	0.845	39.4	0.56	0.14	0.41
30	15	182.9	0.955	82.0	1.17	0.18	1.58
30	30	230.5	1.032	130.2	1.86	0.21	3.69
30	50	273.3	1.092	183.0	2.61	0.24	6.88
10	5	180.5	1.353	27.7	0.40	0.42	0.37
10	50	388.8	1.747	128.6	1.84	0.69	6.13
5	5	227.0	1.838	22.0	0.31	0.78	0.34
5	50	489.2	2.373	102.2	1.46	1.30	5.67
1	5	388.0	3.754	12.9	0.18	3.25	0.28
1	50	836.0	4.848	59.8	0.85	5.44	4.74

Before investigating the flows in detail it is useful to comment on the efficiency of the multigrid method for solving the DAF equations, in particular since their being hyperbolic in nature; this is in contrast to the LUB equation set, which is elliptic in nature, the solutions of which returns a multigid efficiency of O(N), where N is the number of unknowns, see Gaskell *et al.* (2004*a*). Figure 3.2 shows how the CPU time for a typical time step depends on the grid density - the problem used as a benchmark is that of three-dimensional flow over a square, trench topography as considered later in Section 3.3, for the same flow parameters. The slope of the quasi-linear plots in Figure 3.2, for both values of Re which differ by an order of magnitude, show that a solution efficiency of O(N) with only a slight deviation from linearity is achieved by the multigrid

strategy adopted.

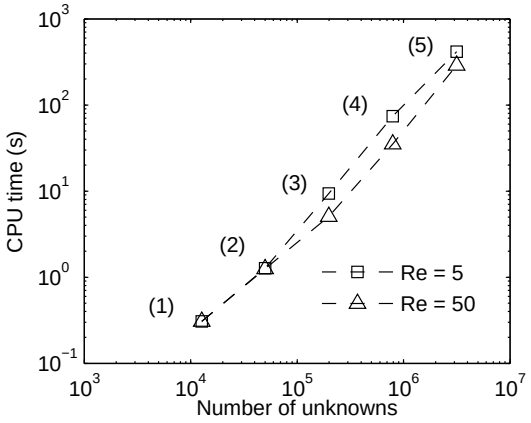

FIGURE 3.2: CPU time dependence for the DAF equation set solved by multigridding, for a typical time step, against mesh density, taking three-dimensional flow over a localised square trench topography as a benchmark, as per Figures 3.10(a) and 3.10(d), for the indicated Re values. Mesh density: (1) 64 × 64; (2) 128 × 128; (3) 256 × 256; (4) 512 × 512; and (5) 1024 × 1024.

3.2 Two-dimensional flow over spanwise topography

The accuracy of the DAF for predicting two-dimensional flow over spanwise topography is quantified by comparison with the experimental data by Decré & Baret (2003) and against accurate full N-S solutions. Figure 3.3 reveals the effect of Re on the streamwise free-surface profile for the flow of a thin water film over a trench topography of width L_t =1.2 mm and depth $S_0 = 20\mu$m. Figures 3.3(a) and (b) show the evolution of the solution towards steady-state for (a) Re = 5 and (b) Re = 15. Such solutions are obtained in a matter of minutes of CPU time, with higher Reynolds number flows taking marginally longer to reach steady-state due to the increased inherent non-linearity of the DAF. Figure 3.3(c) demonstrates the influence of inertia on the free-surface profile, showing predictions for the cases Re = 5, 15 and 30, corresponding to H_0 = 126.8, 182.9 and 230.5 μm, respectively. They reveal

that increasing Re leads to amplification and widening of both the capillary ridge and the free-surface depression over the trench. Note also the larger free-surface disturbance upstream of the capillary ridge with increasing Re.

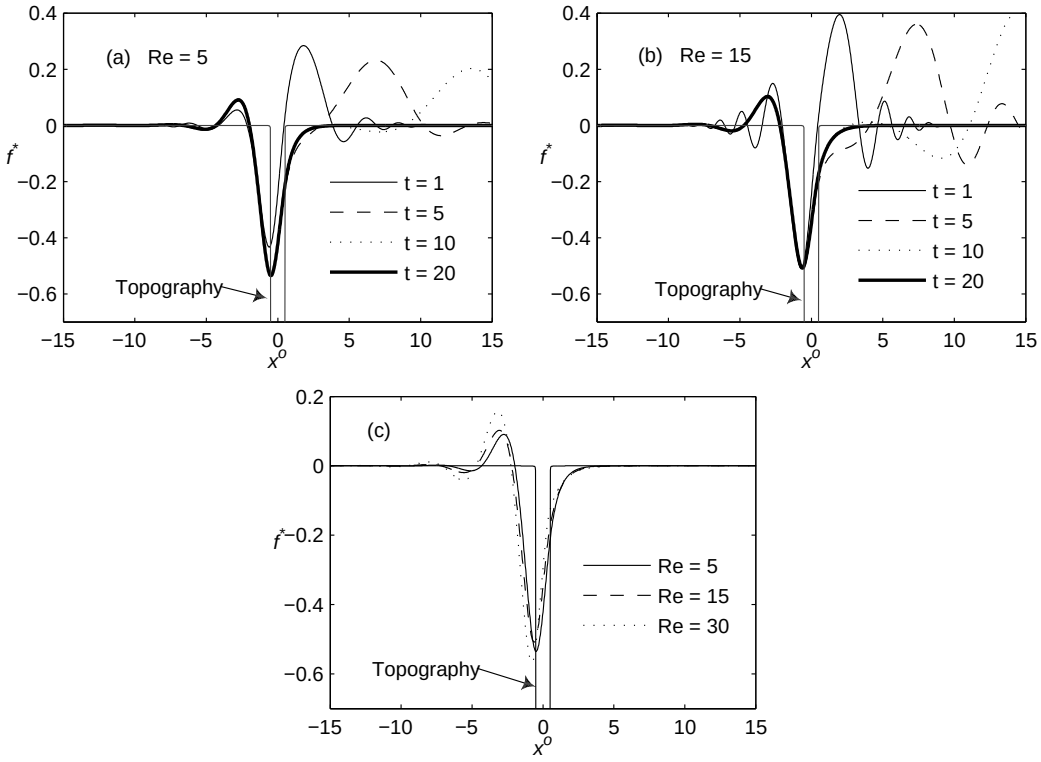

FIGURE 3.3: DAF predicted free-surface profiles for thin film flow over a spanwise trench (width $L_t = 1.2$ mm, depth $S_0 = 20\mu$m): progression from an initial flat surface to predicted steady-state ($t = 20$) for (a) Re = 5, (b) Re = 15; (c) steady-state solutions for Re $= 5, 15, 30$. For illustration purposes only the relevant part of the computational domain, $l_p = 100$, is shown. The associated trench topography profile, s^*, is as indicated.

Figure 3.4 compares steady-state free-surface profiles obtained using the DAF and corresponding N-S solutions for the experimental cases considered by Decré & Baret (2003). Figures 3.4(a) and 3.4(b) are for flow of a thin water film, with Re = 2.45, over spanwise step-up and step-down topographies, respectively, of depth/height $|s_0| = 0.2$, while Figure 3.4(c) is for flow with Re = 2.84 over a spanwise trench of depth $s_0 = 0.19$ and width l_t=1.51. In all three cases, the DAF and N-S predictions are indistinguishable from each other, while the agreement with their experimentally measured counterparts

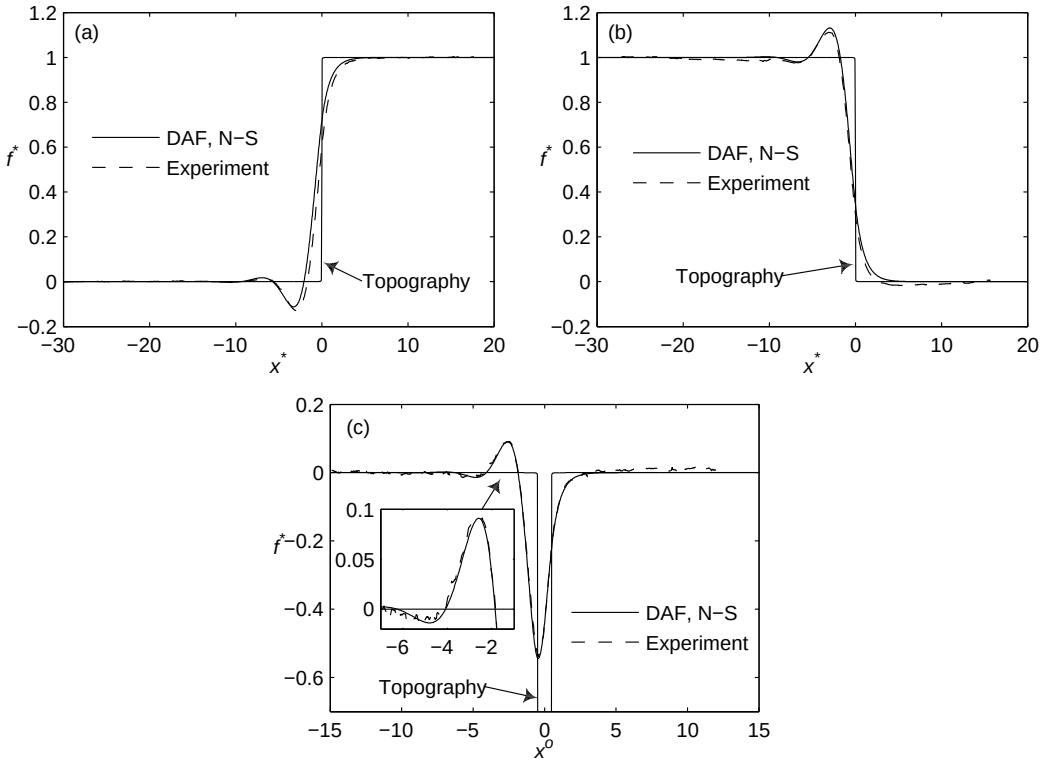

FIGURE 3.4: Comparison between predicted (DAF and N-S) and experimentally obtained, Decré & Baret (2003), free-surface profiles for thin film flow over a spanwise: (a) step-up (height $|s_0| = 0.2$ and Re $= 2.45$); (b) step-down (depth $|s_0| = 0.2$ and Re $= 2.45$); (c) trench (depth $s_0 = 0.19$, width $l_t = 1.51$ and Re $= 2.84$) topography. The associated trench topography profile, s^*, is as indicated.

is excellent as exemplified in the blown-up insert of Figure 3.4(c) showing the free-surface shape across and upstream of the capillary ridge. Indeed the r.m.s. error between the predicted DAF and experimentally obtained free-surface profiles is approximately 1.5% for all three spanwise topographies, which lies well within the reported experimental accuracy of 2%, see Decré & Baret (2003).

A wider range of parameter space is now considered while retaining the same fluid properties as used by Decré & Baret (2003), i.e. those of water, for changing Re - see Table 3.1. Figures 3.5 and 3.6 show the effect of increasing inertia and/or topography amplitude on the free-surface profiles for flow over step-up and step-down topography, respectively, for cases Re = 15 and Re = 30 and $|s_0| = 0.2$ and $|s_0| = 1.0$. The corresponding predictions from the LUB model, are also shown for comparison purposes. These figures show that increasing inertia results in a widening and amplification of the free-surface disturbance, leading to larger free-surface depressions and capillary ridges upstream of the step-up and step-down topography, respectively. It is evident that: (i) the DAF and N-S predictions are in close agreement; (ii) the LUB model, although capturing the essential features, significantly under predicts the associated capillary ridges and depressions; (iii) the discrepancy between both LUB/N-S and DAF/N-S predictions is exacerbated by increasing either Re or $|s_0|$. These findings are consistent with the long-wave approximation (2.27) because, from Table 3.1, $\varepsilon = 0.192$ and 0.223 for Re = 15 and 30, respectively.

These findings are quantified in greater detail in Figures 3.7(a)-(d), which show contour plots of the discrepancy between the LUB, Lee *et al.* (2007), and DAF predictions and corresponding full N-S solutions. Following Gaskell *et al.* (2004*b*), the error is quantified as the maximum percentage discrepancy between the LUB or DAF predictions, measured normal to the N-S profile. This measure is preferred to a r.m.s. error since the latter would be unduly biased by the extensive asymptotic flow regions where all free-surface profiles

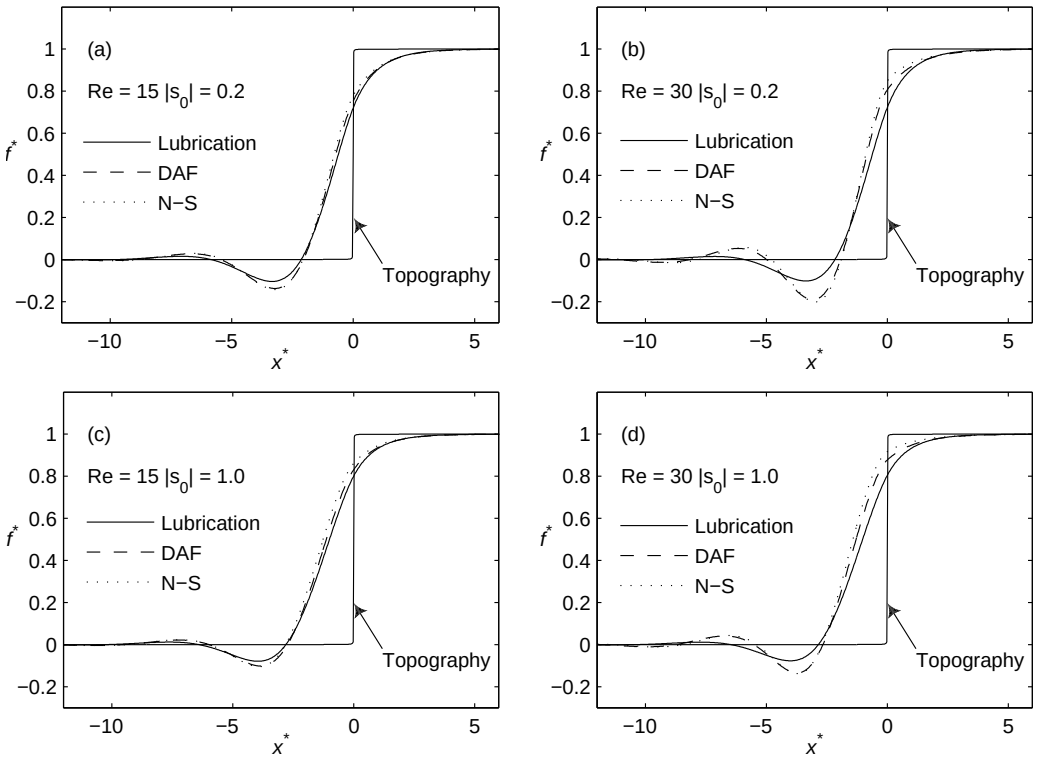

FIGURE 3.5: Comparison between predicted (DAF and N-S) free-surface profiles for thin film flow over a step-up topography when Re = 15 (left) and 30 (right) for two step heights, $|s_0| = 0.2$ (top) and 1.0 (bottom). The corresponding prediction given by LUB model is shown in each case. The topography profile, s^*, is as indicated.

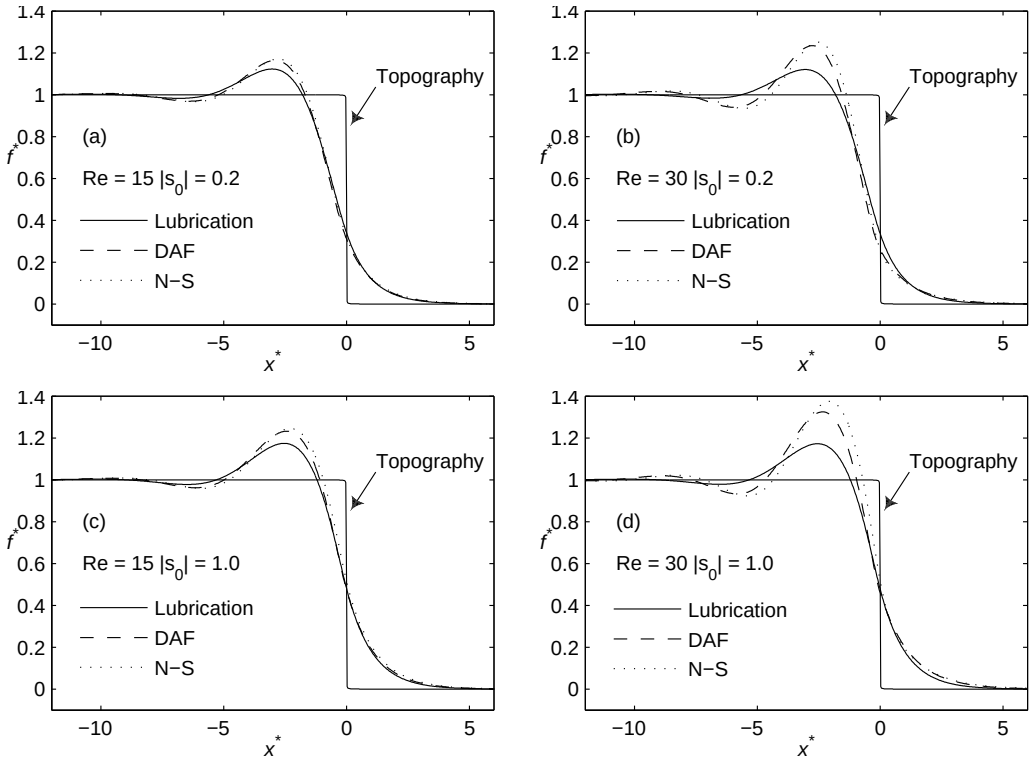

FIGURE 3.6: Comparison between predicted (DAF and N-S) free-surface profiles for thin film flow over a step-down topography when Re = 15 (left) and 30 (right) for two step heights, $|s_0| = 0.2$ (top) and 1.0 (bottom). The corresponding prediction given by LUB model is shown in each case. The topography profile, s^*, is as indicated.

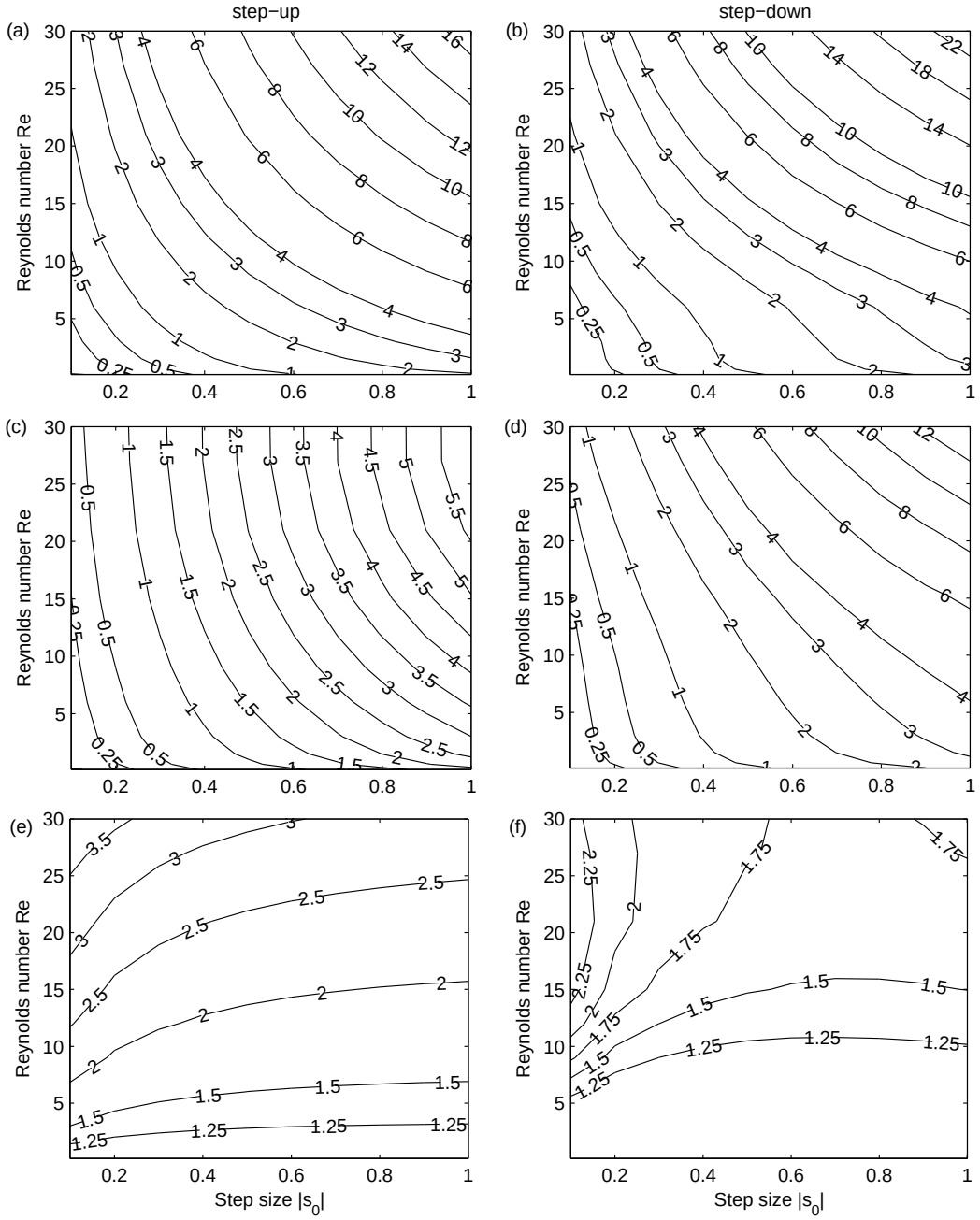

FIGURE 3.7: Flow over spanwise step-up (left) and step-down (right) topography with $\mathrm{Re} \in [0.15, 30]$ and $|s_0| \in [0.1, 1]$. Contours illustrating the maximum percentage discrepancy in the free-surface profiles obtained with the LUB model (top) and the DAF (middle), taking corresponding solutions of the full N-S problem as the benchmark. Relative difference in the magnitude of the error expressed as the ratio of solutions obtained via the LUB model to those found using the DAF (bottom) - for example, a value of 2 indicates the error from the LUB model to be twice that expected with the DAF.

are indistinguishable. Note that the maximum error occurs close to the peak of the topography, over the steeply sloping section of the free-surface, whereas the predicted errors in the vicinity of the free-surface depression (step-up) and capillary ridge (step-down) are typically much less, see Gaskell *et al.* (2004*b*).

For both sets of contours, the discrepancies associated with the step-down flow become larger once the values of Re and $|s_0|$ become significant. The errors in the LUB predictions are consistently greater than those obtained with the DAF, being typically 3 times and 1.5 times larger for the step-up and step-down cases, respectively. For example, for the extreme step-up case with Re = 30 and $|s_0| = 1.0$, the DAF error is only 5.5% compared to the LUB model's 16%, while for a step-down these errors are 12% and 22%, respectively.

Although different in magnitude, the upper two discrepancy contours (top and middle) have roughly the same shape suggesting that the source of error for both step-up and step-down configurations is predominately one of the neglect of inertia, consistent with the basis of the LUB model. The lower discrepancy contours paint a different picture; the step-up ones being much steeper but lower in magnitude than the step-down ones (which are consistent in shape and form, though not magnitude, with their LUB counterpart) suggesting that for the former the relative step height is the more dominant cause of discrepancy.

The source of the greater discrepancy associated with the step-down topography can be traced to the underlying flow structure as Re and $|s_0|$ are increased. Under Stokes flow, Re = 0, conditions the eddy structure associated with an equivalent step-up and step-down would be mirror images of each other. Figures 3.8 and 3.9 show that increasing Re reduces (enlarges) the lateral and vertical extent of the corner eddy which is present in the case of a step-up (step-down); as can be seen, the effect becomes more pronounced the larger the value of $|s_0|$. Accordingly, it is arguably the neglect of vertical velocity terms of $O(\varepsilon^2)$ and the use of the classical Nusselt solution in determining the

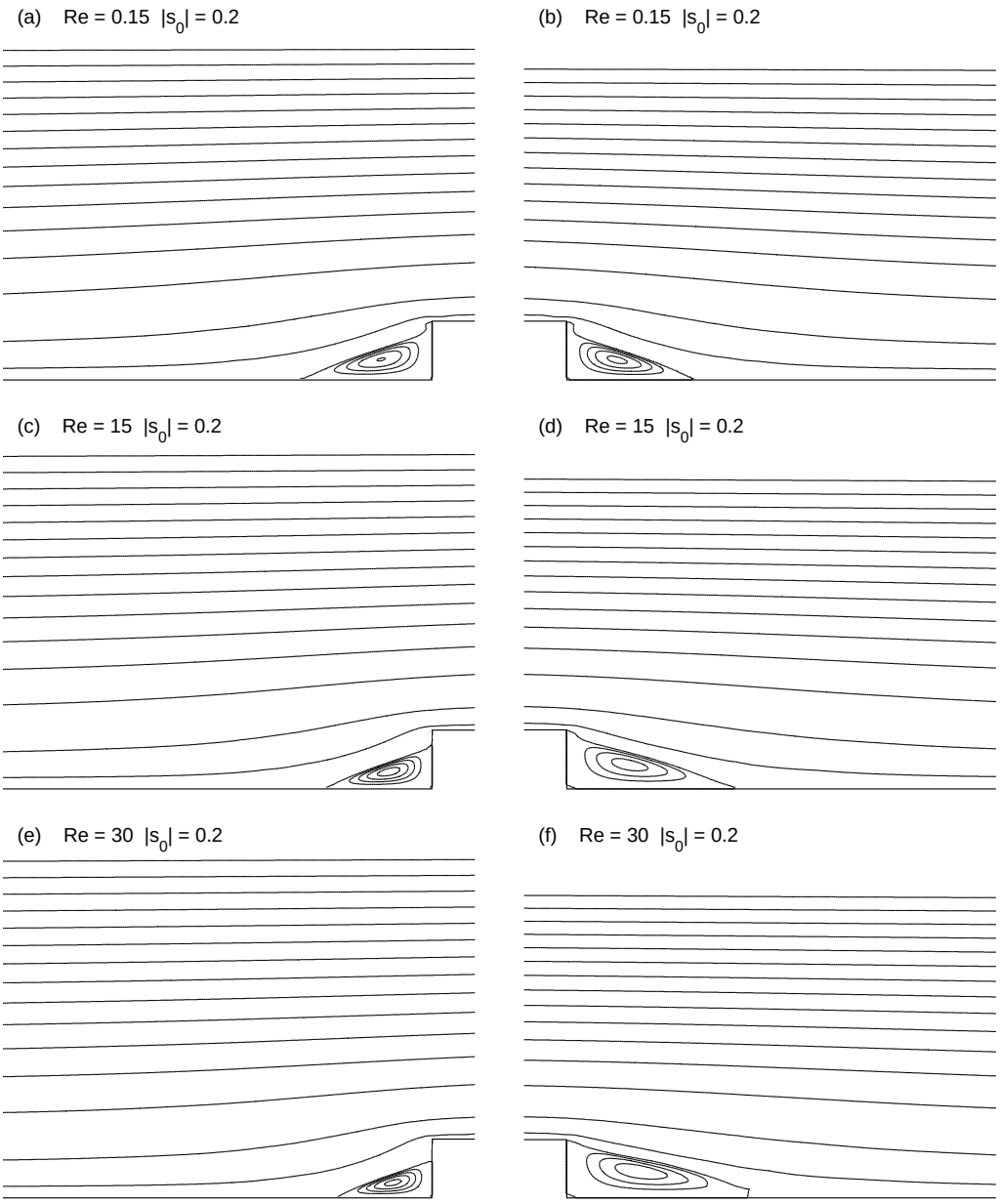

FIGURE 3.8: Streamlines showing the effect of inertia on two-dimensional flow over a step-up (left) and a step-down (right) topography, $|s_0| = 0.2$, for: (a),(b) Re $= 0.15$; (c),(d) Re $= 15$; (e),(f) Re $= 30$.

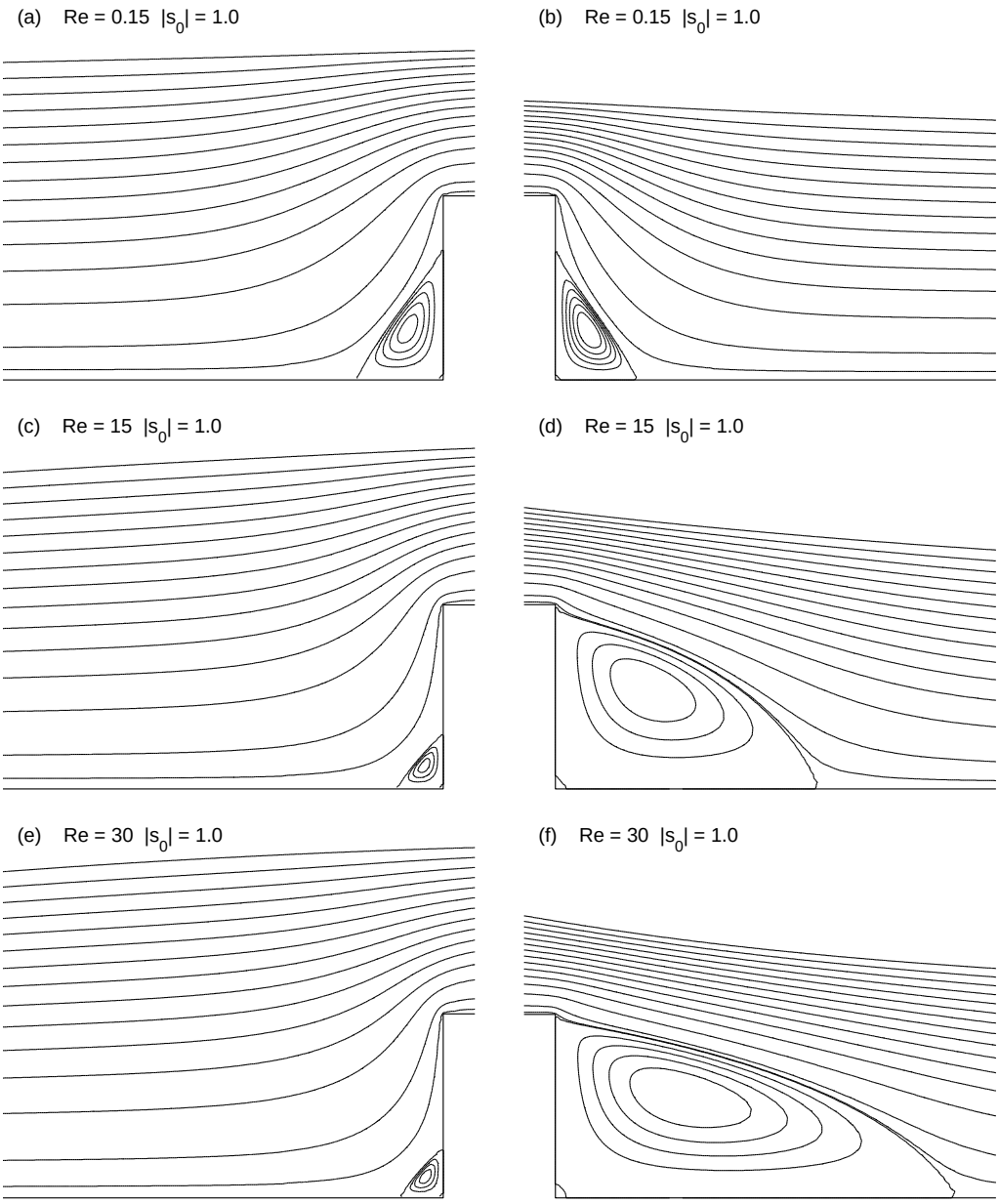

FIGURE 3.9: Streamlines showing the effect of inertia on two-dimensional flow over a step-up (left) and a step-down (right) topography, $|s_0| = 1.0$, for: (a),(b) Re $= 0.15$; (c),(d) Re $= 15$; (e),(f) Re $= 30$.

friction and dispersion terms in regions of the flow where a large eddy exists (as a consequence of the nature of the topography present, Scholle *et al.* (2008)) that leads to a greater discrepancy. That said, except at the extreme values of Re and $|s_0|$ over the range considered, the free-surface profiles obtained with the DAF and provided by the N-S solutions are comparable and encouragingly good.

Taking the solution of the full N-S problem as the benchmark, the relative difference in the magnitude of the error associated with the corresponding solutions obtained with the DAF and LUB equations is shown more concisely in Figures 3.7(e) and 3.7(f) as contours of the ratio of the latter to the former. For the step-up topography, Figure 3.7(e) shows that for fixed $|s_0|$, the relative error increases substantially as Re increases but that increasing $|s_0|$ for a fixed value of Re the effect is less dramatic. For the step-down topography, Figure 3.7(f) reveals that the dependence on $|s_0|$ and Re is more subtle and, for example, increasing $|s_0|$ for a fixed Re can reduce the ratio of the errors significantly.

3.3 Three-dimensional flow over localised topography

The DAF is now used to predict the effect of inertia on three-dimensional thin film flow over localised (two-dimensional) topography based on the square trench used in the experiments of Decré & Baret (2003) with $L_t = W_t = 1.2mm$ and $|S_0| = 25\mu m$. For a topography of this depth and the Re range considered, see Table 3.1, according to Figure 3.7 it is not unreasonable to expect the maximum discrepancy in the predicted free-surface profiles to be of the order of 1% only (since $|s_0| = 0.197$ and 0.092 for Re = 5 and 50, respectively).

Figure 3.10 shows the effect of Re on the three-dimensional free-surface dis-

turbance caused by this square trench. Each case exhibits a characteristic 'horseshoe'-shaped 'bow-wave', a free-surface depression over the trench, a downstream peak or 'surge' caused by the fact that, for three-dimensional flow, liquid exits the trench across a narrower length than across which it enters, Gaskell *et al.* (2004*b*), and a 'comet-tail'; these feature are revisited subsequently in Chapter 4. Note that no such 'surge' mechanism exists for two-dimensional flow over a completely spanwise trench, which explains the lack of a downstream surge in the profiles given in Figures 3.3(c) and 3.4(c). Increasing inertia causes a gradual rise in and widening of the free-surface disturbance and reduction in the extent of the 'comet-tail'. These effects are seen more clearly in Figure 3.11 which gives the corresponding streamwise and spanwise free-surface profiles through the centre of the topography. Figure 3.11(a) shows that increasing Re from 5 to 50 more than doubles the magnitude of the capillary ridge ($f^* = 0.015$ compared with $f^* = 0.037$) and roughly trebles the size of the downstream surge ($f^* = 0.023$ compared to $f^* = 0.067$).

The effect of inertia on the downstream surge can be explored in more detail as follows. For small Re, fluid enters the trench across its upstream side and both spanwise sides due to lateral pressure gradients resulting from the spanwise curvature of the free surface. Since the flow is steady, fluid entering the trench must leave it on the downstream side. As the Re is increased the downstream surge becomes more focused; by the time Re = 50 it creates a free-surface disturbance larger than that of the downstream capillary ridge, Figure 3.11(a); in addition it is positioned further upstream. A plausible explanation for what is observed is that increasing inertia gradually overcomes the lateral pressure gradients causing the flow to become essentially streamwise; in which case fluid enters and exits the trench topography principally across its upstream and downstream sides respectively, and only fractionally if at all via its spanwise sides.

Figures 3.12 and 3.13 analyse how inertia affects the transition to two-dimensional,

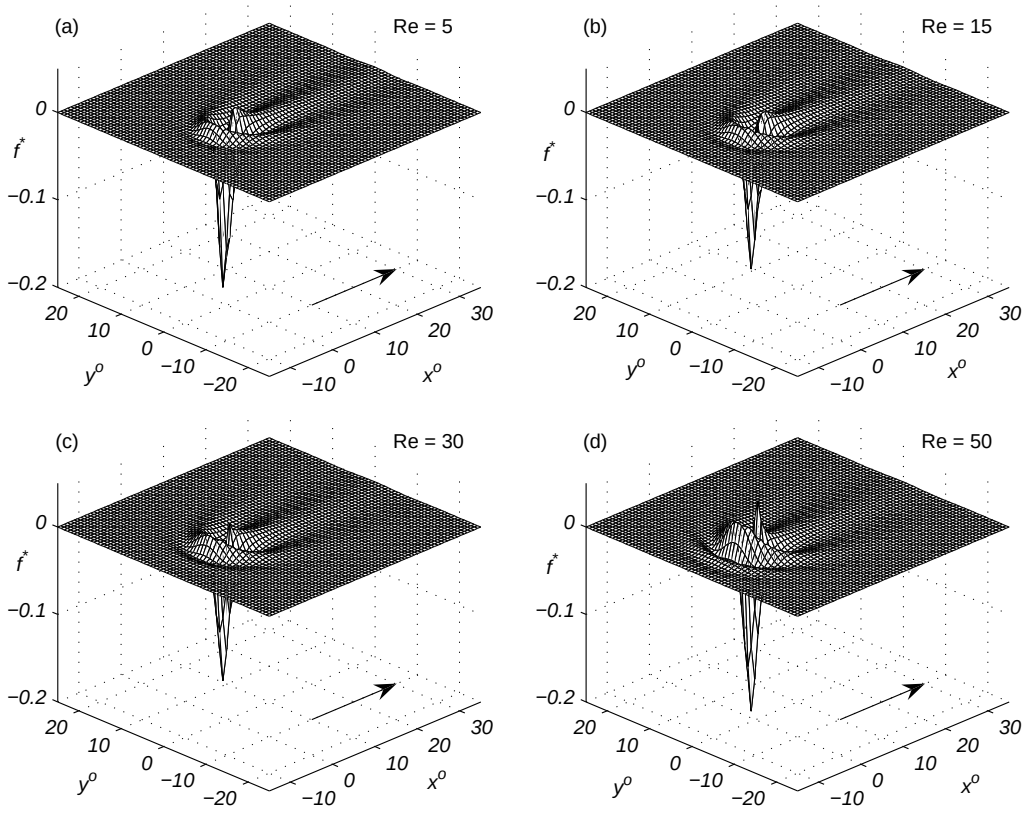

FIGURE 3.10: Three-dimensional free-surface plots for flow over a localised (two-dimensional) square trench topography ($L_t = W_t = 1.2$mm, $S_0 = 25\mu$m): (a) Re = 5; (b) Re = 15; (c) Re = 30; (d) Re = 50. The arrow shows the direction of flow.

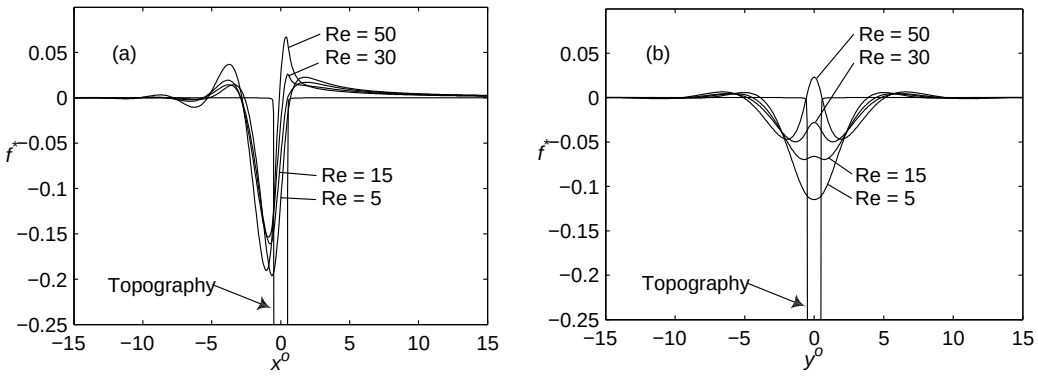

FIGURE 3.11: Flow over a localised (two-dimensional) square trench topography ($L_t = W_t = 1.2$mm, $S_0 = 25\mu$m. Streamwise (left) and spanwise (right) free-surface profiles through the centre ($x^o = 0, y^o = 0$) of the topography for Re = 5, 15, 30 and 50. The associated streamwise and spanwise topography profiles, s^*, are as indicated.

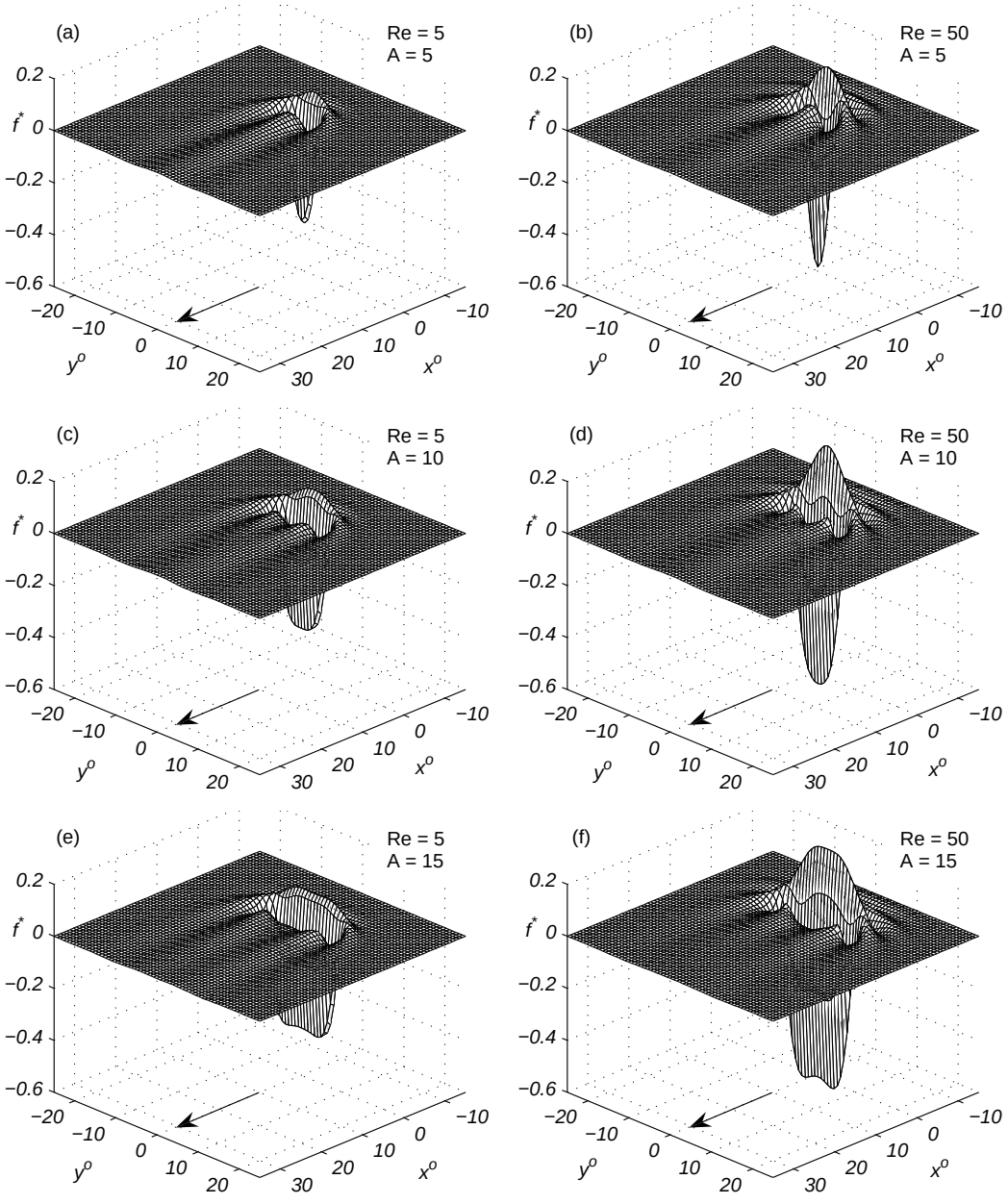

FIGURE 3.12: Three-dimensional free-surface plots for flow over a localised trench topography (L_t = 1.2mm, $S_0 = 25\mu$m) showing the effect of aspect ratio, $A = W_t/L_t$, on the resulting free-surface disturbance. From top to bottom, $A = 5$, 10 and 15; Re = 5 (left) and Re = 50 (right). The arrow shows the direction of flow and the case when $A = 1$ can be viewed in Figures 3.10(a) and 3.10(d).

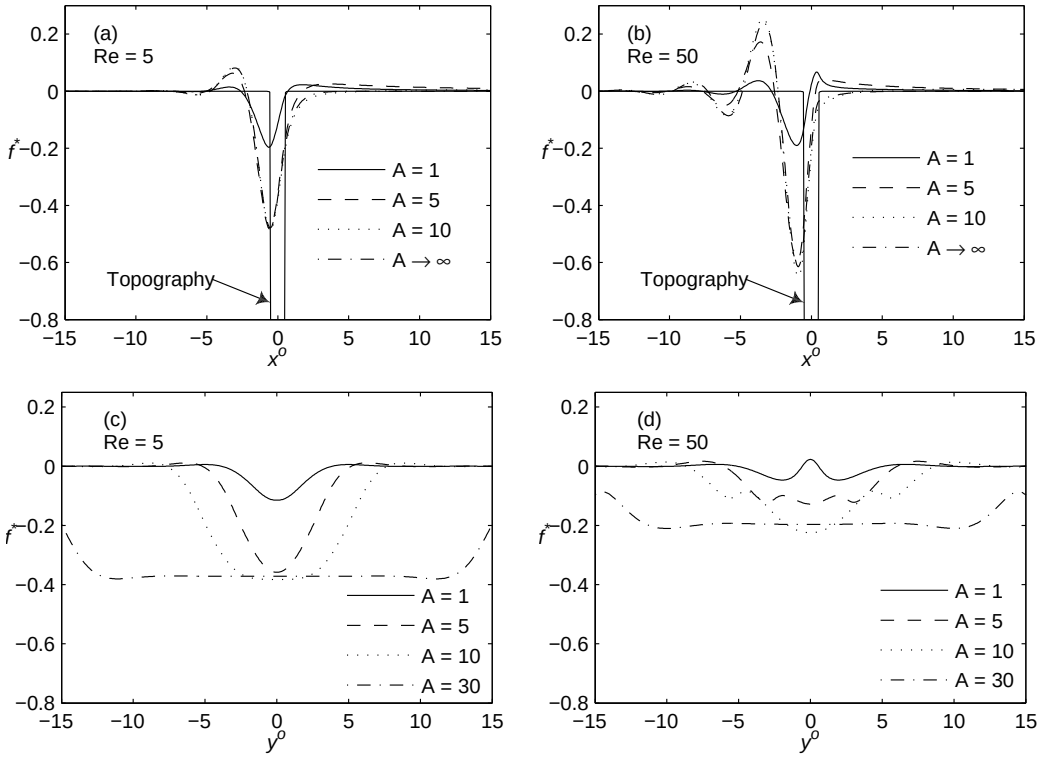

FIGURE 3.13: Streamwise (top) and spanwise (bottom) free-surface profiles through the centre of the topography ($x^o = 0, y^o = 0$) for flow over a localised trench topography ($L_t = 1.2$mm, $S_0 = 25\mu$m) showing the effect of aspect ratio, $A = W_t/L_t$ for Re = 5 (left) and Re = 50 (right). The associated streamwise topography profile, s^*, is as indicated.

spanwise flow as the trench width in the spanwise direction, W_t, is increased for fixed L_t=1.2mm. The free-surface profiles given in Figure 3.12, viewed from the downstream side, show that increasing trench aspect ratio $A = W_t/L_t$, causes the bow wave to broaden while increasing Re leads to larger free-surface disturbances that are more sharply focussed around the streamwise centreline. For the cases shown, increasing A from 5 to 10 causes the downstream surge to bifurcate into two smaller ones lying either side of the streamwise centreline. The progression to two-dimensional flow can be seen more clearly via the streamwise and spanwise free-surface profiles shown in Figure 3.13 for Re = 5 and 50 and trench aspect ratio $A = 1$, 5, 10 and ∞ (i.e. spanwise topography). Increasing A from 1 to 5 has a dramatic effect on the free-surface depression and on the upstream capillary ridge, while for $A = 10$ the streamwise profiles exhibit a greatly reduced downstream surge; the spanwise profiles progress to an essentially flat disturbance when $A = 30$ for both Re = 5 and 50. The sharper focus of the Re = 50 flow around the streamwise centreline is shown by the spanwise free-surface profiles in Figure 3.13(d) and by the fact that a larger aspect ratio is needed for its streamwise profile to approximate that of the spanwise case shown in Figure 3.3. This is reinforced by calculating the difference in the streamwise free-surface profiles obtained for finite A and the case $A \to \infty$ in the same way as the discrepancy contours of Figure 3.7 were generated. For Re = 5, these are found to be 0.74% and 0.24% for $A = 5$ and $A = 10$, respectively; whereas for Re = 50 they are 0.97% and 0.31%, respectively. This behaviour can be explained in physical terms by noting that the Re = 50 case has larger streamwise inertia and therefore will have less of a tendency than the Re = 5 case to spread across a given trench geometry.

The final two figures consider the competing effects of inertia and the normal component of gravity on the free-surface disturbance induced by the square trench topography considered above. The parameter measuring the relative importance of the normal component of gravity is $\mathrm{N} = \mathrm{Ca}^{1/3} \cot\theta$; since the

fluid properties are fixed, the influence of N is explored via changes to the inclination angle θ of the planar surface - see Table 3.1. Figure 3.14 shows how decreasing θ (increasing N) suppresses all free-surface disturbances, reducing considerably the magnitude of the bow wave, downstream surge and free-surface depression over the trench. The streamwise and spanwise free-surface profiles given in Figure 3.15 show more clearly that the bow wave migrates upstream as θ decreases while the downstream surge is more resistant to changes in θ and its location remains effectively constant.

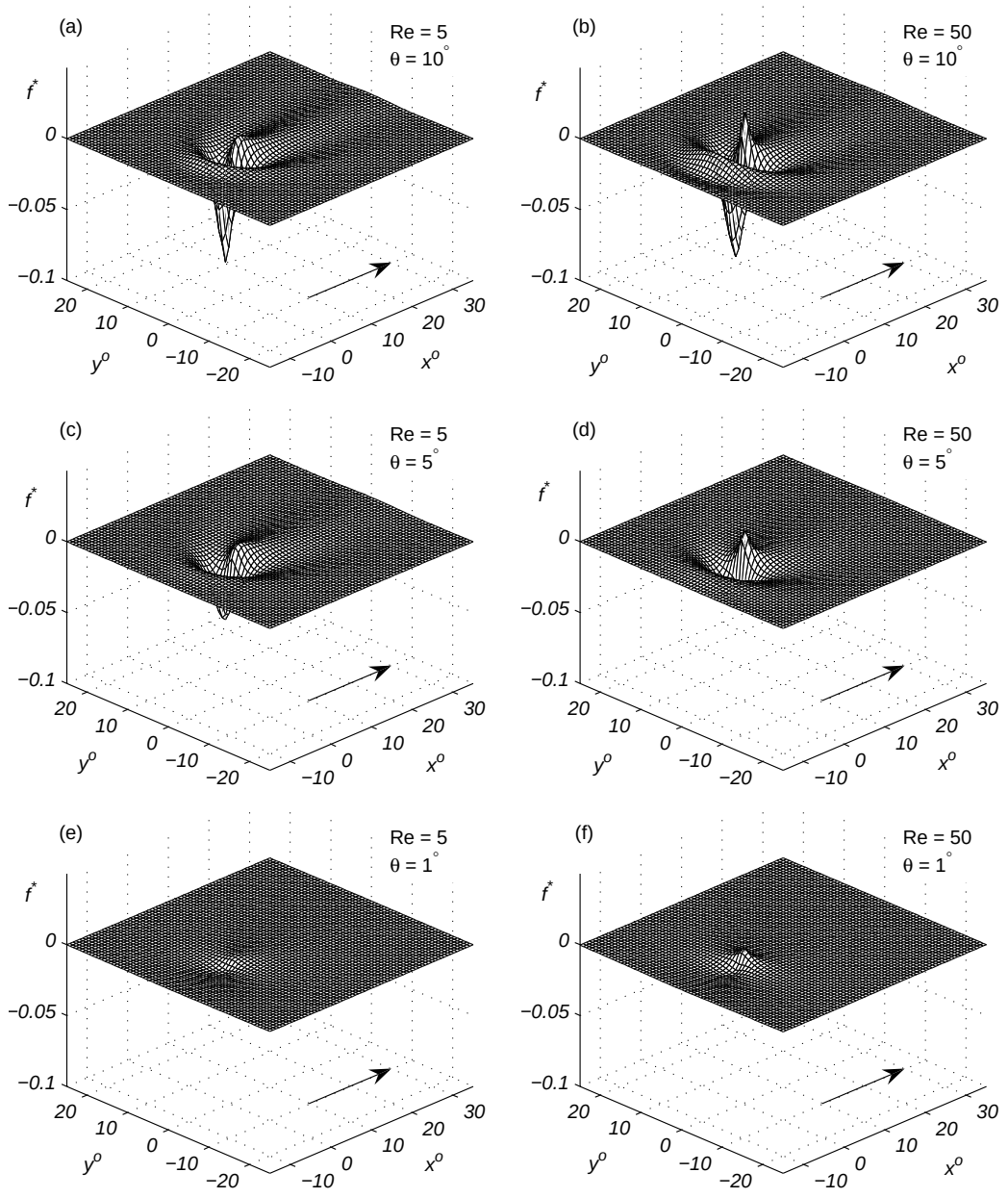

FIGURE 3.14: Three-dimensional free-surface plots for flow over a localised square trench topography ($L_t = W_t = 1.2$mm, $S_0 = 25\mu$m) showing the effect of θ on the resulting free-surface disturbance. From top to bottom, $\theta = 10°$, $5°$ and $1°$; Re $= 5$ (left) and Re $= 50$ (right). The arrow shows the direction of flow and the corresponding free-surface disturbances when $\theta = 30°$ can be viewed in Figures 3.10(a) and 3.10(d).

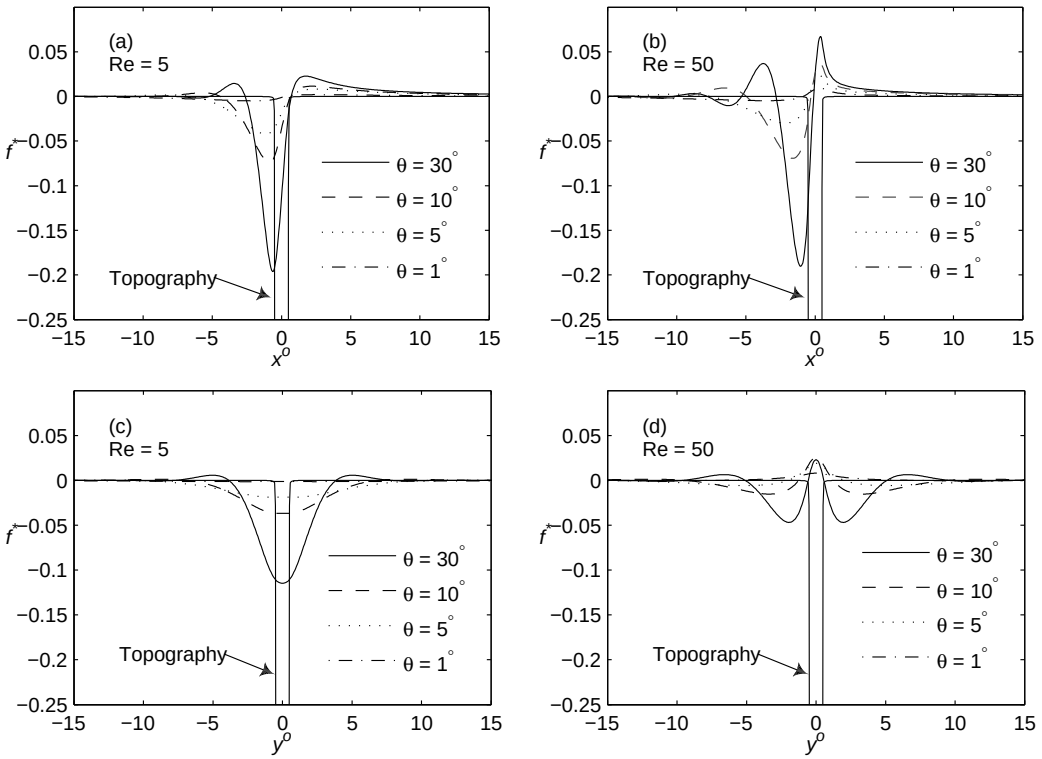

FIGURE 3.15: Streamwise (top) and spanwise (bottom) free-surface profiles through the centre of the topography ($x^o = 0, y^o = 0$) for flow over a localised square trench topography ($L_t = W_t = 1.2$mm, $S_0 = 25\mu$m) for four different inclination angles θ; Re = 5 (left) and Re = 50 (right). The associated streamwise and spanwise topography profiles, s^*, are as indicated.

Chapter 4

Three-dimensional film flow over trench topography: full Navier-Stokes solutions

Contents

In this chapter a set of solutions for three-dimensional Navier-Stokes (N-S) flow over a localised rectangular trench topography is presented. Free-surface plots and streamwise/spanwise free-surface profiles are compared with solutions obtained in Chapter 3 via the lubrication (LUB) model and the depth-averaged Navier-Stokes equations (DAF), and where available corresponding experimental results. N-S solutions are used as a benchmark to investigate the limitations of the LUB model and DAF and to explore the corresponding differences for typical three-dimensional flow. In addition a study of internal flow structure is presented showing how it changes as the Reynolds number is increased.

4.1 Calculation details

The no-slip and inflow/outflow boundary conditions, (2.73) and (2.74), are imposed by replacing the corresponding weighted residual momentum equations (2.78) with the desired velocity there. In the same way, the boundary condition of fully developed flow, $h|_{x=0}$ (2.74), is imposed by replacing the corresponding weighted residual kinematic equations (2.85) with the desired spine value; $n^p = 4$, 7 and 24 integration points are found to be sufficient for line, triangular and tetrahedral elements, respectively, and for obtaining results independent of n^p.

The Nusselt velocity and pressure profiles are chosen to be the initial approximations for the velocity and pressure respectively, while the initial approximation for the spine heights is taken to be that of a flat free-surface profile:

$$\boldsymbol{u}_i = \xi_i \left(2 - \xi_i\right) \boldsymbol{i}, \quad p_j = 2 \left(\xi_j - 1\right), \quad h_k = 1, \tag{4.1}$$

where $s_i = s\left(x_i, y_i\right)$ and $\xi_i = \left(z_i - s_i\right) / \left(1 - s_i\right)$. At those points where the substrate function is multivalued (at the side walls of a right rectangular trench,

for example), the largest possible value is taken for s_i. The substrate grid nodes are fixed and chosen to be the base nodes, while the direction vectors are normal to the substrate and can be found from the initial mesh approximation and the spines definition (2.87):

$$\boldsymbol{x}_i^b = x_i \boldsymbol{i} + y_i \boldsymbol{j} + s_i \boldsymbol{k}, \quad \boldsymbol{d}_i = (z_i - s_i)\, \boldsymbol{k}. \tag{4.2}$$

The initial and consequent mesh approximations are found from the spine method expression (2.87).

In the actual finite element program the Boolean matrices $\widetilde{\Delta}_{i,k}$, $\Delta_{k,\alpha}^{(e)}$, $\Delta_{j,\beta}^{(e)}$ and $\Delta_{k,\gamma}^{(e)}$ defined in Subsection 2.2.1 do not need to be constructed, but instead are replaced by arrays containing global/spine and global/local $\boldsymbol{x}/\boldsymbol{u}$-node, p-node, and free-surface $\boldsymbol{x}/\boldsymbol{u}$-node number correspondence respectively. Matrix $\Delta_{i,k}$ does not need to be created since it is the same as $\widetilde{\Delta}_{i,k}$ if i is a free-surface node. Note also that the Jacobian matrix (2.96), its determinant and cofactors (2.99) have to be calculated for each element since these are required to obtain the gradient of the weighting function (2.98), the normal to the free surface (2.102), and the free-surface curvature in expressions (2.103) and (2.104). Two-dimensional streamlines are found by contouring the stream function, whereas in three dimensions fluid particle trajectories are found by integrating along path lines.

The number of elements in the mesh was systematically increased until the maximum change in the predicted free-surface profiles on consecutive meshes became less than 0.05%. As a result an irregular finite element grid was employed with elements mainly concentrated near to but especially inside the topography in order to capture the associated eddy structure present, see Figures 4.1 and 4.2 for examples of the typical mesh structures used to resolve two- and three-dimensional flow. In two dimensions a total of $2 \times 80 \times 8$ elements and $2 \times 20 \times 16$ elements were employed outwith and across the

trench (parallelograms are divided into 2 triangles), respectively. Equivalently: the total number of elements $n^e = 1920$; the number of free-surface elements $n^s = 80$; the number of $\boldsymbol{u}/\boldsymbol{x}$-nodes $n^i = 4049$, p-nodes $n^j = 1065$ and free-surface $\boldsymbol{u}/\boldsymbol{x}$-nodes $n^k = 161$; and the total number degrees of freedom DOF $= dim \cdot n^i + n^j + n^k = 9324$.

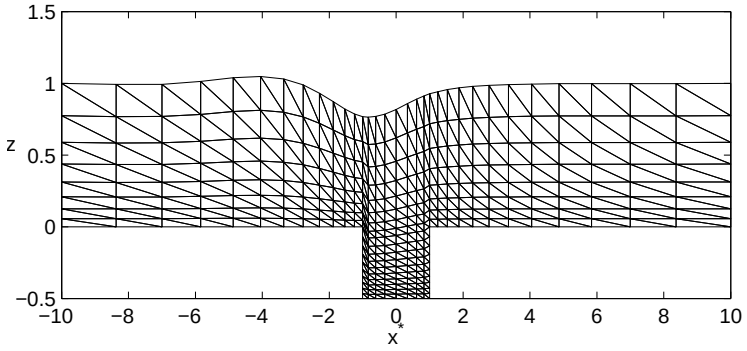

FIGURE 4.1: A typical irregular finite element grid comprised of triangular elements for two-dimensional thin film flow over a spanwise trench topography with $l_t = 2.0$ and $|s_0| = 0.5$. For illustration purposes the number of elements is set to $2 \times 32 \times 8$ and $2 \times 8 \times 10$ outwith and over the trench, respectively.

In three dimensions advantage is taken of the spanwise symmetry involved to solve the problem over half the solution domain only, subdivided using a total of $6 \times 80 \times 40 \times 8$ elements and $6 \times 20 \times 10 \times 16$ elements outwith and over the trench (parallelepipeds are divided into 6 tetrahedrons), respectively. Equivalently: the total number of elements $n^e = 172800$; the number of free-surface elements $n^s = 6400$; the number of $\boldsymbol{u}/\boldsymbol{x}$-nodes $n^i = 249249$, p-nodes $n^j = 33585$ and free-surface $\boldsymbol{u}/\boldsymbol{x}$-nodes $n^k = 13041$; and the total number degrees of freedom DOF $= dim \cdot n^i + n^j + n^k = 794373$. Results were obtained using 64 processors that ensured enough memory for the multifrontal solver and the calculation to be completed in a matter of hours. The above proved sufficient to guarantee grid-independence of the free-surface profiles; see for example the streamwise and spanwise free-surface profiles for flow over a localised (two-dimensional) square trench topography shown in the Figure 4.3.

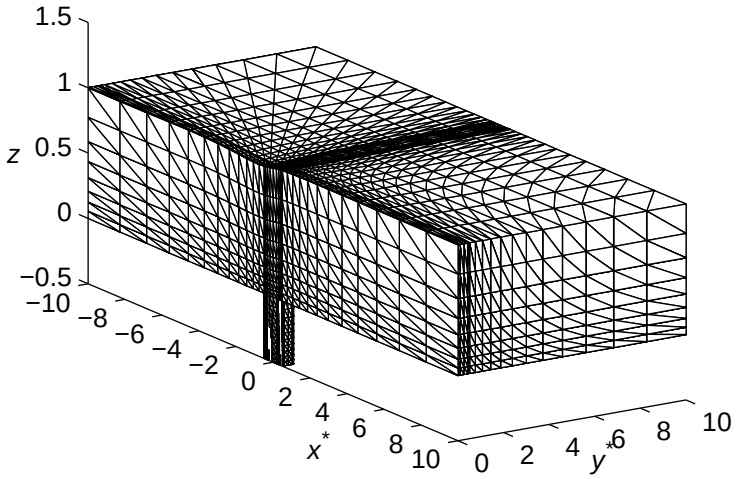

FIGURE 4.2: A typical irregular finite element grid comprised of tetrahedral elements for three-dimensional thin film flow over a localised trench topography with $l_t = w_t = 2.0$ and $|s_0| = 0.5$. For illustration purposes the number of elements in the half solution domain is set to $6 \times 32 \times 16 \times 8$ and $6 \times 8 \times 4 \times 10$ outwith and over the trench, respectively.

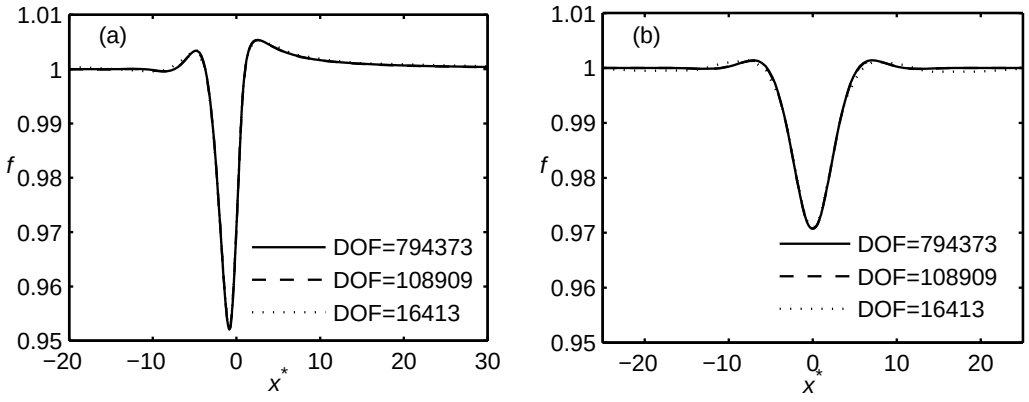

FIGURE 4.3: Grid-independency of N-S predicted (a) streamwise and (b) spanwise free-surface profiles through the centre of a localised trench topography, Decré & Baret (2003), with $l_t = w_t = 1.54$, $|s_0| = 0.25$, $\mathrm{Re} = 2.45$.

4.2 Free-surface solutions

The comparison of the three approaches, N-S, LUB and DAF, carried out in Chapter 3 for the case of two-dimensional flow, is extended to that of three-dimensional flow over a localised square trench topography (Decré & Baret, 2003) with Re = 2.45, $\theta = 30^\circ$, $\varepsilon = 0.128$ and Ca $= \varepsilon^3/6 = 3.5024 \cdot 10^{-4}$, $l_t = w_t = 1.54$, $|s_0| = 0.25$, $l_p = w_p = 100$, $(x_t, y_t) = (30.77, 50)$. The LUB and DAF results were obtained with the same $\delta = 0.001$ and $n_x^4 = n_y^4 = 1024$ values as in Section 3.1.

Figure 4.4 compares the predicted N-S, LUB and DAF three-dimensional free-surface disturbances obtained, while Figures 4.5 and 4.6 present the corresponding streamwise and spanwise free-surface profiles through the centre of the topography, together with the experimental data of Decré & Baret (2003). Due to the relatively small Reynolds number involved, Re = 2.45, all three predictions are virtually indistinguishable from each other, while agreement with their experimentally measured counterparts is extremely good: both the location of the extrema and their amplitudes agree well. There is some noise present on the streamwise and spanwise experimental profiles, which are taken at different spanwise and streamwise locations respectively, and a slightly smaller depression over the trench is observed; however these deviations are insignificant and less than 1% of the depth of the trench. Note also that the steepness of the topography does influence the free-surface disturbance locally and a slightly better match for the depression is obtained with the LUB and DAF models for $\delta = 0.05$, the value used in Gaskell *et al.* (2004*b*); this suggests, as might be anticipated, that the trench topography used in the experiments was not perfectly steep with sharp 90° corners.

A wider range of the parameter space is explored in Figures 4.7 and 4.8; they show the effect of increasing inertia and/or trench depth on the free-surface disturbance generated, for the cases Re = 0 and 50 and with $|s_0| = 0.25$ and

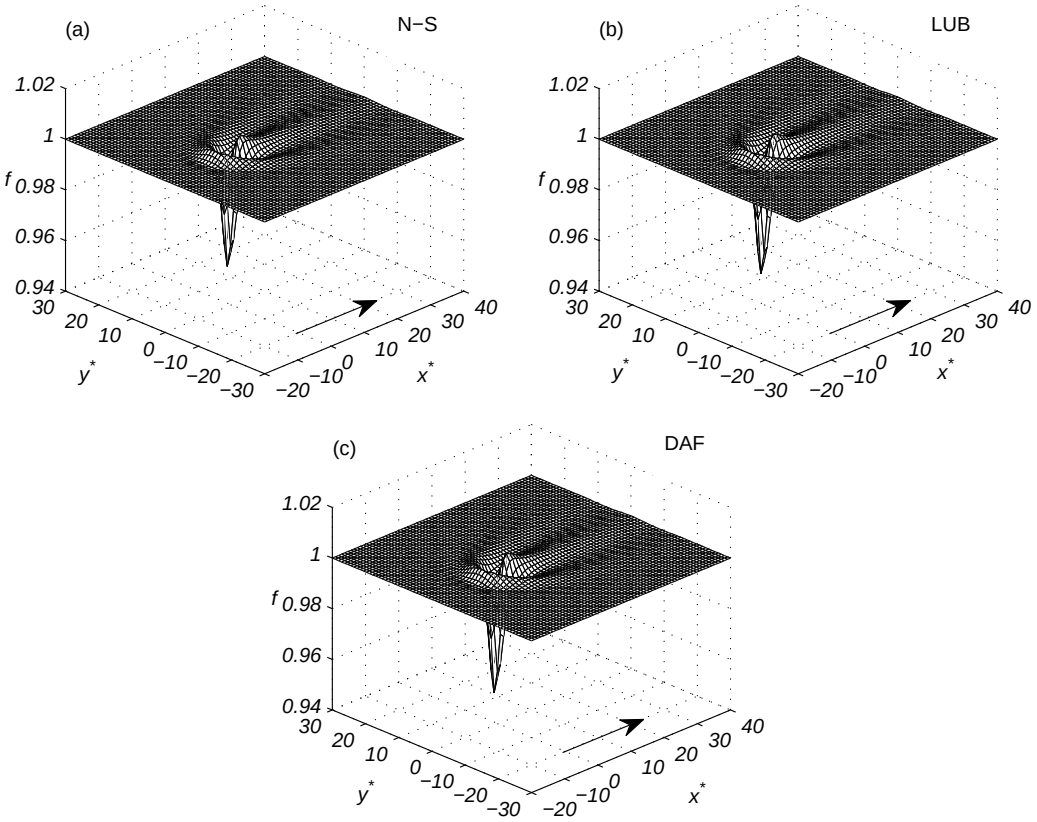

FIGURE 4.4: Comparison of predicted (N-S, LUB and DAF) three-dimensional free-surface plots for flow over a square localised trench topography, Decré & Baret (2003), with $l_t = w_t = 1.54$, $|s_0| = 0.25$, Re $= 2.45$: (a) N-S, (b) LUB and (c) DAF. The arrow shows the direction of flow.

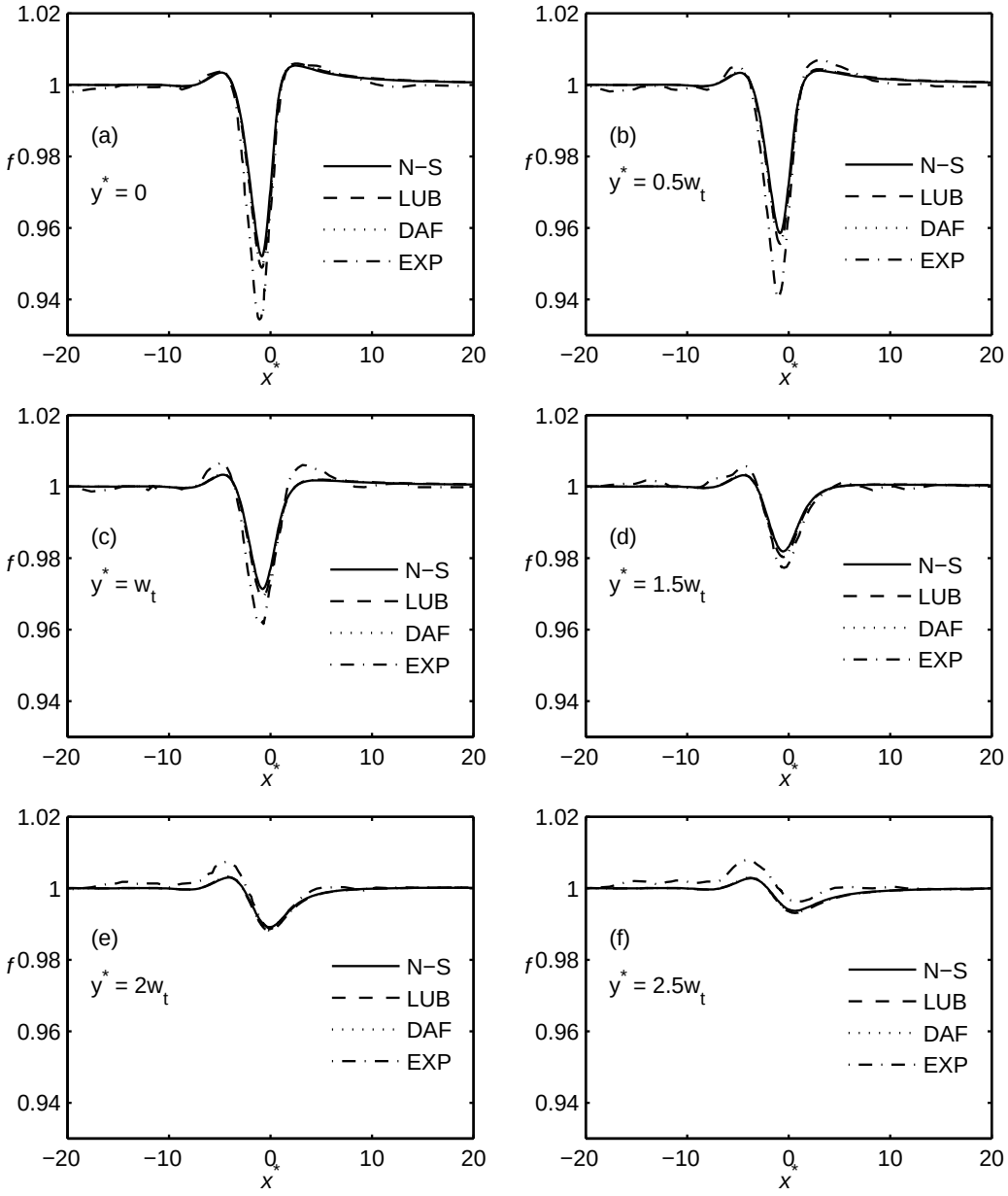

FIGURE 4.5: Comparison between predicted (N-S, LUB and DAF) and experimentally (EXP) obtained streamwise profiles through the centre of a localised square trench of Figure 4.4 at different spanwise locations: (a) $y^* = 0$; (b) $y^* = 0.5w_t$; (c) $y^* = w_t$; (d) $y^* = 1.5w_t$; (e) $y^* = 2w_t$; (f) $y^* = 2.5w_t$.

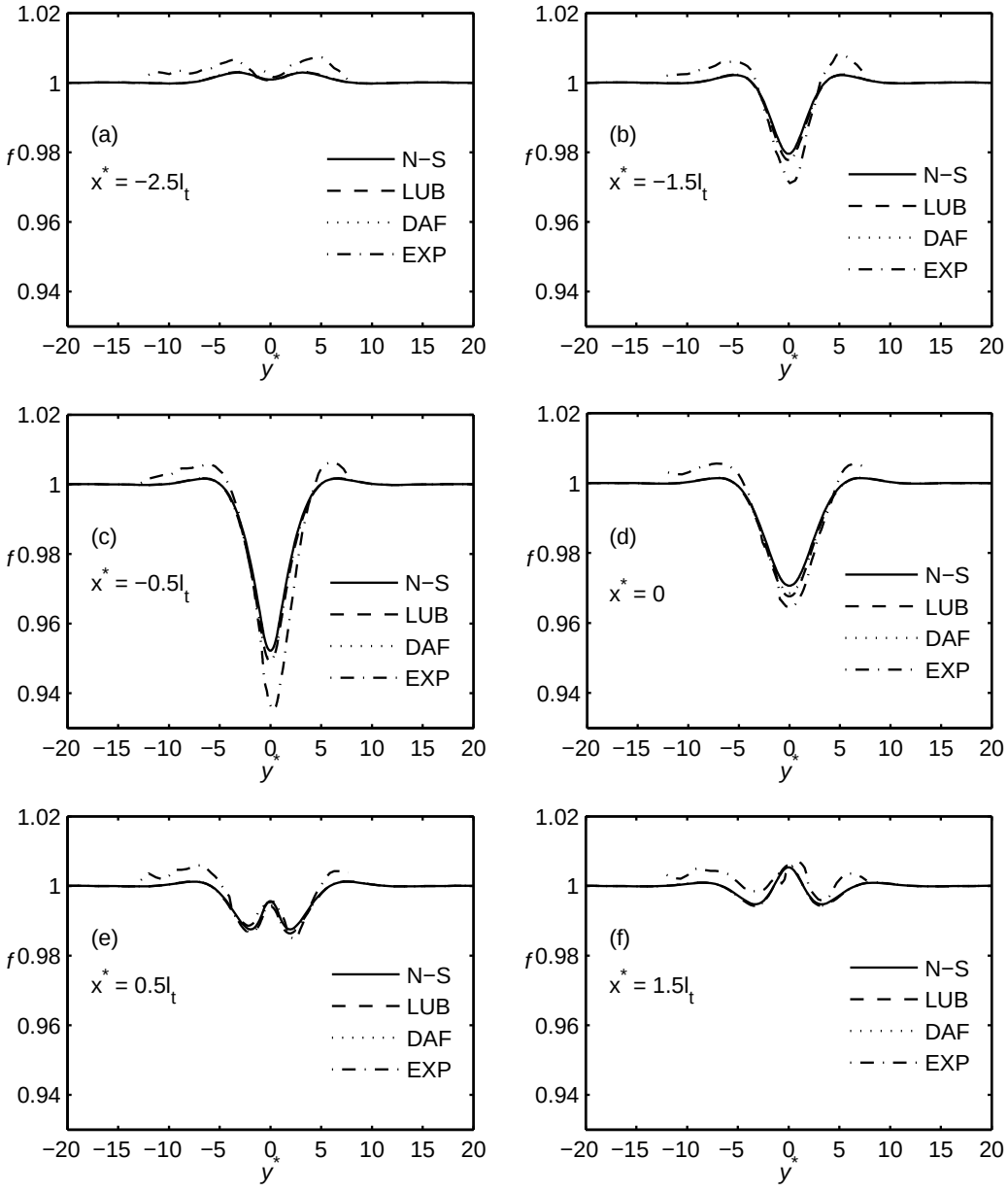

FIGURE 4.6: Comparison between predicted (N-S, LUB and DAF) and experimentally (EXP) obtained spanwise profiles through the centre of a localised square trench of Figure 4.4 at different streamwise locations: (a) $x^* = -2.5l_t$; (b) $x^* = -1.5l_t$; (c) $x^* = -0.5l_t$; (d) $x^* = 0$; (e) $x^* = 0.5l_t$; (f) $x^* = 1.5l_t$.

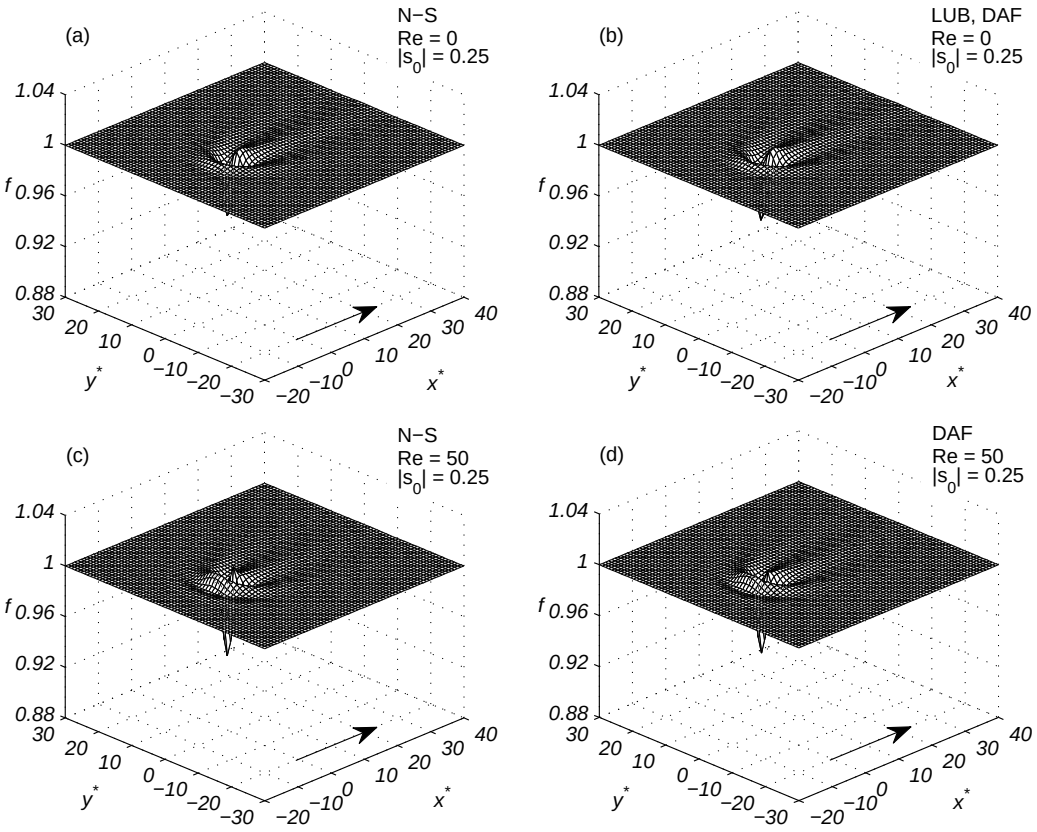

FIGURE 4.7: Comparison of predicted (N-S, LUB and DAF) three-dimensional free-surface plots for flow over a square localised trench topography with $l_t = w_t = 1.54$, $|s_0| = 0.25$: N-S (left) and DAF (right);Re = 0 (top) and Re = 50 (bottom). The LUB plots are shown where applicable. The arrow shows the direction of flow.

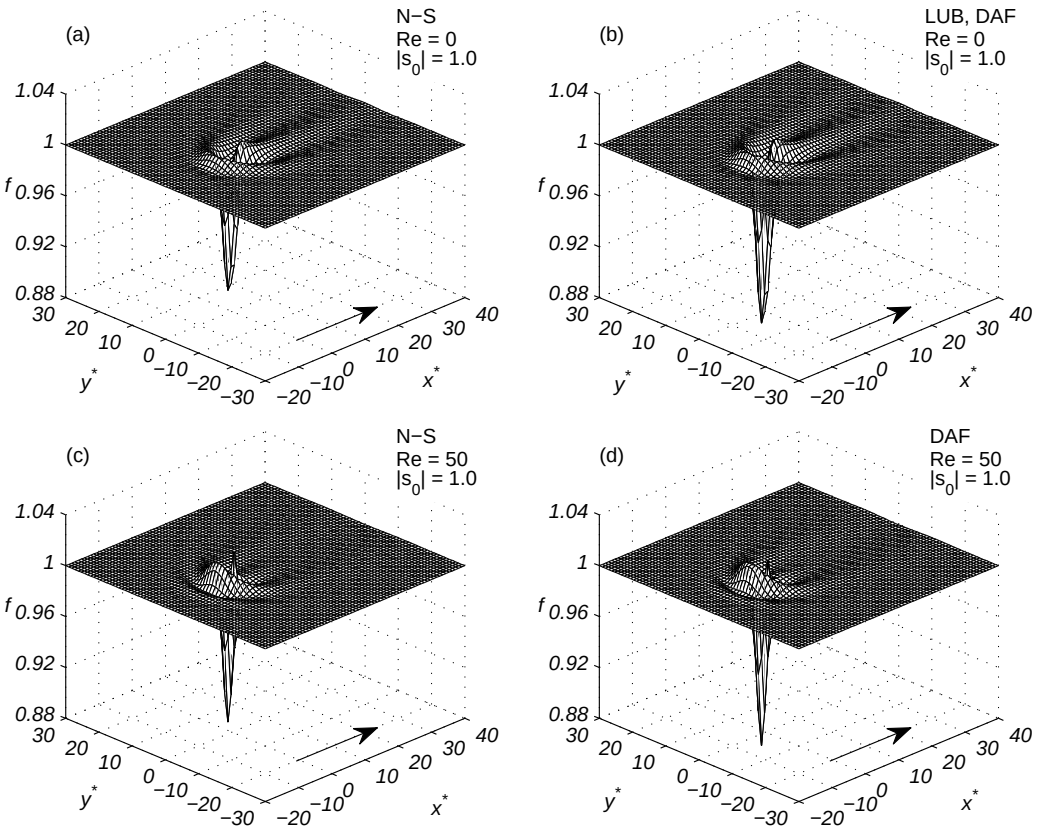

FIGURE 4.8: Comparison of predicted (N-S, LUB and DAF) three-dimensional free-surface plots for flow over a square localised trench topography with $l_t = w_t = 1.54$, $|s_0| = 1.0$: N-S (left) and DAF (right);Re = 0 (top) and Re = 50 (bottom). The LUB plots are shown where applicable. The arrow shows the direction of flow.

1.0. Figures 4.9 and 4.10 present the corresponding streamwise and spanwise free-surface profiles through the centre of the topography. Similar to the three-dimensional DAF predictions discussed in Chapter 3, the N-S solution reveals the significant influence of increased inertia: increasing Re from 0 to 50 causes a gradual rise in and widening of the free-surface disturbance and a reduction in the extent of the 'comet-tail'; in addition the capillary surge is amplified and becomes more focused. The DAF and N-S predictions are seen to be in excellent agreement, while the LUB model underpredicts the free-surface behaviour; the discrepancies becoming larger for larger values of Re and $|s_0|$. Taking the N-S solution as the benchmark it is found that increasing the depth of the localised trench topography, $|s_0|$, from 0.25 to 1.0 leads to an increase in the error present in the DAF streamwise profiles, estimated in the same way as in Figure 3.7, from 0.4% to 2.7% and from 0.4% to 2.1% for Re = 0 and 50, respectively. The LUB and DAF error is the same for Re = 0, while for Re = 50 increasing $|s_0|$ from 0.25 to 1.0 leads to an increase in the error associated with the LUB prediction from 2.3% to 7.3%. These findings are consistent with the results of error estimates associated with both LUB and DAF predictions for two-dimensional film flow over spanwise step-up and step-down topography as depicted in Figure 3.7.

Figure 4.11 depicts the effect of the transition of thin film flow, predicted by the N-S model from three-dimensional to essentially two-dimensional flow through the streamwise centre of the trench as aspect ratio $A = w_t/l_t$ is increased for fixed l_t. Increasing A leads to broadening of the bow wave, bifurcation of the downstream surge into two surges and increase of the free-surface depression; these effects were observed and discussed in relation to the DAF predictions in Chapter 3 and were first reported using the LUB model in Gaskell *et al.* (2004*b*). It can be seen clearly from the streamwise and spanwise profiles of Figure 4.12 that the capillary surge first decreases for $A = 5$ and has almost completely disappeared when $A = 10$.

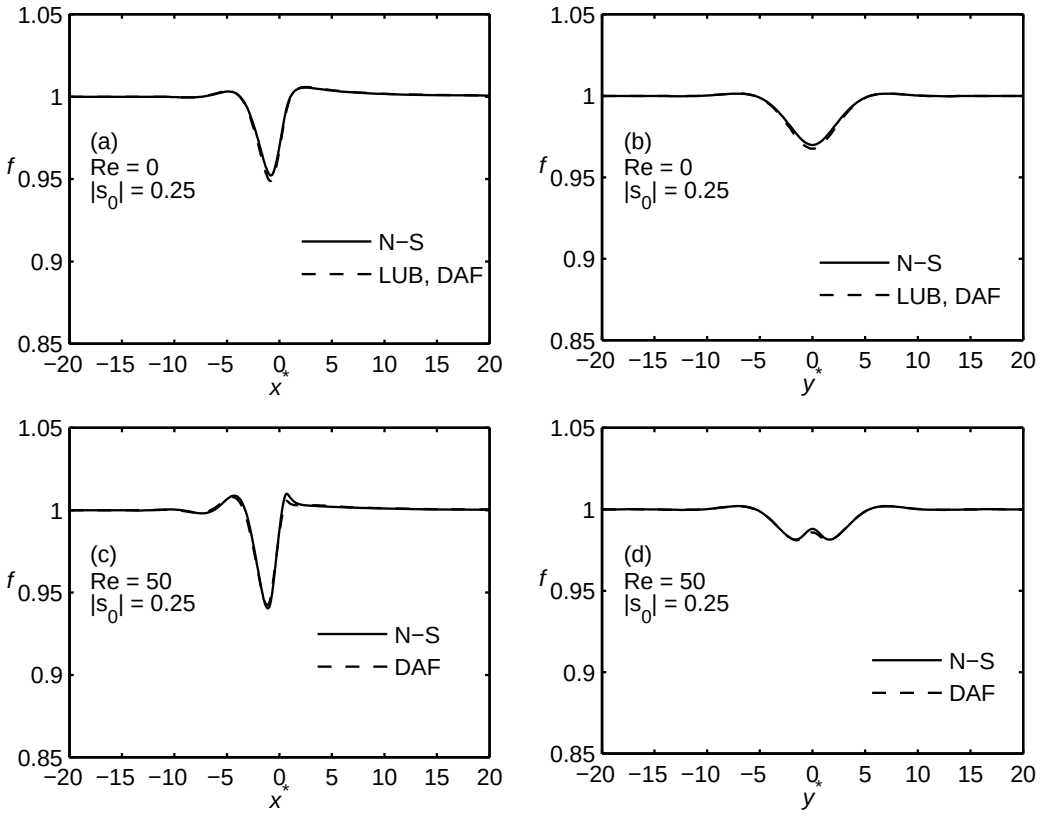

FIGURE 4.9: Comparison of predicted (N-S, LUB and DAF) streamwise (left) and spanwise (right) free-surface profiles through the centre of a localised square trench of Figure 4.7, $|s_0| = 0.25$;Re $= 0$ (top) and Re $= 50$ (bottom). The LUB profiles are shown where applicable.

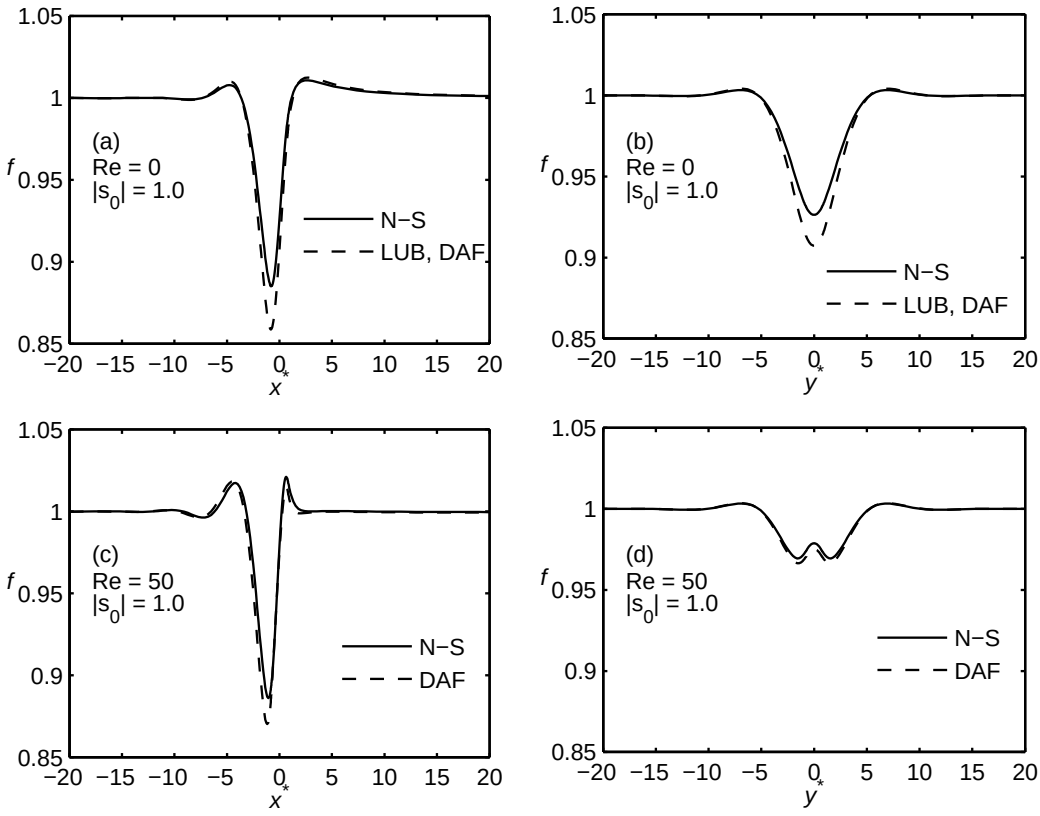

FIGURE 4.10: Comparison of predicted (N-S, LUB and DAF) streamwise (left) and spanwise (right) free-surface profiles through the centre of a localised square trench of Figure 4.7, $|s_0| = 1.0$; $\mathrm{Re} = 0$ (top) and $\mathrm{Re} = 50$ (bottom). The LUB profiles are shown where applicable.

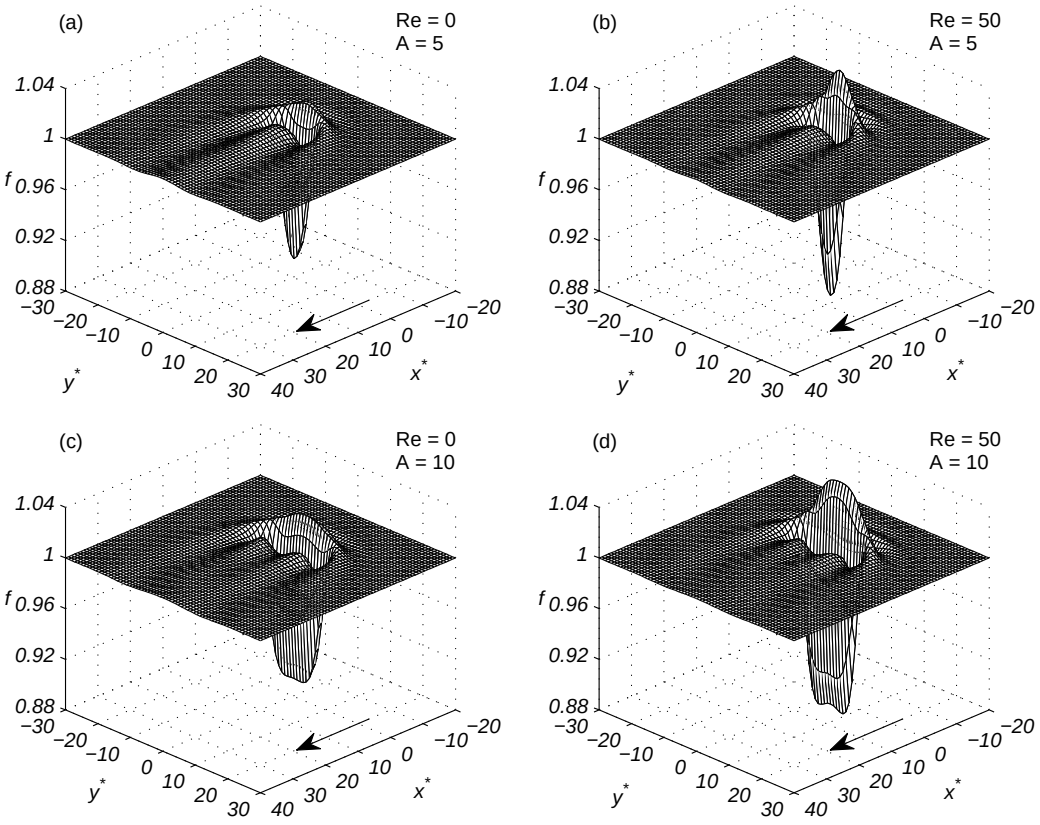

FIGURE 4.11: Three-dimensional N-S predicted free-surface plots for flow over a localised trench topography with $l_t = 1.54$, $|s_0| = 0.25$ showing the effect of aspect ratio, $A = w_t/l_t$: $A = 5$ (top) and $A = 10$ (bottom); Re $= 0$ (left) and Re $= 50$ (right). The arrow shows the direction of flow and the case $A = 1$ can be viewed in Figures 4.7(a) and (c).

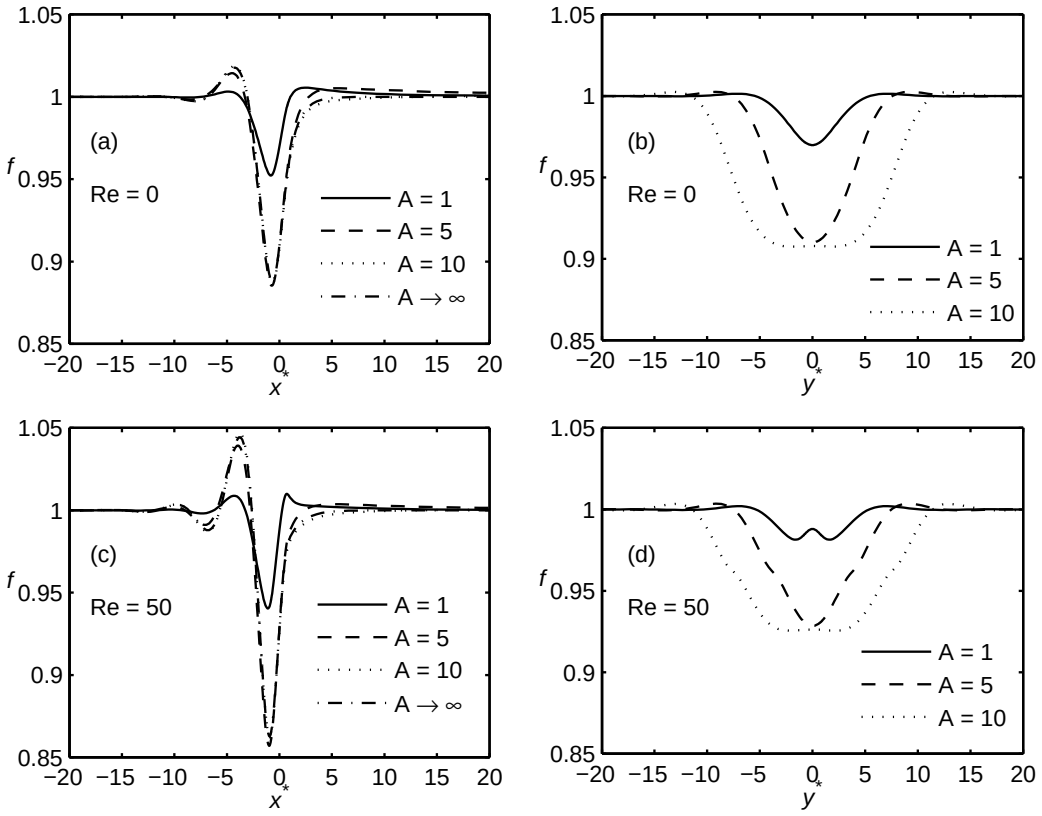

FIGURE 4.12: Streamwise (left) and spanwise (right) N-S free-surface profiles through the centre of a localised trench of Figure 4.11 showing the effect of aspect ratio, $A = w_t/l_t$: Re = 0 (top) and Re = 50 (bottom).

Finally, Figures 4.13 and 4.14 show the influence of Ca on the predicted, N-S, LUB and DAF, three-dimensional free-surface disturbance for flow over a square localised trench with $|s_0| = 0.25$ and $|s_0| = 1.0$, respectively (note that for the presentation purposes these figures are presented for a different range of z coordinate). Since the capillary length, L_0, is dependent on Ca, results are presented in a coordinate system scaled in all directions by the asymptotic film thickness: $(x^*, y^*, z) = (X - X_t, Y - Y_t, Z)/H_0$; in this coordinate system the in-plane trench dimensions are $l_t = w_t = 1.54/0.128 = 12$, the domain dimensions are $l_t = w_t = 450$ and the trench is located at $(x_t, y_t) = (100, 225)$, while $\varepsilon = 1$; flow with Re $= 0$ is considered, for which the LUB and DAF predictions are equivalent. For Ca $= 0.001$ the N-S predicted free-surface disturbance is found to be more pronounced, while for Ca $= 0.1$ it closely follows the topography; as Ca is increased the characteristic capillary features become narrower, the capillary ridge moves upstream and reduces in magnitude, while the capillary surge becomes more focused and increases in magnitude; all these effects are consistent with the results for Stokes flow over a wide spanwise trench obtained in Mazouchi & Homsy (2001), where suppression of the capillary ridge for large Ca was also reported.

For case of $|s_0| = 0.25$, considered in Figure 4.13, the DAF slightly overpredicts the magnitudes of the capillary ridge, the surge and the depression and the difference between both predictions increases with Ca, however staying within an acceptable limit: the error of the streamwise free-surface profile obtained by the DAF, taking the N-S solution as the baseline, is 0.9%, 2.1% and 4.8% for Ca $= 0.001$, 0.01 and 0.1, respectively. For case of $|s_0| = 1.0$, considered in Figure 4.14, this deviation becomes much more obvious with the DAF significantly overpredicting all the characteristic capillary features of the free-surface disturbance. This time the error in the streamwise free-surface profile obtained by the DAF, taking the N-S solution as the baseline, has become unacceptable for Ca $\geqslant 0.01$: it is 5.6%, 14.7% and 28.0% for Ca $= 0.001$, 0.01 and 0.1,

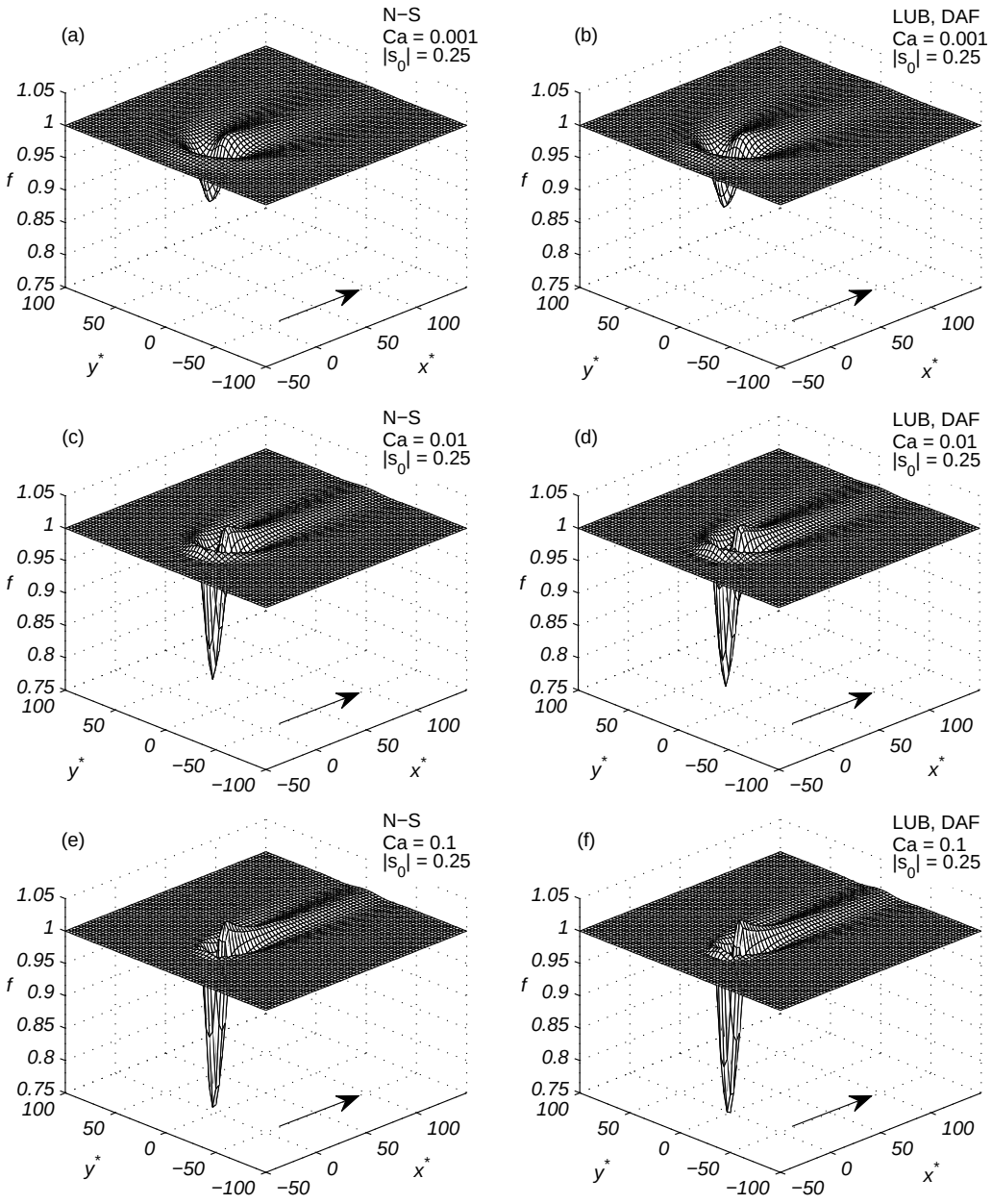

FIGURE 4.13: Comparison of predicted (N-S, LUB and DAF) three-dimensional free-surface plots for flow over a square localised trench topography with $l_t = w_t = 12$, $|s_0| = 0.25$, Re $= 0$: N-S (left) and LUB with DAF (right); from top to bottom Ca $= 0.001$, 0.01 and 0.1. The length scale in all directions is the assimptotic film thickness, H_0. The arrow shows the direction of flow.

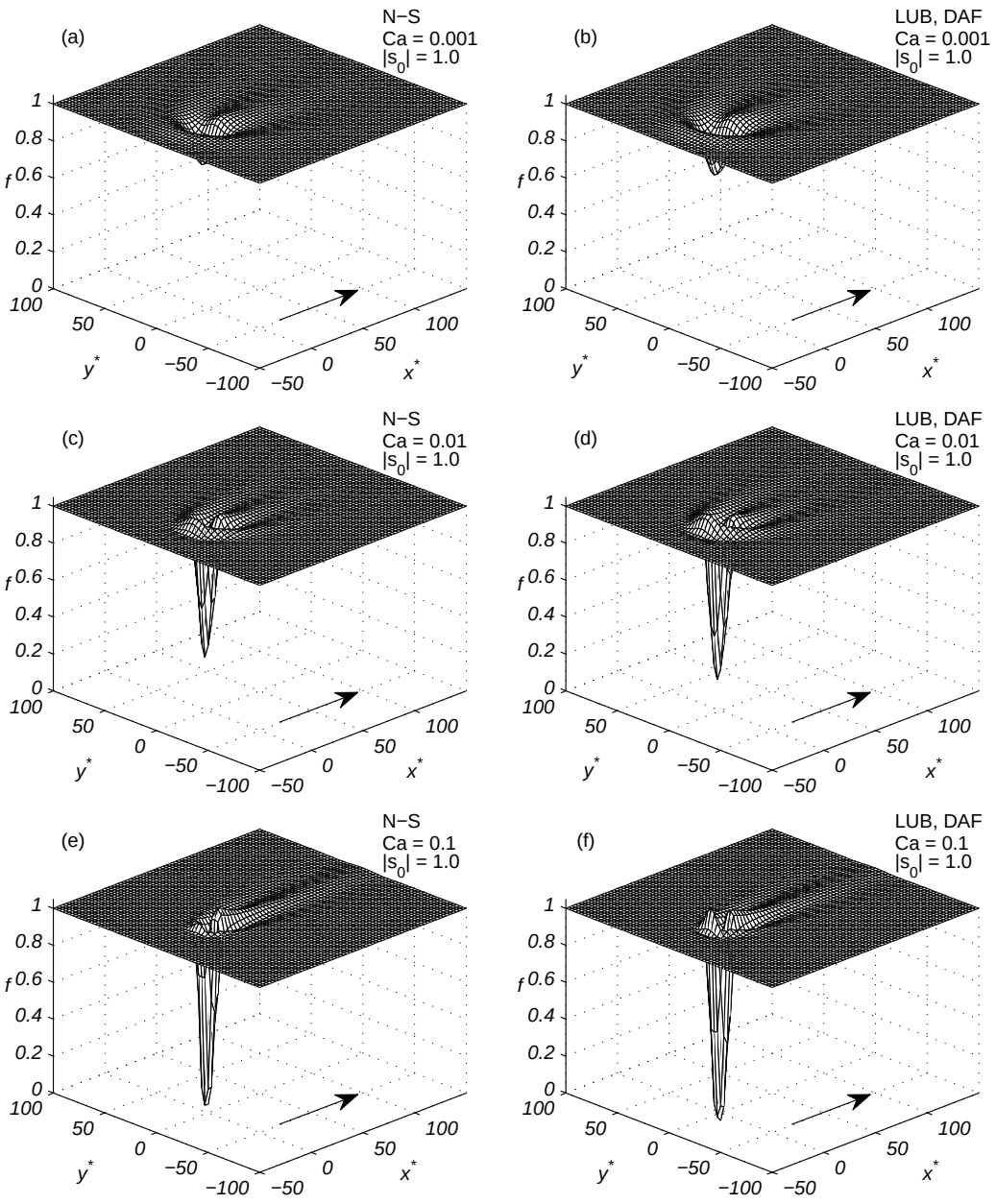

FIGURE 4.14: Comparison of predicted (N-S, LUB and DAF) three-dimensional free-surface plots for flow over a square localised trench topography with $l_t = w_t = 12$, $|s_0| = 1.0$, Re $= 0$: N-S (left) and LUB with DAF (right); from top to bottom Ca $= 0.001$, 0.01 and 0.1. The length scale in all directions is the assimptotic film thickness, H_0. The arrow shows the direction of flow. For the presentation purposes the range of z coordinate is different to that one in Figure 4.13.

respectively.

4.3 Internal flow structure

The internal velocity field and flow structure, that can be obtained accurately only by solving the full N-S system of equations, is analysed in detail. The results are presented in a coordinate system scaled equally in all directions: $(x^*, y^*, z) = (X - X_t, Y - Y_t, Z)/H_0$. The in-plane dimensions of the trench are decreased so as to be comparable with the depth of the trench, see the discussion of characteristic values below; the depth of the trench itself is set equal to the asymptotic film thickness, i.e. $|s_0| = 1.0$; the in-plane dimensions of the domain are $l_p = w_p = 550$ and the centre of the trench is located at $(x_t, y_t) = (195, 225)$. The rest of the parameters, such as number of elements and degrees of freedom in the problem domain, $\theta = 30°$, $\mathrm{Ca} = 3.5024 \cdot 10^{-4}$ are the same as in previous section.

Figure 4.15 considers the effect of the streamwise length of the trench on the resultant flow; to begin with this is done for the case of two-dimensional flow over a spanwise trench ($w_t \to \infty$). In the Stokes flow limit, $\mathrm{Re} = 0$, if the length of the trench is sufficiently small $l_t < 2.15$, see Figure 4.15(a), the flow structure is that of a single eddy similar to that found in the classical lid-driven cavity problem for zero or low Reynolds number, see Pan & Acrivos (1967), Shen & Floryan (1985), Higdon (1985) and Wright & Gaskell (1995). Figure 4.15(c) shows however, that at some critical value of $l_t \approx 2.15$ the eddy bifurcates into two and creates a separatrix across the entire trench width, the same feature has been reported in the case of shear-driven flow by Shen & Floryan (1985) and Higdon (1985) and for thin film flow by Gaskell *et al.* (2004*b*). For larger $l_t > 2.15$, two separate disjoint symmetric corner eddies are observed as reported by Shen & Floryan (1985), Higdon (1985) and Kelmanson & Lonsdale (1996), see Figure 4.15(e).

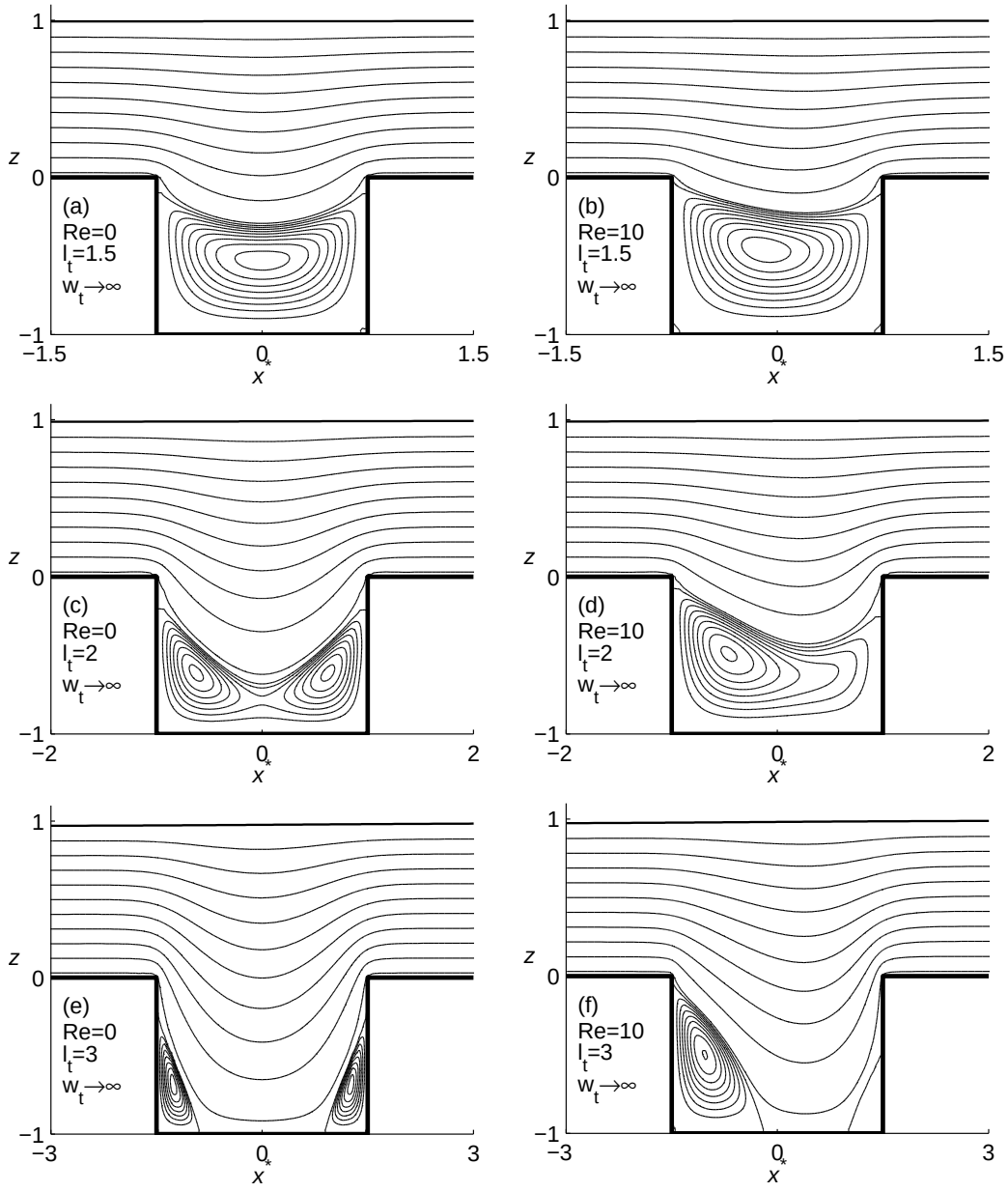

FIGURE 4.15: Structures obtained by contouring the streamfunction for two-dimensional flow over a spanwise trench with $|s_0| = 1.0$: Re = 0 (left) and Re = 10 (right). From top to bottom, $l_t = 1.5$, 2 and 3. The flow is from left to right.

For Re = 10, see Figures 4.15(b), (d) and (f), even though the streamlines are no longer symmetric with respect to $x^* = 0$, they are not different topologically from those for Stokes flow, the same has been noted by Shankar & Deshpande (2000); a larger eddy size on the upstream side and a smaller one on the downstream side of the trench being the only differences, that as a consequence increase the critical separation width of the trench for the presence of two disjoint corner eddies. Dependence of the critical width of the trench and the corresponding eddy separation streamwise coordinate on Re is summarised in Figure 4.16; both these values are monotonous functions of Re with the critical coordinate being closer to $l_t/2$ for higher Re.

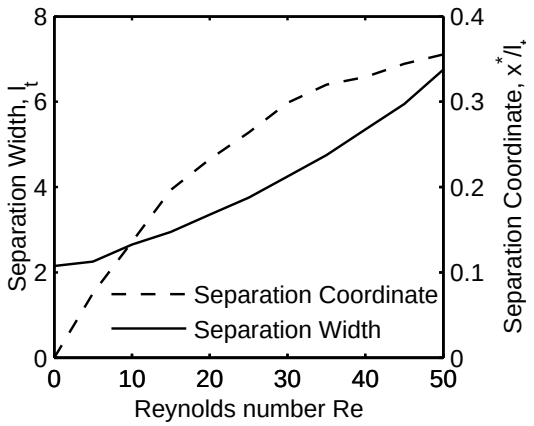

FIGURE 4.16: Critical width (full line) and separation streamwise coordinate (dashed line), at which two separate disjoint corner eddies are observed for two-dimensional thin film flow over a spanwise trench topography with $|s_0| = 1.0$.

For sufficiently large l_t, when the corner eddies are small compared to the extent of the trench, the internal velocity profile becomes effectively self-similar parabolic over the flow domain; a requirement employed to close the DAF system of equations as discussed in Subsection 2.1.5. In order to prove this, in a way similar to Wierschem (2004), Figure 4.17 compares N-S predicted sreamwise and normal to the substrate velocity components with the parabolic velocity profile defined according to equation (2.58); the case of Stokes flow, Re = 0, over a spanwise trench, $l_t = 10$, $w_t \to \infty$, $s_0 = 1.0$ (top) and $s_0 = 0.25$ (bottom) is considered and profiles taken at four different streamwise locations

upstream of the downstream edge of the trench, $x^* = -2l_t, -0.5l_t, -0.45l_t, 0$; perfect agreement between the N-S profile and parabolic profile, results in straight lines connecting the points (0,0) and (1,1). As shown, the streamwise velocity profile is essentially parabolic downstream of the trench at $x^* = -2l_t$ and very close to parabolic in the middle of the trench, $x^* = 0$, while the normal to the substrate velocity component at these locations is negligible. However there is a small region close to the edge of the trench (for $x^* = -0.5l_t$ and $x^* = -0.45l_t$), where the validity of an assumed parabolic profile is doubtful and the normal to the substrate velocity is not negligible: the maximum difference lies within 20% and 10% of the parabolic profile for $s_0 = 1.0$ and 0.25, respectively; consequently it is this small region that is the main source of error associated with the DAF approach.

Figure 4.18 considers the transition of the flow structure at the midplane $y* = 0$ for three-dimensional flow to one for two-dimensional flow as the spanwise width of the trench, w_t, is increased from 1 to 5. The case of Stokes flow, Re = 0, when the nonlinear inertial terms are absent, is considered. For $l_t = 1.5$ the flow structure is very close to the two-dimensional one depicted in Figure 4.15(a), with the increase in w_t having only a minor effect. In contrast for $l_t = 3.0$, even though the flow structure is quite similar, the corner eddies present in the three-dimensional N-S predictions are topologically different from their two-dimensional counterparts, Figure 4.15(e). Whereas for two-dimensional flow the centres of the corner eddies are always elliptic points, in three dimensions they can be foci in the midplane $y* = 0$; this fact has been noted for three-dimensional lid-driven cavity flow by both Shankar & Deshpande (2000), Sheu & Tsai (2002) and by Balaganskii, Zakharov & Shokin (2009). This can be seen clearly in Figures 4.18(b), (d) and (f), in which the streamlines, emanating from the focus on the upstream side of the trench, stream into the focus on its downstream side; this would be impossible in two dimensions. The size of these corner eddies increases as w_t is increased. Since

the foci are not sinks/sources, but stagnation points, there are two symmetric streamlines streaming laterally into the downstream and out of the upstream focus; these are so called *emanating streamlines*, as reported by Torczynski & O'Hern (1995) in their study of shear-driven three-dimensional flow in a cavity-channel geometry. The existence of emanating streamlines at foci within the flow is permitted since the velocity is zero at stagnation (critical) points and thus intersection of the streamlines is possible there. Projections of these emanating lateral streamlines onto the midplane is shown in Figures 4.18(b), (d) and (f) in the same way as in Torczynski & O'Hern (1995).

In contrast to two-dimensional flow, in three dimensions the topology of the streamlines can be different for Stokes flow and flow at non-zero Reynolds number, see Shankar & Deshpande (2000) for a discussion of similar effects in a lid-driven cavity flow. This fact can be seen in Figure 4.19 that extends the analysis of flow transition to the case with Re = 10. For both $l_t = 1.5$ and $l_t = 3.0$ particles entering slightly above the trench swirl around inside it and eventually emanate into the focus existing in the trench. For $l_t = 1.5$ this happens for only one focus existing in the trench, while for $l_t = 3.0$ there are two foci and the trajectories, that enter the trench, emanate into the downstream focus. Similar to the Stokes flow case, there are two symmetric emanating streamlines directed laterally from each focus; projections of these onto the midplane are depicted in Figure 4.19.

In order to have a better picture of the structure of the flow in three dimensions, particle trajectories are presented in Figure 4.20 for the case of $w_t = 3.0$. The particles emanate slightly above the trench at $z = 0.03$ and close to the free surface at $z = 0.8$; the starting positions of the trajectories upstream of the trench are denoted as filled circles. For illustration purposes different colours are used for streamlines corresponding to different starting positions. For the case of Stokes flow, Re = 0, see Figure 4.20(a) and (b), three-dimensional effects are observed mainly near the spanwise sides of the trench, confirming

the fact that fluid enters the trench not only across its upstream side, but also across the spanwise sides as postulated by Gaskell *et al.* (2004*b*) in connection with explaining the downstream surge. The particle trajectories also show that the amount of fluid entering the trench from the sides is increased for larger l_t, this is the reason for an increase in the capillary surge if the aspect ratio of the trench, $A = w_t/l_t$, is decreased, as discussed above in Figure 4.12.

For Re = 10 the three-dimensional effects are much stronger. For $l_t = 1.5$, see Figure 4.20(c), the particles entering the trench near the midplane (see first the blue and red trajectories) swirl around several times during which they are laterally displaced away from the midplane, exit the trench near its downstream corner, and then travel downstream. Similar shaped particle trajectories are reported for flow in a three-dimensional lid-driven cavity at low Reynolds number by Shankar & Deshpande (2000) and Tsorng, Capart, Lai & Young (2006) and in a cavity-channel geometry by Torczynski & O'Hern (1995). For $l_t = 3.0$, see Figure 4.20(d), the particles entering the trench near the downstream corner (see first the black, blue, red and then green trajectories) appear to experience similar-but-opposite trajectories while swirling around several times inside the trench, but now with lateral displacement towards the midplane before again exiting the trench near its downstream corner.

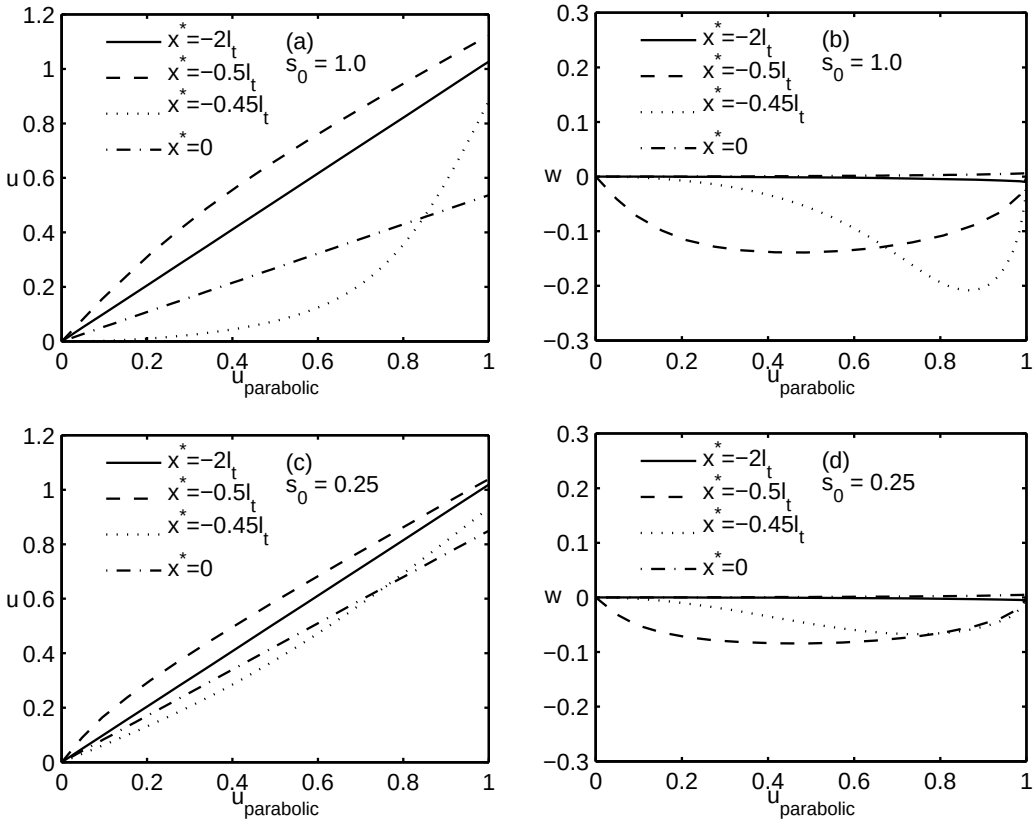

FIGURE 4.17: Comparison of N-S predicted sreamwise (left) and normal to the substrate (right) velocity components with the self-similar parabolic velocity for flow over spanwise trench with $l_t = 10$, Re $= 0$ at different streamwise locations $x^* = -2l_t, -0.5l_t, -0.45l_t, 0$: $|s_0| = 1.0$ (top) and $|s_0| = 0.25$ (bottom).

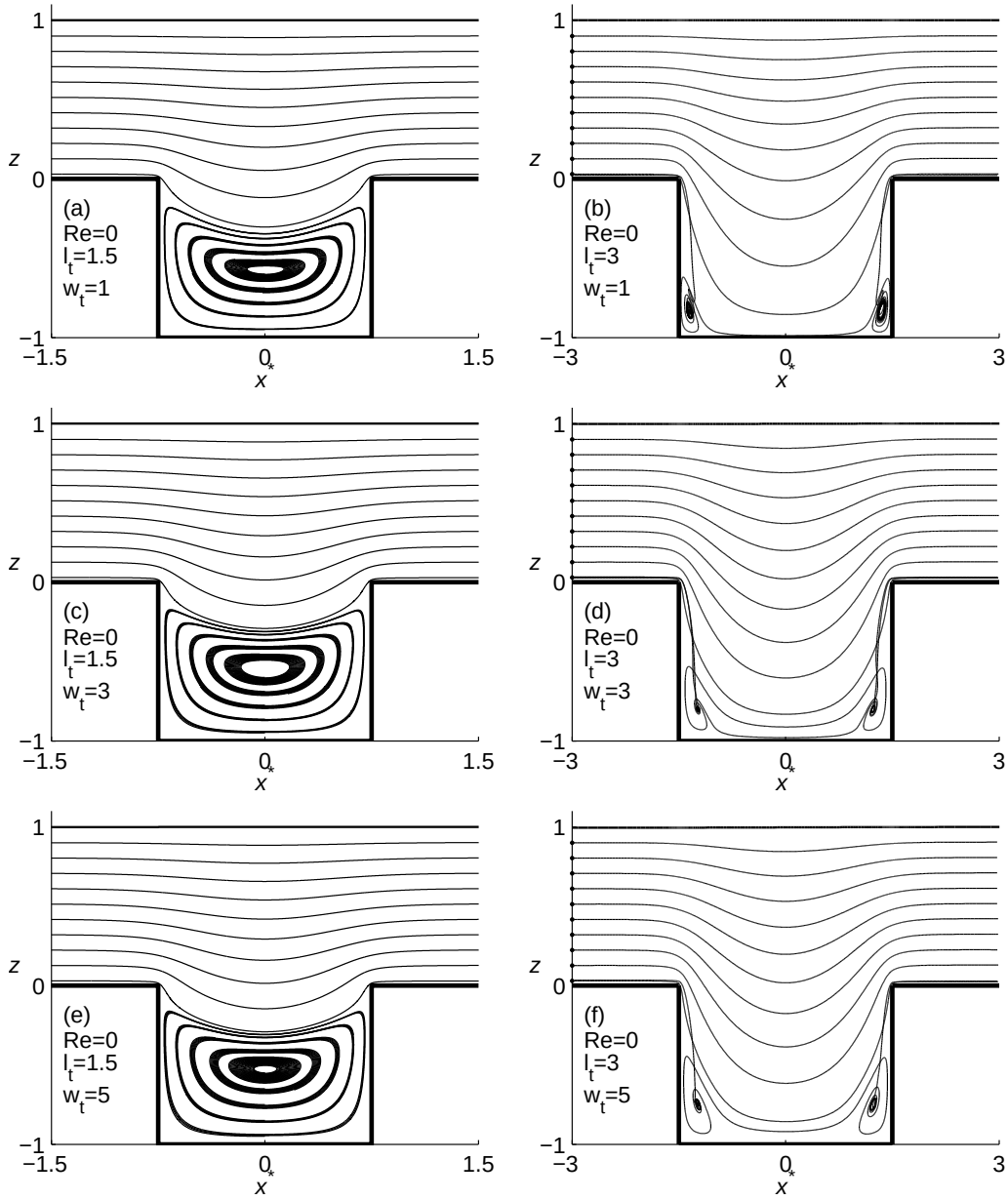

FIGURE 4.18: Flow structures obtained by integrating along path lines in the mid-plane ($y^* = 0$) for three-dimensional flow over a localised rectangular trench topography with $|s_0| = 1.0$, Re $= 0$: $l_t = 1.5$ (left) and $l_t = 3.0$ (right). From top to bottom, $w_t = 1$, 3, 5. The corresponding two-dimensional flow structures can be seen in Figures 4.15(a) and (e). The flow is from left to right. The projection of the laterally emanating streamline onto the plane $y^* = 0$ is shown as in Torczynski & O'Hern (1995).

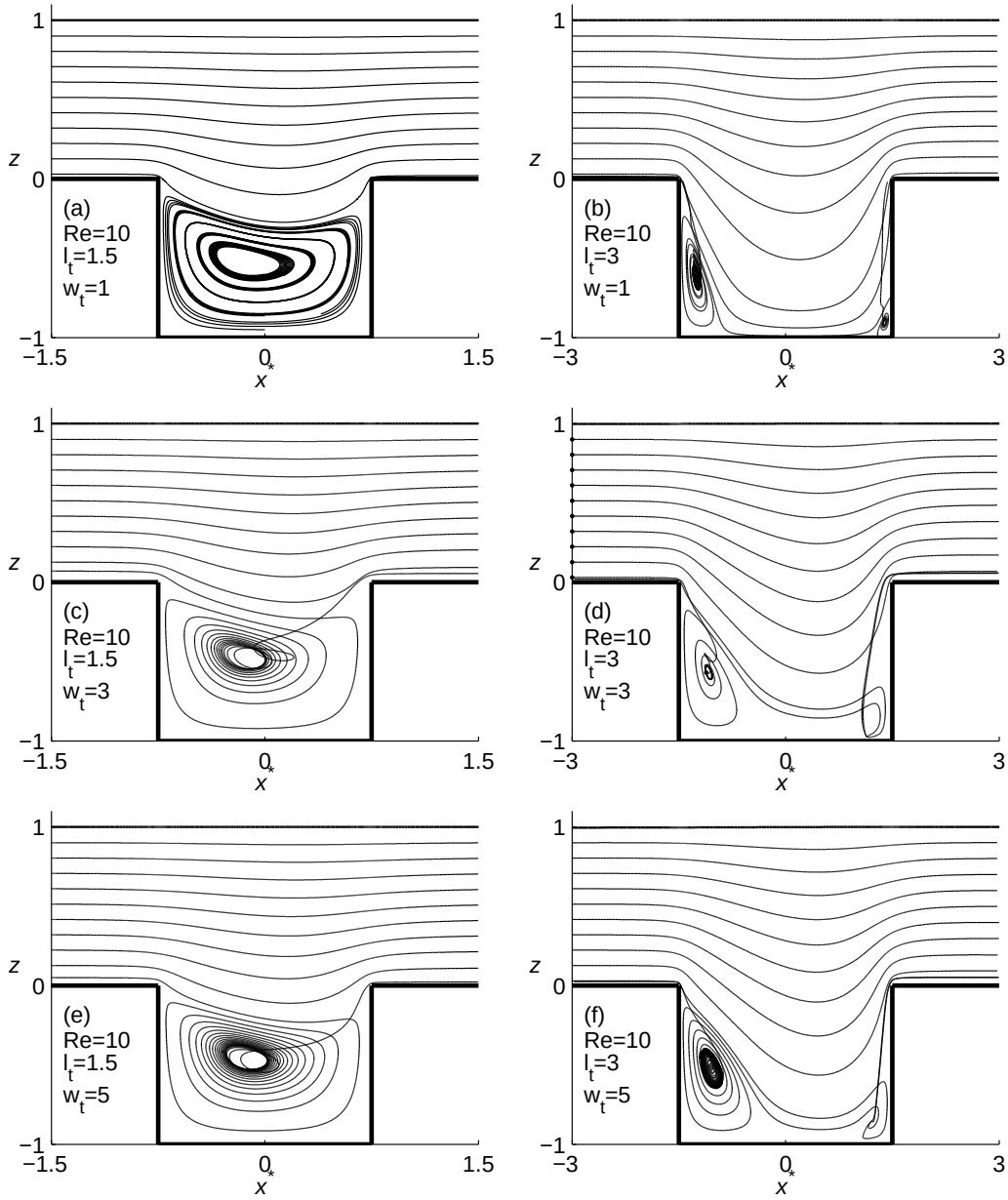

FIGURE 4.19: Flow structures obtained by integrating along the path lines in the midplane ($y^* = 0$) for three-dimensional flow over a localised rectangular trench topography with $|s_0| = 1.0$, Re = 10: $l_t = 1.5$ (left) and $l_t = 3.0$ (right). From top to bottom, $w_t = 1$, 3, 5. The corresponding two-dimensional flow structures can be seen in Figures 4.15(b) and (f). The flow is from left to right. The projection of the emanating streamline onto the plane $y^* = 0$ is shown as in Torczynski & O'Hern (1995).

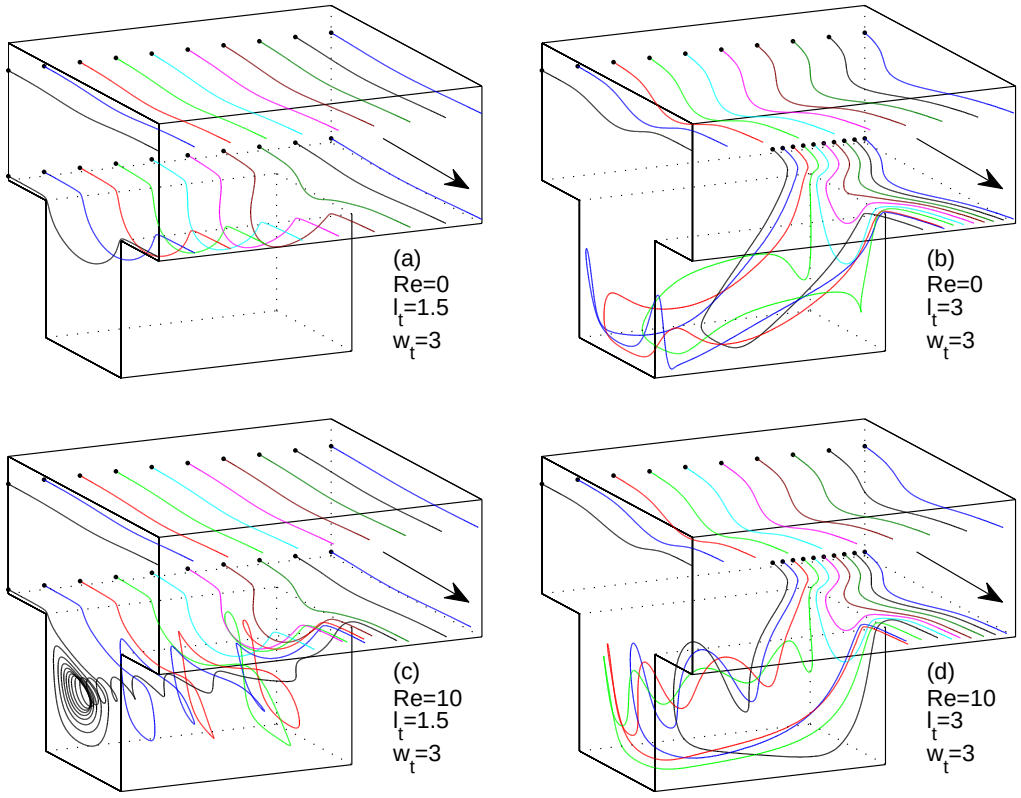

FIGURE 4.20: Three-dimensional structure of the flow, obtained by integrating along the path lines, over a localised rectangular trench topography with $w_t = 3.0$, $|s_0| = 1.0$: $l_t = 1.5$ (left) and $l_t = 3.0$ (right); Re $= 0$ (top) and Re $= 10$ (bottom). Starting positions are denoted as filled circles located slightly above the trench at $z = 0.03$ and close to the free surface at $z = 0.8$. For illustrative purposes different colours are used for streamlines corresponding to different starting positions. The midplane is on the left hand side. The arrow shows the direction of flow.

Chapter 5

Thin film flow in the presence of an electric field

Contents

This chapter is concerned with the problem of thin film flow over a substrate containing topography, in the presence of a normal electric field. The hydrodynamics of the film are modelled via the depth-averaged form (DAF) of the Navier-Stokes equations, which is coupled to a solution of Laplace's equation for the electric potential; the latter is obtained using the Fourier method together with separation of variables. A solution strategy for achieving mesh-independent solutions is based on application of a memory-efficient conjugate gradient normal residual method with Jacobi pre-conditioning. The joint effects of inertia and electric field are investigated for (i) two-dimensional flow over discrete and periodically varying spanwise topography and (ii) three-dimensional localised topography. For case (i) the full Navier-Stokes (N-S) system of equations is also used to investigate the underlying flow structure in the absence of an electric field.

5.1 Problem formulation

The problem investigated, see Figure 5.1, is that of steady, gravity-driven thin film flow down a planar substrate containing topography, shown for illustrative purposes as a discrete trench; a uniform electric field, of strength, E_0, is applied normal to the substrate which is inclined at an angle $\theta \neq 0$ to the horizontal. The air above the film is assumed to be an ideal dielectric with constant electrical permittivity, ε_e, and the liquid assumed to be perfectly conducting, so that there is no electric field inside it and no potential difference between the substrate and the free surface. This prescription is valid for fluids with high electrical conductivity, such as liquid metals or liquid electrolytes with high levels of impurity. The electric field $\boldsymbol{E}$ is related to the electric potential Φ via $\boldsymbol{E} = -\nabla\Phi$, which without loss of generality is given the value zero at both the substrate, $Z = S(X, Y)$, and the free surface, $Z = F(X, Y)$. The hydrodynamic system of equations, (2.1)-(2.2), and boundary conditions,

(2.3), (2.5) and (2.6), take the following form:

$$\rho \boldsymbol{U} \cdot \nabla \boldsymbol{U} = -\nabla P + \nabla \cdot \boldsymbol{T} + \rho \boldsymbol{G}, \tag{5.1}$$

$$\nabla \cdot \boldsymbol{U} = 0, \tag{5.2}$$

$$\boldsymbol{U}|_{Z=S} = \boldsymbol{0}, \tag{5.3}$$

$$\boldsymbol{U}|_{Z=F} \cdot \boldsymbol{n} = 0, \tag{5.4}$$

$$\left(-P\boldsymbol{I} + \boldsymbol{T}\right)|_{Z=F} \boldsymbol{n} = \left(\sigma K \boldsymbol{I} + P_A \boldsymbol{I} + \boldsymbol{M}|_{Z=F}\right) \boldsymbol{n}, \tag{5.5}$$

where $\boldsymbol{M} = \varepsilon_e \left(\boldsymbol{E} \otimes \boldsymbol{E} - \frac{1}{2}\boldsymbol{E}^2 \boldsymbol{I}\right)$ is the Maxwell stress tensor acting on the surface of a conductor; the pressure variable is shifted, $P \to P + P_A$, to denote a reference pressure. Taking reference scales as described in Subsection 2.1.1, while scaling the electric field by its magnitude E_0 and the Maxwell stress tensor by $\varepsilon_e E_0^2$ equations (5.1) to (5.5) become:

$$\mathrm{Re}\left(\boldsymbol{u} \cdot \nabla \boldsymbol{u}\right) = -\nabla p + \nabla \cdot \boldsymbol{\tau} + \mathrm{St}\boldsymbol{g}, \tag{5.6}$$

$$\nabla \cdot \boldsymbol{u} = 0, \tag{5.7}$$

$$\boldsymbol{u}|_{z=s} = 0, \tag{5.8}$$

$$\boldsymbol{u}|_{z=f} \cdot \boldsymbol{n} = 0, \tag{5.9}$$

$$\left(-p\boldsymbol{I} + \boldsymbol{\tau}\right)|_{z=f} \boldsymbol{n} = \left(\frac{\kappa}{\mathrm{Ca}} \boldsymbol{I} + 2\mathrm{We}\boldsymbol{m}|_{z=f}\right) \boldsymbol{n}, \tag{5.10}$$

where $\boldsymbol{m}$ is the dimensionless Maxwell stress tensor; $\mathrm{We} = \varepsilon_e H_0 E_0^2 / 2\mu U_0$ is the Weber number providing a measure of the relative importance of electrical to viscous forces. Taking into account that the electric field is normal at the surface of a conductor, Landau & Lifshitz (1984), namely:

$$\boldsymbol{e}|_{z=f} \cdot \boldsymbol{t} = 0, \tag{5.11}$$

where $\boldsymbol{e}$ is the dimensionless electric field, the normal and tangential components of the stress boundary condition (5.10) can be obtained by taking scalar products with respect to the normal and tangential unit vectors at the free surface, to give:

$$-p|_{z=f} + (\boldsymbol{\tau}|_{z=f} \cdot \boldsymbol{n}) \cdot \boldsymbol{n} = \frac{\kappa}{\mathrm{Ca}} + \mathrm{We}\,(\nabla\varphi)^2\,|_{z=f}, \tag{5.12}$$

$$(\boldsymbol{\tau}|_{z=f} \cdot \boldsymbol{n}) \cdot \boldsymbol{t} = 0. \tag{5.13}$$

where φ is a dimensionless electrical potential scaled by $E_0 H_0$. Conditions (5.12) and (5.13) result in an important fact: the Maxwell stresses do not contribute to the tangential stress balance.

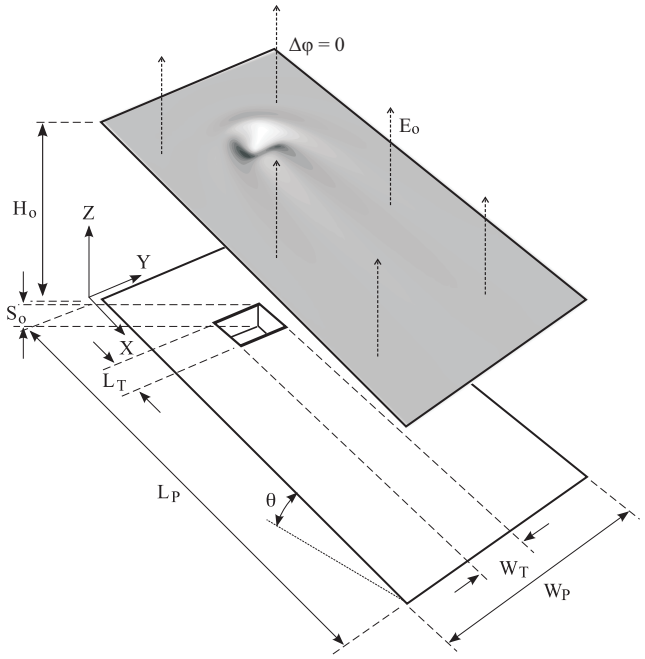

FIGURE 5.1: Schematic of gravity-driven three-dimensional flow over a substrate containing a trench topography in the presence of a uniform electric field applied normal to the substrate.

To ensure solution of the electric field problem using the methods described below the inflow/outflow boundary conditions (2.10) are replaced by periodic boundary conditions in both the x and y directions at the far-field extremities

of the solution domain:

$$(\boldsymbol{u}, p, h, s)\,|_{x=l_p} = (\boldsymbol{u}, p, h, s)\,|_{x=0}, \quad (\boldsymbol{u}, p, h, s)\,|_{y=w_p} = (\boldsymbol{u}, p, h, s)\,|_{y=0}. \tag{5.14}$$

For the case of flow over a discrete trench or peak topography located on a flat inclined substrate, the inflow boundary condition (2.10) for the film thickness is prescribed:

$$h|_{x=0} = 1. \tag{5.15}$$

For the case of flow over periodically repeating, wavy substrates extending to the boundary, the inflow boundary condition (2.10) is replaced by one ensuring that the fixed volume of fluid involved is preserved; setting this as equivalent to the same volume of fluid flowing over a uniformly flat substrate, the same is enforced by requiring that

$$\int_0^{l_p} \int_0^{w_p} h dx dy = l_p w_p. \tag{5.16}$$

The hydrodynamic and electric field problems are coupled via an additional Maxwell stress term, $\mathrm{We}\,(\nabla\varphi)^2\,|_{z=f}$, in the normal stress condition (5.12). This term is determined by solving Laplace's equation for the electric field potential:

$$\nabla^2\varphi = 0, \tag{5.17}$$

together with imposing, without loss of generality, the following condition of zero electric potential at the free surface:

$$\varphi|_{z=f} = 0, \tag{5.18}$$

a uniform electric field at infinity:

$$\nabla\varphi|_{z\to\infty} = (0, 0, -1)\,, \tag{5.19}$$

and periodic boundary conditions in both the x and y directions at the far-field extremities of the domain of interest:

$$\varphi|_{x=l_p} = \varphi|_{x=0}, \quad \varphi|_{y=w_p} = \varphi|_{y=0}. \tag{5.20}$$

The complexity of equations (5.6) - (5.7) and boundary conditions (5.8) - (5.16) as specified above is reduced by (i) rescaling in terms of L_0 according to (2.15), (ii) enforcing the long-wave approximation, $\varepsilon \ll 1$, and (iii) depth-averaging the resulting set of equations; after performing these three steps in the same way as described in Subsection 2.1.4 a system of equations similar to (2.53) - (2.55) follows:

$$\frac{6}{5}\varepsilon \mathrm{Re}\left(\bar{u}\frac{\partial \bar{u}}{\partial x} + \bar{v}\frac{\partial \bar{u}}{\partial y}\right) = -\frac{\partial p}{\partial x} - \frac{3\bar{u}}{h^2} + 2, \tag{5.21}$$

$$\frac{6}{5}\varepsilon \mathrm{Re}\left(\bar{u}\frac{\partial \bar{v}}{\partial x} + \bar{v}\frac{\partial \bar{v}}{\partial y}\right) = -\frac{\partial p}{\partial y} - \frac{3\bar{v}}{h^2}, \tag{5.22}$$

$$p = -\frac{\varepsilon^3}{\mathrm{Ca}}\left(\frac{\partial^2 f}{\partial x^2} + \frac{\partial^2 f}{\partial y^2}\right) + 2\varepsilon\left(f - z\right)\cot\theta - \varepsilon \mathrm{We}\left(\frac{\partial \varphi}{\partial z}\right)^2 |_{z=f}, \tag{5.23}$$

$$\frac{\partial (h\bar{u})}{\partial x} + \frac{\partial (h\bar{v})}{\partial y} = 0, \tag{5.24}$$

which is solved subject to either condition (5.15) or condition (5.16) and the following far-field periodic boundary conditions

$$\left(\bar{u}, \bar{v}, p, h\right)|_{x=l_p} = \left(\bar{u}, \bar{v}, p, h\right)|_{x=0}, \quad \left(\bar{u}, \bar{v}, p, h\right)|_{y=w_p} = \left(\bar{u}, \bar{v}, p, h\right)|_{y=0}. \tag{5.25}$$

The Maxwell stress, which appears as an additional term on the right hand side of boundary condition (5.12) compared to the non-electric field case in (2.13), consequently appears as an additional term in the equation for pressure (5.23). Note also that, the equation for pressure (5.23) is retained, rather than eliminating it as an unknown by substitution into equations (5.21) and (5.22), as in the case with equations (2.53) and (2.54); doing so minimises the time and effort associated with evaluating the Maxwell stress term. The

latter is obtained via the solution of equation (5.17) for the electric potential; although equations (5.21)-(5.24) are valid for non-zero Re, their range of applicability is constrained by virtue of the long-wave limitation, namely to the case of small capillary numbers only, that is Ca $= \mu U_0/\sigma = \varepsilon^3/6 \ll 1$, see (2.27). Attention is restricted to film flows over simple step-up/down, (2.64), peak/trench, (2.65), and wavy bottom topographies; the last one is specified via the appropriate functional form.

5.2 Method of solution

5.2.1 Hydrodynamic equations

Equations (5.21) to (5.24) are solved numerically, subject to the boundary conditions specified, on a rectangular computational domain, $(x, y) \in [0, l_p] \times [0, w_p]$, subdivided using a staggered arrangement of unknowns, see Subsection 2.2.4 for details; taking (i, j) to represent a typical mesh point in the system, values of film thickness, h, and pressure, p, are located at (i, j), with averaged velocities $\bar{u}$ and $\bar{v}$ located at the mid-points $(i + 1/2, j)$ and $(i, j + 1/2)$, respectively. For each unknown $(i, j) \in [1, n_x] \times [1, n_y]$, where n_x and n_y are the total number of nodes, in the x and y directions, respectively; uniform spatial increments were employed, $\Delta x = l_p/n_x$ and $\Delta y = w_p/n_y$, such that $x_1 = 0$, $y_1 = 0$ and $x_{n_x} = l_p - \Delta x$, $y_{n_y} = w_p - \Delta y$.

Writing discrete forms of the momentum equations (5.21) and (5.22) at $(i + 1/2, j)$ and $(i, j + 1/2)$, respectively and the pressure (5.23) and continuity (5.24) equations at (i, j), omitting for the sake of convenience the over-bar denoting averaged values, results in the following second-order accurate system of difference equations:

$$\frac{6}{5}\varepsilon \mathrm{Re} \mathcal{F}\left[u\right]_{i+1/2,j} + \frac{p_{i+1,j} - p_{i,j}}{\Delta x} + \frac{3u_{i+1/2,j}}{h^2_{i+1/2,j}} - 2 = 0, \tag{5.26}$$

$$\frac{6}{5}\varepsilon \mathrm{Re}\mathcal{F}\left[v\right]_{i,j+1/2} + \frac{p_{i,j+1} - p_{i,j}}{\Delta y} + \frac{3v_{i,j+1/2}}{h^2_{i,j+1/2}} = 0, \tag{5.27}$$

$$p_{i,j} + \frac{\varepsilon^3}{\mathrm{Ca}}\left(\frac{f_{i+1,j} + f_{i-1,j} - 2f_{i,j}}{\Delta x^2} + \frac{f_{i,j+1} + f_{i,j-1} - 2f_{i,j}}{\Delta y^2}\right)$$

$$- 2\varepsilon \cot\theta f_{i,j} + \varepsilon \mathrm{We}\left(\frac{\partial \varphi}{\partial z}\right)^2 |_{z=f}|_{i,j} = 0, \tag{5.28}$$

$$\frac{h_{i+1/2,j}u_{i+1/2,j} - h_{i-1/2,j}u_{i-1/2,j}}{\Delta x} + \frac{h_{i,j+1/2}u_{i,j+1/2} - h_{i,j-1/2}u_{i,j-1/2}}{\Delta y} = 0, \tag{5.29}$$

where $\mathcal{F}\left[\omega\right]$ is defined according to (2.125); while the evaluation of discrete values at (i, j) for the last quantity, the Maxwell stress term, on the right hand side of equation (5.28) is discussed subsequently.

The imposition of periodic boundary conditions in the case of flow over localised, discrete topography requires the specification of ghost nodes at the edge of the computational domain in the x and y directions, namely:

$$h_{i\pm n_x, j\pm n_y} = h_{i,j}, \quad p_{i\pm n_x, j\pm n_y} = p_{i,j}, \tag{5.30}$$

$$u_{i+1/2\pm n_x, j\pm n_y} = u_{i+1/2,j}, \quad v_{i\pm n_x, j+1/2\pm n_y} = v_{i,j+1/2}, \tag{5.31}$$

while, the Dirichlet condition for the film thickness at the inlet is assigned as an exact value there:

$$h|_{1,j} = 1. \tag{5.32}$$

In the case of a periodically repeating wavy substrate the volume constraint condition, (5.16), is imposed at the point $(i, j) = (1, 1)$ by replacing equation (5.29) there with:

$$\sum_{i=1}^{n_x}\sum_{j=1}^{n_y} h_{i,j} = n_x n_y. \tag{5.33}$$

5.2.2 Electric field equation

An analytical solution to the three-dimensional Laplace problem (5.17), subject to boundary conditions (5.18)-(5.20) and the restriction $\varepsilon \ll 1$, is obtained as a Fourier series expansion using the method of separation of variables.

First the problem is made more tractable, see Tseluiko *et al.* (2008*b*), by: (i) defining a *shifted* electric field potential, $\tilde{\varphi} = \varphi - 1 + z$, measuring the deviation from a uniform electric field; (ii) rescaling the z-coordinate with respect to ε such that $\tilde{z} = \varepsilon z$. Then with $(x, y, \tilde{z}) = (X, Y, Z)/L_0$ and $\nabla = \left(\frac{\partial}{\partial x}, \frac{\partial}{\partial y}, \frac{\partial}{\partial \tilde{z}}\right)$, the equivalent boundary value problem for $\tilde{\varphi}\,(x, y, \tilde{z})$ is:

$$\nabla^2 \tilde{\varphi} = 0, \tag{5.34}$$

subject to the boundary conditions:

$$\tilde{\varphi}|_{\tilde{z}=\varepsilon f} = f - 1, \tag{5.35}$$

$$\nabla \tilde{\varphi}|_{\tilde{z}\to\infty} = 0, \tag{5.36}$$

$$\tilde{\varphi}|_{x=l_p} = \tilde{\varphi}|_{x=0}, \quad \tilde{\varphi}|_{y=w_p} = \tilde{\varphi}|_{y=0}. \tag{5.37}$$

Under the over arching assumption that $\varepsilon \ll 1$ the free-surface boundary condition (5.35) can be approximated as:

$$\tilde{\varphi}|_{\tilde{z}=0} = f - 1. \tag{5.38}$$

Now, postulating the solution to have a separable form:

$$\tilde{\varphi} = A\,(x)\,B\,(y)\,C\,(\tilde{z})\,, \tag{5.39}$$

substituting it into equation (5.34) and dividing through by $\tilde{\varphi}$ leads to the

following equation for the separable components:

$$\frac{1}{A}\frac{d^2A}{dx^2}+\frac{1}{B}\frac{d^2B}{dy^2}+\frac{1}{C}\frac{d^2C}{d\tilde{z}^2}=0, \tag{5.40}$$

which is satisfied via solutions of the following Sturm-Liouville problems:

$$\frac{d^2A}{dx^2}+\lambda^2A=0, \quad \frac{d^2B}{dy^2}+\mu^2B=0, \quad \frac{d^2C}{d\tilde{z}^2}-\left(\lambda^2+\mu^2\right)C=0, \tag{5.41}$$

where λ and μ are real constants. Solving equations (5.41) subject to boundary conditions (5.36) and (5.37) leads to the following eigenvalues and eigenfunctions:

$$\lambda_m=2\pi m/l_p, \quad A_m(x)=c_{1,m}\cos(\lambda_m x)+c_{2,m}\sin(\lambda_m x),$$

$$\mu_n=2\pi n/w_p, \quad B_n(y)=c_{3,n}\cos(\mu_n y)+c_{4,n}\sin(\mu_n y),$$

$$C_{m,n}(\tilde{z})=c_{5,m,n}\exp\left[-\left(\sqrt{\lambda_m^2+\mu_n^2}\right)\tilde{z}\right], \quad \text{for } m=0,1...\infty, n=0,1...\infty, \tag{5.42}$$

which in turn results in a shifted potential of the form:

$$\tilde{\varphi}(x,y,\tilde{z})=\sum_{m,n=0}^{\infty}\left[a_{m,n}\cos(\lambda_m x)\cos(\mu_n y)+b_{m,n}\sin(\lambda_m x)\sin(\mu_n y)\right.$$

$$\left.+\,c_{m,n}\cos(\lambda_m x)\sin(\mu_n y)+d_{m,n}\sin(\lambda_m x)\cos(\mu_n y)\right]\exp\left[-\left(\sqrt{\lambda_m^2+\mu_n^2}\right)\tilde{z}\right], \tag{5.43}$$

where $a_{m,n}=c_{5,m,n}c_{1,m}c_{3,n}$, $b_{m,n}=c_{5,m,n}c_{2,m}c_{4,n}$, $c_{m,n}=c_{5,m,n}c_{1,m}c_{4,n}$ and $d_{m,n}=c_{5,m,n}c_{2,m}c_{3,n}$ are arbitrary constants. From the free-surface boundary condition (5.38) it follows that these coefficients are the two-dimensional Fourier series expansion coefficients of $(f-1)$:

$$a_{m,n}=\frac{\chi_m\chi_n}{l_pw_p}\int_0^{l_p}\int_0^{w_p}(f-1)\cos(\lambda_m\widehat{x})\cos(\mu_n\widehat{y})\,d\widehat{x}d\widehat{y}, \tag{5.44}$$

$$b_{m,n}=\frac{\chi_m\chi_n}{l_pw_p}\int_0^{l_p}\int_0^{w_p}(f-1)\sin(\lambda_m\widehat{x})\sin(\mu_n\widehat{y})\,d\widehat{x}d\widehat{y}, \tag{5.45}$$

$$c_{m,n} = \frac{\chi_m \chi_n}{l_p w_p} \int_0^{l_p} \int_0^{w_p} (f-1) \cos(\lambda_m \widehat{x}) \sin(\mu_n \widehat{y})\, d\widehat{x} d\widehat{y}, \tag{5.46}$$

$$d_{m,n} = \frac{\chi_m \chi_n}{l_p w_p} \int_0^{l_p} \int_0^{w_p} (f-1) \sin(\lambda_m \widehat{x}) \cos(\mu_n \widehat{y})\, d\widehat{x} d\widehat{y}, \tag{5.47}$$

$$\chi_m = \begin{cases} 1, & \text{if} \quad m = 0 \\ 2, & \text{if} \quad m > 0 \end{cases}. \tag{5.48}$$

Since $\cos(\lambda_m x)\cos(\lambda_m \widehat{x}) + \sin(\lambda_m x)\sin(\lambda_m \widehat{x}) = \cos[\lambda_m (x - \widehat{x})]$ equation (5.43) can be expressed as follows:

$$\tilde{\varphi}(x, y, \tilde{z}) = \frac{1}{l_p w_p} \int_0^{l_p} \int_0^{w_p} (f-1) \sum_{m,n=0}^{\infty} \chi_m \chi_n \cos[\lambda_m (x - \widehat{x})]$$

$$\times \cos[\mu_n (y - \widehat{y})] \exp\left[-\left(\sqrt{\lambda_m^2 + \mu_n^2}\right) \tilde{z}\right] d\widehat{x} d\widehat{y}. \tag{5.49}$$

The potential is obtained by returning from the *rescaled* vertical coordinate $\tilde{z}$ to z and then from the *shifted* to the initial form of the electric potential:

$$\varphi(x, y, z) = 1 - z + \frac{1}{l_p w_p} \int_0^{l_p} \int_0^{w_p} (f-1) \sum_{m,n=0}^{\infty} \chi_m \chi_n \cos[\lambda_m (x - \widehat{x})]$$

$$\times \cos[\mu_n (y - \widehat{y})] \exp\left[-\left(\sqrt{\lambda_m^2 + \mu_n^2}\right) \varepsilon z\right] d\widehat{x} d\widehat{y}. \tag{5.50}$$

The z-derivative of the above potential, $\partial\varphi/\partial z|_{z=f}$, required to determine the vertical component of the electric field, is:

$$\frac{\partial \varphi}{\partial z}|_{z=f} = -1 - \varepsilon \mathcal{E}[f-1](x, y), \tag{5.51}$$

where $\mathcal{E}[f-1]$, the electric field Fourier operator, is given by:

$$\mathcal{E}[f-1] \approx \frac{1}{l_p w_p} \int_0^{l_p} \int_0^{w_p} (f-1) \sum_{m,n=0}^{\infty} \chi_m \chi_n \sqrt{\lambda_m^2 + \mu_n^2}$$

$$\times \cos[\lambda_m (x - \widehat{x})] \cos[\mu_n (y - \widehat{y})]\, d\widehat{x} d\widehat{y}. \tag{5.52}$$

The Maxwell stress term, appearing on the right hand side of the pressure equation (5.23), is obtained by neglecting terms $\mathrm{O}(\varepsilon^3\mathrm{We})$:

$$\varepsilon\mathrm{We}\left(\frac{\partial\varphi}{\partial z}\right)^2|_{z=f} \approx \varepsilon\mathrm{We} + 2\varepsilon^2\mathrm{We}\mathcal{E}\left[f-1\right](x,y)\,, \tag{5.53}$$

where the εWe term on the right hand side of equation (5.53) is a constant pressure term, which can be omitted since the depth-averaged hydrodynamic equations are driven by the gradient of the pressure, not by the pressure itself.

The integrals associated with the $\mathcal{E}\left[f-1\right]$ operator and hence the Maxwell stress term (5.53), which appears in equation (5.28), are evaluated numerically at the point (i,j) using trapezoidal quadrature rule, Atkinson (1989), exploiting the periodicity of the solution, that is:

$$\mathcal{E}\left[f-1\right]_{i,j} = \sum_{k=1}^{n_x}\sum_{l=1}^{n_y} E_{i,j,k,l}\left(f_{k,l}-1\right), \tag{5.54}$$

with

$$E_{i,j,k,l} = \frac{1}{n_x n_y}\sum_{m,n=0}^{N^f}\chi_m\chi_n\sqrt{\lambda_m^2+\mu_n^2}\cos\left(\frac{2\pi m\left(i-k\right)}{n_x}\right)\cos\left(\frac{2\pi n\left(j-l\right)}{n_y}\right). \tag{5.55}$$

N^f is the number of terms in the truncated Fourier series.

5.2.3 Overall numerical procedure

The integro-differential electrohydrodynamic discrete equation set, (5.26)-(5.29), is solved using a numerical approach based on Newton iteration. For three-dimensional flows, the global matrix generated is too large to be stored in memory; consequently an iterative matrix-free method of solution is required - in this thesis the conjugate gradient normal residual (CGNR) method with Jacobi pre-conditioning was employed, full details of which are provided in Kelley (2003). The symmetric matrix required by the conjugate gradient solver

is obtained by multiplying the iterative equations by the transpose of the Jacobian.

Symmetry ensures that only those $n_x \times n_y$ elements of the $E_{i,j,k,l}$ tensor, corresponding to all possible combinations of $|i-k|$ and $|j-l|$, need to be stored; even so, determining $\mathcal{E}\left[f-1\right]_{i,j}$ by evaluating the double summation of equation (5.54) is computationally intensive. The effort required can be reduced considerably, without any loss of accuracy, by neglecting to sum terms that lie far from the diagonals $i=k$ and $j=l$ (electric field tensors are strongly diagonally dominant and at the same time periodic) and far from the centre of the topography where the film approaches its asymptotic thickness. In which case equation (5.54) can be written as:

$$\mathcal{E}\left[f-1\right]_{i,j} \approx \sum_{k,l\in\Omega} E_{i,j,k,l}\left(f_{k,l}-1\right), \tag{5.56}$$

where

$$\begin{aligned} \Omega = &\left[i-\gamma n_x/2+1, i+\gamma n_x/2\right]\times\left[j-\gamma n_y/2+1, j+\gamma n_y/2\right] \\ \cup &\left[i_t-\gamma n_x/2+1, i_t+\gamma n_x/2\right]\times\left[j_t-\gamma n_y/2+1, j_t+\gamma n_y/2\right], \end{aligned} \tag{5.57}$$

such that $(i_t, j_t) = \left(\mathrm{trunc}\left(x_t/\Delta x\right), \mathrm{trunc}\left(y_t/\Delta y\right)\right)$ are the discretised coordinates of the centre of the topography; $\mathrm{trunc}\left(x\right)$ is the truncation function from real to integer. $\gamma \in [0,1]$ is an adjustable parameter that can be varied to ensure guaranteed solution accuracy at an acceptable computational cost; the values 1 and 0 correspond to integration over the entire and none of solution domain, respectively.

Furthermore, in order to produce accurate solutions in an acceptable time, the CGNR method was parallelised using geometric domain decomposition, implemented via a message-passing interface (MPI) distributed memory paradigm, see Snir *et al.* (1996). For simplicity, strip-wise partitioning in the x-direction is used, ensuring that each subdomain has two immediate neighbours, includ-

ing the first and the last subdomains due to the periodic nature of the solution. Each processor is responsible for the calculation of matrix-vector products for one subdomain only, which requires the use of additional columns of the solution immediately to either side of a subdomain; to evaluate expression (5.56) over Ω results in the use of a significant number additional columns.

In brief, on subdomain $i_p \in [0, n_p - 1]$, where n_p is the total number of subdomains, the matrix-vector products are calculated for $i \in [i_1, i_2]$, with:

$$i_1 = \mathrm{loc} \cdot i_p + \min(i_p, \mathrm{rem}) + 1, i_2 = \begin{cases} (\mathrm{loc}+1) \cdot (i_p+1), i_p < \mathrm{rem} \\ \mathrm{loc} \cdot (i_p+1) + \mathrm{rem}, \quad i_p \geqslant \mathrm{rem} \end{cases}, \quad (5.58)$$

where $\mathrm{loc} = \mathrm{trunc}\,(n_x/n_p)$ and $\mathrm{rem} = n_x - \mathrm{loc} \cdot n_p$, which requires the subdomains to overlap and to contain the solution for $i \in [i_3, i_4]$, where:

$$i_3 = \min(i_1, i_t) - \gamma n_x/2 + 1, \quad i_4 = \max(i_2, i_t) + \gamma n_x/2. \quad (5.59)$$

Point-to-point communication is used to exchange data between neighbouring subdomains, i.e. $i_p \to \left\{ {}^{i_p+1, i_p<n_p-1}_{0, i_p=n_p-1} \right.$ and $i_p \to \left\{ {}^{i_p-1, i_p>0}_{n_p-1, i_p=0} \right.$, and one-to-all communication is used to exchange data from subdomains that contain the neighbourhood of the centre of the topography with the remaining subdomains. Proceeding in this way requires the following restriction on the number of subdomains, namely $n_p \leqslant 2/\gamma$; one-to-all communication restricts the location of the centre of the topography so that its neighbourhood covers as small a number of subdomains as possible; for example for $n_p = 2/\gamma$ the centre of the topography is desired to be $i_t = i_2$ so its neighborhood covers only two subdomains: i_p and $i_p + 1$. The amount of communication between subdomains is strictly dependent on the value of the summation parameter γ and has a large influence on the computational time. Good parallel efficiency is achieved for a problem containing 512×512 mesh points by setting $\gamma = 0.2$ and prescribing 8 subdomains; the computational time to convergence is reduced by a factor of between 6 and 7, compared to using a serial method, giving a

parallel efficiency gain in excess of 75 %.

For the case of two-dimensional flow over spanwise topography, the global Jacobian can be stored in memory and iteration performed efficiently using LU decomposition with partial pivoting library routines readily accessible via LAPACK, Anderson *et al.* (1999). For both two- and three-dimensional flows, generally up to 10 Newton iterations are required to reduce the residuals of the discrete equation set to a value below 10^{-6}.

5.3 Results

For the investigation which follows, flows with We up to and including cases where $\mathrm{We} = O(1/\varepsilon^2)$ are considered; the second term on the right hand side of equation (5.53) being significant. The system of the equations (5.21) - (5.24) contains five dimensionless parameters: ε, Re, Ca, We and θ. However the similarity of the results obtained by solving them as well as the physics of the problem, is dependent on three dimensionless groupings only: an inertia parameter $\mathrm{I} = \mathrm{Ca}^{1/3} \cdot \mathrm{Re}$, a gravity parameter $\mathrm{N} = \mathrm{Ca}^{1/3} \cdot \cot\theta$, Bertozzi & Brenner (1997), and an electric field parameter $\mathrm{W} = \mathrm{Ca}^{2/3} \cdot \mathrm{We}$, Tseluiko *et al.* (2008*b*).

To ensure the physical relevance of the results obtained, the characteristic dimensional parameters have to be estimated; film thickness and electric field strength are obtained as follows:

$$H_0 = \left(\frac{2\sigma \mathrm{Ca}}{\rho G_0 \sin\theta}\right)^{1/2}, \quad E_0 = \left(\frac{\mathrm{W}}{\varepsilon_e}\right)^{1/2} (2\sigma\rho G_0 \sin\theta)^{1/4}\, \mathrm{Ca}^{-1/12}. \qquad (5.60)$$

For the thin water film considered (fluid properties $\rho = 1000\mathrm{kg} \cdot \mathrm{m}^{-3}$, $\mu = 0.001\mathrm{Pa} \cdot \mathrm{s}$ and $\sigma = 0.07\mathrm{N} \cdot \mathrm{m}^{-1}$) for $\theta = 30^\circ$ and $\varepsilon_e = 8.85 \cdot 10^{-12}\mathrm{F} \cdot \mathrm{m}^{-1}$, typically $\varepsilon = 0.1$, $\mathrm{Ca} = \varepsilon^3/6 = 0.000167$ and $\mathrm{W} = 3.0$, which results in $H_0 = 6.9 \cdot 10^{-5}$ m and $E_0 = 6.15 \cdot 10^6 \mathrm{V} \cdot \mathrm{m}^{-1}$.

For results to be physically realisable in the laboratory, E_0 has to lie below the critical value for the dielectric breakdown of air; for standard atmospheric conditions involving a lightening discharge this value is approximately equal to $3 \cdot 10^6 \mathrm{V} \cdot \mathrm{m}^{-1}$, Laughton & Warne (2003), which is less than the value of E_0 calculated above.

The problem of interest requires a more subtle approach to the above and as such a more refined condition for determining the critical value for the dielectric breakdown of air and of other gases is needed. Accordingly, Paschen's law, established experimentally, see for example Meek & Craggs (1978) or Kuffel, Zaengl & Kuffel (2000), is invoked:

$$V_B = A\sqrt{P_A D} + BP_A D, \quad E_B = A\sqrt{P_A/D} + BP_A, \tag{5.61}$$

where V_B, E_B, D and P_A is the breakdown potential difference between electrodes, the generated electric field strength, the distance between electrodes and the pressure of the gas concerned, respectively; A and B are dimensional constants characteristic of the gas. Figure 5.2 shows the dependencies V_B vs. $(P_A \cdot D)$ and E_B/P_A vs. $(P_A \cdot D)$ for air with $A = 6.76 \cdot 10^4 \mathrm{V} \cdot (\mathrm{atm} \cdot \mathrm{m})^{-1/2}$ and $B = 2.47 \cdot 10^6 \mathrm{V} \cdot (\mathrm{atm} \cdot \mathrm{m})^{-1}$ based on expressions (5.61), which give an acceptable approximation in a range from 10^{-5} to 10^0 $(\mathrm{atm} \cdot \mathrm{m})$. It shows that for a distance of $D = 2 \cdot 10^{-4}\mathrm{m}$, which is greater than the film thicknesses $H_0 = 6.9 \cdot 10^{-5}\mathrm{m}$, and a pressure of $P_A = 1\mathrm{atm}$ an electric field strength of $E_B = 7.2 \cdot 10^6 \mathrm{V} \cdot \mathrm{m}^{-1}$ represents the dielectric breakdown limit; moreover for pressures larger than atmospheric the breakdown electric field strength is even larger: keeping $D = 2{\cdot}10^{-4}\mathrm{m}$ a value $P_A = 2\mathrm{atm}$ results in $E_B = 1.2{\cdot}10^7 \mathrm{V}{\cdot}\mathrm{m}^{-1}$. Hence, since $E_0 < E_B$ for the results presented in this Chapter, they are realisable in the laboratory and thus of physical as well as academic interest.

Attention is focused initially on two-dimensional electrified film flows involving spanwise topography, in which the proposed problem formulation and method

of solution is compared against related previous work and for a wider range of Reynolds numbers than has been considered before. This is followed by a systematic investigation of both inertia and a normal electric field on three-dimensional film flow over localised topographical features.

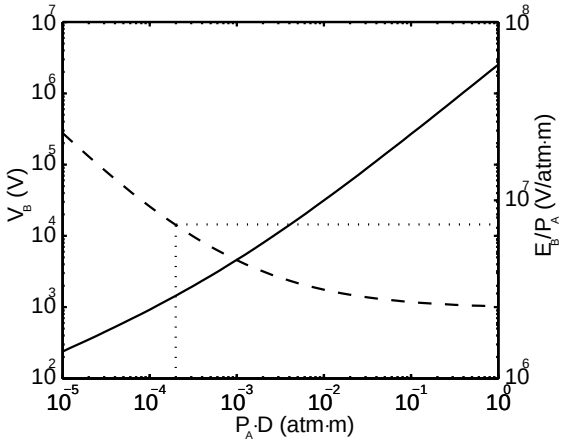

FIGURE 5.2: V_B (full line) and E_B/P_A (dashed line) for the dielectric breakdown of the air. The point at which $D = 2 \cdot 10^{-4}$ m, $P_A = 1$ atm and $E_B = 7.2 \cdot 10^6 \mathrm{V} \cdot \mathrm{m}^{-1}$ is denoted by the dotted lines.

5.3.1 Two-dimensional flow

Since a direct comparison is to be made with earlier work it is essential to outline the differences between the approaches/formulations used. In the work of Tseluiko & Blyth (2009) inertia is accounted for within a standard lubrication model by the inclusion of an additional term of the form $\frac{\partial}{\partial x}\left(\frac{8}{15}\varepsilon \mathrm{Re} h^6 \frac{\partial h}{\partial x}\right)$: first derived by Benney (1966), it has appeared many times subsequently in the context of thin films, Lin (1974); Nakaya (1975); Chang (1986), obtained via a perturbation analysis and long-wave expansion of the unknowns of the problem on the basis that $\varepsilon \ll 1$. This model, which for comparison purposes is henceforth referred as lubrication with inertia (LUBI), in accounting for inertia does so only in terms of the first-order dynamics of the perturbation analysis: the Reynolds number therefore is strictly $O(1)$. In the current DAF model a perturbation analysis is not performed and the long-wave approxima-

tion is used to determine the leading terms to $O(1)$ and $O(\varepsilon)$ that are solved in a coupled way: as a result there is no $O(1)$ restriction on Re, indeed for small ε and $|s_0|$ it provides accurate results even for values of Re up to 100. The remainder of the terms in the LUBI model are the same as those in the standard lubrication model and therefore for the degenerate case $\mathrm{Re} = 0$ both models are equivalent.

For two-dimensional flow the dimensionless steady-state LUBI model for the film thickness, h, is:

$$\frac{\partial}{\partial x}\left[\frac{2}{3}h^3 + \frac{8}{15}\varepsilon \mathrm{Re} h^6 \frac{\partial h}{\partial x} - \frac{2}{3}\varepsilon \cot\theta h^3 \frac{\partial f}{\partial x}\right.$$

$$\left. + \frac{\varepsilon^3}{3\mathrm{Ca}} h^3 \frac{\partial^3 f}{\partial x^3} + \frac{1}{3}\varepsilon \mathrm{We} h^3 \frac{\partial}{\partial x}\left(\frac{\partial \varphi}{\partial z}\right)^2 |_{z=f}\right] = 0, \tag{5.62}$$

where ε, Re, x, θ and We equate to δ, R, ξ, β and W_e in Tseluiko *et al.* (2008*a*,*b*); Tseluiko & Blyth (2009). Note that in addition, in order to compare with their results Ca and W correspond to $\delta^3 C'$ and W_e' Tseluiko *et al.* (2008*a*,*b*) and to $\delta^2 C'$ and $\delta W_e'$ Tseluiko & Blyth (2009), respectively (in contrast to $\mathrm{Ca} = \varepsilon^3/6$ and $\mathrm{W} = \mathrm{Ca}^{2/3}\mathrm{We}$ for the remaining results).

In each of the above three studies, the Maxwell stress in equation (5.62) is obtained using complex variable theory, which is applicable in two dimensions only, and has a form similar to (5.53), namely:

$$\varepsilon \mathrm{We}\left(\frac{\partial \varphi}{\partial z}\right)^2 |_{z=f} \approx \varepsilon \mathrm{We} + 2\varepsilon^2 \mathrm{We}\mathcal{H}\left[\frac{\partial f}{\partial x}\right](x), \tag{5.63}$$

where $\mathcal{H}$ is the Hilbert transform operator defined as:

$$\mathcal{H}[g](x) = \frac{1}{\pi} PV \int_{-\infty}^{\infty} \frac{g(\widehat{x})}{x - \widehat{x}} d\widehat{x}, \tag{5.64}$$

with $g(x) = \partial f/\partial x$ and PV denoting the principal value of the integral. For

periodic functions the Hilbert operator takes the particular form:

$$\mathcal{H}\left[g\right](x) = \frac{1}{l_p} PV \int_0^{l_p} g\left(\widehat{x}\right) \cot\left[\frac{\pi\left(x-\widehat{x}\right)}{l_p}\right] d\widehat{x}. \tag{5.65}$$

In two dimensions, the Fourier operator, $\mathcal{E}\left[f-1\right]$:

$$\mathcal{E}\left[f-1\right](x) = \frac{1}{l_p} \int_0^{l_p} (f-1) \sum_{m=1}^{\infty} \chi_m \lambda_m \cos\left[\lambda_m\left(x-\widehat{x}\right)\right] d\widehat{x}, \tag{5.66}$$

and the Hilbert operator, $\mathcal{H}\left[\partial f/\partial x\right]$, are equivalent; for completeness a proof of this is provided in Appendix E.

Figure 5.3 shows predicted free-surface profiles for the case of gravity-driven, electrified film flow over a narrow, spanwise trench topography with $\theta = 30°$, $\varepsilon = 0.1$, Re $= 50$, Ca $= 0.000167$, $l_t = 2$, $x_t = 110$, $|s_0| = 0.25$ and $l_p = 160$. Profiles for the cases W $= 1.5$ and W $= 3.0$ are presented, obtained using the current hydrodynamic model with the Maxwell stress evaluated via both the Fourier solution of the Laplace problem and the Hilbert form. To illustrate the effect of N^f, the number of Fourier terms taken, and choice of γ, mesh-independent solutions were obtained on an ultra-fine grid, $n_x = 3072$, and with a small enough topography steepness parameter, $\delta = 0.001$ – the one used in Chapter 3. Figures 5.3(a) and (b) show the effect of N^f, when $\gamma = 0.1$, on the accuracy of the predicted free-surface profile: $N^f = 100$ terms is sufficient to produce a solution in excellent agreement with its Hilbert counterpart. Figures 5.3(c) and (d), on the other hand, confirm that with $N^f = 200$ terms a value of $\gamma = 0.1$ yields the same agreement. Accordingly, the predictions reported henceforth were obtained with $N^f = 200$ and a sufficiently large value of γ: for the two- and three-dimensional flow problems considered these were $\gamma = 1.0$ and $\gamma = 0.2$, respectively; in each case δ has the value 0.001 unless stated otherwise. As discussed in Tseluiko *et al.* (2008*b*) and shown in Figure 5.3, the main effect of increasing W from 0 to 1.5 is the formation of a sharper, larger capillary ridge and deeper free-surface depression accompanied by the

formation of small wavelength free-surface variations upstream of the trench. Increasing W further to 3.0 suppresses the capillary ridge altogether.

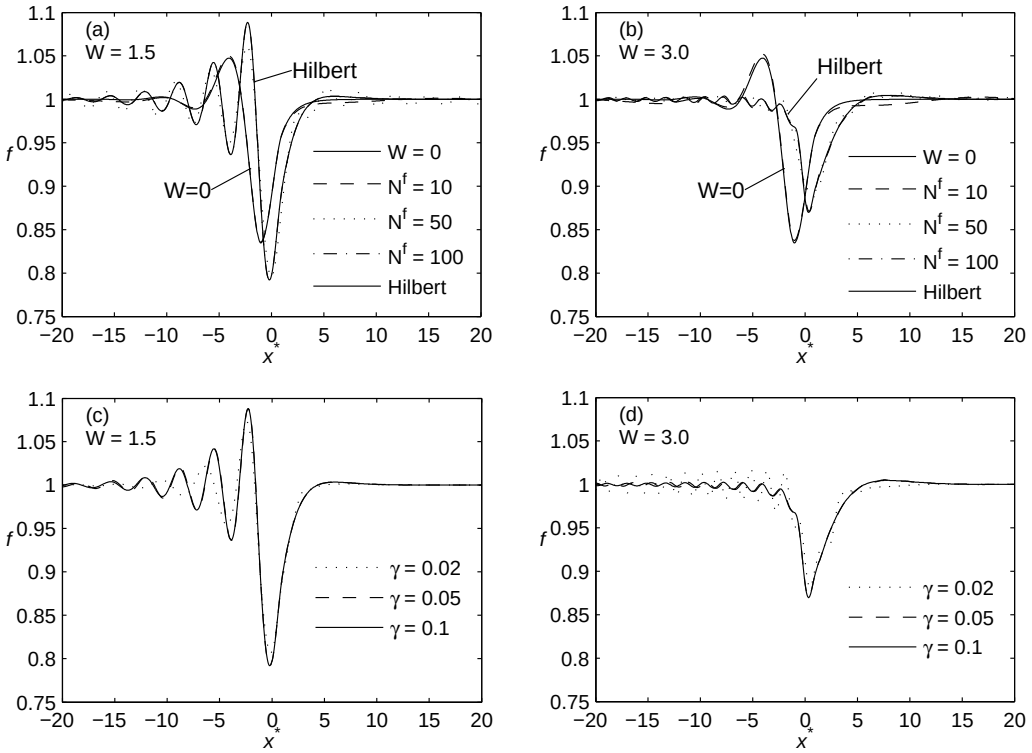

FIGURE 5.3: The effect of the value of N^f for $\gamma = 0.1$ (top) and γ for $N^f = 200$ (bottom) on DAF predicted free-surface profiles for thin film flow over a spanwise narrow trench topography ($\theta = 30^o$, Re = 50, $l_t = 2$, $|s_0| = 0.25$); W = 1.5 (left) and W = 3.0 (right). The corresponding results obtained with the Hilbert integral operator (5.65) are included for comparison purposes, and found to be in excellent agreement, as is the solution when W = 0. Flow is from left to right.

Figure 5.4 revisits the problem considered by Tseluiko *et al.* (2008*b*), their Figure 7, namely that of a vertical plane ($\theta = 90°$) for electrified film flow over both step-down and step-up topography forming a spanwise wide trench ($\varepsilon = 0.1$, Re = 0, Ca = 0.001, $l_t = 30$, $|s_0| = 2.0$, $l_p = 90$ and $x_t = 45$); note that for reasons of consistency, the step topography in this particular instance only is defined by hyperbolic tangent, as opposed to arctangent, functions with a steepness factor $\delta = 0.2$. All of the results shown in Figure 5.4 are grid-independent and are obtained with $n_x = 3000$ using either the DAF model for Re = 0 or the LUBI one in tandem with either the Fourier or Hilbert

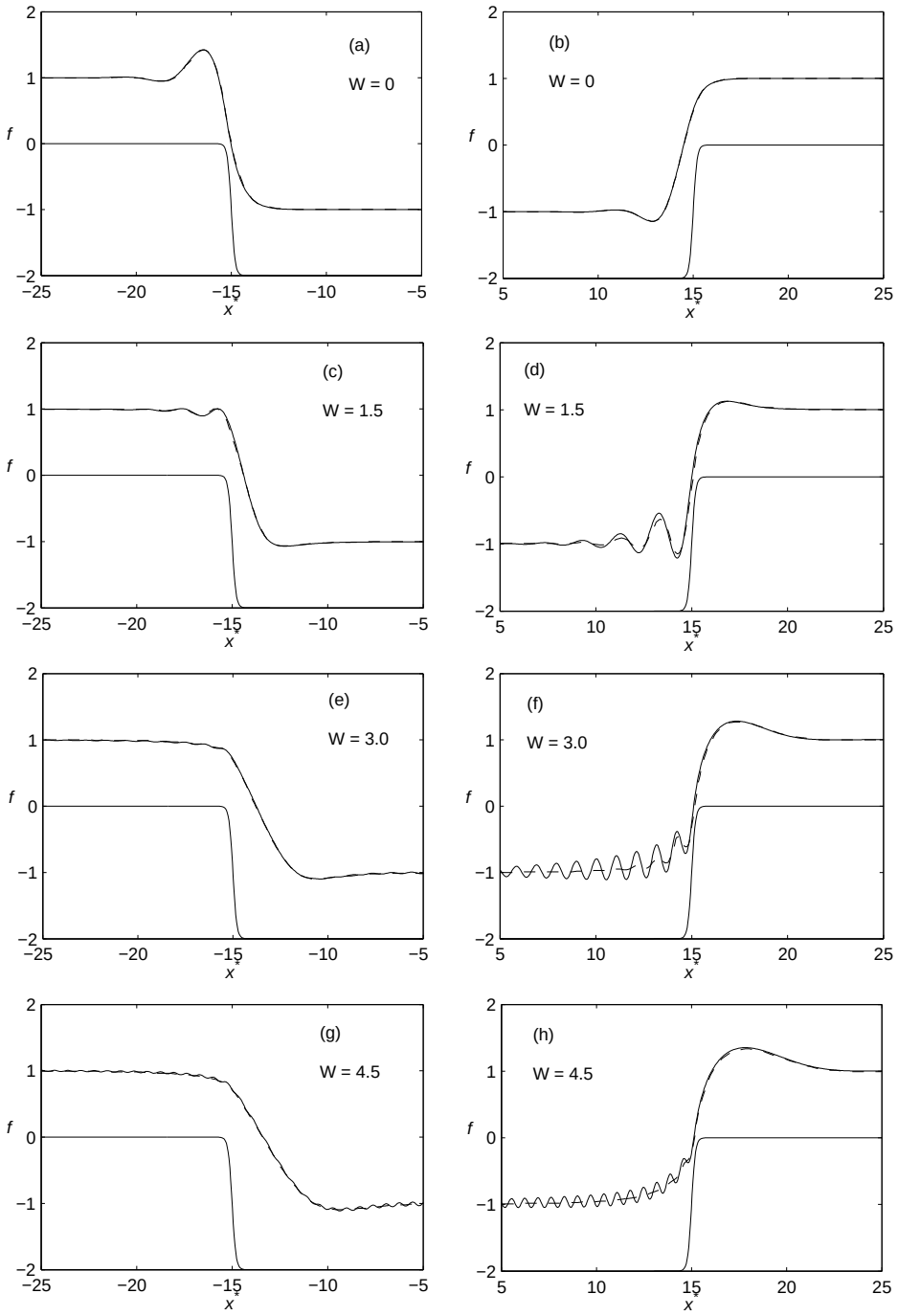

FIGURE 5.4: Comparison of predicted LUBI free-surface profiles for electrified thin film over a spanwise wide trench topography ($\theta = 90^o$, Re = 0, $l_t = 30$, $|s_0| = 2.0$): (dashed line) as in Figure 7 of Tseluiko *et al.* (2008*b*); (solid line) present work. (a), (b) W = 0; (c), (d) W = 1.5; (e), (f) W = 3.0; (g), (h) W = 4.5. Flow is from left (step-down side) to right (step-up side).

form for the Maxwell stresses. For the step-down case, increasing the electric field suppresses the capillary ridge and leads to a broader depression beyond the step; while for the step-up case increasing W leads to the emergence of a downstream free-surface hump and the amplification of the small wavelength free-surface disturbances upstream of both the step-down and step-up; the nature and occurrence of these latter oscillations is a function of the competition between the geometry (topography height and steepness) producing the free-surface curvature and surface tension tending to oppose it, see for example Kalliadasis *et al.* (2000) and the experimental work of Stillwagon & Larson (1988, 1990). Note that while the step-down predictions agree well with those of Tseluiko *et al.* (2008*b*), the step-up ones do not, showing greater divergence for larger values of W; contact with the authors concerned and further investigations by them, Blyth (2010), established the validity of the current predictions.

Figures 5.5 and 5.6 compare predicted free-surface profiles against the only other previously reported solutions of inertial, electrified thin film flow over topography, namely those of Tseluiko & Blyth (2009) for flow with $\varepsilon = 0.2$, Ca $= 0.04$, $\theta = 30^{\circ}$, $n_x = 1024$ over a periodically wavy substrate defined as $s(x^*) = s_0 \sin(2\pi x^*/l_p - \pi/2)$ with amplitude $s_0 = 1.0$ and wavelength $l_p = 2\pi$. Cases of inertial flow in the absence of an electric field (W $= 0$) are considered first in Figures 5.5(a)-(f), where DAF and LUBI solutions are contrasted against the solutions of the full N-S equations, obtained as in Scholle *et al.* (2008). All three solutions are indistinguishable when Re $= 0$; however, increasing Re to 10 and then 30 results in a growing discrepancy between the LUBI solution and the other two. The reason for the excellent agreement between the DAF and N-S solutions can be explained with reference to Figures 5.5(b), (d) & (f): the steamline plots reveal the unidirectional nature of the underlying flow in all three instances and thus the appropriateness of the assumed classical Nusselt like velocity profile underpinning the DAF model.

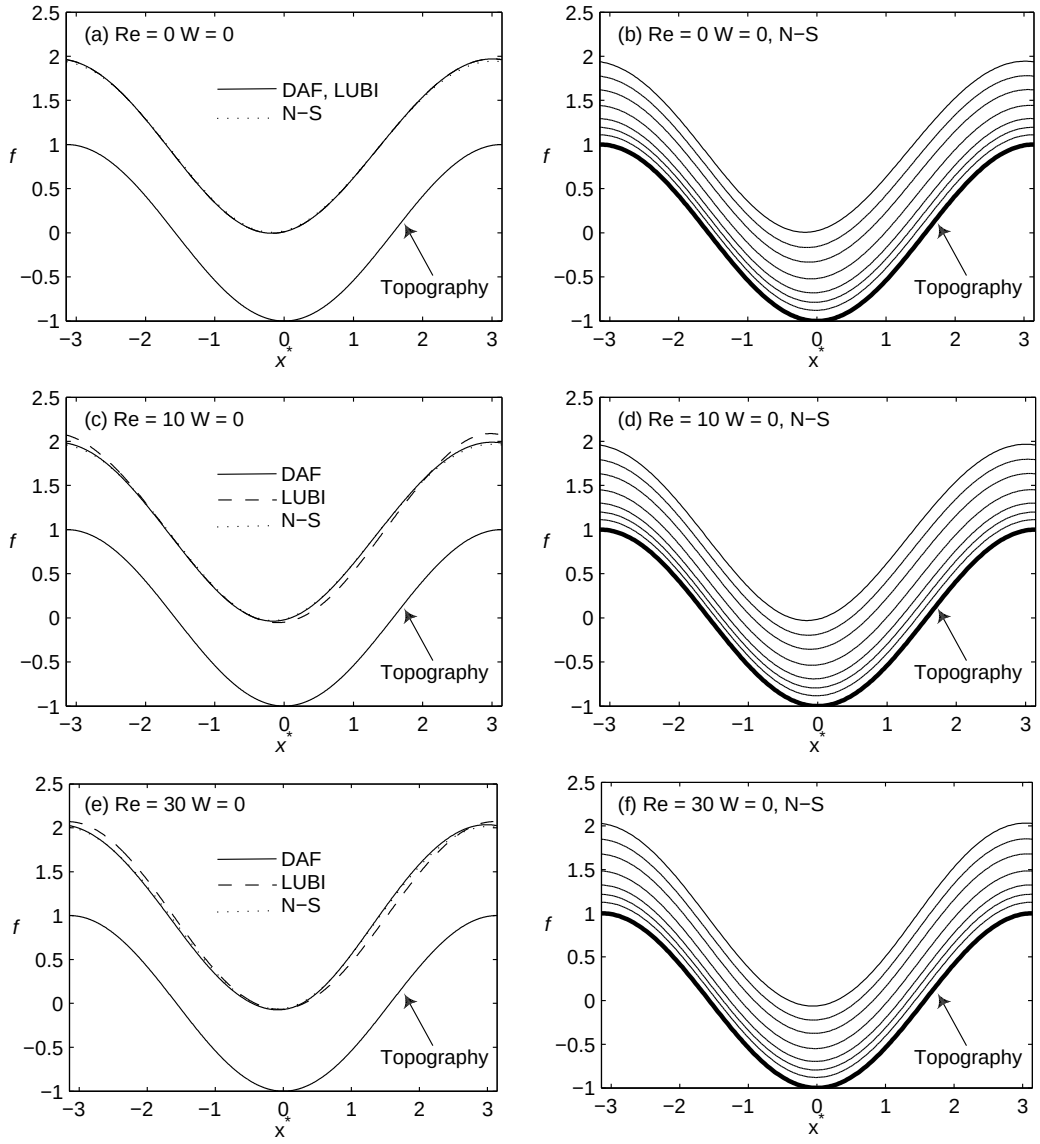

FIGURE 5.5: Flow over a spanwise wavy topography (wavelength $l_p = 2\pi$, amplitude $s_0 = 1.0$), as in Figure 9 of Tseluiko & Blyth (2009), in the absence of an electric field. Comparison between DAF, LUBI and N-S predictions: (a), (b) Re = 0; (c), (d) Re = 10; (e), (f) Re = 30. Flow is from left (free-surface profile) to right (streamlines showing the flow structure)

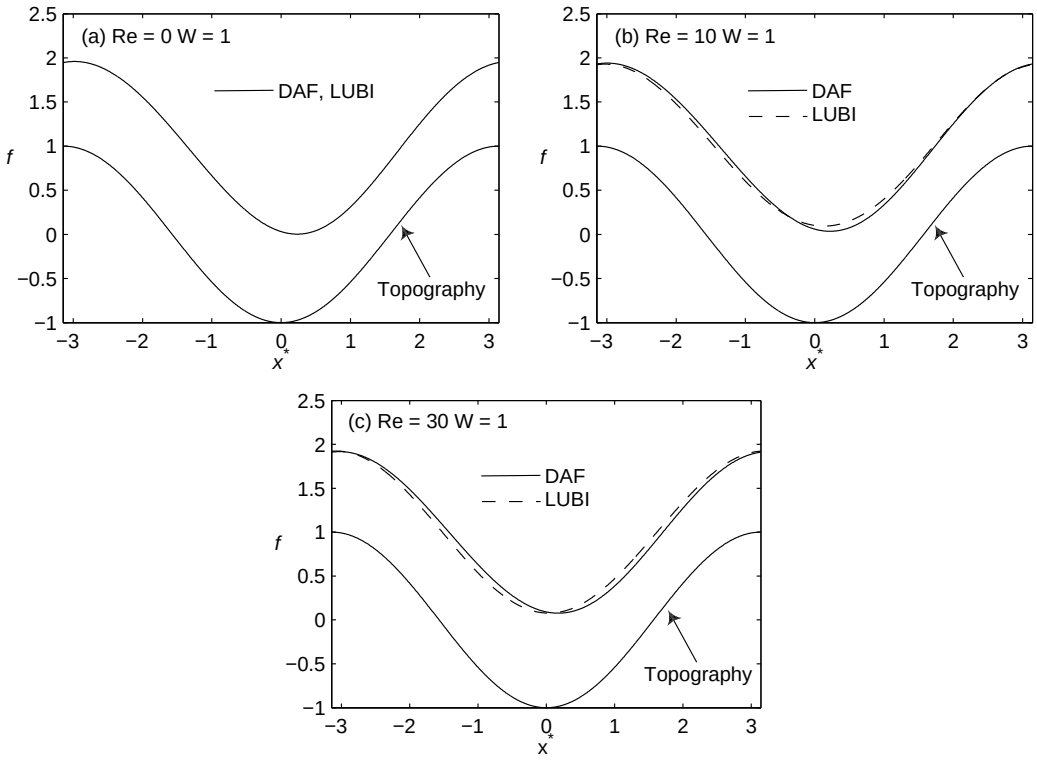

FIGURE 5.6: Flow over a spanwise wavy topography (wavelength $l_p = 2\pi$, amplitude $s_0 = 1.0$), as in Figure 9 of Tseluiko & Blyth (2009), in the presence of an electric field, W = 1. Comparison between DAF and LUBI predicted free-surface profiles: (a) Re = 0; (b) Re = 10; (c) Re = 30. Flow is from left to right.

The flow structure present also agrees with the findings of Scholle *et al.* (2008), who predict that no eddy, inertial or kinematic, is present when $h \ll 1$. The discrepancy for Re ≥ 10 in the LUBI predictions is attributable to the fact that for this model, Re must be strictly O(1) or smaller. Figures 5.6(a)-(c) compares the free-surface profiles obtained with the DAF and the LUBI models for electrified film flow; in particular the problem considered in Figure 9 of Tseluiko & Blyth (2009) with W = 1 (note that in their paper they use $W_e^{'} = \mathrm{W}/\varepsilon = 5$). Once again, although the solutions obtained with the two different approaches are indistinguishable for Re = 0, discrepancies between the two begin to emerge for Re > 0 for the reason discussed above.

Figures 5.7 and 5.8 extend the results of Tseluiko *et al.* (2008*a*,*b*), and Tseluiko & Blyth (2009) by considering the combined effects of inertia and electric field strength on gravity-driven, electrified film flow over step-down, step-up and trench topography ($\theta = 30^{\circ}$, $\varepsilon = 0.1$ and Ca = 0.000167). As previously, the step topographies are approximated by the upstream and downstream portions of a wide spanwise trench ($l_t = 80$, $|s_0| = 0.25$, $l_p = 200$, $x_t = 120$) while the spanwise narrow trench case has $l_t = 2$, $|s_0| = 0.25$, $l_p = 160$ and $x_t = 110$. Fine grids with $n_x = 4096$ and $n_x = 3072$ were used to generate grid-independent solutions for the wide and narrow trenches, respectively.

For the step-down cases, Figures 5.7(a) and (b), increasing Re to 50 leads to only a slight increase in the size of the capillary ridge, whereas increasing the electric field strength has a much greater impact on the overall free-surface profile. Increasing W to 1.5 leads to a downstream displacement and narrowing of the capillary ridge and to a broader and deeper free surface trough just upstream of the step-down. Increasing W further to 3.0 is sufficient to completely suppress the capillary ridge; this is accompanied by a widening and deepening the free-surface trough. For the step-up cases, Figures 5.7(c) and (d), increasing Re to 50 in the absence of an electric field results in a slightly deeper free-surface trough, just upstream of the step-up, while increasing W

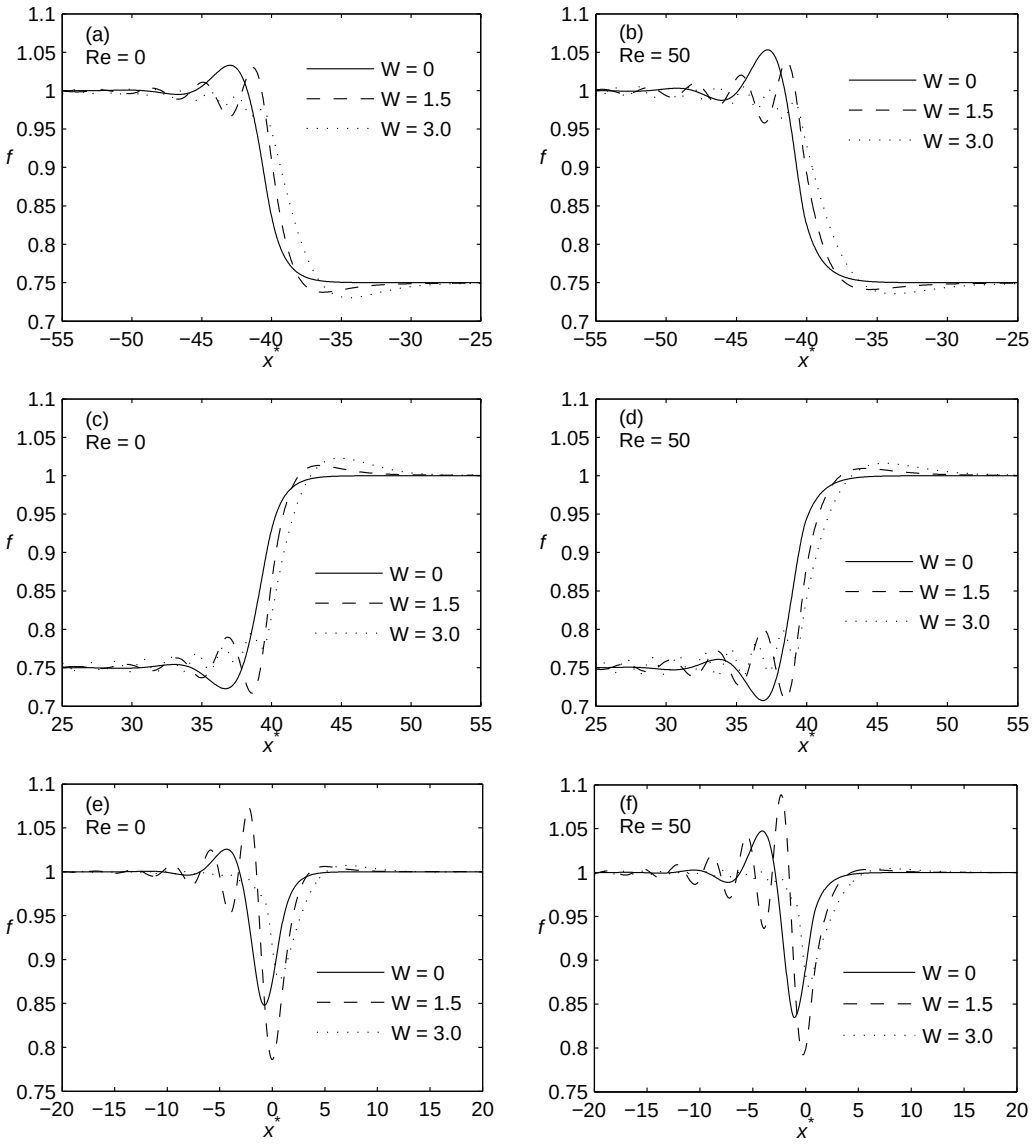

FIGURE 5.7: Predicted free-surface profiles for electrified film flow ($W = 0, 1.5, 3.0$), $Re = 0$ (left) and $Re = 50$ (right) over: (a), (b) the step-down and (c), (d) step-up part of a spanwise wide trench ($l_t = 80$ and $|s_0| = 0.25$); (e), (f) a spanwise narrow trench ($l_t = 2$ and $|s_0| = 0.25$). Flow is from left to right.

to 1.5 leads to a downstream displacement and narrowing of the free-surface trough together with an enhancement and downstream displacement of the free-surface hump. In this case, increasing W further to 3.0 results in the formation of small wavelength standing waves and the disappearance of the free-surface trough, upstream of the step-up, and a further enhancement and downstream displacement of the hump. The flow over the trench topography, Figures 5.7(e) and (f), is only slightly affected by increasing inertia in the absence of an electric field, resulting in slight enhancement of both the capillary ridge and free-surface depression. However, it is much more sensitive to the value of W than the step cases: increasing W to 1.5 leads to significant amplification of both the capillary ridge and free-surface depression, while increasing W further to 3.0 gives rise to almost complete suppression of the capillary ridge and a diminution of the free-surface depression.

The results of a far more detailed parameter study into the effects of Re and W on the free-surface profiles associated with the step-up and step-down sides of the wide trench problems considered in Figure 5.7, are summarised in Figure 5.8. Figure 5.8(a) shows that for the step-down case, for a fixed Re, the predicted maximum value of the capillary ridge increases monotonically with increasing W for $\mathrm{W} \lesssim 1$ but then diminishes more rapidly and again monotonically for $\mathrm{W} \gtrsim 1$; this is in contrast to the case of $|s_0| = 2.0$ considered by Tseluiko *et al.* (2008*b*), their Figure 8(a), for which only the effect of a diminishing capillary ridge was observed. It shows clearly that the larger the value of Re the larger is the W value required to suppress the inertially-enhanced free-surface disturbances. For example, complete suppression of the capillary ridge (corresponding to a maximum value $f = 1$) for Re = 0, 10, 30 and 50 is achieved by values of W = 2.11, 2.13, 2.23 and 2.41, respectively. In the case of a step-up, Figure 5.8(b), the maximum value corresponds to the free-surface hump that appears just downstream of it. In contrast to the step-down cases, the maximum value of the hump remains more or less unaffected by the value

of the Re for $W \lesssim 1$; after which point the curves diverge while continuing to increases monotonically above $f = 1$ beyond $W > 1$. In the step-up case, increasing inertia acts to reduce the size of the electric-field induced free-surface amplification.

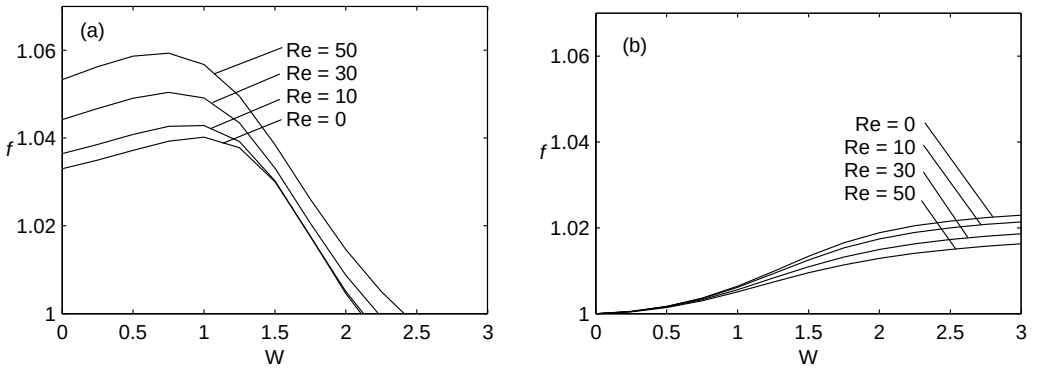

FIGURE 5.8: The effect of electric field strength on predicted maximum values of the capillary ridge and free-surface hump for thin film flow over: (a) the step-down part of a spanwise wide trench; (b) the step-up part of a spanwise wide trench. Results obtained for $W \in [0, 3.0]$, Re = 0, 10, 30 and 50, $l_t = 80$ and $|s_0| = 0.25$.

Figure 5.9 considers the effect of W on the various stress contributions to the fluid pressure for zero Reynolds number flow over the narrow trench topography considered in Figure 5.8(e). Since the hydrostatic pressure is only $O(\varepsilon)$, the free-surface profile for $W > 0$ is dominated by the competition between the O(1) capillary and Maxwell stress terms. For $W = 1.5$, the large negative Maxwell stress just upstream of the trench requires a compensating large, positive capillary pressure which acts so as to enhance the capillary ridge. Similarly, the large positive Maxwell stress peak over the trench requires a large negative capillary pressure to counterbalance it which enhances the size of the free-surface trough. For $W = 3.0$, the significantly reduced Maxwell stresses upstream of the topography lead to much smaller capillary pressures (smaller even than for the $W = 0$ case) resulting in an effective suppression of the capillary ridge.

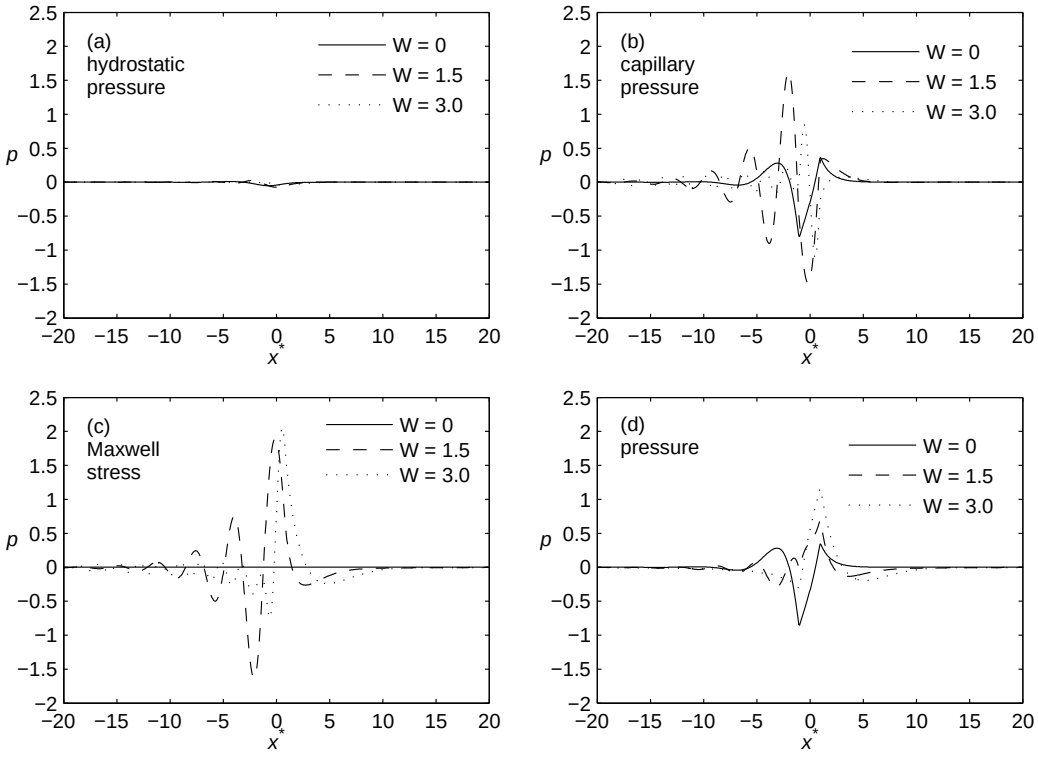

FIGURE 5.9: Predicted contributions to the overall pressure for different electrified strengths, W = 0, 1.5 and 3.0, when Re = 0, for thin film flow over the spanwise narrow trench of Figure 5.7(e): (a) hydrostatic pressure; (b) capillary pressure; (c) Maxwell stress; (d) overall pressure. Flow is from left to right.

5.3.2 Three-dimensional flow

Turning now to the problem of three-dimensional flow, use is made of the electrohydrodynamic problem formulation of Section 5.1 to investigate a series of problems associated with the flow of a thin electrified film over a localised trench topography. The substrate, $l_p = w_p = 100$, containing the trench, aspect ratio $A = w_t/l_t$, $l_t = 2$, $|s_0| = 0.25$, centred at $x_t = y_t = 50$, is inclined at $\theta = 30^\circ$ to the horizontal ($\varepsilon = 0.1$, Ca $= 0.000167$). The results presented are all mesh and formulation parameter independent having been obtained on a computational grid having $n_x = n_y = 512$ cells in each coordinate direction.

Figures 5.10 and 5.11 analyse the effect of W on the transition of the flow from a three- to an essentially two-dimensional one through the centre of the topography in the steamwise direction, as the trench aspect ratio $A = w_t/l_t$ is increased. Figure 5.10(a)-(f) shows the free-surface disturbance that is generated for the cases A = 5 and 10 when W = 0, 1.5 and 3.0. As reported in Gaskell *et al.* (2004*b*), for W = 0 as shown in Figures 5.11(a) and (b), decreasing A leads to a much reduced upstream capillary ridge and the formation of a small downstream surge caused by liquid entering the sides of the trench. Increasing W to 1.5 leads to a significant amplification of both the capillary ridge, just upstream of the trench, and the free-surface depression over the trench. This is accompanied by the disappearance of the downstream surge for $A = 1$. Increasing W further to 3.0 causes a general diminution in the magnitude of the free-surface disturbances; this is seen most clearly by the free-surface profiles given in Figures 5.11(e) and (f). Shown for comparison purposes on each of the plots is the free-surface disturbance for infinite A, that is an equivalent spanwise trench.

Figure 5.12 shows the effect of gradually increasing W, for Re = 0, in steps of 0.5 from 0 to 3.5, on the free-surface disturbances generated by flow over a square trench topography, $A = 1$. It reveals that increasing W from 0 to 0.5

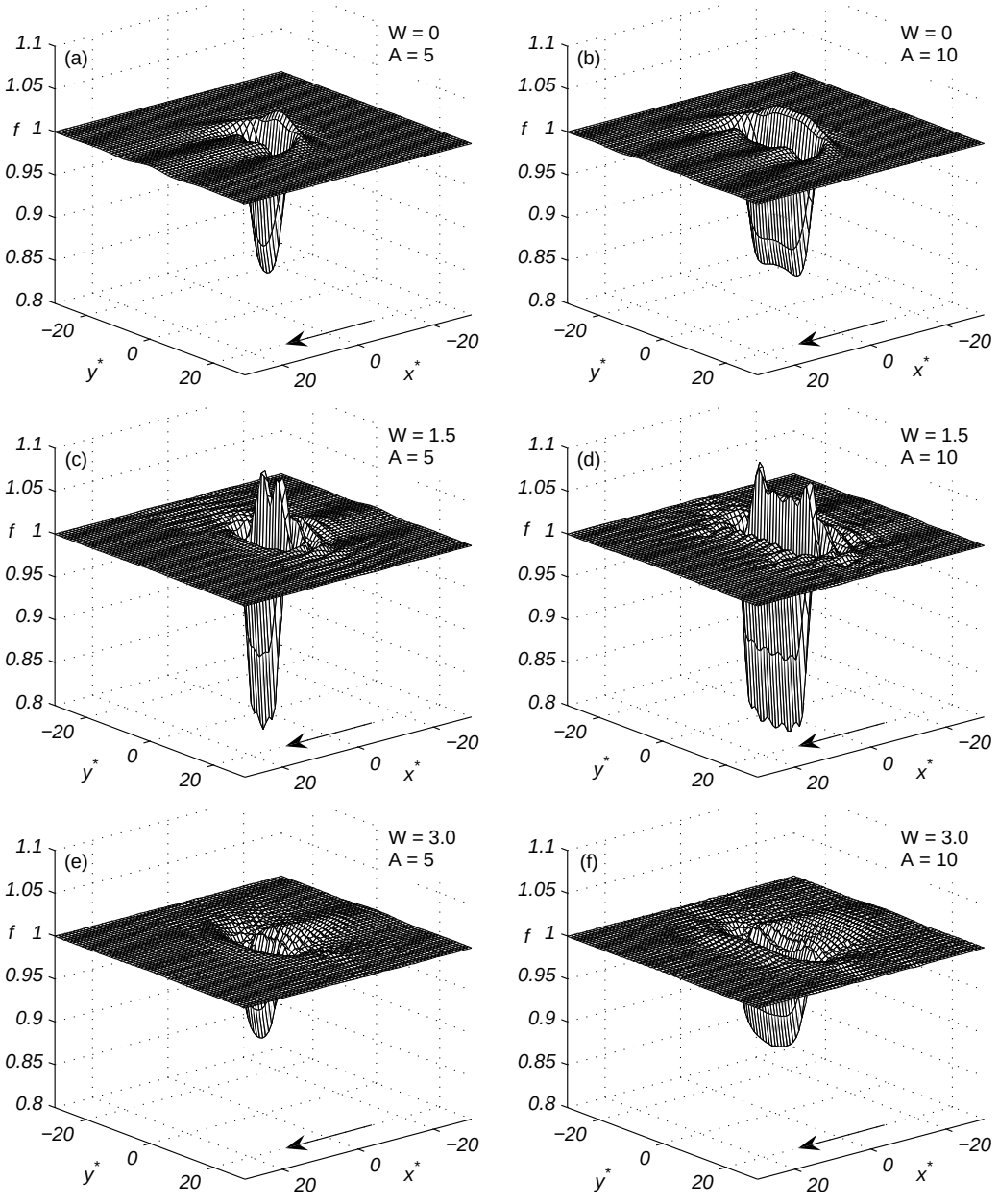

FIGURE 5.10: Three-dimensional predicted surface plots of the disturbance resulting from film flow, Re = 0, over a localised rectangular trench topography, $l_t = 2$ and $|s_0| = 0.25$, showing the effect of aspect ratio, $A = w_t/l_t$. From top to bottom, $\mathrm{W} = 0, 1.5, 3.0$; $A = 5$ (left) and $A = 10$ (right). The arrow indicates the direction of flow.

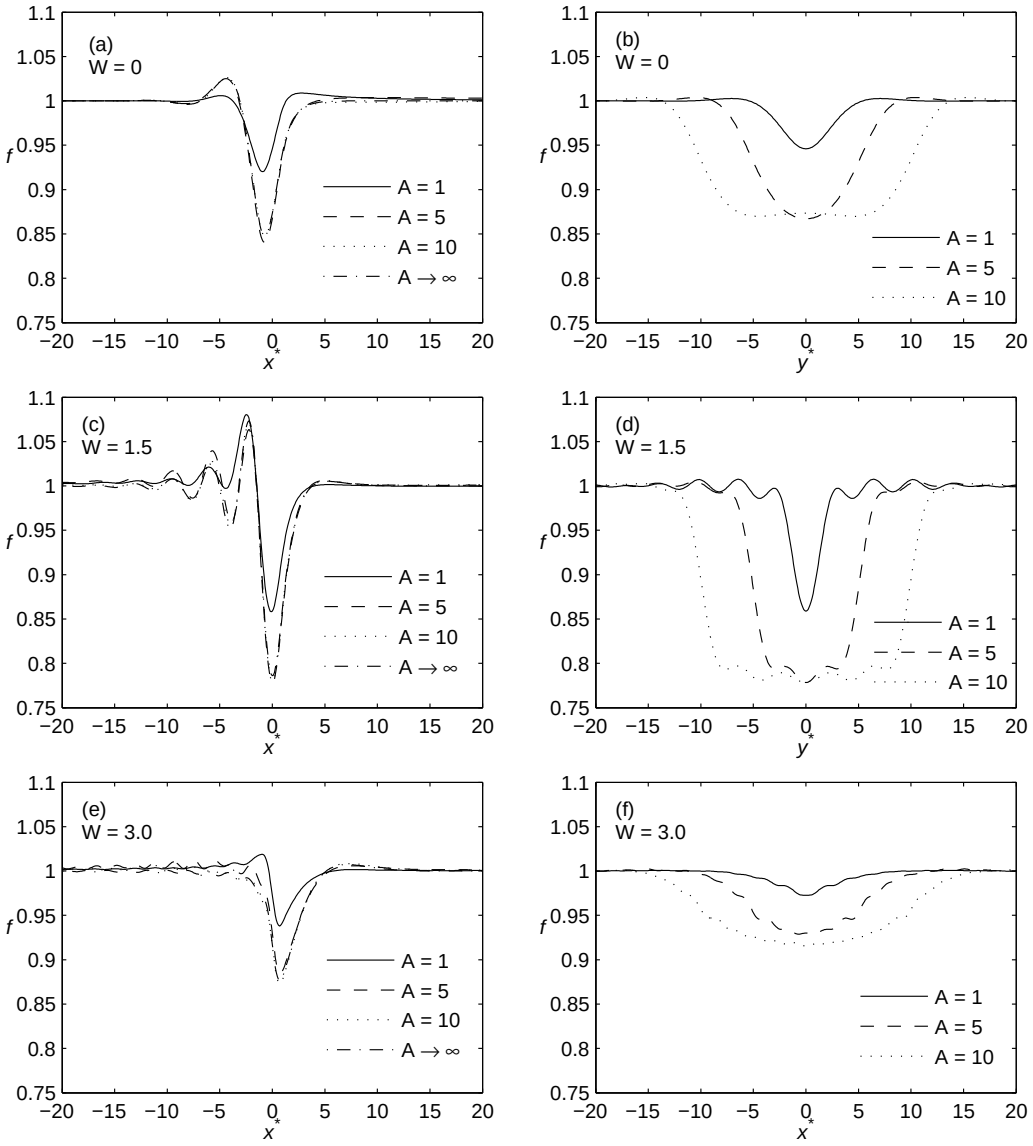

FIGURE 5.11: Streamwise (left) and spanwise (right) predicted free-surface profiles through the centre of the localised rectangular trench topography of Figure 5.10, showing the effect of aspect ratio, $A = w_t/l_t$. From top to bottom, W $= 0, 1.5, 3.0$. The streamwise profile obtained when A is infinite, that is the corresponding spanwise flow, is shown as a comparison.

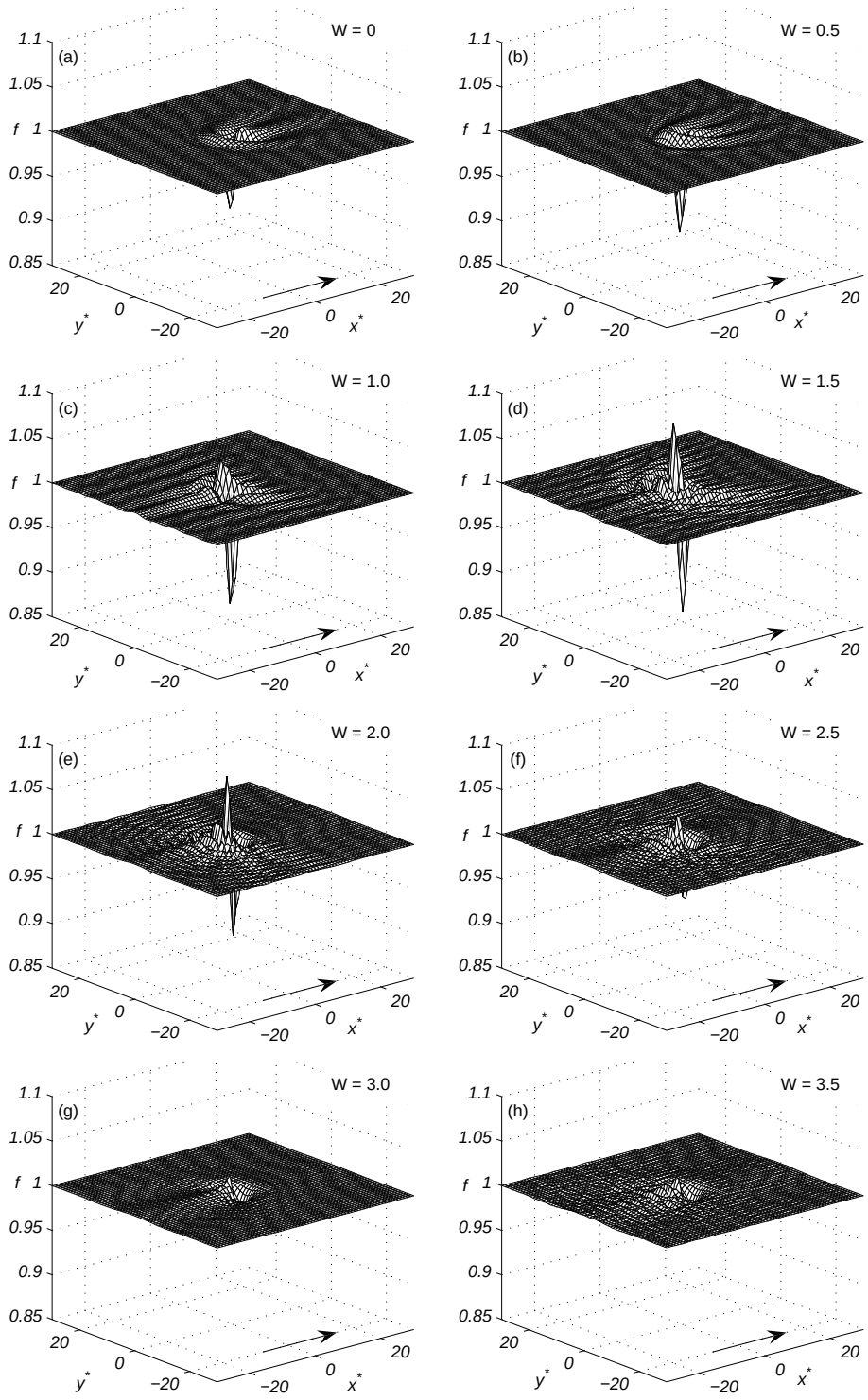

FIGURE 5.12: Three-dimensional predicted surface plots of the disturbance resulting from film flow, Re = 0, over a localised square trench topography, $l_t = w_t = 2$ and $|s_0| = 0.25$: W = (a) 0, (b) 0.5, (c) 1.0, (d) 1.5, (e) 2.0, (f) 2.5, (g) 3.0 and (h) 3.5. The arrow indicates the direction of flow.

causes the horseshoe-shaped disturbance typical of such flows to broaden in the spanwise direction, accompanied by enhancement of the upstream capillary ridge and a diminution of the downstream surge. As in the two-dimensional spanwise trench case, Figure 5.7(e), increasing W beyond 0.5 leads to a significant amplification of both the free-surface peak and trough. This is seen particularly clearly for $W = 1.5$, where the maximum non-dimensional height of the free surface increases from 1.01 (for $W = 0$) to 1.08 and the minimum free-surface height decreases from 0.89 to 0.86. For $W \geqslant 1$ the familiar comet tail and bow-wave disturbances have all but disappeared. In contrast, increasing W from 1.0 to 2.0 causes the upstream capillary ridge to grow in magnitude and at $W \approx 1.5$ a second capillary ridge is formed upstream of the first one. Beyond $W = 1.5$ the magnitude of the primary free-surface peaks and troughs are reduced and become more sharply focussed. For $W = 3.5$ the free-surface disturbances have been effectively planarised with maximum and minimum non-dimensional free-surface heights of just 1.02 and 1.05, respectively. The effect of W on the magnitude of the free-surface disturbances are shown more clearly by the streamwise and spanwise free-surface profiles shown in Figure 5.13.

Next the same sequence of events is considered but this time for the case $Re = 50$. The three cases shown in Figures 5.14 and 5.15 can be compared directly with their $Re = 0$ counterparts in Figures 5.12 and 5.13. Clearly, increasing W has a much larger influence than increasing Re and these are shown more distinctly via the corresponding streamwise and spanwise free-surface profiles through the centre of the topography. In essence, increasing inertia when the value of W is fixed simply results in a slightly greater minimum streamwise depression across the trench that is shifted upstream. As noted in Subsection 5.3.1 for the case of two-dimensional flow, free-surface disturbances in electrified films arise due to the competition between the capillary and Maxwell stresses that act in opposition to each other.

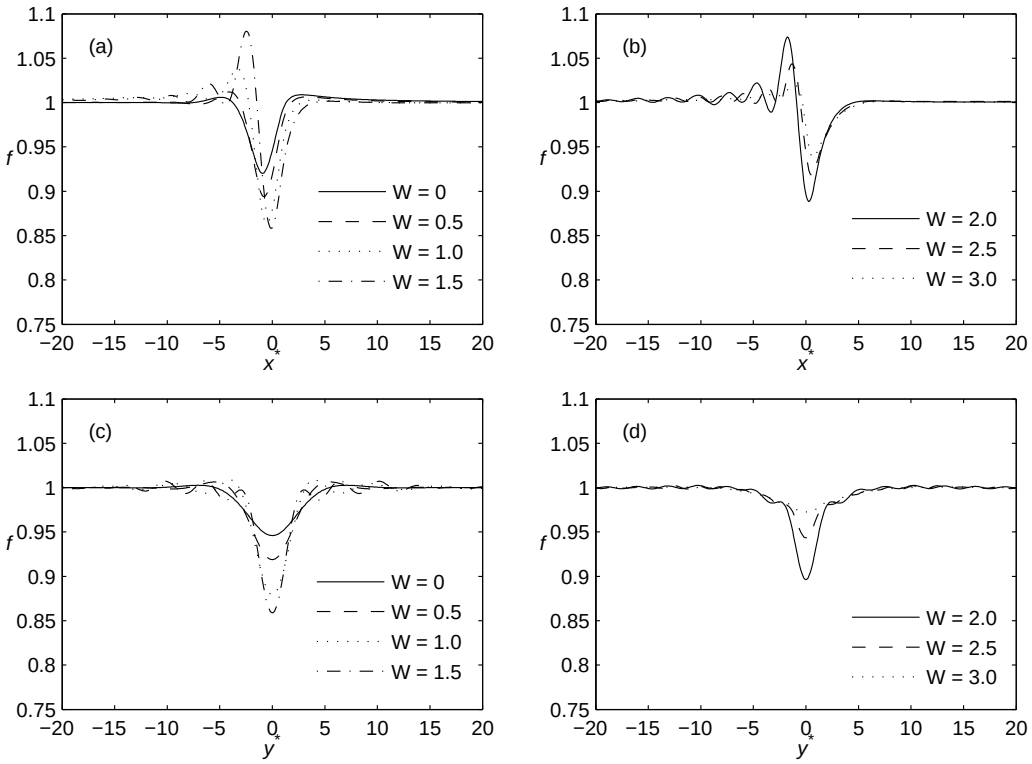

FIGURE 5.13: Streamwise (top) and spanwise (bottom) predicted free-surface profiles through the centre of the localised square trench topography of Figure 5.12: (a), (c) W = 0, 0.5, 1.0 and 1.5; (b), (d) W = 2.0, 2.5 and 3.0.

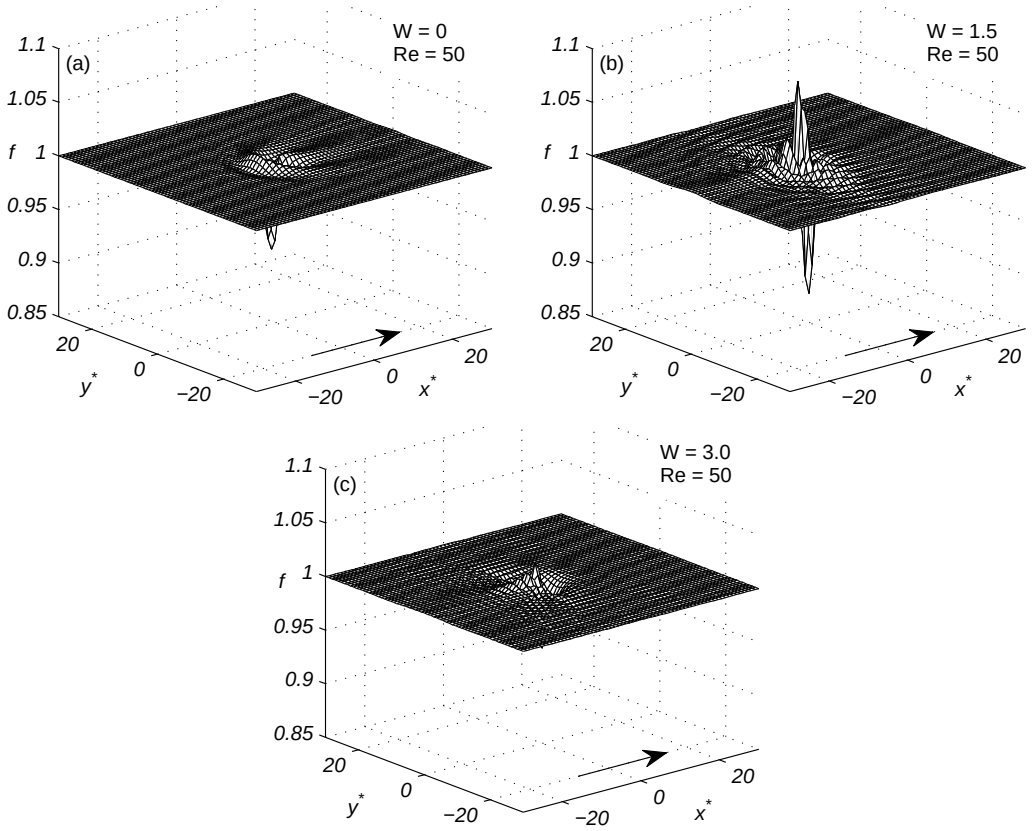

FIGURE 5.14: Three-dimensional predicted surface plots of the disturbance resulting from film flow, Re = 50, over a localised square trench topography, $l_t = w_t = 2$ and $|s_0| = 0.25$: from top to bottom, W $= 0, 1.5, 3.0$. The arrow indicates the direction of flow.

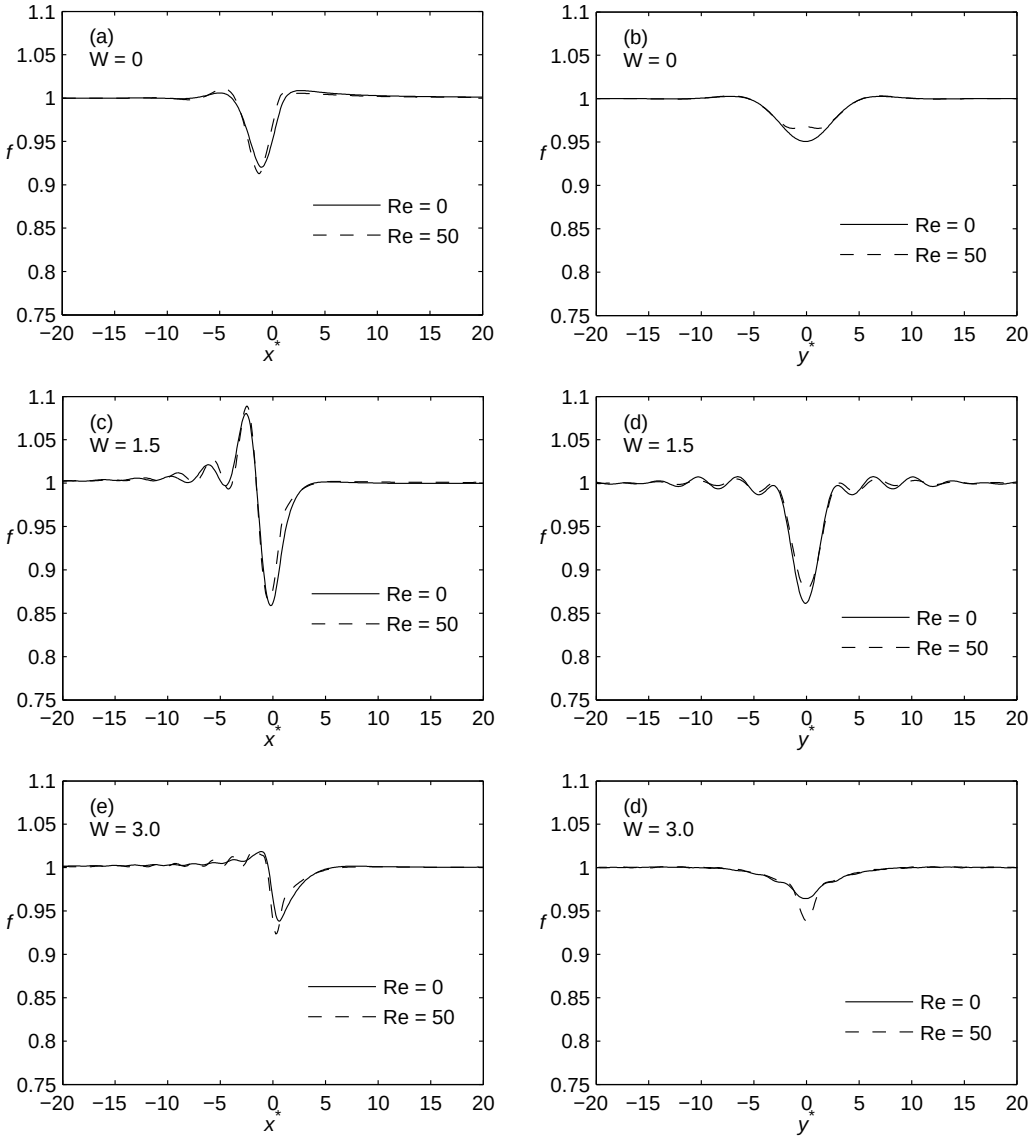

FIGURE 5.15: Streamwise (left) and spanwise (right) predicted free-surface profiles through the centre of the localised square trench topography of Figure 5.14, showing the effect of changing Re from 0 to 50. From top to bottom, W = 0, 1.5, 3.0.

Figure 5.16 illustrates the distribution of the capillary pressure and Maxwell stress in three-dimensional flow via contour plots for the W = 0, 1.5 and 3.0 cases considered in Figures 5.12 and 5.13. In the absence of Maxwell stresses, W = 0, the regions of negative and positive capillary pressure upstream and downstream of the trench topography, respectively, result in the capillary ridge and downstream surge. Increasing W to 1.5, leads to larger regions of significant positive and negative capillary pressure that are opposed by the development of larger regions of significant Maxwell stress. The larger values of negative capillary pressure, in particular, result in the large free-surface peak seen in Figure 5.12(d) while the large positive capillary pressures give rise to a larger free-surface depression over the topography. The competition between the capillary pressure and Maxwell stresses is seen more clearly in the free-surface profiles given in Figure 5.17. This shows, in particular, how the capillary pressure and Maxwell stresses effectively cancel each other out at the higher W values, resulting in the highly planarised free-surface profiles shown in Figures 5.12 and 5.13.

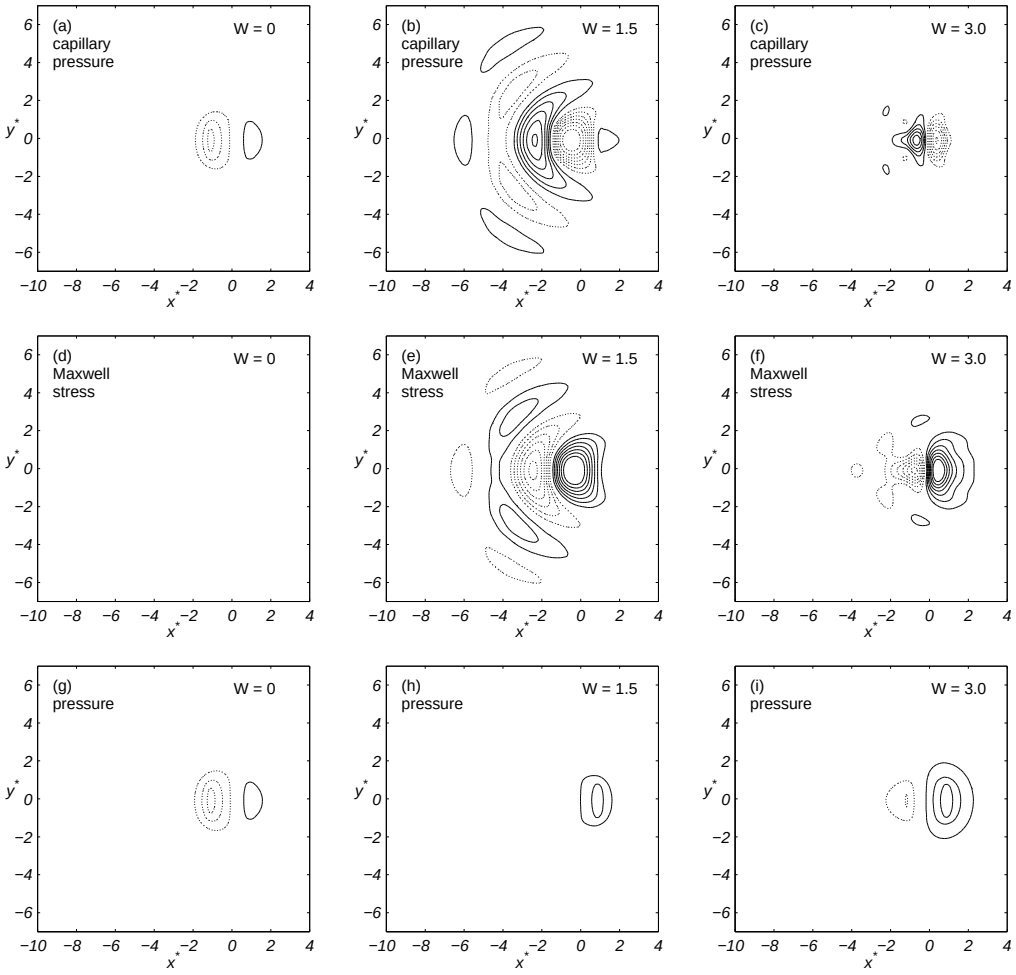

FIGURE 5.16: Predicted pressure budget contour plots for thin film flow, Re = 0, over the localised square trench topography of Figure 5.12: (a), (b), (c) capillary pressure for W = 0, 1.5, 3.0; (d), (e), (f) Maxwell stress for W = 0, 1.5, 3.0; (g), (h), (i) overall pressure for W = 0, 1.5, 3.0. Contour values are chosen to be equal in magnitude but opposite in sign $|p| = 0.2,0.4,0.6,0.8,1.0,1.2,1.4$. Negative contour values are indicated as dotted lines. Hydrostatic pressure is not plotted since its modulus is less than the smallest contour value. The direction of flow is from left to right.

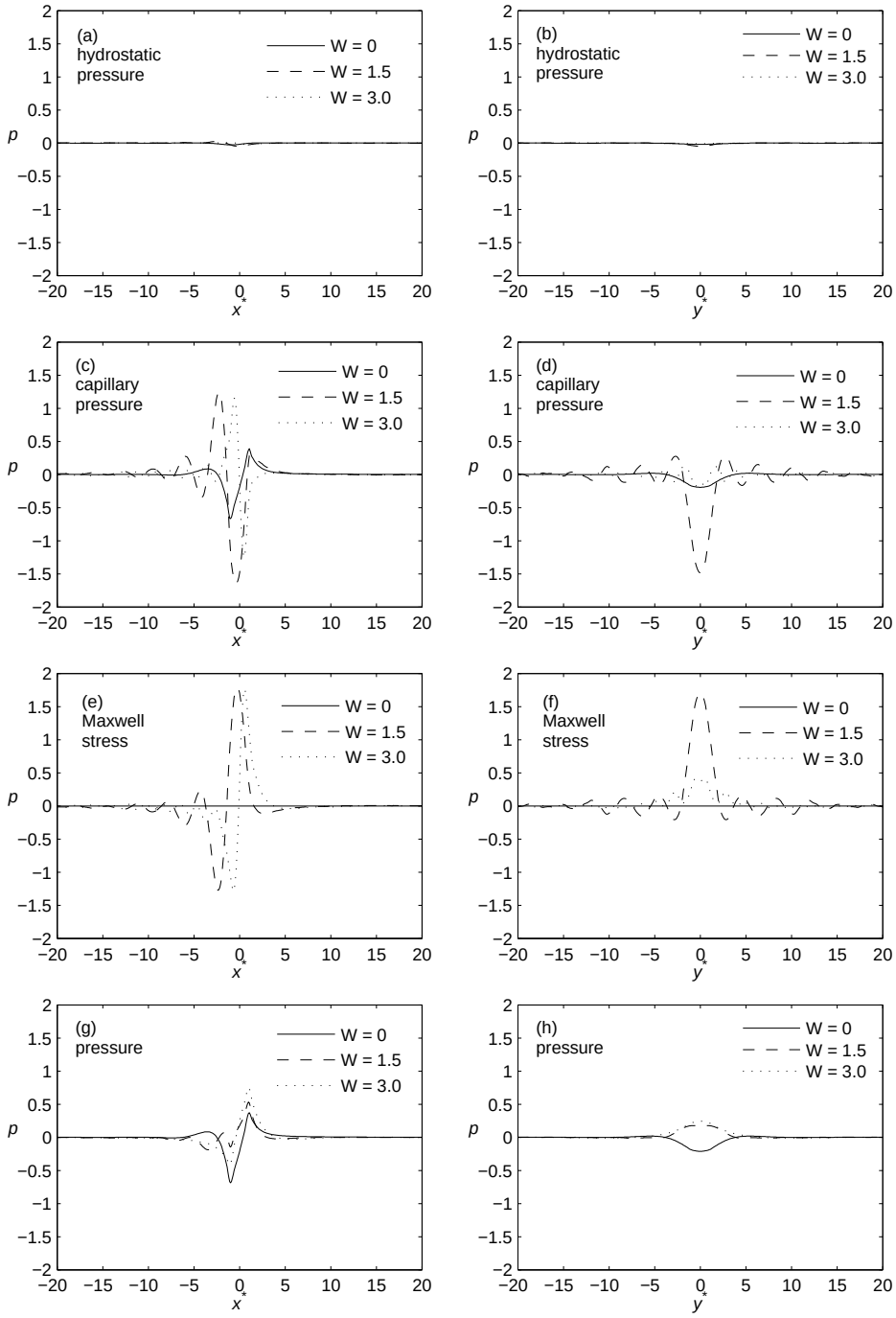

FIGURE 5.17: Streamwise (left) and spanwise (right) predicted pressure budget profiles through the centre of the localised square trench topography of Figure 5.12, Re = 0: (a), (b) hydrostatic pressure; (c), (d) capillary pressure; (e), (f) Maxwell stress; (g), (h) overall pressure. Comparison is made for W = 0, 1.5 and 3.0.

Chapter 6

Conclusions and future work

Contents

6.1 Conclusions

The ubiquitous occurrence of thin film flows in many areas of scientific and engineering relevance keeps the investigation of the same at the forefront of research interest. The work presented in this thesis reflects an important contribution to the field on two counts:

(i) it provides an important addition to the body of knowledge which has appeared in the literature to date associated with the modelling of gravity-driven thin film flow over topography;

(ii) it represents a significant step forward with regard to the efficient numerical solution of the different equation sets involved, as an aid for predicting the behaviour of a particular class of fluid flow problem.

The hierarchy of models utilised in the work, in order of decreasing complexity, are: the full Navier-Stokes (N-S) system of equations; a depth averaged form (DAF) of the latter; the lubrication (LUB) equations. In solving their discrete forms every effort was made to do so efficiently using state-of-the-art solution strategies, while ensuring accurate and mesh-independent predictions. Solution of the LUB and DAF models centres on the use of a multigrid methodology together with automatic, error controlled, time-stepping; in addition the DAF model, which assumes a parabolic velocity profile to hold through the film, requires the use of a second-order accurate TVD scheme in conjunction with a suitable flux limiter to handle the associated nonlinear advective terms present. For both models the solution efficiency achieved is found to be of O(N), where N is the number of unknowns. The solution strategy adopted for the full N-S equations involves mixed-interpolation using a Bubnov-Galerkin finite element scheme, free surface parametrisation based on the Arbitrary Lagrangian-Eulerian method of spines, the use of a direct parallel multifrontal method from the MUMPS library and utilisation of the memory-efficient out-

of-core approach for storing matrix cofactors on the hard drive. The three-dimensional solutions obtained in this way represent the first of their kind, enabling both the internal flow structure and free-surface disturbance generated to be explored in tandem.

LUB and DAF solutions for film flow over various spanwise topography, based on flow conditions/parameters for which corresponding experimental data exists, show the two to be in very good agreement with each other and with predictions obtained of the same via corresponding finite-element solutions of the full N-S problem. A subsequent detailed numerical investigation of flow over spanwise step-up and step-down topography, involving varying the step height/depth and Reynolds number range, is used to quantify the accuracy of solutions viz. the DAF equation set. To this end comparisons are made with the predictions obtained with the LUB equations and with corresponding N-S solutions. Taking the latter as the benchmark, the results are summarised as contour plots in one of two ways: (i) the discrepancy which arises, measured relative to the N-S solution; (ii) the relative magnitude of the error associated with the ratio of discrepancies. The related contour plots clearly show the benefits of the depth-averaged formulation over the use of lubrication theory, as the step-height/depth and Reynolds number become significant, and that the former provides a reasonably good approximation to the flow when compared to its N-S generated counterparts. It is interesting to note also that, as in the case of using the LUB model to predict free-surface disturbances for flow over topography having dimensions approaching that of the film thickness, the DAF model is found to produce results, comparable with those obtained with the N-S model, for capillary number values beyond that for which it is strictly no longer valid.

For thin film flow over a localised square trench topography, it is found that the general shape of the predicted free-surface disturbance agrees well with its experimentally obtained counterpart, while revealing the subtle effects

of increasing inertia. Attention is focused on changes in the characteristic 'horseshoe'-shaped 'bow-wave' and 'comet-tail' features that are present and the effect on the accompanying downstream surge which is not present for flow over spanwise topography. Increased inertia is found to lead to a rise in and sharper focusing of the disturbances in the vicinity of the topography, since streamwise inertia reduces their tendency to spread in the spanwise direction. This finding is consistent with free-surface instabilities arising at critical values of the Reynolds number. Considered also is the effect of the aspect ratio of the trench topography and the substrate inclination angle on the free-surface disturbance as inertia is increased. The results show that despite the tendency of inertia to amplify and focus the associated free-surface features, decreasing the inclination angle, and hence the normal component of gravity, suppresses them; however, the downstream surge proves to be more resilient to a decreased angle of inclination than the upstream bow-wave. Increasing the trench aspect ratio leads to a broadening of the upstream capillary ridge and an eventual bifurcation of the surge; the latter divides to form two decoupled surges and when the aspect ratio is large enough the mid-plane streamwise free-surface profile is found to approach its spanwise equivalent.

The above effects, as observed in the framework of the approximate long-wave LUB and DAF models, are found to be mirrored in the equivalent results obtained following solution of the full N-S equations; revealed too is the accompanying internal flow structure and velocity profiles existing across the film at different locations along the length of the topography containing the substrate. The latter are used to explore the validity of the assumed parabolic velocity profile used to close the DAF model for the case of flow over a spanwise trench with a depth less or equal to the overlying film thickness. The N-S solutions support the assumed parabolic velocity profile, in that the velocity profile through the liquid film is found to have a parabolic form everywhere, except in negligibly small regions in close proximity to the sides of steep to-

pographical features.

Turning to the specific issue of the internal flow structure, an investigation was undertaken of film flow over one-dimensional (spanwise) step-down, step-up and trench topographies and two-dimensional (localised) trench topography, with a depth smaller or equal to the film thickness. For the one-dimensional step-down, step-up and trench topographies the results obtained are found to be consistent with ones reported by Gaskell *et al.* (2004*b*). The underlying flow structure, revealed in the form of streamline plots, shows why a step-down topography leads to a greater discrepancy between LUB, DAF and N-S predicted free-surface profiles as the step height/depth and Reynolds number become significant, compared to a step-up topography. The complementary exploration, using the N-S model, of internal flow structure, shows that both two-dimensional flow over spanwise topography and three-dimensional Stokes and Navier-Stokes flow over localised trench topography lead to different internal, inertia dependent, flow topologies; findings that are consistent with previously reported results for the well-known lid-driven cavity problem, Shankar & Deshpande (2000). In two dimensions, for a sufficiently wide spanwise trench, there are two corner eddies, the centres of which are always elliptic points; in three dimensions, for flow over a localised trench, they are foci in the mid-plane and the streamlines, emanating from the focus on the upstream side of the trench, stream into the focus on its downstream side.

Finally the prospects of using a normal electrostatic field for controlling gravity-driven continuous thin film flow over topography at finite Reynolds numbers is explored by coupling the DAF equation set with a Fourier series solution of Laplace's equation for the electric field potential. The latter is a generalisation to three-dimensional flow of a recently-developed, Tseluiko *et al.* (2008*a*), Tseluiko *et al.* (2008*b*) and Tseluiko & Blyth (2009), Hilbert solution for two-dimensional flow. In addition utilisation of the DAF model, in contrast to previous studies, where a variation of the LUB model was employed, enables

the combined effects of inertia and electric field to be explored for both two- and three-dimensional flow.

The spanwise topography investigated includes discrete step-up and step-down features and a trench comprised of the same in close proximity, together with a smooth periodically varying profile; localised trench topography only is considered in the case of three-dimensional flow. The general observation is that for both flow types, the resultant free-surface disturbance is a consequence of the competition between the dominant capillary pressures and Maxwell stresses generated, with hydrostatic pressure having only a minor influence. The corresponding variations in the balancing capillary pressure explain the initial enhancement and then suppression of free-surface disturbances as Weber number increases. The Maxwell stress depends not only on the Weber number but also on the magnitude of the free-surface disturbance; for higher Weber number values the free surface becomes more planar and the Maxwell stresses diminish, which as a consequence reduces the capillary pressure making the free surface even more planar.

For the parameter range considered, the presence of an electric field dominates inertial effects so that inertially-induced disturbances are generally suppressed by increasing the electric field strength. Electrified thin film flow over the trench topography cases considered clearly demonstrates that although the introduction of an electric field initially amplifies the size of the free-surface disturbances in the neighbourhood of a localised trench topography, increasing its strength eventually suppresses the persistent bow-wave disturbances that arise, leading to a highly planarised film surface. In addition, higher electric field strengths increase the pressure inside of the trench which acts to prevent flow into the sides of the trench as the film passes over it, thus reducing the amount of the fluid emerging from the trench at its downstream side and hence the size of the downstream surge. This capability has yet to be fully exploited in practical coating applications where the achievement of flat free-surface

profiles can significantly enhance product quality.

With regard to the issue of product quality, it is found that for flow over both steep spanwise and localised topography, regardless of whether or not inertia is present, while an electric field can be used to suppress the principal gross free-surface disturbances, large values lead to unwanted oscillatory behaviour in the form of a sequence of many more smaller free-surface oscillations. Their presence is reminiscent of the ribbing instability that arises in the nip region of a forward roll coater, in that beyond a critical roll speed ratio additional free-surface curvature is created in the form of ribs to increase capillary pressure and maintain pressure equilibrium at the liquid-air interface, Weinstein & Ruschak (2004).

6.2 Future work

The modelling methodologies and the efficiency of the solution strategies presented for both the full N-S problem and the long-wave approximations, LUB and DAF, are readily extendable for the investigation of a wealth of related three-dimensional flow phenomena.

First of all, based on the above observations concerning the effects of inertia apropos thin film flow over both spanwise and local topography, the DAF model can be easily implemented for further investigations of free-surface planarisation with respect to photolithography together with droplet spreading and coalescence on patterned (topographically and/or chemically) surfaces. Likewise it is a relatively simple task to include additional physics into the DAF model such as evaporation, thermal, insoluble surfactant effects and/or the influences of a porous or flexible substrate. A further potential way forward is to explore the possibility of lifting the staggered mesh restriction required to avoid the occurrence of the well know checkerboard instability by develop-

ing a collocated variable approach; the obvious benefit of proceeding in this way would be to open up the ease of introducing automatic error controlled adaptive mesh refinement, to complement the existing error controlled adaptive time-stepping routine employed, which has been shown to be extremely beneficial in the context of solving LUB models for film flows, Lee *et al.* (2007).

Furthermore, an analysis of the influence of topography can be applied to substrate features with different shapes to the ones considered in this thesis, or to ones of a more complex nature, in particularly those with a sparsely distributed structure. For example, the finite element representation of the full N-S model is readily applicable for flow over hemispherically shaped particle or to flow around a hemispherical or cylindrical occlusion which penetrates through the free surface; such flows as the latter have only previously been solved for in the Stokes flow limit using the boundary element method, see Blyth & Pozrikidis (2006) and Baxter *et al.* (2009), respectively. In addition the N-S model is not constrained to the solution of flows with a low capillary number and can be used to investigate flows of arbitrary film thickness over complex and depth-heterogeneous three-dimensional topographical features, for which the long-wave approximation, LUB and DAF, models would prove inaccurate or would simply not be applicable.

The state-of-the-art high performance parallel solution strategies adopted to produce the, first of their kind, three-dimensional N-S results, open up opportunities for solving advanced thin film flow problems requiring a large amount of computer memory and power, such as free-surface interactions with non-steady electromagnetic or thermal fields, fluid-structure interactions with retentive flexible geometry and many other such complex applications. With this in mind, the advantages of employing other parallel solvers, for example algebraic multigrids or hybrid direct and iterative solvers, for achieving better memory-efficiency or larger parallel scalability, remain to be explored. In the fullness of time the goal should be one of generating fully time-dependent N-S

predictions for problems of the type explored in this thesis.

Last but not least, the current dearth of experimental data for comparison purposes and the validation of theoretical models for thin film flow problems, represents a challenging and timely opportunity for someone to make significant and important contribution to the area. However, obtaining useful experimental data when additional physics are included, such as the application of an electric field, represents a huge challenge for the wouldbe experimentalist.

Appendix A

Gaussian quadrature

Gaussian quadrature is one of the most accurate and widely used numerical methods for the calculation integrals arising from finite element discretisations, see for example Chung (2002). The method allows integrals over unit orthogonal segments, triangles and tetrahedrons, to be approximated as:

$$\int_0^1 \int_0^{1-L_1} ... \int_0^{1-\sum_{\beta=1}^{n^o-1} L_\beta} f\left(L_1, L_2 ... L_{n^o+1}\right) dL_1 dL_2 ... dL_{n^o}$$

$$\approx \sum_{p=1}^{n^p} w^p f\left(L_1^p, L_2^p ... L_{n^o+1}^p\right), \tag{A.1}$$

where w^p and L_β^p for $\beta \in [1, n^o + 1]$ are weight coefficients and quadrature points (abscissae), respectively; n^p is the number of integration points and n^o is the order of the integral (for example $n^o = 2$ for a two-dimensional integral over domain Ω as well as a three-dimensional integral over a free-surface boundary Γ). The actual values of the n^p weight coefficients and n^p abscissae can be found by representing the function $f\left(L_1, L_2 ... L_{n^o+1}\right)$ as a polynomial of degree $2n^p$ or less, substituting it into (A.1) and resolving the system of nonlinear algebraic equations obtained for the $2n^p$ unknowns. This is reported in several text books and the tabulated results of weight coefficients and abscissae provided. Unsymmetric quadrature formulas can be found in the work of Rathod, Nagaraja, Venkatesudu & Ramesh (2004) for triangular and Rathod, Venkatesudu & Nagaraja (2006) for tetrahedral element. Symmetric quadrature weight coefficients and abscissae, which allow minimisation of the number of integration points and therefore reduce the computaional cost, are provided in studies employing triangular element, see for example Liu & Vinokur (1998), Wandzura & Xiao (2003) and Rathod, Nagaraja & Venkatesudu (2007); while for tetrahedral element see for example Jinyun (1984), Keast (1986), Liu & Vinokur (1998) and Nagaraja & Rathod (2010).

The most widely used tabulated symmetric quadrature weight coefficients and

abscissae for one-dimensional integration over a line, two-dimensional integration over a triangular element and three-dimensional integration over a tetrahedral element are given in Table A.1, A.2 and A.3, respectively. Due to the symmetry of these quadrature rules the sampling points fall into symmetry groups; namely, if a point with coordinates $(L_1, L_2...L_{n^o+1})$ is the sampling point, then any points with the possible permutations of the coordinates, m^p, are also sampling points and they have a single weight w^p.

TABLE A.1: Weight coefficients and abscissae for segmental element ($n^o = 1$). The total number of quadrature points, n^p, is from 2 to 5. m^p is the number of possible permutations of the quadrature points.

n^p	m^p	Weight w^p	L_1^p	L_2^p
2	2	0.5	0.21132487	0.78867513
3	1	0.44444444	0.5	0.5
	2	0.27777778	0.11270167	0.88729833
4	2	0.17392742	0.06943184	0.93056816
	2	0.32607258	0.33000948	0.66999052
5	1	0.28444444	0.5	0.5
	2	0.23931434	0.76923466	0.23076534
	2	0.11846344	0.95308992	0.04691008

TABLE A.2: Weight coefficients and abscissae for triangular element ($n^o = 2$). The total number of quadrature points, n^p, is from 3 to 25. m^p is the number of possible permutations of the quadrature points.

n^p	m^p	Weight w^p	L_1^p	L_2^p	L_3^p
3	3	0.16666667	0.16666667	0.16666667	0.66666667
7	1	0.1125	0.33333333	0.33333333	0.33333333
	3	0.062969590	0.10128651	0.10128651	0.79742699
	3	0.066197076	0.47014206	0.47014206	0.059715872
25	1	0.041761600	0.33333333	0.33333333	0.33333333
	3	0.0036149253	0.49786543	0.49786543	0.0042691341
	3	0.037246089	0.42801245	0.42801245	0.14397510
	3	0.039323237	0.18475641	0.18475641	0.63048717
	3	0.0034641615	0.020481219	0.020481219	0.95903756
	6	0.014759160	0.82842343	0.13657358	0.035002990
	6	0.019789684	0.62970733	0.33274360	0.037549070

TABLE A.3: Weight coefficients and abscissae for tetrahedral element ($n^o = 3$). The total number of quadrature points, n^p, is from 11 to 45. m^p is the number of possible permutations of the quadrature points.

n^p	m^p	Weight w^p	L_1^p	L_2^p	L_3^p	L_4^p
11	1	-0.013155555	0.25	0.25	0.25	0.25
	4	0.0076222222	0.071428571	0.071428571	0.071428571	0.78571428
	6	0.024888889	0.39940358	0.39940358	0.10059642	0.10059642
14	6	0.0031746032	0.5	0.5	0.0	0.0
	4	0.014764971	0.10052677	0.10052677	0.10052677	0.69841970
	4	0.022139791	0.31437287	0.31437287	0.31437287	0.056881380
15	4	0.0060267857	0.33333333	0.33333333	0.33333333	0.0
	1	0.030283678	0.25	0.25	0.25	0.25
	4	0.011645249	0.090909091	0.090909091	0.090909091	0.72727273
	6	0.010949142	0.066550154	0.066550154	0.43344985	0.43344985
24	4	0.0066537917	0.21460287	0.21460287	0.21460287	0.35619139
	4	0.0016795352	0.040673959	0.040673959	0.040673959	0.87797812
	4	0.0092261969	0.32233789	0.32233789	0.32233789	0.032986330
	12	0.0080357143	0.063661002	0.063661002	0.26967233	0.60300566
31	6	0.00097001764	0.5	0.5	0.0	0.0
	1	0.018264223	0.25	0.25	0.25	0.25
	4	0.010599942	0.078213192	0.078213192	0.078213192	0.765360423
	4	-0.062517740	0.12184322	0.12184322	0.12184322	0.63447035
	4	0.0048914253	0.33253916	0.33253916	0.33253916	0.0023825067
	12	0.027557319	0.1	0.1	0.2	0.6
45	1	0.039327007	0.25	0.25	0.25	0.25
	4	0.0040813161	0.12747094	0.12747094	0.12747094	0.61758719
	4	0.00065808677	0.032078830	0.032078830	0.032078830	0.90376351
	6	0.0043842588	0.049777096	0.049777096	0.45022290	0.45022290
	6	0.013830064	0.18373045	0.18373045	0.31626955	0.31626955
	12	0.0042404374	0.23190109	0.23190109	0.022917788	0.51328003
	12	0.0022387397	0.037970048	0.037970048	0.73031343	0.19374648

Appendix B

Newton-Raphson method for the full Navier-Stokes equations

The Newton-Raphson method is used to linearise the global system of discretised N-S equations (2.88):

$$\frac{\partial \boldsymbol{\mathcal{N}}}{\partial \boldsymbol{z}} \Delta \boldsymbol{z} = -\boldsymbol{\mathcal{N}} \tag{B.1}$$

where the global Jacobian matrix, $\frac{\partial \boldsymbol{\mathcal{N}}}{\partial \boldsymbol{z}}$, and the solution increment, $\Delta \boldsymbol{z}$, are, respectively:

$$\frac{\partial \boldsymbol{\mathcal{N}}}{\partial \boldsymbol{z}} = \begin{pmatrix} \frac{\partial \boldsymbol{\mathcal{N}}_i^{mom}}{\partial \boldsymbol{u}_l} & \frac{\partial \boldsymbol{\mathcal{N}}_i^{mom}}{\partial p_j} & \frac{\partial \boldsymbol{\mathcal{N}}_i^{mom}}{\partial h_m} \\ \frac{\partial \mathcal{N}_j^{cont}}{\partial \boldsymbol{u}_l} & 0 & \frac{\partial \mathcal{N}_j^{cont}}{\partial h_m} \\ \frac{\partial \mathcal{N}_k^{kin}}{\partial \boldsymbol{u}_l} & 0 & \frac{\partial \mathcal{N}_k^{kin}}{\partial h_m} \end{pmatrix}, \quad \Delta \boldsymbol{z} = \begin{pmatrix} \Delta \boldsymbol{u_i} \\ \Delta p_j \\ \Delta h_k \end{pmatrix}. \tag{B.2}$$

After obtaining the increment, $\Delta \boldsymbol{z}$, the solution is updated as follows:

$$\widetilde{\boldsymbol{z}} = \boldsymbol{z} + \Delta \boldsymbol{z}, \tag{B.3}$$

with typically 2-3 iterations required to reduce the norm of the residual $\boldsymbol{\mathcal{N}}$ to below 10^{-6}. Similar to the residuals (2.91), the global Jacobian matrix, $\frac{\partial \boldsymbol{\mathcal{N}}}{\partial \boldsymbol{z}}$, is derived by assembling the integral contributions for the domain, Ω_e, and free-surface, Γ_s, elements:

$$\frac{\partial \boldsymbol{\mathcal{N}}_i^{mom}}{\partial \boldsymbol{u}_l} = \bigcup_{e=1}^{n^e} \Delta_{i,\alpha}^{(e)} \Delta_{l,\delta}^{(e)} \frac{\partial \boldsymbol{\mathcal{N}}_\alpha^{mom,dom,(e)}}{\partial \boldsymbol{u}_\delta}, \quad \frac{\partial \boldsymbol{\mathcal{N}}_i^{mom}}{\partial p_j} = \bigcup_{e=1}^{n^e} \Delta_{i,\alpha}^{(e)} \Delta_{j,\beta}^{(e)} \frac{\partial \boldsymbol{\mathcal{N}}_\alpha^{mom,dom,(e)}}{\partial p_\beta}, \tag{B.4}$$

$$\frac{\partial \boldsymbol{\mathcal{N}}_i^{mom}}{\partial h_m} = \widetilde{\Delta}_{l,m} \bigcup_{e=1}^{n^e} \Delta_{i,\alpha}^{(e)} \Delta_{l,\delta}^{(e)} \boldsymbol{d}_\delta \frac{\partial \boldsymbol{\mathcal{N}}_\alpha^{mom,dom,(e)}}{\partial \boldsymbol{x}_\delta} + \Delta_{i,k} \bigcup_{s=1}^{n^s} \Delta_{k,\gamma}^{(s)} \Delta_{m,\zeta}^{(e)} \boldsymbol{d}_\zeta \frac{\partial \boldsymbol{\mathcal{N}}_\gamma^{mom,f.s.,(s)}}{\partial \boldsymbol{x}_\zeta}, \tag{B.5}$$

$$\frac{\partial \mathcal{N}_j^{cont}}{\partial \boldsymbol{u}_l} = \bigcup_{e=1}^{n^e} \Delta_{j,\beta}^{(e)} \Delta_{l,\delta}^{(e)} \frac{\partial \mathcal{N}_\beta^{cont,e}}{\partial \boldsymbol{u}_\delta}, \quad \frac{\partial \mathcal{N}_j^{cont}}{\partial h_m} = \widetilde{\Delta}_{l,m} \bigcup_{e=1}^{n^e} \Delta_{j,\beta}^{(e)} \Delta_{l,\delta}^{(e)} \boldsymbol{d}_\delta \frac{\partial \mathcal{N}_\beta^{cont,e}}{\partial \boldsymbol{x}_\delta}, \tag{B.6}$$

$$\frac{\mathcal{N}_k^{kin}}{\partial \boldsymbol{u}_l} = \Delta_{l,m} \bigcup_{s=1}^{n^s} \Delta_{k,\gamma}^{(s)} \Delta_{m,\zeta}^{(e)} \frac{\partial \mathcal{N}_\gamma^{kin,(s)}}{\partial \boldsymbol{u}_\zeta}, \quad \frac{\mathcal{N}_k^{kin}}{\partial h_m} = \bigcup_{s=1}^{n^s} \Delta_{k,\gamma}^{(s)} \Delta_{m,\zeta}^{(s)} \boldsymbol{d}_\zeta \frac{\partial \mathcal{N}_\gamma^{kin,(s)}}{\partial \boldsymbol{x}_\zeta}, \tag{B.7}$$

where the spine definition (2.87) is used to express h-derivatives through the

$\boldsymbol{x}$-derivatives; $l \in [1, n^i]$, $m \in \left[1, n^k\right]$, $\delta \in [1, n^\alpha]$, $\zeta \in [1, n^\gamma]$, with the Boolean matrices $\Delta^{(e)}_{l,\delta}$, $\Delta^{(s)}_{m,\zeta}$, $\Delta_{l,m}$ and $\widetilde{\Delta}_{l,m}$ equivalent to the Boolean matrices $\Delta^{(e)}_{i,\alpha}$, $\Delta^{(s)}_{k,\gamma}$, $\Delta_{i,k}$ and $\widetilde{\Delta}_{i,k}$, respectively. The local Jacobians are found analytically by explicitly differentiating the corresponding residuals:

$$\frac{\partial \boldsymbol{\mathcal{N}}^{mom,dom,(e)}_{\alpha}}{\partial \boldsymbol{u}_\delta} = \int_0^1 \int_0^{1-L_1} ... \int_0^{1-\sum_{\beta=1}^{dim-1} L_\beta} \Big\{ -\mathrm{Re}\phi_\delta \big[\boldsymbol{I} \left(\boldsymbol{u} \cdot \nabla \phi_\alpha \right) + \boldsymbol{u} \otimes \nabla \phi_\alpha \big] + \boldsymbol{I} \left(\nabla \phi_\delta \cdot \nabla \phi_\alpha \right) + \nabla \phi_\delta \otimes \nabla \phi_\alpha \Big\} \left| J \right| dL_1 dL_2 ... dL_{dim}, \tag{B.8}$$

$$\frac{\partial \boldsymbol{\mathcal{N}}^{mom,dom,(e)}_{\alpha}}{\partial p_\beta} = - \int_0^1 \int_0^{1-L_1} ... \int_0^{1-\sum_{\beta=1}^{dim-1} L_\beta} \psi_\beta \nabla \phi_\alpha \left| J \right| dL_1 dL_2 ... dL_{dim}, \tag{B.9}$$

$$\frac{\partial \boldsymbol{\mathcal{N}}^{mom,dom,(e)}_{\alpha}}{\partial \boldsymbol{x}_\delta} = \int_0^1 \int_0^{1-L_1} ... \int_0^{1-\sum_{\beta=1}^{dim-1} L_\beta} \Big[(-\mathrm{Re}\boldsymbol{u} \otimes \boldsymbol{u} - p\boldsymbol{I} + \boldsymbol{\tau}) \times \frac{\partial}{\partial \boldsymbol{x}_\delta} \left(\nabla \phi_\alpha \left| J \right| \right) + \mathrm{St} \boldsymbol{g} \phi_\alpha \frac{\partial \left| J \right|}{\partial \boldsymbol{x}_\delta} \Big] dL_1 dL_2 ... dL_{dim}, \tag{B.10}$$

$$\frac{\partial \mathcal{N}^{cont,(e)}_{\beta}}{\partial \boldsymbol{u}_\alpha} = \int_0^1 \int_0^{1-L_1} ... \int_0^{1-\sum_{\beta=1}^{dim-1} L_\beta} \nabla \phi_\alpha \left| J \right| \psi_\beta dL_1 dL_2 ... dL_{dim}, \tag{B.11}$$

$$\frac{\partial \mathcal{N}^{cont,(e)}_{\beta}}{\partial \boldsymbol{x}_\delta} = \int_0^1 \int_0^{1-L_1} ... \int_0^{1-\sum_{\beta=1}^{dim-1} L_\beta} \frac{\partial}{\partial \boldsymbol{x}_\delta} \Big(\nabla \phi_\alpha \left| J \right| \Big) \psi_\beta dL_1 dL_2 ... dL_{dim}, \tag{B.12}$$

$$\frac{\partial \boldsymbol{\mathcal{N}}^{mom,f.s.,2D,(s)}_{\gamma}}{\partial \boldsymbol{x}_\zeta} = \frac{1}{\mathrm{Ca}} \int_0^1 \frac{\partial}{\partial \boldsymbol{x}_\zeta} \Big[\boldsymbol{i} \left(\boldsymbol{n} \cdot \boldsymbol{k} \right) - \boldsymbol{k} \left(\boldsymbol{n} \cdot \boldsymbol{i} \right) \Big] \left(\frac{\partial \phi_\gamma}{\partial L_2} - \frac{\partial \phi_\gamma}{\partial L_3} \right) |_{L_1=0} dL_2, \tag{B.13}$$

$$\frac{\partial \boldsymbol{\mathcal{N}}^{mom,f.s.,3D,(s)}_{\gamma}}{\partial \boldsymbol{x}_\zeta} = \frac{1}{\mathrm{Ca}} \int_0^1 \int_0^{1-L_2} \frac{\partial}{\partial \boldsymbol{x}_\zeta} \Big\{ \big[\nabla \phi_\gamma - \boldsymbol{n} \left(\boldsymbol{n} \cdot \nabla \phi_\gamma \right) \big] |_{L_1=0} \left| \boldsymbol{N} \right| \Big\} dL_2 dL_3, \tag{B.14}$$

$$\frac{\partial \mathcal{N}^{kin,(s)}_{\gamma}}{\partial \boldsymbol{u}_\zeta} = \int_0^1 \int_0^{1-L_2} ... \int_0^{1-\sum_{\beta=2}^{dim-1} L_\beta} \boldsymbol{N} \phi_\zeta \phi_\gamma dL_2 dL_3 ... dL_{dim}, \tag{B.15}$$

$$\frac{\partial \mathcal{N}^{kin,(s)}_{\gamma}}{\partial \boldsymbol{x}_\zeta} = \int_0^1 \int_0^{1-L_2} ... \int_0^{1-\sum_{\beta=2}^{dim-1} L_\beta} \frac{\partial}{\partial \boldsymbol{x}_\zeta} \left(\boldsymbol{N} \cdot \boldsymbol{u} \right) |_{L_1=0} \phi_\gamma dL_2 dL_3 ... dL_{dim}. \tag{B.16}$$

The missing derivatives are derived as follows by making use of the expressions (2.96), (2.98) and (2.102):

$$\frac{\partial \left| J \right|}{\partial x_\delta} = \left| J_{x\delta} \right|, \tag{B.17}$$

$$\frac{\partial}{\partial x_\delta}\Big(\nabla\phi_\alpha\,|J|\Big) = \sum_{\beta=1}^{n^\beta}\frac{\partial\phi_\alpha}{\partial L_\beta}\frac{\partial}{\partial x_\delta}\Big[\boldsymbol{i}C_{\beta x}(J)+\boldsymbol{j}C_{\beta y}(J)+\boldsymbol{k}C_{\beta z}(J)\Big]$$

$$= \sum_{\beta=1}^{n^\beta}\frac{\partial\phi_\alpha}{\partial L_\beta}\Big[\boldsymbol{j}C_{\beta y}(J_{x\delta})+\boldsymbol{k}C_{\beta z}(J_{x\delta})\Big], \tag{B.18}$$

$$\frac{\partial \boldsymbol{N}}{\partial x_\delta} = \frac{\partial}{\partial x_\delta}\Big[\boldsymbol{i}C_{1x}(J)+\boldsymbol{j}C_{1y}(J)+\boldsymbol{k}C_{1z}(J)\Big]|_{L_1=0} = \Big[\boldsymbol{j}C_{1y}(J_{x\delta})+\boldsymbol{k}C_{1z}(J_{x\delta})\Big]|_{L_1=0}, \tag{B.19}$$

where an expression $\frac{\partial}{\partial x_\delta}\left(\frac{\partial x}{\partial L_\beta}\right) = \frac{\partial\phi_\delta}{\partial L_\beta}$ is used to obtain the matrix $J_{x\delta}$:

$$J_{x\delta} = \begin{pmatrix} 1 & 1 & 1 & 1 \\ \frac{\partial\phi_\delta}{\partial L_1} & \frac{\partial\phi_\delta}{\partial L_2} & \frac{\partial\phi_\delta}{\partial L_3} & \frac{\partial\phi_\delta}{\partial L_4} \\ \frac{\partial y}{\partial L_1} & \frac{\partial y}{\partial L_2} & \frac{\partial y}{\partial L_3} & \frac{\partial y}{\partial L_4} \\ \frac{\partial z}{\partial L_1} & \frac{\partial z}{\partial L_2} & \frac{\partial z}{\partial L_3} & \frac{\partial z}{\partial L_4} \end{pmatrix}; \tag{B.20}$$

for the sake of simplicity only x_δ-derivatives are shown, the y_δ- and z_δ-derivatives are obtained similarly.

Appendix C

Full weighting restriction and interpolation operators

Contents

C.1 Lubrication equations on collocated grids

The full weighting restriction operators $R^h_{k\to k-1}$ (for h) and $R^p_{k\to k-1}$ (for p) are:

$$\begin{aligned} h^{k-1}_{i,j} = \frac{1}{16}\big[&h^k_{2i-1,2j-1} + h^k_{2i-1,2j+1} + h^k_{2i+1,2j-1} + h^k_{2i+1,2j+1} \\ &+2\left(h^k_{2i,2j-1} + h^k_{2i,2j+1} + h^k_{2i-1,2j} + h^k_{2i+1,2j}\right) + 4h^k_{2i,2j}\big], \end{aligned} \tag{C.1}$$

$$\begin{aligned} p^{k-1}_{i,j} = \frac{1}{16}\big[&p^k_{2i-1,2j-1} + p^k_{2i-1,2j+1} + p^k_{2i+1,2j-1} + p^k_{2i+1,2j+1} \\ &+2\left(p^k_{2i,2j-1} + p^k_{2i,2j+1} + p^k_{2i-1,2j} + p^k_{2i+1,2j}\right) + 4p^k_{2i,2j}\big]. \end{aligned} \tag{C.2}$$

The bilinear interpolation operators $I^h_{k-1\to k}$ (for h) and $I^p_{k-1\to k}$ (for p) are:

$$\begin{aligned} h^k_{2i,2j} &= h^{k-1}_{i,j}, \\ h^k_{2i+1,2j} &= \frac{1}{2}\left(h^{k-1}_{i,j} + h^{k-1}_{i+1,j}\right), \\ h^k_{2i,2j+1} &= \frac{1}{2}\left(h^{k-1}_{i,j} + h^{k-1}_{i,j+1}\right), \\ h^k_{2i+1,2j+1} &= \frac{1}{4}\left(h^{k-1}_{i,j} + h^{k-1}_{i,j+1} + h^{k-1}_{i+1,j} + h^{k-1}_{i+1,j+1}\right), \end{aligned} \tag{C.3}$$

$$\begin{aligned} p^k_{2i,2j} &= p^{k-1}_{i,j}, \\ p^k_{2i+1,2j} &= \frac{1}{2}\left(p^{k-1}_{i,j} + p^{k-1}_{i+1,j}\right), \\ p^k_{2i,2j+1} &= \frac{1}{2}\left(p^{k-1}_{i,j} + p^{k-1}_{i,j+1}\right), \\ p^k_{2i+1,2j+1} &= \frac{1}{4}\left(p^{k-1}_{i,j} + p^{k-1}_{i,j+1} + p^{k-1}_{i+1,j} + p^{k-1}_{i+1,j+1}\right). \end{aligned} \tag{C.4}$$

C.2 Depth-averaged form on staggered grids

The full weighting restriction operators $R^u_{k\to k-1}$ (for u), $R^v_{k\to k-1}$ (for v), $R^h_{k\to k-1}$ (for h) are:

$$u^{k-1}_{i+1/2,j} = \frac{1}{32}\left[u^k_{2i-1/2,2j-1} + u^k_{2i-1/2,2j+2} + u^k_{2i+3/2,2j-1} + u^k_{2i+3/2,2j+2}\right.$$
$$+ 2\left(u^k_{2i+1/2,2j-1} + u^k_{2i+1/2,2j+2}\right) + 6\left(u^k_{2i+1/2,2j} + u^k_{2i+1/2,2j+1}\right)$$
$$\left.+3\left(u^k_{2i-1/2,2j} + u^k_{2i+3/2,2j} + u^k_{2i-1/2,2j+1} + u^k_{2i+3/2,2j+1}\right)\right], \tag{C.5}$$

$$v^{k-1}_{i,j+1/2} = \frac{1}{32}\left[v^k_{2i-1,2j-1/2} + v^k_{2i+2,2j-1/2} + v^k_{2i-1,2j+3/2} + v^k_{2i+2,2j+3/2}\right.$$
$$+ 2\left(v^k_{2i-1,2j+1/2} + v^k_{2i+2,2j+1/2}\right) + 6\left(v^k_{2i,2j+1/2} + v^k_{2i+1,2j+1/2}\right)$$
$$\left.+3\left(v^k_{2i,2j-1/2} + v^k_{2i,2j+3/2} + v^k_{2i+1,2j-1/2} + v^k_{2i+1,2j+3/2}\right)\right], \tag{C.6}$$

$$h^{k-1}_{i,j} = \frac{1}{64}\left[h^k_{2i-1,2j-1} + h^k_{2i-1,2j+2} + h^k_{2i+2,2j-1} + h^k_{2i+2,2j+2} + 3\left(h^k_{2i,2j-1} + h^k_{2i,2j+2}\right.\right.$$
$$+h^k_{2i+1,2j-1} + h^k_{2i+1,2j+2}h^k_{2i-1,2j} + h^k_{2i-1,2j+1} + h^k_{2i+2,2j} + h^k_{2i+2,2j+1}\Big)$$
$$\left.+9\left(h^k_{2i,2j} + h^k_{2i+1,2j} + h^k_{2i,2j+1} + h^k_{2i+1,2j+1}\right)\right]. \tag{C.7}$$

The bilinear interpolation operators $I^u_{k-1\to k}$ (for u), $I^v_{k-1\to k}$ (for v), $I^h_{k-1\to k}$ (for h) are:

$$u^k_{2i+1/2,2j} = \frac{1}{4}\left[3u^{k-1}_{i+1/2,j} + u^{k-1}_{i+1/2,j-1}\right],$$
$$u^k_{2i+3/2,2j} = \frac{1}{8}\left[3\left(u^{k-1}_{i+1/2,j} + u^{k-1}_{i+3/2,j}\right) + u^{k-1}_{i+1/2,j-1} + u^{k-1}_{i+3/2,j-1}\right],$$
$$u^k_{2i+1/2,2j+1} = \frac{1}{4}\left[3u^{k-1}_{i+1/2,j} + u^{k-1}_{i+1/2,j+1}\right],$$
$$u^k_{2i+3/2,2j+1} = \frac{1}{8}\left[3\left(u^{k-1}_{i+1/2,j} + u^{k-1}_{i+3/2,j}\right) + u^{k-1}_{i+1/2,j+1} + u^{k-1}_{i+3/2,j+1}\right], \tag{C.8}$$
$$v^k_{2i,2j+1/2} = \frac{1}{4}\left[3v^{k-1}_{i,j+1/2} + v^{k-1}_{i-1,j+1/2}\right],$$
$$v^k_{2i+1,2j+1/2} = \frac{1}{4}\left[3v^{k-1}_{i,j+1/2} + v^{k-1}_{i+1,j+1/2}\right],$$
$$v^k_{2i,2j+3/2} = \frac{1}{8}\left[3\left(v^{k-1}_{i,j+1/2} + v^{k-1}_{i,j+3/2}\right) + v^{k-1}_{i-1,j+1/2} + v^{k-1}_{i-1,j+3/2}\right],$$
$$v^k_{2i+1,2j+3/2} = \frac{1}{8}\left[3\left(v^{k-1}_{i,j+1/2} + v^{k-1}_{i,j+3/2}\right) + v^{k-1}_{i+1,j+1/2} + v^{k-1}_{i+1,j+3/2}\right], \tag{C.9}$$

$$h^k_{2i,2j} = \frac{1}{16}\left[9h^{k-1}_{i,j} + 3\left(h^{k-1}_{i-1,j} + h^{k-1}_{i,j-1}\right) + h^{k-1}_{i-1,j-1}\right],$$

$$h^k_{2i+1,2j} = \frac{1}{16}\left[9h^{k-1}_{i,j} + 3\left(h^{k-1}_{i+1,j} + h^{k-1}_{i,j-1}\right) + h^{k-1}_{i+1,j-1}\right],$$

$$h^k_{2i,2j+1} = \frac{1}{16}\left[9h^{k-1}_{i,j} + 3\left(h^{k-1}_{i-1,j} + h^{k-1}_{i,j+1}\right) + h^{k-1}_{i-1,j+1}\right],$$

$$h^k_{2i+1,2j+1} = \frac{1}{16}\left[9h^{k-1}_{i,j} + 3\left(h^{k-1}_{i+1,j} + h^{k-1}_{i,j+1}\right) + h^{k-1}_{i+1,j+1}\right]. \tag{C.10}$$

Appendix D

Relaxation using the Newton-Raphson method

Contents

The relaxation technique $\tilde{\boldsymbol{z}} = \text{RELAX}^{\nu}\left(\boldsymbol{z}, \boldsymbol{\mathcal{R}}\right)$ needed for the multigrid method is dependent on the type of equations to be solved for: the relaxation technique for the lubrication equations (LUB) and the depth-averaged form (DAF) equation set is defined in Sections D.1 and D.2, respectively. In both cases the relaxation scheme is obtained using the Newton-Raphson method with the parameter ν signifying the number of times the relaxation scheme is applied.

D.1 Point smoothing for the lubrication equations

The LUB equations are disretesed on collocated grids using a five points stencil operators, see Figure 2.5; therefore a simple, widely used Red-Black Gauss-Seidel relaxation scheme is employed, enabling approximately double the convergency rate compared to an ordinary lexicografic scheme to be achieved, see Trottenberg *et al.* (2001) and Briggs *et al.* (2000). For each node two coupled equations (one for h and one for p):

$$\frac{\partial \mathcal{N}^h_{i,j}}{\partial h_{i,j}} \Delta h_{i,j} + \frac{\partial \mathcal{N}^h_{i,j}}{\partial p_{i,j}} \Delta p_{i,j} = \mathcal{R}^h_{i,j} - \mathcal{N}^h_{i,j}, \tag{D.1}$$

$$\frac{\partial \mathcal{N}^p_{i,j}}{\partial h_{i,j}} \Delta h_{i,j} + \frac{\partial \mathcal{N}^p_{i,j}}{\partial p_{i,j}} \Delta p_{i,j} = -\mathcal{N}^p_{i,j}, \tag{D.2}$$

are solved for the unknown increments $\Delta h_{i,j}$ and $\Delta p_{i,j}$ with the new approximations given by:

$$\begin{aligned} \tilde{h}_{i,j} &= h_{i,j} + \Delta h_{i,j}, \\ \tilde{p}_{i,j} &= p_{i,j} + \Delta p_{i,j}, \end{aligned}$$

updated simultaneously, once per relaxation sweep.

D.2 Box smoothing for the depth-averaged form

Due to the staggered nature of the discretisation involved, the relaxation methodology for the DAF equation set employs a lexicographic collective box smoothing Gauss-Seidel scheme, Trottenberg *et al.* (2001), that efficiently retains the diagonal dominance of the relaxation scheme. For each cell, see Figure 2.6, five coupled equations (two each from the u-momentum and v-momentum equations and one from the continuity equation):

$$\frac{\partial \mathcal{N}^u_{i+1/2,j}}{\partial u_{i+1/2,j}}\Delta u_{i+1/2,j} + \frac{\partial \mathcal{N}^u_{i+1/2,j}}{\partial u_{i-1/2,j}}\Delta u_{i-1/2,j} + \frac{\partial \mathcal{N}^u_{i+1/2,j}}{\partial v_{i,j+1/2}}\Delta v_{i,j+1/2}$$
$$+ \frac{\partial \mathcal{N}^u_{i+1/2,j}}{\partial v_{i,j-1/2}}\Delta v_{i,j-1/2} + \frac{\partial \mathcal{N}^u_{i+1/2,j}}{\partial h_{i,j}}\Delta h_{i,j} = \mathcal{R}^u_{i+1/2,j} - \mathcal{N}^u_{i+1/2,j}, \tag{D.3}$$

$$\frac{\partial \mathcal{N}^u_{i-1/2,j}}{\partial u_{i+1/2,j}}\Delta u_{i+1/2,j} + \frac{\partial \mathcal{N}^u_{i-1/2,j}}{\partial u_{i-1/2,j}}\Delta u_{i-1/2,j} + \frac{\partial \mathcal{N}^u_{i-1/2,j}}{\partial v_{i,j+1/2}}\Delta v_{i,j+1/2}$$
$$+ \frac{\partial \mathcal{N}^u_{i-1/2,j}}{\partial v_{i,j-1/2}}\Delta v_{i,j-1/2} + \frac{\partial \mathcal{N}^u_{i-1/2,j}}{\partial h_{i,j}}\Delta h_{i,j} = \mathcal{R}^u_{i-1/2,j} - \mathcal{N}^u_{i-1/2,j}, \tag{D.4}$$

$$\frac{\partial \mathcal{N}^v_{i,j+1/2}}{\partial u_{i+1/2,j}}\Delta u_{i+1/2,j} + \frac{\partial \mathcal{N}^v_{i,j+1/2}}{\partial u_{i-1/2,j}}\Delta u_{i-1/2,j} + \frac{\partial \mathcal{N}^v_{i,j+1/2}}{\partial v_{i,j+1/2}}\Delta v_{i,j+1/2}$$
$$+ \frac{\partial \mathcal{N}^v_{i,j+1/2}}{\partial v_{i,j-1/2}}\Delta v_{i,j-1/2} + \frac{\partial \mathcal{N}^v_{i,j+1/2}}{\partial h_{i,j}}\Delta h_{i,j} = \mathcal{R}^v_{i,j+1/2} - \mathcal{N}^v_{i,j+1/2}, \tag{D.5}$$

$$\frac{\partial \mathcal{N}^v_{i,j-1/2}}{\partial u_{i+1/2,j}}\Delta u_{i+1/2,j} + \frac{\partial \mathcal{N}^v_{i,j-1/2}}{\partial u_{i-1/2,j}}\Delta u_{i-1/2,j} + \frac{\partial \mathcal{N}^v_{i,j-1/2}}{\partial v_{i,j+1/2}}\Delta v_{i,j+1/2}$$
$$+ \frac{\partial \mathcal{N}^v_{i,j-1/2}}{\partial v_{i,j-1/2}}\Delta v_{i,j-1/2} + \frac{\partial \mathcal{N}^v_{i,j-1/2}}{\partial h_{i,j}}\Delta h_{i,j} = \mathcal{R}^v_{i,j-1/2} - \mathcal{N}^v_{i,j-1/2}, \tag{D.6}$$

$$\frac{\partial \mathcal{N}^h_{i,j}}{\partial u_{i+1/2,j}}\Delta u_{i+1/2,j} + \frac{\partial \mathcal{N}^h_{i,j}}{\partial u_{i-1/2,j}}\Delta u_{i-1/2,j} + \frac{\partial \mathcal{N}^h_{i,j}}{\partial v_{i,j+1/2}}\Delta v_{i,j+1/2}$$
$$+ \frac{\partial \mathcal{N}^h_{i,j}}{\partial v_{i,j-1/2}}\Delta v_{i,j-1/2} + \frac{\partial \mathcal{N}^h_{i,j}}{\partial h_{i,j}}\Delta h_{i,j} = \mathcal{R}^h_{i,j} - \mathcal{N}^h_{i,j}, \tag{D.7}$$

are solved for the unknown increments $\Delta u_{i+1/2,j}$, $\Delta u_{i-1/2,j}$, $\Delta v_{i,j+1/2}$, $\Delta v_{i,j-1/2}$, $\Delta h_{i,j}$, with the new approximations given by:

$$\begin{aligned}
\tilde{u}_{i+1/2,j} &= u_{i+1/2,j} + \Delta u_{i+1/2,j}, \\
\tilde{u}_{i-1/2,j} &= u_{i-1/2,j} + \Delta u_{i-1/2,j}, \\
\tilde{v}_{i,j+1/2} &= v_{i,j+1/2} + \Delta v_{i,j+1/2}, \\
\tilde{v}_{i,j-1/2} &= v_{i,j-1/2} + \Delta v_{i,j-1/2}, \\
\tilde{h}_{i,j} &= h_{i,j} + \Delta h_{i,j},
\end{aligned}$$

updated simultaneously; and where each velocity component is updated twice, while the film thickness is updated only once per relaxation sweep.

Appendix E

Proof of equivalence of Hilbert and Fourier operators

Proof of the equivalence of the Hilbert operator, $\mathcal{H}\left[\partial f/\partial x\right]$, and two-dimensional Fourier operator, $\mathcal{E}\left[f-1\right]$, for the Maxwell stress is as follows.

Use is made of the following two expressions:

1. The Fourier expansions of $(f-1)$ and $\partial f/\partial x$:

$$f\left(x\right)-1=\sum_{m=0}^{\infty}\left[a_m\cos\left(\lambda_m x\right)+b_m\sin\left(\lambda_m x\right)\right], \tag{E.1}$$

$$\frac{\partial f}{\partial x}=\sum_{m=1}^{\infty}\lambda_m\left[-a_m\sin\left(\lambda_m x\right)+b_m\cos\left(\lambda_m x\right)\right], \tag{E.2}$$

where:

$$a_m=\frac{\chi_m}{l_p}\int_0^{l_p}\left(f-1\right)\cos\left(\lambda_m\widehat{x}\right)d\widehat{x},\quad b_m=\frac{\chi_m}{l_p}\int_0^{l_p}\left(f-1\right)\sin\left(\lambda_m\widehat{x}\right)d\widehat{x}. \tag{E.3}$$

2. The Principal Values (PV) of integrals for positive number, $\lambda_m>0$:

$$PV\int_{-\infty}^{\infty}\frac{\sin\left[\lambda_m\left(x-\widehat{x}\right)\right]}{\widehat{x}}d\widehat{x}=\sin\left(\lambda_m x\right)PV\int_{-\infty}^{\infty}\frac{\cos\left(\lambda_m\widehat{x}\right)}{\widehat{x}}d\widehat{x}$$

$$-\cos\left(\lambda_m x\right)PV\int_{-\infty}^{\infty}\frac{\sin\left(\lambda_m\widehat{x}\right)}{\widehat{x}}d\widehat{x}=-\pi\cos\left(\lambda_m x\right), \tag{E.4}$$

$$PV\int_{-\infty}^{\infty}\frac{\cos\left[\lambda_m\left(x-\widehat{x}\right)\right]}{\widehat{x}}d\widehat{x}=\cos\left(\lambda_m x\right)PV\int_{-\infty}^{\infty}\frac{\cos\left(\lambda_m\widehat{x}\right)}{\widehat{x}}d\widehat{x}$$

$$+\sin\left(\lambda_m x\right)PV\int_{-\infty}^{\infty}\frac{\sin\left(\lambda_m\widehat{x}\right)}{\widehat{x}}d\widehat{x}=\pi\sin\left(\lambda_m x\right), \tag{E.5}$$

where Dirichlet integration has been used.

Starting with the Hilbert operator (5.64), inserting into it the Fourier representation (E.2) and taking into account the PV integrals (E.4) and (E.5) gives:

$$\mathcal{H}\left[\frac{\partial f}{\partial x}\right]\left(x\right)=\frac{1}{\pi}PV\int_{-\infty}^{\infty}\frac{\partial f\left(\widehat{x}\right)}{\partial\widehat{x}}\frac{d\widehat{x}}{x-\widehat{x}}=\frac{1}{\pi}PV\int_{-\infty}^{\infty}\frac{\partial f\left(x-\widehat{x}\right)}{\partial\widehat{x}}\frac{d\widehat{x}}{\widehat{x}}$$

$$= \frac{1}{\pi} \sum_{m=1}^{\infty} \lambda_m PV \int_{-\infty}^{\infty} \left\{ -a_m \frac{\sin\left[\lambda_m \left(x - \widehat{x}\right)\right]}{\widehat{x}} + b_m \frac{\cos\left[\lambda_m \left(x - \widehat{x}\right)\right]}{\widehat{x}} \right\} d\widehat{x}$$

$$= \sum_{m=1}^{\infty} \lambda_m \left[a_m \cos\left(\lambda_m x\right) + b_m \sin\left(\lambda_m x\right) \right]$$

$$= \frac{1}{l_p} \int_0^{l_p} \left(f - 1\right) \sum_{m=1}^{\infty} \chi_m \lambda_m \cos\left[\lambda_m \left(x - \widehat{x}\right)\right] d\widehat{x} = \mathcal{E}\left[f - 1\right](x), \qquad \text{(E.6)}$$

which is the two-dimensional Fourier operator (5.66).

The above proof was constructed in collaboration with Professors P.H. Gaskell and M. Scholle (Heilbronn University, 74081 Heilbronn, Germany).

Bibliography

Abbott, S.J. & Gaskell, P.H. 2007 Mass production of bio-inspired structured surfaces. *Proc. I. Mech. E. part C, J. Mech. Sci.* **221** (10), 1181–1191.

Agullo, E., Guermouche, A. & L'Excellent, J.-Y. 2008 A parallel out-of-core multifrontal method: Storage of factors on disk and analysis of models for an out-of-core active memory. *Parallel Comput.* **34** (6-8), 296–317.

Alekseenko, S.V., Nakoryakov, V.E. & Pokusaev, B.G. 1994 *Wave Flow of Liquid Films*, 3rd edn. New York: Begell House.

Alexeev, A., Gambaryan-Roisman, T. & Stephan, P. 2005 Marangoni convection and heat transfer in thin liquid films on heated walls with topography: Experiments and numerical study. *Phys. Fluids* **17** (6), 13.

Altas, I., Dym, J., Gupta, M.M. & Manohar, R.P. 1998 Multigrid solution of automatically generated high-order discretizations for the biharmonic equation. *SIAM J. Sci. Comput.* **19** (5), 1575–1585.

Amaouche, M., Mehidi, N. & Amatousse, N. 2005 An accurate modeling of thin film flows down an incline for inertia dominated regimes. *Eur. Phys. J. B.* **24** (1), 49–70.

Amestoy, P.R., Duff, I.S. & L'Excellent, J.-Y. 2000 Multifrontal parallel distributed symmetric and unsymmetric solvers. *Comp. Meth. Appl. Mech. Engrg.* **184** (2-4), 501–520.

Amestoy, P.R., Duff, I.S., L'Excellent, J.-Y. & Koster, J. 2001 A fully asynchronous multifrontal solver using distributed dynamic scheduling. *SIAM J. Matr Anal. Appl.* **23** (1), 15–41.

Amestoy, P.R., Guermouche, A., L'Excellent, J.-Y. & Pralet, S. 2006 Hybrid scheduling for the parallel solution of linear systems. *Parallel Comput.* **32** (2), 136–156.

Ancey, C. 2007 Plasticity and geophysical flows: A review. *J. Non-Newton. Fluid Mech.* **142** (1-3), 4–35.

Anderson, E., Bai, Z., Bischof, C., Blackford, S., Demmel, J., Dongarra, J., Du Croz, J., Greenbaum, A., Hammarling, S., McKenney, A. & Sorensen, D. 1999 *LAPACK Users' Guide*, 3rd edn. SIAM.

Argyriadi, K., Vlachogiannis, M. & Bontozoglou, V. 2006 Experimental study of inclined film flow along periodic corrugations: The effect of wall steepness. *Phys. Fluids* **18** (1), 15.

Atkinson, K.E. 1989 *An Introduction to Numerical Analysis*, 2nd edn. New York: John Wiley & Sons.

Babuška, I. 1971 Error-bounds for finite element method. *Numerische Mathematik* **16** (4), 322–333.

Baer, T.A., Cairncross, R.A., Schunk, P.R., Rao, R.R. & Sackinger, P.A. 2000 A finite element method for free surface flows of incompressible fluids in three dimensions. Part II. Dynamic wetting lines. *Int. J. Num. Meth. Fl.* **33** (3), 405–427.

Balaganskii, M.Y., Zakharov, Y.N. & Shokin, Y.I. 2009 Comparison of two- and three-dimensional steady flows of a homogeneous viscous incompressible fluid. *Russ. J. Numer. Anal. Math. Model.* **24** (1), 1–14.

Bankoff, S.G., Griffing, E.M. & Schluter, R.A. 2002 Use of an electric field in an electrostatic liquid film radiator. *Ann. N.Y. Acad. Sci.* **974**, 1–9.

Bankoff, S.G., Miksis, M.J., Kim, H. & Gwinner, R. 1994 Design considerations for the rotating electrostatic liquid-film radiator. *Nucl. Eng. Des.* **149** (1-3), 441–447.

Baral, D.R., Hutter, K. & Greve, R. 2001 Asymptotic theories of large-scale motion, temperature, and moisture distribution in land-based polythermal ice sheets: A critical review and new developments. *Appl. Mech. Rev.* **54** (3), 215–256.

Baret, J.C. & Decré, M.M.J. 2000 Gravity driven flows over two-dimensional topographies: Measurement of the free surface using phase stepped interferometry. Unclassified report: NL-UR 2000/829. Philips Research.

Baxter, S.J., Power, H., Cliffe, K.A. & Hibberd, S. 2009 Three-dimensional thin film flow over and around an obstacle on an inclined plane. *Phys. Fluids* **21** (3), 032102.

Baxter, S.J., Power, H., Cliffe, K.A. & Hibberd, S. 2010 Free surface Stokes flows obstructed by multiple obstacles. *Int. J. Num. Meth. Fl.* **62** (5), 530–564.

Behr, M. & Abraham, F. 2002 Free-surface flow simulations in the presence of inclined walls. *Comp. Meth. Appl. Mech. Engrg.* **191** (47-48), 5467–5483.

Benjamin, T.B. 1957 Wave formation in laminar flow down an inclined plane. *J. Fluid Mech.* **2** (6), 554–574.

Benney, D.J. 1966 Long waves in liquid films. *J. Math. Phys.* **45** (2), 150–155.

Bertozzi, A.L. & Brenner, M.P. 1997 Linear stability and transient growth in driven contact lines. *Phys. Fluids* **9** (3), 530–539.

Bestehorn, M., Pototsky, A. & Thiele, U. 2003 3D large scale Marangoni convection in liquid films. *Eur. Phys. J. B.* **33** (4), 457–467.

Bielarz, C. & Kalliadasis, S. 2003 Time-dependent free-surface thin film flows over topography. *Phys. Fluids* **15** (9), 2512–2524.

Blackford, L.S., Choi, J., Cleary, A., D'Azevedo, E., Demmel, J., Dhillon, I., Dongarra, J., Hammarling, S., Henry, G., Petitet, A., Stanley, K., Walker, D. & Whaley, R.C. 1997 *ScaLAPACK Users' Guide*. SIAM.

Blyth, M.G. 2008 Effect of an electric field on the stability of contaminated film flow down an inclined plane. *J. Fluid Mech.* **595**, 221–237.

Blyth, M.G. 2010 Private communication.

Blyth, M.G. & Pozrikidis, C. 2004 Effect of surfactant on the stability of film flow down an inclined plane. *J. Fluid Mech.* **521**, 241–250.

Blyth, M.G. & Pozrikidis, C. 2006 Film flow down an inclined plane over a three-dimensional obstacle. *Phys. Fluids* **18** (5), 052104.

Bontozoglou, V. 2000 Laminar film flow along a periodic wall. *CMES-Comp. Model. Eng. Sci.* **1** (2), 133–142.

Bontozoglou, V. & Papapolymerou, G. 1997 Laminar film flow down a wavy incline. *Int. J. Multiphas. Flow* **23** (1), 69–79.

Bontozoglou, V. & Serifi, K. 2008 Falling film flow along steep two-dimensional topography: The effect of inertia. *Int. J. Multiphas. Flow* **34** (8), 734–747.

Brezzi, F. 1974 On the existence, uniqueness and approximation of saddle-point problems arising from lagrangian multipliers. *Revue Francaise D Automatique Informatique Recherche Operationnelle* **8** (NR2), 129–151.

Briggs, W.L., Henson, V.E. & McCormick, S.F. 2000 *A Multigrid Tutorial*, 2nd edn. SIAM.

Bunner, B. & Tryggvason, G. 1999 Direct numerical simulations of three-dimensional bubbly flows. *Phys. Fluids* **11** (8), 1967–1969.

Burelbach, J.P., Bankoff, S.G. & Davis, S.H. 1988 Nonlinear stability of evaporating/condensing liquid films. *J. Fluid Mech.* **195**, 463–494.

Burelbach, J.P., Bankoff, S.G. & Davis, S.H. 1990 Steady thermocapillary flows of thin liquid layers. II. Experiment. *Phys. Fluids A* **2** (3), 322–333.

Cairncross, R.A., Schunk, P.R., Baer, T.A., Rao, R.R. & Sackinger, P.A. 2000 A finite element method for free surface flows of incompressible fluids in three dimensions. Part I. Boundary fitted mesh motion. *Int. J. Num. Meth. Fl.* **33** (3), 375–403.

Chang, H.C. 1986 Traveling waves on fluid interfaces: Normal form analysis of the kuramoto-sivashinsky equation. *Phys. Fluids* **29** (10), 3142–3147.

Chang, H.C. 1994 Wave evolution on a falling film. *Annu. Rev. Fluid Mech.* **26**, 103–136.

Chanson, H. 2004 *The Hydraulics of Open Channel Flow: an Introduction*, 2nd edn. Oxford: Elsevier Butterworth-Heinemann.

Chapra, S.C. & Canale, R.P. 2002 *Numerical Methods for Engineers*, 4th edn. New York: McGraw-Hill.

Christodoulou, K.N., Kistler, S.F. & Schunk, P.R. 1997 Advances in computational methods for free surface flows. In *Liquid Film Coating* (ed. S.F. Kistler & P.M. Schweizer), pp. 297–366. Chapman and Hall.

Christov, C.I., Pontes, J., Walgraef, D. & Velarde, M.G. 1997 Implicit time splitting for fourth-order parabolic equations. *Comp. Meth. Appl. Mech. Engrg.* **148** (3-4), 209–224.

Chung, T.J. 2002 *Computational Fluid Dynamics*. Cambridge: Cambridge University Press.

Cowling, N.P., Gaskell, P.H., Lee, Y.C. & Thompson, H.M. 2011 Towards the efficient numerical solution of three-dimensional thin film flows on real surfaces: an evolution of finite-difference based schemes. *Proc. I. Mech. E. part C, J. Mech. Sci.* In Press.

Craster, R.V. & Matar, O.K. 2009 Dynamics and stability of thin liquid films. *Rev. Mod. Phys.* **81** (3), 1131–1198.

Daniels, N., Ehret, P., Gaskell, P.H., Thompson, H.M. & Decré, M.M.J. 2001 Multigrid methods for thin liquid film spreading flows. In *Proc. 1st conf. on computational fluid dynamics 2000* (ed. N. Satofuka), pp. 279–284. Springer.

Davis, J.M. & Troian, S.M. 2005 Generalized linear stability of noninertial coating flows over topographical features. *Phys. Fluids* **17** (7).

Davis, S.H. 1987 Thermocapillary instabilities. *Annu. Rev. Fluid Mech.* **19**, 403–435.

de Santos, J.M., Melli, T.R. & Scriven, L.E. 1991 Mechanics of gas-liquid flow in packed-bed contactors. *Annu. Rev. Fluid Mech.* **23**, 233–260.

Decré, M.M.J. & Baret, J.C. 2003 Gravity-driven flows of viscous liquids over two-dimensional topographies. *J. Fluid Mech.* **487**, 147–166.

Dongarra, J.J., Du Cruz, J., Hammerling, S. & Duff, I.S. 1990 Algorithm 679: A set of level 3 basic linear algebra subprograms: model implementation and test programs. *Acm T. Math. Software* **16** (1), 18–28.

Dormand, J.R. 1996 *Numerical Methods for Differential Equations Computational Approach*. Boca Raton: CRC Press.

Duff, I.S. & Reid, J.K. 1983 The multifrontal solution of indefinite sparse symmetric linear equations. *Acm T. Math. Software* **9** (3), 302–325.

Duff, I.S. & Reid, J.K. 1984 The multifrontal solution of unsymmetric sets of linear equations. *SIAM J. Sci. Comput.* **5** (3), 633–641.

Eberl, H.J. & Sudarsan, R. 2008 Exposure of biofilms to slow flow fields: The convective contribution to growth and disinfection. *J. Theor. Biol.* **253** (4), 788–807.

Fernandez Parent, C., Lammers, J.H. & Decré, M.M.J. 1998 Flow of a gravity driven thin liquid film over one-dimensional topographies. Unclassified report: NL-UR 823/98. Philips Research.

Focke, W.W. & Knibbe, P.G. 1986 Flow visualization in parallel-plate ducts with corrugated walls. *J. Fluid Mech.* **165**, 73–77.

Fosdick, R. & Tang, H. 2009 Surface transport in continuum mechanics. *Math. Mech. Solids* **14** (6), 587–598.

Gallez, D. & Coakley, W.T. 1996 Far-from-equilibrium phenomena in bioadhesion processes. *Heterogeneous Chem. Rev.* **3** (4), 443–475.

Gallez, D., Dewit, A. & Kaufman, M. 1996 Dynamics of a thin liquid film with a surface chemical reaction. *J. Colloid Interf. Sci.* **180** (2), 524–536.

Gaskell, P.H., Jimack, P.K., Koh, Y.Y. & Thompson, H.M. 2008 Development and application of a parallel multigrid solver for the simulation of spreading droplets. *Int. J. Num. Meth. Fl.* **56** (8), 979–989.

Gaskell, P.H., Jimack, P.K., Sellier, M. & Thompson, H.A. 2004*a* Efficient and accurate time adaptive multigrid simulations of droplet spreading. *Int. J. Num. Meth. Fl.* **45** (11), 1161–1186.

Gaskell, P.H., Jimack, P.K., Sellier, M. & Thompson, H.M. 2006 Flow of evaporating, gravity-driven thin liquid films over topography. *Phys. Fluids* **18** (1), 013601.

Gaskell, P.H., Jimack, P.K., Sellier, M., Thompson, H.M. & Wilson, M.C.T. 2004*b* Gravity-driven flow of continuous thin liquid films on non-porous substrates with topography. *J. Fluid Mech.* **509**, 253–280.

Gaskell, P.H. & Lau, A.K.C. 1988 Curvature-compensated convective transport: SMART, a new boundedness- preserving transport algorithm. *Int. J. Num. Meth. Fl.* **8** (6), 617–641.

Gaskell, P.H., Lee, Y.C. & Thompson, H.M. 2010 Thin film flow over and around surface topography: a general solver for the long-wave approximation and related equations. *CMES-Comp. Model. Eng. Sci.* **62** (1), 77–112.

Gaver, D.P. & Grotberg, J.B. 1990 The dynamics of a localized surfactant on a thin-film. *J. Fluid Mech.* **213**, 127–148.

Glass, C.R., Walters, K.F.A., Gaskell, P.H., Lee, Y.C., Thompson, H.M., Emerson, D.R. & Gu, X.J. 2010 Recent advances in computational fluid dynamics relevant to the modelling of pesticide flow on leaf surfaces. *Pest Manag. Sci.* **66** (1), 2–9.

González, A. & Castellanos, A. 1996 Nonlinear electrohydrodynamic waves on films falling down an inclined plane. *Phys. Rev. E* **53** (4), 3573–3578.

Gramlich, C.M., Kalliadasis, S., Homsy, G.M. & Messer, C. 2002 Optimal leveling of flow over one-dimensional topography by Marangoni stresses. *Phys. Fluids* **14** (6), 1841–1850.

Gramlich, C.M., Mazouchi, A. & Homsy, G.M. 2004 Time-dependent free surface Stokes flow with a moving contact line. II. Flow over wedges and trenches. *Phys. Fluids* **16** (5), 1660–1667.

Griffing, E.M., Bankoff, S.G., Miksis, M.J. & Schluter, R.A. 2006 Electrohydrodynamics of thin flowing films. *J. Fluid. Eng.-T. ASME* **128** (2), 276–283.

Griffiths, R.W. 2000 The dynamics of lava flows. *Annu. Rev. Fluid Mech.* **32**, 477–518.

Grotberg, J.B. 1994 Pulmonary flow and transport phenomena. *Annu. Rev. Fluid Mech.* **26**, 529–571.

Grotberg, J.B. 2001 Respiratory fluid mechanics and transport processes. *Annu. Rev. Biomed. Eng.* **3**, 421–457.

Grotberg, J.B. & Jensen, O.E. 2004 Biofluid mechanics in flexible tubes. *Annu. Rev. Fluid Mech.* **36**, 121–147.

Gu, F., Liu, C.J., Yuan, X.G. & Yu, G.C. 2004 CFD simulation of liquid film flow on inclined plates. *Chem. Eng. Technol.* **27** (10), 1099–1104.

Hayes, M., O'Brien, S.B.G. & Lammers, J.H. 2000 Green's function for steady flow over a small two-dimensional topography. *Phys. Fluids* **12** (11), 2845–2858.

Heining, C. 2009 Influence of two- and three-dimensional topography on viscous gravity-driven film flow. PhD thesis, University of Bayreuth.

Heining, C. & Aksel, N. 2009 Bottom reconstruction in thin-film flow over topography: Steady solution and linear stability. *Phys. Fluids* **21** (8), 083605.

Heining, C. & Aksel, N. 2010 Effects of inertia and surface tension on a power-law fluid flowing down a wavy incline. *Int. J. Multiphas. Flow* **36** (11-12), 847–857.

Heining, C., Bontozoglou, V., Aksel, N. & Wierschem, A. 2009 Nonlinear resonance in viscous films on inclined wavy planes. *Int. J. Multiphas. Flow* **35** (1), 78–90.

Helbig, K., Alexeev, A., Gambaryan-Roisman, T. & Stephan, P. 2005 Evaporation of falling and shear-driven thin films on smooth and grooved surfaces. *Flow Turbul. Combust.* **75** (1-4), 85–104.

Helbig, K., Nasarek, R., Gambaryan-Roisman, T. & Stephan, P. 2009 Effect of longitudinal minigrooves on flow stability and wave characteristics of falling liquid films. *J. Heat Trans.-T. ASME* **131** (1), 011601.

Helfrich, K.R. & Melville, W.K. 2006 Long nonlinear internal waves. *Annu. Rev. Fluid Mech.* **38**, 395–425.

Henn, S. 2005 A multigrid method for a fourth-order diffusion equation with application to image processing. *SIAM Journal on Scientific Computing* **27** (3), 831–849.

Hervouet, J.M. 2007 *Hydrodynamics of Free Surface Flows: Modelling with the Finite Element Method*. Chichester: John Wiley & Sons.

Higdon, J.J.L. 1985 Stokes flow in arbitrary two-dimensional domains: shear flow over ridges and cavities. *J. Fluid Mech.* **159** (OCT), 195–226.

Ho, W.K., Tay, A., Lee, L.L. & Schaper, C.D. 2004 On control of resist film uniformity in the microlithography process. *Control Eng. Pract.* **12** (7), 881–892.

Hood, P. & Taylor, C. 1974 Navier-Stokes equations using mixed interpolation. In *Finite Element Method in Flow Problems* (ed. J.T. Oden, O.C. Zienkiewicz, R.H. Gallagher & C. Taylor), pp. 121–132. Huntsville: UAH Press.

Howell, P.D. 2003 Surface-tension-driven flow on a moving curved surface. *J. Eng. Math.* **45** (3-4), 283–308.

Howison, S.D., Moriarty, J.A., Ockendon, J.R., Terrill, E.L. & Wilson, S.K. 1997 A mathematical model for drying paint layers. *J. Eng. Math.* **32** (4), 377–394.

Huppert, H.E. 2006 Gravity currents: a personal perspective. *J. Fluid Mech.* **554**, 299–322.

Jinyun, Y. 1984 Symmetric Gaussian quadrature formulae for tetrahedronal regions. *Comp. Meth. Appl. Mech. Engrg.* **43** (3), 349–353.

Joo, S.W., Davis, S.H. & Bankoff, S.G. 1991 Long-wave instabilities of heated falling films - two-dimensional theory of uniform layers. *J. Fluid Mech.* **230**, 117–146.

Joo, S.W., Davis, S.H. & Bankoff, S.G. 1993 Two- and three-dimensional instabilities and rupture of thin liquid films falling on heated inclined plate. *Nucl. Eng. Des.* **141** (1-2), 225–236.

Kalliadasis, S., Bielarz, C. & Homsy, G.M. 2000 Steady free-surface thin film flows over topography. *Phys. Fluids* **12** (8), 1889–1898.

Kalliadasis, S., Demekhin, E.A., Ruyer-Quil, C. & Velarde, M.G. 2003*a* Thermocapillary instability and wave formation on a film falling down a uniformly heated plane. *J. Fluid Mech.* **492**, 303–338.

Kalliadasis, S. & Homsy, G.M. 2001 Stability of free-surface thin-film flows over topography. *J. Fluid Mech.* **448**, 387–410.

Kalliadasis, S., Kiyashko, A. & Demekhin, E.A. 2003*b* Marangoni instability of a thin liquid film heated from below by a local heat source. *J. Fluid Mech.* **475**, 377–408.

Karypis, G. & Kumar, V. 1998 METIS: A software package for partitioning unstructured graphs, partitioning meshes, and computing fill-reducing orderings of sparse matrices. *Tech. Rep.*. University of Minnesota, Minneapolis, MN.

Keast, P. 1986 Moderate-degree tetrahedral quadrature-formulas. *Comp. Meth. Appl. Mech. Engrg.* **55** (3), 339–348.

Kelley, C.T. 2003 *Solving Nonlinear Equations with Newton's Method*. SIAM.

Kelmanson, M.A. & Lonsdale, B. 1996 Eddy genesis in the double-lid-driven cavity. *Q. J. Mech. Appl. Math.* **49**, 635–655.

Khayat, R.E., Kim, K.T. & Delosquer, S. 2004 Influence of inertia, topography and gravity on transient axisymmetric thin-film flow. *Int. J. Num. Meth. Fl.* **45** (4), 391–419.

Kim, H., Bankoff, S.G. & Miksis, M.J. 1992 The effect of an electrostatic field on film flow down an inclined plane. *Phys. Fluids A* **4** (10), 2117–2130.

Kim, H., Bankoff, S.G. & Miksis, M.J. 1994 The cylindrical electrostatic liquid film radiator for heat rejection in space. *J. Heat Trans.-T. ASME* **116** (4), 986–992.

Kistler, S.F. & Schweizer, P.M, ed. 1997 *Liquid Film Coating*. Chapman and Hall.

Kistler, S.F. & Scriven, L.E. 1983 Coating flows. In *Computational Analysis of Polymer Processing* (ed. J.R.A. Pearson & S.M. Richardson), chap. 8, pp. 243–299. London: Elsevier Applied Science.

Kondic, L. & Diez, J. 2001 Pattern formation in the flow of thin films down an incline: Constant flux configuration. *Phys. Fluids* **13** (11), 3168–3184.

Kondic, L. & Diez, J.A. 2005 On nontrivial traveling waves in thin film flows including contact lines. *Phys. D Nonlinear Phenom.* **209** (1-4), 135–144.

Kuffel, E., Zaengl, W.S. & Kuffel, J. 2000 *High Voltage Engineering*, 2nd edn. Butterworth-Heinemann.

Ladyzhenskaya, O.A. 1963 *The Mathematical Theory of Viscous Incompressible Flow*, 2nd edn. New York: Gordon and Breach.

Landau, L.D. & Lifshitz, E.M. 1984 *Electrodynamics of Continuous Media*, 2nd edn. Oxford: Pergamon.

Landau, L.D. & Lifshitz, E.M. 1987 *Fluid Mechanics*, 2nd edn. Oxford: Pergamon.

Laughton, M.A. & Warne, D.F. 2003 *Electrical Engineer's Reference Book*, 16th edn. Newnes.

Lee, S.Y., Bush, J.W.M., Hosoi, A.E. & Lauga, E. 2008*a* Crawling beneath the free surface: Water snail locomotion. *Phys. Fluids* **20** (8), 082106.

Lee, Y.C., Thompson, H.M. & Gaskell, P.H. 2007 An efficient adaptive multigrid algorithm for predicting thin film flow on surfaces containing localised topographic features. *Comput. Fluids* **36** (5), 838–855.

Lee, Y.C., Thompson, H.M. & Gaskell, P.H. 2008*b* The efficient and accurate solution of continuous thin film flow over surface patterning and past occlusions. *Int. J. Num. Meth. Fl.* **56** (8), 1375–1381.

Lee, Y.C., Thompson, H.M. & Gaskell, P.H. 2009*a* FILMPAR: A parallel algorithm designed for the efficient and accurate computation of thin film flow on functional surfaces containing micro-structure. *Comput. Phys. Commun.* **180** (12), 2634–2649.

Lee, Y.C., Thompson, H.M. & Gaskell, P.H. 2009*b* Thin film flow over flexible membranes containing surface texturing: bio-inspired solutions. *Proc. I. Mech. E. part J, J. Eng. Tribol.* **223** (J3), 337–345.

Lin, S.P. 1974 Finite amplitude side-band stability of a viscous film. *J. Fluid Mech.* **63** (3), 417–429.

Liu, J.W.H. 1990 The role of elimination trees in sparse factorization. *SIAM J. Matr Anal. Appl.* **11** (1), 134–172.

Liu, J.W.H. 1992 The multifrontal method for sparse matrix solution: Theory and practice. *SIAM Rev.* **34** (1), 82–109.

Liu, J. & Gollub, J.P. 1993 Onset of spatially chaotic waves on flowing films. *Phys. Rev. Lett.* **70** (15), 2289–2292.

Liu, J. & Gollub, J.P. 1994 Solitary wave dynamics of film flows. *Phys. Fluids* **6** (5), 1702–1712.

Liu, J., Paul, J.D. & Gollub, J.P. 1993 Measurements of the primary instabilities of film flows. *J. Fluid Mech.* **250**, 69–101.

Liu, Y. & Vinokur, M. 1998 Exact integrations of polynomials and symmetric quadrature formulas over arbitrary polyhedral grids. *J. Comput. Phys.* **140** (1), 122–147.

Lucea, M., Decré, M.M.J. & Lammers, J.H. 1999 Flow of a gravity driven thin liquid film over one-dimensional topographies: A detailed comparison of theory and experiments. Unclassified report: NL-UR 823/98. Philips Research.

Luo, H. & Pozrikidis, C. 2006 Effect of inertia on film flow over oblique and three-dimensional corrugations. *Phys. Fluids* **18** (12), 078107.

Luo, H. & Pozrikidis, C. 2007 Gravity-driven film flow down an inclined wall with three-dimensional corrugations. *Acta Mech.* **188** (3-4), 209–225.

Mahlmann, S. & Papageorgiou, D.T. 2009 Numerical study of electric field effects on the deformation of two-dimensional liquid drops in simple shear flow at arbitrary Reynolds number. *J. Fluid Mech.* **626**, 367–393.

Malamataris, N.A. & Bontozoglou, V. 1999 Computer aided analysis of viscous film flow along an inclined wavy wall. *J. Comput. Phys.* **154** (2), 372–392.

Malamataris, N.A., Vlachogiannis, M. & Bontozoglou, V. 2002 Solitary waves on inclined films: Flow structure and binary interactions. *Phys. Fluids* **14** (3), 1082–1094.

Matar, O.K., Craster, R.V. & Kumar, S. 2007 Falling films on flexible inclines. *Phys. Rev. E* **76** (5).

Mazouchi, A., Gramlich, C.M. & Homsy, G.M. 2004 Time-dependent free surface Stokes flow with a moving contact line. I. Flow over plane surfaces. *Phys. Fluids* **16** (5), 1647–1659.

Mazouchi, A. & Homsy, G.M. 2001 Free surface Stokes flow over topography. *Phys. Fluids* **13** (10), 2751–2761.

Meek, J.M. & Craggs, J.D. 1978 *Electrical Breakdown of Gases*. John Wiley & Sons.

Melcher, J.R. & Smith, C.V. 1969 Electrohydrodynamic charge relaxation and interfacial perpendicular-field instability. *Phys. Fluids* **12** (4), 778–790.

Menetrier-Deremble, L. & Tabeling, P. 2006 Droplet breakup in microfluidic junctions of arbitrary angles. *Phys. Rev. E* **74** (3), 4.

Messé, S. & Decré, M.M.J. 1997 Experimental study of a gravity driven water film flowing down inclined plates with different patterns. Unclassified report: NL-UR 030/97. Philips Research.

Morton, K.W. 1996 *Numerical Solution of Convection-Diffusion Problems*. London: Chapman and Hall.

Nagaraja, K.V. & Rathod, H.T. 2010 Symmetric Gauss Legendre quadrature rules for numerical integration over an arbitrary linear tetrahedra in Euclidean three-dimensional space. *Int. J. Math. Anal.* **4** (19), 921–928.

Nakajima, K. & Miyamoto, K. 1993 Coating method. European patent 0,530,752 A1.

Nakaya, C. 1975 Long waves on a thin fluid layer flowing down an inclined plane. *Phys. Fluids* **18** (11), 1407–1412.

Nguyen, L.T. & Balakotaiah, V. 2000 Modeling and experimental studies of wave evolution on free falling viscous films. *Phys. Fluids* **12** (9), 2236–2256.

Oddy, M.H., Santiago, J.G. & Mikkelsen, J.C. 2001 Electrokinetic instability micromixing. *Anal. Chem.* **73** (24), 5822–5832.

Oron, A. 2000 Nonlinear dynamics of three-dimensional long-wave Marangoni instability in thin liquid films. *Phys. Fluids* **12** (7), 1633–1645.

Oron, A., Davis, S.H. & Bankoff, S.G. 1997 Long-scale evolution of thin liquid films. *Rev. Mod. Phys.* **69** (3), 931–980.

Oron, A. & Rosenau, P. 1992 Formation of patterns induced by thermocapillarity and gravity. *J. Phys. II France* **2** (2), 131–146.

Pan, F. & Acrivos, A. 1967 Steady flows in rectangular cavities. *J. Fluid Mech.* **28**, 643–655.

Peurrung, L.M. & Graves, D.B. 1991 Film thickness profiles over topography in spin coating. *J. Electrochem. Soc.* **138** (7), 2115–2124.

Peurrung, L.M. & Graves, D.B. 1993 Spin coating over topography. *IEEE Trans. Semicond. Manu.* **6** (1), 72–76.

Pozrikidis, C. 1988 The flow of a liquid film along a periodic wall. *J. Fluid Mech.* **188**, 275–300.

Pozrikidis, C. 2003 Effect of surfactants on film flow down a periodic wall. *J. Fluid Mech.* **496**, 105–127.

Pozrikidis, C. & Thoroddsen, S.T. 1991 The deformation of a liquid-film flowing down an inclined plane wall over a small particle arrested on the wall. *Phys. Fluids A* **3** (11), 2546–2558.

Pritchard, W.G., Scott, L.R. & Tavener, S.J. 1992 Numerical and asymptotic methods for certain viscous free-surface flows. *Philos. T. Roy. Soc. A* **340** (1656), 1–45.

Ramaswamy, B., Chippada, S. & Joo, S.W. 1996 A full-scale numerical study of interfacial instabilities in thin-film flows. *J. Fluid Mech.* **325**, 163–194.

Rathod, H.T., Nagaraja, K.V. & Venkatesudu, B. 2007 Symmetric Gauss Legendre quadrature formulas for composite numerical integration over a triangular surface. *Appl. Math. Comput.* **188** (1), 865–876.

Rathod, H.T., Nagaraja, K.V., Venkatesudu, B. & Ramesh, N.L. 2004 Gauss Legendre quadrature over a triangle. *J. Indian Inst. Sci.* **84**, 183–188.

Rathod, H.T., Venkatesudu, B. & Nagaraja, K.V. 2006 Gauss Legendre quadrature formulas over a tetrahedron. *Numer. Meth. Part. D. E.* **22** (1), 197–219.

Roberts, A.J. & Li, Z.Q. 2006 An accurate and comprehensive model of thin fluid flows with inertia on curved substrates. *J. Fluid Mech.* **553**, 33–73.

Roy, R.V., Roberts, A.J. & Simpson, M.E. 2002 A lubrication model of coating flows over a curved substrate in space. *J. Fluid Mech.* **454**, 235–261.

Ruyer-Quil, C. & Manneville, P. 1998 Modeling film flows down inclined planes. *Eur. Phys. J. B.* **6** (2), 277–292.

Ruyer-Quil, C. & Manneville, P. 2000 Improved modeling of flows down inclined planes. *Eur. Phys. J. B.* **15** (2), 357–369.

Ruyer-Quil, C. & Manneville, P. 2002 Further accuracy and convergence results on the modeling of flows down inclined planes by weighted-residual approximations. *Phys. Fluids* **14** (1), 170–183.

Ruyer-Quil, C., Scheid, B., Kalliadasis, S., Velarde, M.G. & Zeytounian, R.K. 2005 Thermocapillary long waves in a liquid film flow. Part 1. Low-dimensional formulation. *J. Fluid Mech.* **538**, 199–222.

Sackinger, P.A., Schunk, P.R. & Rao, R.R. 1996 A Newton-Raphson pseudo-solid domain mapping technique for free and moving boundary problems: A finite element implementation. *J. Comput. Phys.* **125** (1), 83–103.

Saint-Venant, A.J.C. 1871 Théorie du mouvement non-permanent des eaux avec application aux crues des rivières et à l'introduction des marées dans leur lit. *Compte-Rendu à l'Académie des Sciences de Paris* **73**, 147–154.

Saprykin, S., Koopmans, R.J. & Kalliadasis, S. 2007*a* Free-surface thin-film flows over topography: influence of inertia and viscoelasticity. *J. Fluid Mech.* **578**, 271–293.

Saprykin, S., Trevelyan, P.M.J., Koopmans, R.J. & Kalliadasis, S. 2007*b* Free-surface thin-film flows over uniformly heated topography. *Phys. Rev. E* **75** (2).

Schaffer, E., Thurn-Albrecht, T., Russell, T.P. & Steiner, U. 2000 Electrically induced structure formation and pattern transfer. *Nature* **403** (6772), 874–877.

Scheid, B., Kalliadasis, S., Ruyer-Quil, C. & Colinet, P. 2008 Interaction of three-dimensional hydrodynamic and thermocapillary instabilities in film flows. *Phys. Rev. E* **78** (6).

Scheid, B., Oron, A., Colinet, P., Thiele, U. & Legros, J.C. 2002 Nonlinear evolution of nonuniformly heated falling liquid films. *Phys. Fluids* **14** (12), 4130–4151.

Scheid, B., Ruyer-Quil, C., Kalliadasis, S., Velarde, M.G. & Zeytounian, R.K. 2005 Thermocapillary long waves in a liquid film flow. Part 2. Linear stability and nonlinear waves. *J. Fluid Mech.* **538**, 223–244.

Scholle, M. & Aksel, N. 2007 A general free surface rule for Stokes flow of fluid films over obstacles. *Acta Mech.* **191** (3-4), 155–159.

Scholle, M., Haas, A., Aksel, N., Thompson, H.M., Hewson, R.W. & Gaskell, P.H. 2009*a* The effect of locally induced flow structure on global heat transfer for plane laminar shear flow. *Int. J. Heat Fluid Fl.* **30** (2), 175–185.

Scholle, M., Haas, A., Aksel, N., Wilson, M.C.T., Thompson, H.M. & Gaskell, P.H. 2008 Competing geometric and inertial effects on local flow structure in thick gravity-driven fluid films. *Phys. Fluids* **20** (12), 123101.

Scholle, M., Haas, A., Aksel, N., Wilson, M.C.T., Thompson, H.M. & Gaskell, P.H. 2009*b* Eddy genesis and manipulation in plane laminar shear flow. *Phys. Fluids* **21** (7).

Scholle, M., Rund, A. & Aksel, N. 2006 Drag reduction and improvement of material transport in creeping films. *Arch. Appl. Mech.* **75** (2-3), 93–112.

Scholle, M., Wierschem, A. & Aksel, N. 2004 Creeping films with vortices over strongly undulated bottoms. *Acta Mech.* **168** (3-4), 167–193.

Schwartz, L.W. & Eley, R.R. 1998 Simulation of droplet motion on low-energy and heterogeneous surfaces. *J. Colloid Interf. Sci.* **202** (1), 173–188.

Sellier, M. 2008 Substrate design or reconstruction from free surface data for thin film flows. *Phys. Fluids* **20** (6), 062106.

Sellier, M., Lee, Y.C., Thompson, H.M. & Gaskell, P.H. 2009 Thin film flow on surfaces containing arbitrary occlusions. *Comput. Fluids* **38** (1), 171–182.

Sellier, M. & Panda, S. 2010 Beating capillarity in thin film flows. *Int. J. Num. Meth. Fl.* **63** (4), 431–448.

Serifi, K., Malamataris, N.A. & Bontozoglou, V. 2004 Transient flow and heat transfer phenomena in inclined wavy films. *Int. J. Therm. Sci.* **43** (8), 761–767.

Shankar, P.N. & Deshpande, M.D. 2000 Fluid mechanics in the driven cavity. *Annu. Rev. Fluid Mech.* **32**, 93–136.

Shen, C. & Floryan, J.M. 1985 Low Reynolds number flow over cavities. *Phys. Fluids* **28** (11), 3191–3202.

Sheu, T.W.H. & Tsai, S.F. 2002 Flow topology in a steady three-dimensional lid-driven cavity. *Comput. Fluids* **31** (8), 911–934.

Shinbrot, M. 1970 Shallow water equations. *J. Eng. Math.* **4** (4), 293–304.

Shkadov, V.Y. 1967 Wave flow regimes of a thin layer of viscous fluid subject to gravity. *Izv. Akad. Nauk SSSR Fluid Dynamics* **2** (1), 29–34.

Shkadov, V.Y. 1968 Wave-flow theory for a thin viscous liquid layer. *Izv. Akad. Nauk SSSR Fluid Dynamics* **3** (2), 12–15.

Shuaib, N.H., Power, H. & Hibberd, S. 2006 Multiple solutions of gravity and surface shear driven thin film flows over a rectangular cavity. *Phys. Fluids* **18** (5).

Shuaib, N.H., Power, H. & Hibberd, S. 2009 Bem solution of thin film flows on an inclined plane with a bottom outlet. *Eng. Anal. Bound. Elem.* **33** (3), 388–398.

Shyy, W., Francois, M., Udaykumar, H.S., N'dri, N. & Tran-Son-Tay, R. 2001 Moving boundaries in micro-scale biofluid dynamics. *Appl. Mech. Rev.* **54** (5), 405–454.

Shyy, W., Udaykumar, H.S., Rao, M.M. & Smith, R.W. 2007 *Computational Fluid Dynamics with Moving Boundaries*. Dover Publications.

Skotheim, J.M., Thiele, U. & Scheid, B. 2003 On the instability of a falling film due to localized heating. *J. Fluid Mech.* **475**, 1–19.

Snir, M., Otto, S.W., Huss-Lederman, S., Walker, D.W. & Dongarra, J. 1996 *MPI: The Complete Reference*. Cambridge, Massachusetts: The MIT Press.

Spurk, J.H. & Aksel, N. 2008 *Fluid Mechanics*, 2nd edn. Springer.

Stillwagon, L.E. & Larson, R.G. 1988 Fundamentals of topographic substrate leveling. *J. Appl. Phys.* **63** (11), 5251–5258.

Stillwagon, L.E. & Larson, R.G. 1990 Leveling of thin-films over uneven substrates during spin coating. *Phys. Fluids A* **2** (11), 1937–1944.

Stillwagon, L.E., Larson, R.G. & Taylor, G.N. 1987 Planarization of substrate topography by spin coating. *J. Electrochem. Soc.* **134** (8), 2030–2037.

Streeter, V.L. & Wylie, E.B. 1981 *Fluid Mechanics*. Toronto: McGraw-Hill.

Tabeling, P. 2005 *Introduction to Microfluidics*. Oxford: Oxford University Press.

Tan, M.J., Bankoff, S.G. & Davis, S.H. 1990 Steady thermocapillary flows of thin liquid layers. I. Theory. *Phys. Fluids A* **2** (3), 313–321.

Taneda, S. 1979 Visualization of separating Stokes flow. *J. Phys. Soc. Jpn.* **46** (6), 1935–1942.

Tiwari, N. & Davis, J.M. 2010 Stabilization of thin liquid films flowing over locally heated surfaces via substrate topography. *Phys. Fluids* **22** (4).

Torczynski, J.R. & O'Hern, T.J. 1995 Numerical simulations of flow in a three-dimensional cavity-channel geometry. *Tech. Rep.*. Sandia National Laboratories.

Trifonov, Y.Y. 1999 Viscous liquid film flows over a periodic surface. *Int. J. Multiphas. Flow* **24** (7), 1139–1161.

Trifonov, Y.Y. 2004 Viscous film flow down corrugated surfaces. *J. Appl. Mech. Tech. Phys.* **45** (3), 389–400.

Trifonov, Y.Y. 2007 Stability of a viscous liquid film flowing down a periodic surface. *Int. J. Multiphas. Flow* **33**, 1186–1204.

Trottenberg, U., Oosterlee, C.W. & Schüller, A. 2001 *Multigrid*. Academic Press.

Tseluiko, D. & Blyth, M.G. 2009 Effect of inertia on electrified film flow over a wavy wall. *J. Eng. Math.* **65** (3), 229–242.

Tseluiko, D., Blyth, M.G., Papageorgiou, D.T. & Vanden-Broeck, J.M. 2007 Free-surface film flow over topography under electric fields. In *Proc. 6th International Congress on Industrial Applied Mathematics (ICIAM07)*. Zurich, Switzerland.

Tseluiko, D., Blyth, M.G., Papageorgiou, D.T. & Vanden-Broeck, J.M. 2008*a* Effect of an electric field on film flow down a corrugated wall at zero Reynolds number. *Phys. Fluids* **20** (4), 042103.

Tseluiko, D., Blyth, M.G., Papageorgiou, D.T. & Vanden-Broeck, J.M. 2008*b* Electrified viscous thin film flow over topography. *J. Fluid Mech.* **597**, 449–475.

Tseluiko, D., Blyth, M.G., Papageorgiou, D.T. & Vanden-Broeck, J.M. 2009 Viscous electrified film flow over step topography. *SIAM J. Appl. Math.* **70** (3), 845–865.

Tseluiko, D. & Papageorgiou, D.T. 2006*a* Nonlinear dynamics of electrified thin liquid films. *SIAM J. Appl. Math.* **67** (5), 1310–1329.

Tseluiko, D. & Papageorgiou, D.T. 2006*b* Wave evolution on electrified falling films. *J. Fluid Mech.* **556**, 361–386.

Tsorng, S.J., Capart, H., Lai, J.S. & Young, D.L. 2006 Three-dimensional tracking of the long time trajectories of suspended particles in a lid-driven cavity flow. *Exp. Fluids* **40** (2), 314–328.

Uma, B. & Usha, R. 2008 A thin conducting viscous film on an inclined plane in the presence of a uniform normal electric field: Bifurcation scenarios. *Phys. Fluids* **20** (3), 032102–032117.

Usha, R. & Uma, B. 2004 Modeling of stationary waves on a thin viscous film down an inclined plane at high Reynolds numbers and moderate Weber numbers using energy integral method. *Phys. Fluids* **16** (7), 2679–2696.

VanHook, S.J., Schatz, M.F., McCormick, W.D., Swift, J.B. & Swinney, H.L. 1995 Long-wave instability in surface-tension-driven Benard convection. *Phys. Rev. Lett.* **75** (24), 4397–4400.

Veremieiev, S., Gaskell, P.H., Lee, Y.C. & Thompson, H.M. 2009 Electric fields as a means of controlling thin film flow over topography. In *Proceedings on CDROM of 2nd Micro and Nano Flows Conference MNF-2009*, pp. 21:1–8. Brunel University, West London, UK.

Veremieiev, S., Gaskell, P.H., Lee, Y.C. & Thompson, H.M. 2011*a* Predicting three-dimensional inertial thin film flow over micro-scale topography. In *Computational Fluid Dynamics 2010*. Springer, Engineering series. In Press, Accepted for Publication.

Veremieiev, S., Thompson, H.M., Lee, Y.C. & Gaskell, P.H. 2010*a* Inertial thin film flow on planar surfaces featuring topography. *Comput. Fluids* **39** (3), 431–450.

Veremieiev, S., Thompson, H.M., Lee, Y.C. & Gaskell, P.H. 2010*b* Inertial two- and three-dimensional thin film flow over topography. *Chem. Eng. Process.: Process Intens.* In Press, Corrected Proof.

Veremieiev, S., Thompson, H.M., Lee, Y.C. & Gaskell, P.H. 2010*c* Three-dimensional inertial thin film flow on planar substrates containing occlusions. In *Proceedings on CDROM of 5th European Conference on Computational Fluid Dynamics ECCOMAS CFD 2010* (ed. J.C.F. Pereira, A. Sequeira & J.M.C. Pereira), pp. 01399:1–11. Lisbon, Portugal.

Veremieiev, S., Thompson, H.M., Scholle, M., Lee, Y.C. & Gaskell, P.H. 2011*b* Electrified thin film flow at finite Reynolds number on planar surfaces featuring topography. In Press, Submitted for Review.

Vlachogiannis, M. & Bontozoglou, V. 2002 Experiments on laminar film flow along a periodic wall. *J. Fluid Mech.* **457**, 133–156.

Walkley, M.A., Gaskell, P.H., Jimack, P.K., Kelmanson, M.A. & Summers, J.L. 2005 Finite element simulation of three-dimensional free-surface flow problems. *J. Sci. Comput.* **24** (2), 147–162.

Walters, D.R. 2006 Disguising the leaf surface: the use of leaf coatings for plant disease control. *Eur. J. Plant Pathol.* **114** (3), 255–260.

Wandzura, S. & Xiao, H. 2003 Symmetric quadrature rules on a triangle. *Comput. Math. Appl.* **45** (12), 1829–1840.

Wang, C.Y. 1981 Liquid film flowing slowly down a wavy incline. *A.I.Ch.E. J.* **27** (2), 207–212.

Wang, C.Y. 1984 Thin film flowing down a curved surface. *Zeitschrift Fur Angewandte Mathematik Und Physik* **35** (4), 532–544.

Wang, C.Y. 2005 Low Reynolds number film flow down a three-dimensional bumpy surface. *J. Fluid. Eng.-T. ASME* **127** (6), 1122–1127.

Wang, X.P. & Li, X.K. 2010 Numerical simulation of three dimensional non-Newtonian free surface flows in injection molding using ALE finite element method. *Finite Elem. Anal. Des.* **46** (7), 551–562.

Webb, R.L. 1994 *Principles of Enhanced Heat Transfer*. The University of Michigan: John Wiley & Sons.

Weinstein, S.J. & Ruschak, K.J. 2004 Coating rows. *Annu. Rev. Fluid Mech.* **36**, 29–53.

Wierschem, A. 2004 Gravity driven film flow over undulated substrates. Habilitationsschrift. University of Bayreuth.

Wierschem, A. & Aksel, N. 2003 Instability of a liquid film flowing down an inclined wavy plane. *Phys. D Nonlinear Phenom.* **186** (3-4), 221–237.

Wierschem, A. & Aksel, N. 2004 Influence of inertia on eddies created in films creeping over strongly undulated substrates. *Phys. Fluids* **16** (12), 4566–4574.

Wierschem, A., Bontozoglou, V., Heining, C., Uecker, H. & Aksel, N. 2008 Linear resonance in viscous films on inclined wavy planes. *Int. J. Multiphas. Flow* **34** (6), 580–589.

Wierschem, A., Lepski, C. & Aksel, N. 2005 Effect of long undulated bottoms on thin gravity-driven films. *Acta Mech.* **179** (1-2), 41–66.

Wierschem, A., Pollak, T., Heining, C. & Aksel, N. 2010 Suppression of eddies in films over topography. *Phys. Fluids* **22** (11), 113603.

Wierschem, A., Scholle, M. & Aksel, N. 2002 Comparison of different theoretical approaches to experiments on film flow down an inclined wavy channel. *Exp. Fluids* **33** (3), 429–442.

Wierschem, A., Scholle, M. & Aksel, N. 2003 Vortices in film flow over strongly undulated bottom profiles at low Reynolds numbers. *Phys. Fluids* **15** (2), 426–435.

Wilson, S.K. & Duffy, B.R. 1998 On the gravity-driven draining of a rivulet of viscous fluid down a slowly varying substrate with variation transverse to the direction of flow. *Phys. Fluids* **10** (1), 13–22.

Wilson, S.K. & Duffy, B.R. 2005 A rivulet of perfectly wetting fluid draining steadily down a slowly varying substrate. *IMA J. Appl. Math.* **70** (2), 293–322.

Wilson, S.K., Duffy, B.R. & Davis, S.H. 2001 On a slender dry patch in a liquid film draining under gravity down an inclined plane. *Eur. J. Appl. Math.* **12**, 233–252.

Wilson, S.K., Duffy, B.R. & Ross, A.B. 2002 On the gravity-driven draining of a rivulet of a viscoplastic material down a slowly varying substrate. *Phys. Fluids* **14** (2), 555–571.

Wright, N.G. & Gaskell, P.H. 1995 An efficient multigrid approach to solving highly recirculating flows. *Comput. Fluids* **24** (1), 63–79.

Wu, N., Pease, L.F. & Russel, W.B. 2005 Electric-field-induced patterns in thin polymer films: Weakly nonlinear and fully nonlinear evolution. *Langmuir* **21** (26), 12290–12302.

Yeo, L.Y., Craster, R.V. & Matar, O.K. 2007 Drop manipulation and surgery using electric fields. *J. Colloid Interf. Sci.* **306** (2), 368–378.

Yih, C.S. 1963 Stability of liquid flow down an inclined plane. *Phys. Fluids* **6** (3), 321–334.

Yoshimura, P.N., Nosoko, T. & Nagata, T. 1996 Enhancement of mass transfer into a falling laminar liquid film by twig-dimensional surface waves - Some experimental observations and modeling. *Chem. Eng. Sci.* **51** (8), 1231–1240.

Yue, B.Z. & Wang, Z.L. 2006 Numerical study of three-dimensional free surface dynamics. *Acta Mech. Sinica* **22** (2), 120–126.

Zhao, L. & Cerro, R.L. 1992 Experimental characterization of viscous film flows over complex surfaces. *Int. J. Multiphas. Flow* **18** (4), 495–516.

Zhornitskaya, L. & Bertozzi, A.L. 2000 Positivity-preserving numerical schemes for lubrication-type equations. *SIAM J. Numer. Anal.* **37** (2), 523–555.